In Situ X-ray Scattering Studies of Ultrathin Epitaxial Metal Oxide Films

DISSERTATION

in fulfilment of the requirements for the degree of
Doctor of Natural Sciences (Dr. rer. nat.)
of the Faculty of Mathematics and Natural Sciences
at Kiel University
submitted by

Finn Reikowski

Kiel, 2019

First examiner:	Prof. Dr. Olaf M. Magnussen
Second examiner:	Prof. Dr. Jan Benedikt
Date of the oral examination:	07.06.2019

Abstract

This work combines electrochemical studies of thin epitaxial metal and metal oxide films with advanced *in situ* and *operando* surface X-ray diffraction (SXRD). This combination enables the correlation of reactive processes with the structure of the interfaces at which they occur. In the focus of our studies are Co oxides, which are promising candidates for the precious-metal-free catalysis of the oxygen evolution reaction (OER).

One way to obtain thin oxide films is the anodic metal oxidation. Co deposition on Au(111) single crystal electrodes results in thin epitaxial films with a thickness of a few nanometer and a (001) orientation. Subsequent oxidation commences with the adsorption of OH followed by the rapid formation of an ultra thin passive film of $Co(OH)_2$ covering the entire surface. On longer timescales, inhomogeneous growth of 3D $Co(OH)_2$ crystallites is observed. Direct observation of the continuous passive films and of passive films of higher oxidation states was not possible.

Therefore, thin epitaxial films of Co_3O_4 and CoOOH, which are the phases of interest for OER catalysis, were directly electrodeposited on Au(111) substrates. To investigate these films under operation conditions, a novel electrochemical cell was developed, which allows measurements under strong gas evolution and current densities of $150\,\mathrm{mA\,cm^{-2}}$. While the CoOOH film is completely stable in the whole OER potential regime, Co_3O_4 forms an ≈ 1 nm thick skin layer 300 mV negative of the onset of OER. The formation of this skin layer is fast, highly reversible and its thickness increases linearly with the applied potential. Despite this very different structural behaviour, the catalytic activity of the two phases is very similar. This is at variance with previous assumptions about the catalytically active sites in Co oxide based catalysts.

Aside from the OER motivated studies, we investigated magnetic Pd/Co/Au(111) stacks. Pd deposition on Co/Au(111) grown analogous to the oxidation experiments results in an epitaxial capping layer with (111) orientation. Magneto optical Kerr effect (MOKE) measurements show that the magnetic anisotropy of the film can be reversibly modified by the electrochemically induced absorption/removal of H from the Pd capping layer. Structural analysis by SXRD reveals that the resulting Pd lattice expansion/contraction induces a reversible strain in the Co film. However, this strain appears to be too small to account for the full changes observed in the magnetic anisotropy.

Furthermore, transmission surface diffraction (TSD), a novel high-energy SXRD technique, was developed. TSD uses a transmission geometry which has the advantage that large 2D detectors placed behind the sample capture a large fraction of the in-plane structure in a single acquisition. Due to the normal incidence, the beam footprint is given by the focus of the beam which enables real space mapping of the structural properties. This makes TSD an interesting method for the investigation of interfaces exhibiting inhomogeneities on the micrometer scale.

Kurzfassung

In dieser Arbeit werden elektrochemische Untersuchungen von dünnen epitaktischen Metall- und Metalloxidfilmen mit detaillierter *in situ* und *operando* oberflächensensitiver Röntgenbeugung (SXRD) kombiniert. Dadurch können reaktive Prozesse mit der Struktur der Grenzfläche, an der sie auftreten, korreliert werden. Im Mittelpunkt stehen dabei Kobaltoxide im Hinblick auf die edelmetallfreie Katalyse der Sauerstoffentwicklungsreaktion (OER).

Dazu wird Kobalt auf Au(111)-Einkristallelektroden abgeschieden und anschließend anodisch oxidiert. Die Kobaltfilme wachsen epitaktisch mit einer (001)-Ausrichtung und einer Dicke von einigen Nanometern. Anschließende Oxidation beginnt mit der Adsorption von OH, gefolgt von der schnellen Bildung einer ultradünnen und vollständigen $Co(OH)_2$-Passivschicht. Auf längeren Zeitskalen ergibt sich ein inhomogenes Wachstum von 3D $Co(OH)_2$-Kristalliten. Die Passivschicht, auch von höheren Oxidationsstufen, war nur indirekt nachweisbar.

Daher werden dünne epitaktische Co_3O_4- und CoOOH-Filme, direkt auf Au(111)-Substraten abgeschieden und in einer eigens entwickelten elektrochemischen Zelle unter Operationsbedingungen (starke Gasentwicklung, Stromdichten bis 150 mA cm^{-2}) untersucht. Während der CoOOH-Film im Potenzialbereich der Sauerstoffentwicklung nahezu vollständig stabil ist, bildet Co_3O_4 eine ≈ 1 nm dicke Deckschicht aus. Die Schichtbildung beginnt 300 mV negativer als die Sauerstoffentwicklung und ist sowohl schnell als auch reversibel, wobei die Schichtdicke linear vom Elektrodenpotenzial abhängt. Trotz dieser strukturell sehr unterschiedlichen Verhaltensweise, ist die katalytische Aktivität beider Phasen sehr ähnlich. Dies steht im Widerspruch zu bisherigen Annahmen über die katalytisch aktiven Zentren kobaltoxidbasierter Katalysatoren.

Des Weiteren wurden magnetische Pd/Co/Au(111)-Schichtsysteme untersucht. Die Palladiumabscheidung auf Co(001)/Au(111) (s. o.), führt zu einer epitaktischen Deckschicht mit (111)-Ausrichtung. Magneto-Optischer Kerr-Effekt (MOKE) Messungen zeigen, dass die magnetische Anisotropie des Filmes durch die elektrochemisch induzierte Wasserstoff-Aufnahme/Abgabe des Palladiums verändert werden kann. Oberflächenempfindliche Röntgenbeugungsanalyse zeigt, dass die resultierende Palladiumgitter-Ausdehnung/Kontraktion teilweise in das Kobaltgitter übertragen wird. Die Modifikation der Kobaltgitterparameter erscheint dabei allerdings zu gering, um die vollständigen Veränderungen der magnetischen Anisotropie zu erklären.

Darüber hinaus wurde “Transmission Surface Diffraction” (TSD), eine neuartige Hochenergie-SXRD-Methode, entwickelt. TSD verwendet eine Transmissionsgeometrie, bei der große 2D-Detektoren in einer einzigen Aufnahme große Teile der Struktur parallel zur Oberfläche erfassen. Da der Strahl senkrecht auf die Probe trifft, ist die Projektion des Strahls auf die Oberfläche durch den Strahlenquerschnitt gegeben, was eine ortsaufgelöste Bestimmung der Struktureigenschaften der Probe möglich macht. Dadurch ist TSD eine interessante Methode zur Untersuchung von Grenzflächen, welche Inhomogenitäten auf der Mikrometerskala aufweisen.

Contents

1 Introduction

Among the greatest challenges of this century is the development of a sustainable energy infrastructure based on renewable energy sources and the renunciation of fossil fuels[1]. While the production of renewable energy is already possible at industrial dimensions by solar, wind and hydroelectric power plants, the storage of renewable energy is still a mayor issue[2]. The production rate of renewable energy is largely dependent on the meteorological conditions. However, at any time, the amount of energy produced has to tightly match the amount of energy that is consumed to ensure the stability of the power grid[3]. With conventional power plants, this is achieved by producing the base load with large power plants (e.g. nuclear and coal) and compensating the variations in load using load-following plants like gas turbines. Predictions of the power consumption greatly assist the regulation of the network to ensure smooth and economical operation. With an increasing fraction of renewable power plants the regulation of the network becomes more challenging since the uncertain rate of production has to be accounted for additionally. As a result the demand for load-following plants increases. For an energy infrastructure entirely based on renewable energy sources, large-scale buffer solutions which store energy in periods of overproduction and release it again if the demand exceeds the production are therefore essential. Convenient buffers are pumped-storage hydropower plants which are already in use today. Unfortunately, they can only be built in very specific locations since two nearby water reservoirs located at different altitudes are required. Additional technology for the intermediate storage of renewable energy is therefore essential.

Hydrogen is an excellent candidate for such a buffer solution. It has the highest mass energy density of any fuel[4] and its combustion to water is comparatively clean. Alternatively, hydrogen can be used in fuel cells in a more efficient, quieter and cleaner way than in combustion engines[5]. Although hydrogen is primarily produced by reforming of natural gases today, its production by water splitting powered by electricity from renewable energy sources is in principle straight forward and would make this technology sustainable. Despite these promising prerequisites, the sustainable large scale production of hydrogen is still problematic. Water is split into H_2 by the hydrogen evolution reaction (HER) at the cathode and to O_2 by the oxygen evolution reaction (OER) at the anode if a potential $\geq 1.23\,\mathrm{V}$ is applied between the two electrodes in a water based electrolyte[6]. While the HER can proceed at sufficiently high rates at small overpotential, the slow kinetics of the OER requires a larger overpotential. By using catalysts, the required overpotentials can be minimized, increasing the energy conversion efficiency. A key part for enabling a sustainable hydrogen based energy infrastructure is therefore the development of suitable catalysts.

In addition to exhibiting small overpotentials, catalysts have to be stable in the harsh conditions at which water splitting takes place (i.e., very high/low pH, large polarization)[7]. Furthermore,

they have to be produced from highly abundant and low cost raw materials in order to be deployable at large scales. Owing to their stability in highly oxidizing conditions, metal oxides are the material of choice for OER catalysts. Even noble metal catalysts like platinum form an oxide layer at potentials of the OER so that the actual catalyst is always a metal oxide. Currently, the most active and stable catalysts for the OER in acidic media are based on Ru and Ir[8]. Although being good catalysts, these materials have a low natural abundance and are expensive which renders them unattractive for large scale water splitting. Promising candidates for the OER in alkaline electrolyte are first row transition metal oxides, which are abundant and show good catalytic properties[9].

At present, OER catalysts are mainly developed by a trial and error approach. The method of preparation, its composition and its surface morphology can all influence the catalytic performance so that the intrinsic activity of the material often remains unsettled[10]. Therefore, it is important to develop preparation methods which result in well-defined model catalysts that clearly allow the determination of the active surface and simplify the uncovering of the mechanistic details of efficient catalysis. A particularly convenient approach is the electrochemical deposition of the catalyst material which was used throughout this work. Electrochemical measurements were combined with *in situ* and *operando* surface X-ray diffraction (SXRD) to characterize the crystalline structure of the films.

With SXRD, lattice parameters can be measured with high precision so that even small changes in the strain of $< 10^{-4}$ can be easily identified. X-rays penetrate deep into the material so that the crystalline structure of the entire film is probed. Opposed to scanning probe microscopy, SXRD does not require a probe to be brought close to the sample which could modify the applied potential or the diffusion of species to the sample. The large current densities and massive gas evolution present during OER are another experimental challenge. For these reasons SXRD is the method of choice for the structural characterization of OER catalysts under operation conditions.

Throughout this work, we investigated thin epitaxial films deposited on single crystal substrates. Single crystals can be obtained with a high crystalline quality, a small miscut and a mirror-like polished surface and therefore serve as extremely flat, well-defined substrates. Thin film deposits were used since they tend to be less rough than thicker films. Furthermore, the loss of material through dissolution or conversion to another phase can be monitored with sub-monolayer precision if the film is sufficiently thin. Additional advantages arise due to the epitaxy of the films. First of all, the exposed surface of the film is well-known, which is important in catalysis since different crystal faces show different catalytic behaviour. Opposed to polycrystalline samples, where the intensity of Bragg peaks is distributed on spherical shells, the peak intensity of epitaxial films is scattered into distinct directions resulting in a signal to noise ratio which is better by orders of magnitude. Since the peaks are well-defined, an analysis of the peak shape provides further information on the morphology of the samples (e.g., the dimensions of the crystallites in the vertical and horizontal direction) which is not possible with SXRD for

polycrystalline samples.

One of the central questions in catalysis is the determination of the active sites at which the reaction takes place. It is for instance not obvious if a small amount of highly active sites or a large amount of less active sites is involved in the OER. It is not even evident that the phase present at the interface during OER is the same as in the as-prepared state. On the contrary, the high positive potentials at which OER occurs favour oxidation of the electrode. For this reason *operando* investigations of structurally well-defined model catalysts are inevitable.

A first step towards obtaining well-defined metal oxide films is described in Chapter 5. Epitaxial films of cobalt were deposited on Au(111) electrodes which were subsequently anodically oxidized in alkaline solution. In this chapter only the first stages of oxide formation were investigated. The anodic oxidation to higher oxidation states which are relevant at potentials of the OER did not result in films which could be detected by SXRD. Therefore, a different approach was applied in Chapter 6 to study Co oxides under OER conditions. Thin epitaxial films of Co_3O_4 and CoOOH were directly electrodeposited on Au(111) electrodes in a reflux cell. These films were then transferred into the SXRD cell and characterized as a function of potential deep into the OER regime.

Besides the potential of the oxides of Co as promising catalysts for the OER, Co also possesses interesting magnetic properties which are of great importance for spintronics and data storage devices. Chapter 7 contains studies of ultrathin magnetic Pd/Co/Au(111) stacks prepared by sequential electrodeposition. Pd is well-known for its capability to absorb large amounts of hydrogen. In an electrochemical cell, hydrogen can be reversibly absorbed or released from the Pd depending on the applied voltage. It was shown that the hydrogenation of Pd capped Co layers in vacuum leads to reversible changes of the magnetic properties of the Co layer[11–13]. In this chapter, the behaviour of the same system is investigated in electrochemical environment. In particular, the question whether the changes in the magnetic properties are related to the strain induced in the Co layer due to the hydrogentation of the adjacent Pd layer, is addressed.

In addition to the pure scientific questions examined in Chapter 5–7, instrumentation and the development of a transmission based SXRD technique were part of this work. Chapter 8 focuses on the development of transmission surface diffraction (TSD), a novel high-energy SXRD technique which uses a transmission geometry instead of the conventional reflection geometry. In this geometry the beam impinges the sample at (or near) normal incidence and penetrates the sample. The advantage of this method is that the full in-plane structure of the sample can be obtained in a single acquisition using large 2D detectors. Due to the normal (or near normal) incidence, the beam footprint can be as small as the beam itself which enables spatially resolved measurements with very high resolution. This is impossible in the conventional scattering geometry where the beam footprint usually has an extent of millimeters. For this reason TSD is particularly well suited for the investigation of samples exhibiting heterogeneities on the micrometer scale.

An introduction to the basics of electrochemistry can be found in Chapter 2. The fundamentals

of X-ray diffraction, along with the concepts of the advanced Bragg peak analysis employed in this work, are presented in Chapter 3. The experimental setup is introduced in Chapter 4, with an emphasis on the novel *operando* SXRD cell developed for the investigation of water splitting catalysts.

2 Electrochemistry

This chapter provides an introduction to the fundamentals of electrochemistry relevant for this thesis. A more comprehensive introduction can be found in many excellent text books[14–17].

2.1 Electrochemical Cells

Electrochemistry is the study of processes involving charge transfer across the interface between a solid and a fluid phase (or two fluid phases in some rare cases). The charge carriers in the electrode (solid phase) are electrons or holes, whereas the charge carriers in the electrolyte (fluid phase) are ions. To investigate the transfer of charges across an interface between a solid and a liquid phase it is inevitable to introduce another electrode into the electrolyte. Using a high-impedance voltmeter a potential difference can then be measured between the two electrodes which is called open-circuit potential (OCP). The whole system consisting of two electrodes separated by at least one electrolyte phase is called an electrochemical cell. We can separate this cell in two half-cells consisting of an electrode and the surrounding electrolyte.

Often one is only interested in the processes happening in one half-cell. In order to modify the reactions occurring at the electrode of interest, often called the working electrode (WE), we can apply a potential bias to the electrodes. However, it is usually more convenient to adjust the potential difference between the electrolyte and the WE to separate the response of the WE from the response of the other electrode. To achieve this we can introduce a reference electrode (RE). Reference electrodes are electrodes with a stable and well-known equilibrium potential. They are usually connected to the cell via a Luggin capillary, a small tube usually made from glass, which can be brought very close to the WE and defines a precise reference point. The potential of the WE can then be measured with respect to the RE. In order to ensure that the potential of the RE remains stable it has to be connected via a large resistance so that only negligible current can flow through it.

The Ag/AgCl reference electrode is a commonly used reference electrode which was used for most experiments in this work. The electrode consists of a Ag wire which is coated with AgCl. This wire is surrounded by a Cl containing electrolyte, in our case 3.5 M KCl. The potential of this reference electrode is the equilibrium potential of the reaction $\mathrm{AgCl} \rightleftharpoons \mathrm{Ag^+} + \mathrm{Cl^-}$. Since the potential difference between the WE and the RE is the parameter that is adjusted and measured, results obtained with different reference electrodes differ by an offset. By convention the standard hydrogen electrode (SHE) is chosen as the primary reference and its potential is defined as zero. This electrode consists of a platinized platinum sheet immersed in an aqueous solution with unit activity of $\mathrm{H^+}$(aq) in contact with hydrogen gas at a pressure of one

atmosphere. For this reference electrode the potential determining reaction is $2H^+(aq) + 2e^- \leftrightharpoons H_2$. Another useful reference electrode is the reversible hydrogen electrode (RHE), which differs from the SHE only in the activity of $H^+(aq)$ which is identical to that of the electrolyte being investigated. With this reference electrode the measured potentials are independent of pH which is useful for example in the comparison of different water splitting catalysts. The relationship between potentials measured with a Ag/AgCl(3.5 M KCl) RE and a RHE is $V_{\mathrm{RHE}} = 0.205\,\mathrm{V} + 0.059\,\mathrm{V} \times \mathrm{pH} + V_{\mathrm{Ag/AgCl}}$.

To modify the potential difference between the WE and the RE we use a counter electrode (CE) which is usually made from an inert material such as platinum or carbon. A current is driven through the WE and the CE until the desired potential difference between the WE and the RE is established. For electrochemical experiments a potentiostat which uses a feedback loop is commonly used to apply the desired potential.

At small current densities the potential within the electrolyte is constant and the applied potential is mainly dropped across thin layers at the interfaces of the WE and the CE. In this case the position of the RE is not so important, however at larger currents part of the potential is dropped in the electrolyte. In this case the potential difference measured between the RE and WE does not represent the correct potential of the WE. It is therefore important to bring the RE as close to the WE as possible which can be achieved by using a Luggin capillary. However, this is not always possible or not sufficient if the current densities are too large. In this case the cell resistance has to be measured and the potential drop across the electrolyte has to be subtracted from the measured potential in order to determine the correct potential of the WE. The corrected potential E_{corr} is given by

$$E_{\mathrm{corr}} = E - I \cdot R_{\mathrm{cell}} \,, \tag{2.1}$$

where E, I and R_{cell} are the measured potential, the measured current and the cell resistance, respectively.

2.2 Cyclic Voltammetry

A common method to investigate an electrochemical system is cyclic voltammetry (CV). In CV the current density j is measured while the potential E of the WE is linearly cycled between a low and a high limit which results in a triangular potential curve. Processes which involve charge transfer can be identified in the curve of j as a function of E and the potential at which these processes occur can be determined. Two types of processes are distinguished: faradaic and nonfaradaic. Faradaic processes are those which involve charge transfer across the electrode-solution interface which causes oxidation or reduction to occur. Examples are the oxide formation on a metal electrode, metal deposition or dissolution. Nonfaradaic processes do not involve charge transfer across the electrode-solution interface, but they often still cause an external current to flow which is visible in the CV. Examples of nonfaradaic processes are adsorption and

desorption. If no charge transfer across the electrode-solution interface is possible, the electrode is called ideal polarizable. Ideal polarizability of an electrode can be approached with real electrodes, but only over limited potential ranges. If a potential is applied to an ideal polarizable electrode, an excess or deficiency of electrons will accumulate in a very thin layer on the surface (< 0.1 Å on metals). The ions in solution will redistribute so that an excess of ions with the opposite charge will accumulate close to the electrode. The arrangement of the charged species at the electrode-solution interface is known as the electric double layer in which charges on the electrode are separated from the ions of opposite polarity by a monolayer of solvent molecules. This arrangement is very similar to a parallel plate capacitor with a separation of only a few Angstroms and it possesses a capacitance in the order of 10 to 80 $\mu F/cm^2$.

The different processes can be clearly distinguished since their signatures in the CV are very different. By integrating the current over time, the total charge that was transferred in the process can be determined. For instance adsorption will lead to a current that will go to zero once all adsorption sites have been occupied. If the current is caused by deposition of metal ions from solution, we might see a peak in current which saturates once all ions close to the surface have been deposited and the deposition current is limited by diffusion of ions to the surface from the bulk of the electrolyte. Other important sources of current are oxidation or reduction of the electrode. Furthermore, the double layer capacitance leads to a charging/discharging current which is also visible in the CVs.

Using different scan rates $\Delta E/\Delta t$ or different limits of the applied voltage E we can distinguish between different processes. For example the current due to charging of the double layer will be proportional to the scan rate, whereas the deposition current in the diffusion limited range will be independent of the scan rate. Choosing different potential limits can be used to test if a peak on the positive sweep is related to a peak on the negative sweep. This is possible for example in the case of metal deposition on a more noble metal substrate. On the negative sweep a deposition and on the positive sweep a dissolution peak should be visible in the CV. If the negative going sweep is reversed at potentials more positive of the deposition peak, the dissolution peak has to be absent since nothing was deposited.

The potential window in which electrochemical data can be obtained is usually limited by the decomposition of the electrolyte, in the case of aqueous solution the splitting of water into hydrogen and oxygen gas. Even though electrochemistry is very sensitive in determining that a process is happening and at which potential it occurs, it is essential to use complementary methods to determine the structural details. This is the reason why an increasing number of *in situ* and *operando* measurements have been undertaken in the past few decades.

2.3 Electrochemical Reactions

For a process in which a species O is reduced to R by a reaction in which n electrons are transferred:

$$\mathrm{O} + n\mathrm{e} \leftrightharpoons \mathrm{R} \,, \tag{2.2}$$

the electrode potential at equilibrium E_{eq} can be described by the Nernst equation. The Nernst equation is given by[14]:

$$E_{\mathrm{eq}} = E_0 + \frac{RT}{nF} \ln \frac{a_{\mathrm{O}}}{a_{\mathrm{R}}} \,, \tag{2.3}$$

where E_0 is the standard potential of the redox couple, R is the gas constant, T is the temperature, F is the Faraday constant, and a_{O} and a_{R} are the activities of the oxidized and reduced species, respectively. The standard potential E_0 of a redox couple is obtained by measuring its potential with respect to the standard hydrogen electrode under standard conditions (ion concentration of 1 M, pressure of 1 atm, temperature of 25 °C). The standard potentials of common redox couples are tabulated and given with respect to the SHE whose potential is defined to be 0 V.

At equilibrium the rates of oxidation and reduction must be equal. Usually these rates are nonzero and the equilibrium is dynamic. The great advantage of electrochemistry is that by the application of an overpotential $\eta = E - E_{\mathrm{eq}}$ the ratio of the rates of reduction and oxidation can be modified such that a net reduction/oxidation can be achieved. Electrodes at which oxidation and reduction occur are called anode and cathode, respectively. In this work the anodic current is defined as positive and the cathodic current as negative. In the case of high concentration of electrolyte salt (i.e. if the concentration of the educts is not significantly altered by the reaction), the current density as a function of overpotential η is given by the Butler-Volmer equation[14, 18]:

$$j(\eta) = j_a(\eta) + j_c(\eta) = j_0 \cdot \left[\exp\left(\frac{\alpha_a F}{RT} \eta \right) - \exp\left(-\frac{\alpha_c F}{RT} \eta \right) \right] \,, \tag{2.4}$$

where $j_{a/c}(\eta)$ are the anodic/cathodic current densities, j_0 is the exchange current density and $\alpha_{a/c}$ are the anodic/cathodic transfer coefficients. For a reaction which involves multiple steps, usually one step will be slower than all other steps. This step will determine the overall rate of the reaction and is therefore referred to as the rate determining step (RDS). All other steps are considered to be in a quasi-equilibrium which means that they only marginally contribute to the overpotential and the overpotential is mainly dictated by the RDS. In the case where n electrons are transferred in the whole process, n_f electrons are transferred in steps before the RDS and n_r electrons are transferred in the RDS, the transfer coefficients are given by[14]:

$$\alpha_a = \frac{n - n_f}{\nu} - n_r \beta \tag{2.5a}$$

$$\alpha_c = \frac{n_f}{\nu} + n_r \beta \,. \tag{2.5b}$$

ν is the stoichiometric number which is the number of times the RDS occurs during the full

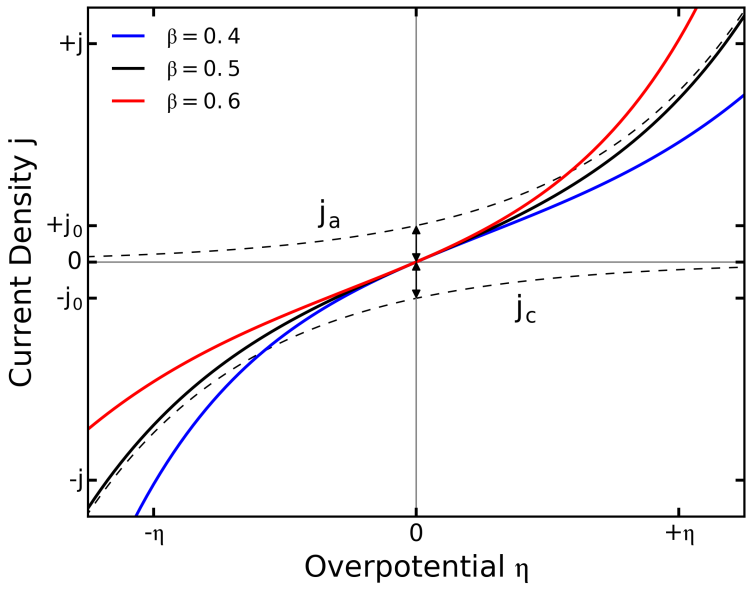

Fig. 2.1: Butlet-Volmer equation for a single electron transfer process. The dashed lines are the anodic and the cathodic contribution to the total current which demonstrate the significance of the exchange current density j_0. The blue and red curves show the effect of the symmetry factor β which is usually found to be close to 0.5.

reaction and β is the symmetry factor ($0 \leq \beta \leq 1$), which often has a value close to 0.5. These expressions are valid if the RDS is the same for the anodic and the cathodic reaction.

As mentioned earlier, the equilibrium is a dynamic one at which the reaction $\mathrm{O} + ne \leftrightharpoons R$ proceeds in both directions with equal rates such that the net current density is zero. The magnitude of the current flowing in both directions is the exchange current density j_0 given by[14]:

$$j_0 = nFk_{r,c}\left[\prod_{i=1}^{n_f}\frac{k_{i,c}}{k_{i,a}}\right]^{\frac{1}{\nu}} c_O \exp\left(\frac{-\alpha_c F E_{\mathrm{eq}}}{RT}\right) \tag{2.6a}$$

$$= nFk_{r,a}\left[\prod_{i=n-n_f-1}^{n}\frac{k_{i,c}}{k_{i,a}}\right]^{\frac{1}{\nu}} c_R \exp\left(\frac{\alpha_a F E_{\mathrm{eq}}}{RT}\right), \tag{2.6b}$$

where $k_{i,c}$ and $k_{i,a}$ are the cathodic and anodic rate constants of the i^{th} step of the reaction, $k_{r,c/a}$ are the rate constants of the RDS and c_O and c_R are the concentrations of the oxidized and reduced species, respectively.

Fig. 2.1 shows a plot of the current density j for a single electron transfer step (i.e. $\alpha_a = 1-\beta$ and $\alpha_c = \beta$). For $\beta = 0.5$ (black) the curve is point symmetric. If $\beta > 0.5$ (red) the anodic reaction is more efficient than the cathodic reaction, i.e. a smaller $|\eta|$ is required to obtain a given $|j|$. For $\beta < 0.5$ (blue) the cathodic reaction is more efficient than the anodic reaction.

At small overpotential, we can expand the exponential terms and we find that the current

density is proportional to the overpotential, i.e.:

$$j(\eta \approx 0) = j_0 \frac{nF}{\nu RT} \eta \ . \tag{2.7}$$

At larger overpotentials, either the anodic or the cathodic current density will dominate the other, so that the current density grows exponentially with overpotential. If we consider the anodic current density at large positive overpotentials

$$j(\eta \gg 0) \approx j_a(\eta) = j_0 \exp\left(\frac{\alpha_a F}{RT}\eta\right) \ . \tag{2.8}$$

Using the natural logarithm we obtain:

$$\ln(j) = \ln(j_0) + \frac{\alpha_a F}{RT}\eta \ . \tag{2.9}$$

It is immediately evident that the anodic transfer coefficient α_a and the exchange current density j_0 can be obtained by measuring the current density as a function of positive overpotential. α_a can be obtained from the slope of the straight line if $\ln(j)$ is plotted versus η. The exchange current density j_0 can be obtained from the axis intercept. Similarly, if we consider large negative overpotentials, the cathodic transfer coefficient α_c can be obtained. For a proposed reaction mechanism the expected transfer coefficients can then be calculated using Eq. 2.5 and can be compared with the experimental result. For historic reasons often the logarithm to the basis 10 is calculated and the so called Tafel equation which has the form

$$\eta = A + B \cdot \log_{10}|j| \tag{2.10}$$

is considered, where B is known as the Tafel slope. Plots of this function are known as Tafel plots and usually the overpotential η is plotted as a function of $\log_{10}|j|$. In the literature often the Tafel slope B is given from which the transfer coefficients can easily be obtained by:

$$\alpha_a = \frac{2.303RT}{B_a F} \tag{2.11}$$

$$\alpha_c = \frac{2.303RT}{B_c F} \ , \tag{2.12}$$

where B_a and B_c are the Tafel slopes of the anodic and cathodic curves, respectively. The factor of 2.303 appears due to the conversion between the natural and the decadic logarithm.

2.4 Pourbaix Diagrams

Pourbaix diagrams of metals describe their thermodynamic stability as a function of potential and pH. Pourbaix introduced these diagrams which are similar to phase diagrams. Usually the pH is given on the horizontal axis and the potential is given on the vertical axis. Lines show the equilibrium conditions of the metal and its oxides and hydroxides. It is important to keep in mind that the Pourbaix diagram only represents the thermodynamically most stable phase. It is possible that the kinetics are too slow to actually form significant amounts of a phase. Furthermore, stable oxides often form a passivation layer which protects the material underneath from further oxidation. Fig. 2.2 shows a Pourbaix diagram for the Co-H_2O system. Generally the Pourbaix diagram can be divided in three regions: protection (green), corrosion (red) and passivation (yellow). In the region of protection the metal is stable, in the region of corrosion the material is dissolved and in the region of passivation an oxide film is formed on the metal which prevents or significantly reduces dissolution. In aqueous electrolytes the accessible potential window is determined by the decomposition of water into H_2 and O_2. The corresponding potentials are marked by dashed lines. Only the region within the two dashed lines is accessible. In practice the accessible region is larger due to overpotentials of the water splitting reaction. The mechanism of water decomposition depends on pH. The reaction equations are given in the figure.

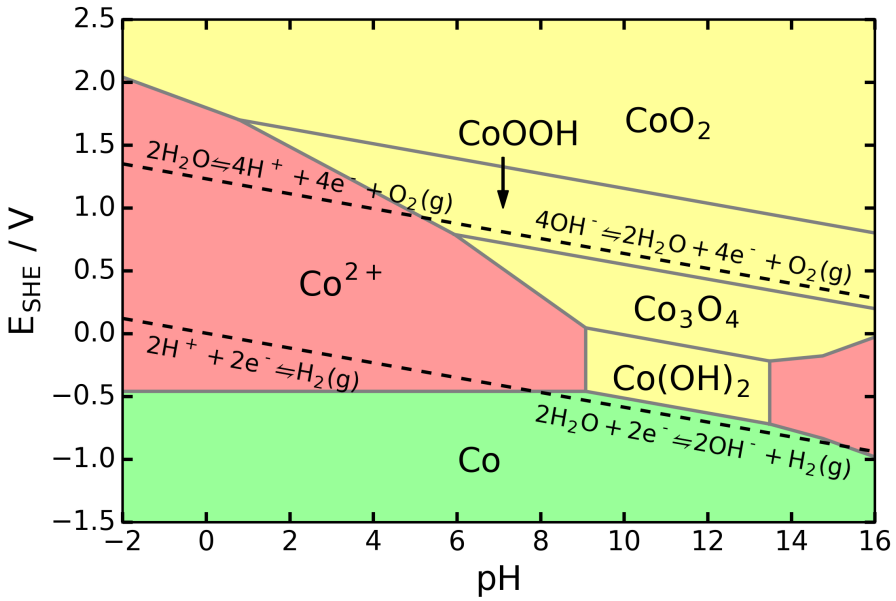

Fig. 2.2: Pourbaix diagram of Co in H_2O at 25 °C. The plot shows the regions of thermodynamic stability of cobalt and its oxides as a function of potential and pH. The regions of protection, corrosion and passivation are colored in green, red and yellow, respectively. Dashed lines indicate the potential at which water decomposition occurs. The data for the figure was taken from [19, 20].

2.5 Electrochemical Deposition

If metal ions Me^{n+} are present in the electrolyte, we can electrochemically deposit the metal on the working electrode by applying a potential sufficiently negative of the Nernst potential corresponding to the reaction $Me^{n+} + ne^- \leftrightharpoons Me$. At potentials more positive than the Nernst potential, the metal will be dissolved again. The potentials of deposition and dissolution can easily be determined from CV.

In the case of Co deposition on Au(111), bulk deposition occurs for potentials 0.25 V negative of the Nernst potential of the reaction $Co^{2+} + 2e^- \leftrightharpoons Co$ [21]. After deposition the metal ions can be removed from solution and the film can be stabilized at low potentials. By introducing an electrolyte containing other metal ions, stacks of different metals can be deposited sequentially. In this work stacks of Pd/Co/Au(111) were deposited in this way.

It is also possible to deposit more complex structures than simple metals. The Co_3O_4 and CoOOH samples investigated in this work were grown by electrochemical deposition. Tartaric acid was used to complex Co^{2+} ions to be soluble at high pH (around 14) at which the oxides are thermodynamically stable according to the Pourbaix diagram. Under these conditions Co oxide is deposited. It is believed that in the case of Co_3O_4 the deposition process proceeds via the route[22]

$$2Co^{2+}(\text{tart}) \leftrightharpoons 2Co^{3+} + 2(\text{tart}) + 2e^- \tag{2.13}$$

$$2Co^{3+} + Co^{2+}(\text{tart}) + 8OH^- \rightarrow Co_3O_4 + 4H_2O + (\text{tart})\ . \tag{2.14}$$

2.6 Electrochemical Dissolution and Passivation

Positive of the Nernst potential of the reaction $Me^{n+} + ne^- \leftrightharpoons Me$ the metal will be dissolved. From the Butler-Volmer equation (Eq. 2.4) we expect that the dissolution current should increase exponentially with increasing potential. However, for many metals it is observed that once a critical potential is exceeded the current decreases to a value several orders of magnitude lower than the maximum dissolution current. The decrease in the dissolution current is the result of a passivation layer which is formed on the metal surface which drastically reduces the rate of dissolution. The passivation of metals is a phenomenon which has been known for almost two centuries and has been systematically investigated since the second half of the past century. Passivation is the enabler of our current metals-based civilization since it ensures that metals are not simply dissolved[23]. Many theories for the passive state have been developed[24–33], driven by its great technological importance. However, a complete theoretical understanding of the mechanism of the formation of passive layers is still missing. A full treatment of the passivation of metals is out of the scope of this work but the basics will be briefly outlined in the following.

The formation of passive layers commences with the adsorption of oxygen or hydroxyl ions.

After the formation of a monolayer of the adsorbate a place exchange of the oxygen ion and the underlying metal ion takes place which transfers the oxygen into the metal. For some metals, especially for noble metals like platinum or palladium, this monolayer of surface oxide is sufficient to completely passivate the material. In this case the formation rate of a thicker layer is very small. On other metals like iron, nickel, chromium, aluminum, titanium or tantalum passive layers of several nanometer to tens of nanometer thickness are formed[29].

Experimentally it is observed that the thicker oxide films are composed of a bilayer consisting of a highly defective barrier layer which grows into the metal and an outer layer which is formed by the precipitation of an oxide species. The steady-state thickness of the barrier layer varies linearly with the applied voltage unless a change in the oxidation state within the passive film occurs. This implies that the electric field within the film is independent of the applied voltage. To form the passive layer it is essential that ions can be transported through the barrier layer. By simple diffusion the ion transport cannot be explained at room temperature, but the strong electric field within the film which can easily be of the order 1×10^8 V/m can greatly enhance the transport.

In the point defect model (PDM) developed by Macdonald[33] the transport through the barrier layer occurs via the migration of point defects. The point defects present in the barrier layer are predicted to be cation vacancies, oxygen vacancies and cation interstitials. Since the cation vacancies are electron acceptors they dope the barrier p-type, whereas n-type doping is obtained by the oxygen vacancies and metal interstitials which are electron donors. Therefore, the barrier layer can be described as a highly doped defect semiconductor. During film growth, cation vacancies are produced at the barrier/outer layer interface and are subsequently transported to the metal/barrier layer interface where they are annihilated. Likewise oxygen vacancies are produced at the metal/barrier layer interface and transported to the barrier/outer layer interface where they are consumed. So the direction of movement of the two vacancy species is in opposite directions. In addition dissolution takes place at the interface to the solution. In the steady-state the rate of oxygen vacancy creation and the rate of dissolution will be equal.

In this work Co deposition and anodic oxidation as well as the behaviour of Co_3O_4 and CoOOH films at potentials deep into the oxygen evolution regime were investigated. In alkaline electrolyte the formation of a passive layer on Co commences with OH adsorption followed by the formation of an ultrathin passive film covering the entire Co surface. Subsequently, inhomogeneous growth of $Co(OH)_2$ occurs on the surface[34]. At more positive potentials $Co(OH)_2$ is oxidized to Co_3O_4 which is further oxidized to CoOOH at even higher potentials[35, 36]. The Pourbaix diagram of Co in Fig. 2.2 shows the thermodynamic stability ranges of Co and its oxides as a function of potential and pH.

2.7 Oxygen Evolution Reaction in Alkaline Media

The reaction which produces oxygen at the anode during water splitting is known as the oxygen evolution reaction (OER). Simultaneously, hydrogen gas is formed at the cathode by the hydrogen evolution reaction (HER). The equilibrium potentials for the OER and HER are $1.23\,V_{RHE}$ and $0.0\,V_{RHE}$, respectively. While the HER can produce adequate current densities close to the equilibrium potential, the OER requires an overpotential of several 100 mV to occur at a sufficiently high rate. The reason for this overpotential can be found in the complex four electron transfer process taking place at the anode. Since first-row transition metal oxides which have been investigated in this work are not stable in acidic media, an alkaline electrolyte was used. Depending on the pH of the solution the OER reaction path differs. In alkaline media the reaction is thought to proceed by the path which is described in the following[20]. A graphical representation of the reaction is shown in Fig. 2.3. In the first step a hydroxyl radical is adsorbed on an active site "M" and oxidized by the transfer of one electron. The reaction proceeds by the coupled removal of the proton and an electron by the formation of H_2O with a second hydroxyl radical and the transfer of a second electron. The reaction equations are given by:

$$M + OH^- \rightarrow M{-}OH + e^- \text{ and} \tag{2.15}$$

$$M{-}OH + OH^- \rightarrow M{-}O + H_2O + e^- \,. \tag{2.16}$$

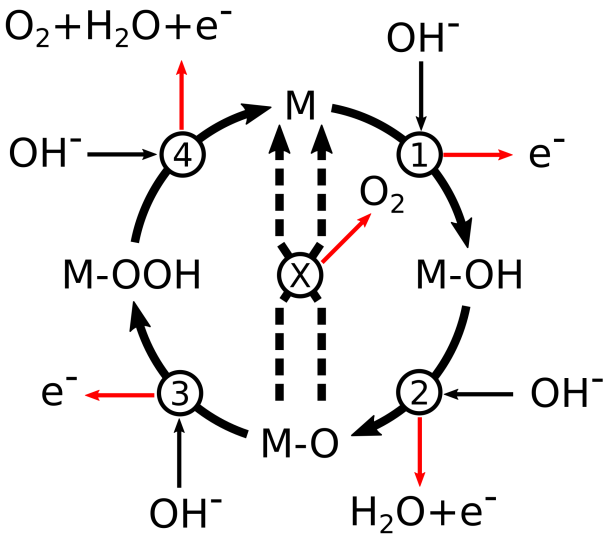

Fig. 2.3: Mechanism of the OER in alkaline electrolyte. One route involves steps (1)-(4) in which four hydroxyl radicals subsequently react with the catalytic site M. The intermediate states of the reaction are M−OH, M−O and M−OOH. In the last step O_2 is formed and the initial state M is recovered. The alternative route involves two intermediate species M−O formed in step (1) and (2), which can combine via (X) to directly form O_2 and to recover the initial state of the two active sites. The small black arrows indicate the species reacting with the active site in each step, the small red arrows indicate the species produced in the step.

At this point two reaction routes are possible. In the first pathway (indicated by dashed lines in Fig. 2.3, reaction step marked by "X") two M−O species are directly combined to form O_2 by:

$$2\mathrm{M}-\mathrm{O} \rightarrow 2\mathrm{M} + \mathrm{O}_2 \, . \tag{2.17}$$

The alternative route (solid lines, reaction step 3 and 4) involves two further reactions with OH^- in which M−OOH is the intermediate species and one electron is transferred in each of the two steps according to:

$$\mathrm{M}-\mathrm{O} + \mathrm{OH}^- \rightarrow \mathrm{M}-\mathrm{OOH} + \mathrm{e}^- \tag{2.18}$$

$$\mathrm{M}-\mathrm{OOH} + \mathrm{OH}^- \rightarrow \mathrm{M} + \mathrm{O}_2 + \mathrm{H}_2\mathrm{O} + \mathrm{e}^- \, . \tag{2.19}$$

After a full cycle the catalytic site is in its original state and the process can start from the beginning. The thermodynamic barrier for step X is almost always the largest so that the route involving step 3 and 4 is usually the relevant path. Calculations show that the rate determining step depends on the surface termination. For CoOOH(104) step 3 was found to be the potential determining step, while step 1 is the rate determining step for CoOOH(012)[20].

3 Theory of X-ray Diffraction

This chapter is an introduction to structural characterization using X-ray diffraction. Throughout this work single crystalline samples were investigated. Opposed to powder diffraction where a single scan is sufficient to obtain the full structural information, experiments on single crystals require the scanning of large fractions of reciprocal space which is very time consuming. It is therefore convenient to have some knowledge about the expected structures in advance. Bragg peak positions of known structures (for example from powder diffraction data in the literature) can be calculated and can greatly reduce the volume of reciprocal space that has to be sampled. While simple structures like gold single crystals can be easily calculated by hand, the structure of the Co-oxides investigated in this work containing tens of atoms in the unit cell require computer-aided simulations. To simulate the Bragg peak positions and their intensity for an arbitrary combination of crystalline phases with defined orientations, a simulation software was written within this work. For that reason this chapter contains a detailed description of the basics of X-ray scattering which is necessary to perform these simulations.

From the analysis of the peak positions and their relative intensity the crystalline structure can be determined. However, for thin film samples additional information about the sample morphology can be obtained from the peak shape. Different kinds of disorder in the film lead to a broadening of the Bragg peaks in various directions. This chapter explains how these additional details can be extracted by a detailed peak shape analysis.

3.1 Crystals and the Real Space Lattice

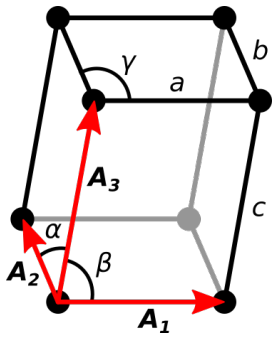

Fig. 3.1: Schematic of the crystal unit cell. The unit cell is defined by the parallelepiped spanned by the vectors $\boldsymbol{A_1}$, $\boldsymbol{A_2}$ and $\boldsymbol{A_3}$. The vectors have the norm a, b and c, respectively. In combination with the angles $\alpha = \sphericalangle(\boldsymbol{A_2}, \boldsymbol{A_3})$, $\beta = \sphericalangle(\boldsymbol{A_1}, \boldsymbol{A_3})$ and $\gamma = \sphericalangle(\boldsymbol{A_1}, \boldsymbol{A_2})$ an arbitrary lattice can be defined.

An ideal crystal consists of identical building blocks (atoms or molecules) periodically and

infinitely repeated in space. Such a structure is best described by a lattice, a periodical arrangement of points in space defined by three translation vectors $\boldsymbol{A_1}$, $\boldsymbol{A_2}$ and $\boldsymbol{A_3}$. The lattice has lattice points at all

$$\boldsymbol{R_n} = n_1\boldsymbol{A_1} + n_2\boldsymbol{A_2} + n_3\boldsymbol{A_3}\ , \tag{3.1}$$

where n_1, n_2 and n_3 are arbitrary integers. A crystal is formed by attaching an identical ensemble of atoms, known as the basis to each lattice point. The unit cell of a crystal is the parallelepiped spanned by the vectors $\boldsymbol{A_1}$, $\boldsymbol{A_2}$ and $\boldsymbol{A_3}$ (see Fig. 3.1). An arbitrary lattice can be described by the lattice parameters a, b, c (the norms of the lattice vectors) and α, β, γ (the angles between the lattice vectors).

Without loss of generality we can choose the lattice vectors $\boldsymbol{A_1}$ to be along the x-axis and $\boldsymbol{A_2}$ to lie in the xy-plane of a Cartesian coordinate system. Then $\boldsymbol{A_1}$ and $\boldsymbol{A_2}$ are readily determined as $\boldsymbol{A_1} = (a,\ 0,\ 0)$ and $\boldsymbol{A_2} = (b\cdot\cos\gamma, b\cdot\sin\gamma,\ 0)$. By applying the definition of the vector scalar product $\boldsymbol{u}\cdot\boldsymbol{v} = |\boldsymbol{u}||\boldsymbol{v}|\cos\sphericalangle(\boldsymbol{u},\boldsymbol{v})$ to $\boldsymbol{A_1}\cdot\boldsymbol{A_3}$ and $\boldsymbol{A_2}\cdot\boldsymbol{A_3}$ the first and second components of $\boldsymbol{A_3}$, A_{31} and A_{32}, can be calculated. The third component A_{33} is then simply found by considering the norm of the vector: $c^2 = A_{31}^2 + A_{32}^2 + A_{33}^2$. Following this procedure the real space lattice vectors are given by

$$\boldsymbol{A_1} = \begin{pmatrix} a \\ 0 \\ 0 \end{pmatrix}, \boldsymbol{A_2} = \begin{pmatrix} b\cdot\cos\gamma \\ b\cdot\sin\gamma \\ 0 \end{pmatrix}, \boldsymbol{A_3} = \begin{pmatrix} c\cdot\cos\beta \\ c\cdot(\cos\alpha - \cos\beta\cdot\cos\gamma)\,/\,\sin\gamma \\ \sqrt{c^2 - \left(A_{31}^2 + A_{32}^2\right)} \end{pmatrix}. \tag{3.2}$$

The volume of the unit cell is simply the volume of a parallelepiped defined by the three axes:

$$V = \boldsymbol{A_1}\cdot(\boldsymbol{A_2}\times\boldsymbol{A_3})\,. \tag{3.3}$$

3.2 Basics of X-ray Diffraction

X-rays can interact with atoms or molecules in two ways. Firstly, quanta of the beam can be absorbed or secondly, the beam can be scattered. By far the most relevant process in the structural analysis of materials is the X-ray scattering on which we will focus here. Classically, when a plane wave is incident on an electron, the electron will oscillate in the electric field of the X-ray and radiate a spherical wave. The superposition of the spherical waves radiated from all electrons in the sample is the signal that can be measured experimentally. Since X-rays have a wavelength comparable to the interatomic distances in matter, interference leads to the patterning of the observed intensity distribution from which the atomic structure of the sample can be reconstructed.

An introduction to the basics of X-ray diffraction and surface X-ray scattering (SXRD) can be found in textbooks like [37, 38]. The following section builds on a particularly useful introduction

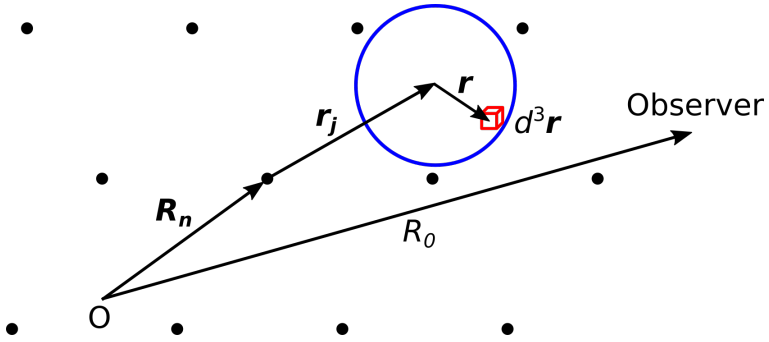

Fig. 3.2: Schematical representation of a volume element $d^3\boldsymbol{r}$ of the integration shown in Eq. 3.5. The element is described by the vector sum of $\boldsymbol{R_n}$, $\boldsymbol{r_j}$ and $\boldsymbol{r}$. The vector $\boldsymbol{R_n}$ points from the origin of the crystal (O) to the n$^{\text{th}}$ lattice point (black dots) of the crystal. $\boldsymbol{r_j}$ is the position of the j$^{\text{th}}$ atom (blue circle) relative to the n$^{\text{th}}$ lattice point and $\boldsymbol{r}$ is the position of the volume element $d^3\boldsymbol{r}$ for the integration of the electron density of this atom.

by Robinson and Tweet[39].

In an X-ray scattering experiment the beam which can be described by a wavevector $\boldsymbol{k_i}$ pointing along its direction of propagation is incident on the sample. The magnitude of the wavevector is $2\pi/\lambda$, where λ is the wavelength of the beam. The scattered beam propagating in the direction $\boldsymbol{k_f}$ is recorded by a detector. In this work only elastic scattering was investigated so that the wavelength of the incident and scattered beam are equivalent i.e. that $|\boldsymbol{k_i}| = |\boldsymbol{k_f}|$. It is convenient to define the wavevector transfer as

$$\boldsymbol{q} \equiv \boldsymbol{k_f} - \boldsymbol{k_i} \ . \tag{3.4}$$

Then the independent variable of a scattering experiment is the wavevector transfer $\boldsymbol{q}$ and we can think of the experiment as mapping the scattered intensity in $\boldsymbol{q}$-space which is commonly called reciprocal space.

The scattered amplitude from a crystal is found by adding the scattered waves from each electron it contains taking into account the correct phases. For this we have to sum over all unit cells n, all atoms j in each unit cell and integrate over the electron density of each atom which is given by the wave functions of the electrons. The scattered amplitude $A(\boldsymbol{q})$ observed at a distance R_0 is then found by[39]:

$$A(\boldsymbol{q}) = A_0 \frac{e^2}{mc^2} \frac{1}{R_0} \sum_n \sum_j \int_{-\infty}^{+\infty} \rho_j(\boldsymbol{r}) \exp\left(i\boldsymbol{q} \cdot (\boldsymbol{R_n} + \boldsymbol{r_j} + \boldsymbol{r})\right) d^3\boldsymbol{r} \ , \tag{3.5}$$

where A_0 is the amplitude of the incident beam, ρ_j is the electron density of the j$^{\text{th}}$ atom and the constants e, m and c are the electron charge, electron mass and the speed of light, respectively. The position of the volume element over which the electron density is integrated is given by the vector sum of $\boldsymbol{R_n}$, $\boldsymbol{r_j}$ and $\boldsymbol{r}$. $\boldsymbol{R_n}$ is pointing from the origin to the n$^{\text{th}}$ unit cell, $\boldsymbol{r_j}$ is pointing from the origin of this unit cell to the center of the j$^{\text{th}}$ atom and $\boldsymbol{r}$ is the position relative to the

center of the jth atom. A schematical representation of the scattering is shown in Fig. 3.2. Eq. 3.5 is valid within the kinematical approximation which assumes that the interaction between the X-ray and the crystal is weak. Within this approximation the possibility of a scattered beam to scatter another time is neglected. In Eq. 3.5 the variables can be separated, resulting in:

$$A(\boldsymbol{q}) = A_0 \frac{e^2}{mc^2} \frac{1}{R_0} \sum_n \exp(i\boldsymbol{q}\cdot\boldsymbol{R_n}) \sum_j \exp\left(i\boldsymbol{q}\cdot\boldsymbol{r_j}\right) \int_{-\infty}^{+\infty} \rho_j(\boldsymbol{r}) \exp(i\boldsymbol{q}\cdot\boldsymbol{r})) \, d^3\boldsymbol{r} \tag{3.6}$$

$$= A_0 \frac{e^2}{mc^2} \frac{1}{R_0} \sum_n \exp(i\boldsymbol{q}\cdot\boldsymbol{R_n}) \sum_j \exp\left(i\boldsymbol{q}\cdot\boldsymbol{r_j}\right) f_j(\boldsymbol{q}) \tag{3.7}$$

$$= A_0 \frac{e^2}{mc^2} \frac{1}{R_0} F(\boldsymbol{q}) \sum_n \exp(i\boldsymbol{q}\cdot\boldsymbol{R_n}) \ , \tag{3.8}$$

where $f(\boldsymbol{q})$ is called the atomic form factor and $F(\boldsymbol{q})$ is called the structure factor.

3.3 Reciprocal Lattice

If we are considering a crystal with N_1, N_2 and N_3 unit cells along the crystal axes $\boldsymbol{A_1}$, $\boldsymbol{A_2}$ and $\boldsymbol{A_3}$, Eq. 3.8 becomes:

$$A(\boldsymbol{q}) = A_0 \frac{e^2}{mc^2} \frac{1}{R_0} F(\boldsymbol{q}) \sum_{n_1=0}^{N_1-1} \sum_{n_2=0}^{N_2-1} \sum_{n_3=0}^{N_3-1} \exp(i\boldsymbol{q}\cdot(n_1\boldsymbol{A_1} + n_2\boldsymbol{A_2} + n_3\boldsymbol{A_3})) \tag{3.9}$$

$$= A_0 \frac{e^2}{mc^2} \frac{1}{R_0} F(\boldsymbol{q}) \sum_{n_1=0}^{N_1-1} \exp(in_1\boldsymbol{q}\cdot\boldsymbol{A_1}) \sum_{n_2=0}^{N_2-1} \exp(in_2\boldsymbol{q}\cdot\boldsymbol{A_2}) \sum_{n_3=0}^{N_3-1} \exp(in_3\boldsymbol{q}\cdot\boldsymbol{A_3}) \ , \tag{3.10}$$

where we have separated the term in the sums to obtain a product of three independent sums. These sums are simple geometric series for which the trivial expression

$$S_N(x) = \sum_{n=0}^{N-1} \exp(ixn) = \frac{1-\exp(ixN)}{1-\exp(ix)} \tag{3.11}$$

exists. With this expression $A(\boldsymbol{q})$ simplifies to:

$$A(\boldsymbol{q}) = A_0 \frac{e^2}{mc^2} \frac{1}{R_0} F(\boldsymbol{q}) S_{N_1}(\boldsymbol{q}\cdot\boldsymbol{A_1}) S_{N_2}(\boldsymbol{q}\cdot\boldsymbol{A_2}) S_{N_3}(\boldsymbol{q}\cdot\boldsymbol{A_3}) \tag{3.12}$$

In a scattering experiment, we measure the intensity $I(\boldsymbol{q}) = |A(\boldsymbol{q})|^2$ rather than the amplitude. The measured signal is therefore proportional to $|F(\boldsymbol{q})|^2 |S_{N_1}(\boldsymbol{q}\cdot\boldsymbol{A_1})|^2 |S_{N_2}(\boldsymbol{q}\cdot\boldsymbol{A_2})|^2 |S_{N_3}(\boldsymbol{q}\cdot\boldsymbol{A_3})|^2$. The function $|S_N(x)|^2$ is the so called "N-slit interference function" which is commonly used in optics and has the form

$$|S_N(x)|^2 = \frac{\sin^2(Nx/2)}{\sin^2(x/2)} \ . \tag{3.13}$$

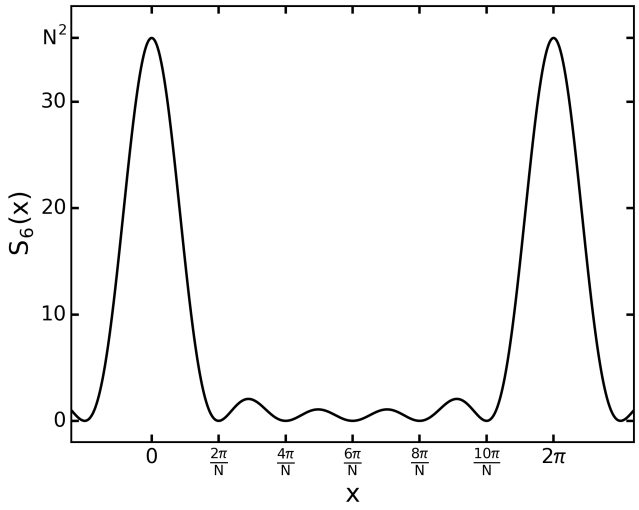

Fig. 3.3: N-slit interference function for $N = 6$. The function has primary maxima spaced by 2π and $N-2$ subsidiary maxima in-between. The peak intensity of the primary maxima is N^2. The subsidiary maxima have a period of $2\pi/N$.

Fig. 3.3 shows the N-slit function for $N = 6$. The function has intense peaks with an amplitude of N^2 at multiples of 2π and shows $N-2$ subsidiary maxima in-between. The spacing of the subsidiary maxima is $2\pi/N$. In the limit of $N \to \infty$ the function approaches a series of δ-functions separated by 2π. For the intensity to be at a maximum we therefore have to simultaneously satisfy the Laue conditions:

$$\boldsymbol{q} \cdot \boldsymbol{A_1} = 2\pi H \tag{3.14}$$

$$\boldsymbol{q} \cdot \boldsymbol{A_2} = 2\pi K \tag{3.15}$$

$$\boldsymbol{q} \cdot \boldsymbol{A_3} = 2\pi L \,, \tag{3.16}$$

where H, K, L are integers and are called Miller indices.

The Laue conditions can be simultaneously satisfied by

$$\boldsymbol{q} = H\boldsymbol{B_1} + K\boldsymbol{B_2} + L\boldsymbol{B_3} \tag{3.17}$$

if the vectors $\boldsymbol{B_i}$ have the property $\boldsymbol{B_i} \cdot \boldsymbol{A_j} = 2\pi\delta_{ij}$. Such a set of vectors is straight forward to obtain from the real space lattice vectors $\boldsymbol{A_i}$ by

$$\boldsymbol{B_1} = \frac{2\pi}{V}\left(\boldsymbol{A_2} \times \boldsymbol{A_3}\right) \tag{3.18}$$

$$\boldsymbol{B_2} = \frac{2\pi}{V}\left(\boldsymbol{A_3} \times \boldsymbol{A_1}\right) \tag{3.19}$$

$$\boldsymbol{B_3} = \frac{2\pi}{V}\left(\boldsymbol{A_1} \times \boldsymbol{A_2}\right) \,. \tag{3.20}$$

If we compare Eq. 3.17 to Eq. 3.1 we notice that they have the same form. Analog to the

real space lattice describing the periodic repetition of the crystals unit cell in space we have a lattice of points in reciprocal space to which the X-rays are scattered. The Miller indices H, K, L are commonly used to refer to a position in reciprocal space. However, for calculations, especially when several different structures are involved, $\boldsymbol{q}$ is often more appropriate. Therefore it is convenient to define a transformation matrix M in order to convert from HKL-space to $\boldsymbol{q}$-space:

$$M = \begin{pmatrix} B_{11} & B_{21} & B_{31} \\ B_{12} & B_{22} & B_{32} \\ B_{13} & B_{23} & B_{33} \end{pmatrix} . \tag{3.21}$$

Since we defined the matrix M we can use simple algebra to calculate the inverse of M which allows us to convert between HKL-space and $\boldsymbol{q}$-space in both directions:

$$\boldsymbol{q} = \begin{pmatrix} q_x \\ q_y \\ q_z \end{pmatrix} = M \cdot \begin{pmatrix} H \\ K \\ L \end{pmatrix} , \tag{3.22}$$

$$\begin{pmatrix} H \\ K \\ L \end{pmatrix} = M^{-1} \cdot \begin{pmatrix} q_x \\ q_y \\ q_z \end{pmatrix} . \tag{3.23}$$

3.4 Atomic Form Factor and Structure Factor

The atomic form factor is the Fourier transform of the electron density of an atom. In general the electron density of an atom is spherically symmetric so that it depends only on the magnitude $Q \equiv |\boldsymbol{q}|$ of the wavevector transfer. Furthermore, the atomic form factor also depends on the photon energy E_{ph} and can be written as

$$f(Q, E_{\mathrm{ph}}) = f_0(Q) + f'(E_{\mathrm{ph}}) + i f''(E_{\mathrm{ph}}) . \tag{3.24}$$

The dispersion correction terms f' and f'' only significantly alter the atomic form factors close to absorption edges. They can therefore be neglected in this work since all experiments were carried out at constant photon energies far from any atomic transitions so that $f(Q, E_{\mathrm{ph}}) = f_0(Q)$ is a good approximation. Values of $f_0(Q)$ for all atoms are tabulated but are more conveniently approximated by:

$$f_0(Q) = c + \sum_{i=1}^{5} a_i \cdot \exp\left(-b_i \left(\frac{Q}{4\pi} \right)^2 \right) , \tag{3.25}$$

where the coefficients c, a_i and b_i were obtained by fits to the tabulated values [40].

While the symmetry of the real space lattice dictates the positions of the reciprocal lattice points, the relative intensities at these lattice points are dictated by the structure factor. The structure factor contains the symmetry of the basis and is given by:

$$F(\boldsymbol{q}, E_{\mathrm{ph}}) = \sum_j \exp\left(i\boldsymbol{q}\cdot\boldsymbol{r_j}\right) f_j(Q, E_{\mathrm{ph}}) \ . \tag{3.26}$$

The position of the j$^{\mathrm{th}}$ atom of the basis relative to each lattice point is given in fractions of the lattice vectors by:

$$\boldsymbol{r_j} = x_j\boldsymbol{A_1} + y_j\boldsymbol{A_2} + z_j\boldsymbol{A_3}, \tag{3.27}$$

with $0 \leq x_j, y_j, z_j < 1$. If we substitute $\boldsymbol{r_j}$ and $\boldsymbol{q}$ (Eq. 3.17) into Eq. 3.26, we obtain a particularly convenient expression of the structure factor:

$$F(H,K,L,E_{\mathrm{ph}}) = \sum_j f_j(Q(H,K,L),E_{\mathrm{ph}}) \cdot \exp\left(2\pi i\left(Hx_j + Ky_j + Lz_j\right)\right) \ . \tag{3.28}$$

3.5 Crystal Truncation Rods

In surface X-ray scattering experiments one usually uses single crystals with a surface that is cut along a very specific crystalline direction. This surface is then usually polished such that an extremely flat surface with a known orientation of the crystalline axis is obtained. This surface is then usually further treated by sputtering and annealing in order to obtain a flat surface at atomic length scales. Due to the broken symmetry at this interface non-zero intensity along the surface normal direction is observed between the Bragg peaks. These rod like structures are known as crystal truncation rods (CTR). The intensity distribution between the Bragg peaks is extremely sensitive to the surface and the shape of the CTRs can be fitted with a model of the interface structure. However, if the sample is not homogeneous enough or too rough, a CTR might not be visible or too complicated to fit. In this work we investigated different metals and metal oxides deposited on well-defined Au(111) single crystals. Although these films were in epitaxy with the substrate, they were too heterogeneous to show a CTR which could be analyzed. The following section demonstrates how surface sensitive information can still be obtained for such systems.

3.6 Surface Diffraction of Imperfect Thin Films

If a thin epitaxial film is too heterogeneous to exhibit a visible CTR and the scan only shows a series of Bragg peaks, several useful film properties can still be obtained by detailed studies of the Bragg peaks and their shape. For the data analysis it is often more convenient to convert the $\boldsymbol{q}$-coordinates into an in-plane component $q_{\parallel}$ (parallel to the surface) and an out-of-plane component $q_{\perp}$ (perpendicular to the surface). This has the advantage, that data obtained from

symmetry equivalent peaks can be directly compared. Furthermore, these directions are most relevant in the peak shape analysis as will be seen later. In this work we always defined the reciprocal space in a way that q_x and q_y are in the surface plane and q_z is perpendicular to the surfac, with this definition:

$$q_{\parallel} = \sqrt{q_x^2 + q_y^2} \tag{3.29}$$

$$q_{\perp} = q_z \, . \tag{3.30}$$

3.6.1 Strain

The strain of the deposit is the most obvious parameter that can be measured, since it is simply obtained from the peak position. The convention of the in-plane strain $\varepsilon_{\parallel}$ and out-of-plane strain $\varepsilon_{\perp}$ used in this work are given by:

$$\varepsilon_{\parallel} = \frac{q_{\parallel,b}}{q_{\parallel}} - 1 = \frac{a - a_b}{a_b} \tag{3.31}$$

$$\varepsilon_{\perp} = \frac{q_{\perp,b}}{q_{\perp}} - 1 = \frac{c - c_b}{c_b} \, , \tag{3.32}$$

where a/c are characteristic length scales of the crystal in the in-plane/out-of-plane directions, (e.g. the lattice parameters a and c of a hexagonal unit cell) and $q_{\parallel/\perp}$ are the corresponding spacings in reciprocal space. The subscript "b" denotes the corresponding bulk values taken from the literature.

3.6.2 Crystallite Size

The width of the Bragg peaks contains information about the spatial extent of crystalline material which is in exact translational symmetry. These characteristic lengths are good estimations of the film thickness and the lateral dimensions of the crystallites of which the film consists. By consideration of the N-slit interference function $|S_N(qa)|^2$ (Eq. 3.13) we can rationalize this. In the ideal case the intensity is zero at all q which are multiples of $\frac{2\pi}{Na}$ with the exception of multiples of $\frac{2\pi}{a}$, the position of the primary maxima (see Fig. 3.3). Therefore, the full width of the primary peaks (from zero to zero) is $\frac{4\pi}{Na}$ and to a good approximation the FWHM $\Gamma = \frac{2\pi}{Na}$. Although an analytic expression for the width cannot be determined for the N-slit function, we can find the width numerically. For $N = 2$ the FWHM $\Gamma = \frac{2\pi}{Na}$. At larger values the width decreases and saturates at $\Gamma \approx 0.89\frac{2\pi}{Na}$. These values are only true for ideal crystals for which the crystal is perfectly correlated within a spatial region which is sharply defined by step functions. In reality the correlation function cannot be described by a step function but will decrease gradually which modifies the relation between Γ and N. Within this work it was however impossible to determine the correlation function since inhomogeneities of the film dominated these effects.

The central problem is that the X-ray signal is a superposition of contributions from a large number of crystallites with a distribution in size and orientation. This leads to broadening of the peaks in different directions which complicates the shape of the peaks. For simplicity we therefore assumed a sharp truncation of the crystallites and used the relation $\Gamma = \frac{2\pi}{Na}$ for the peak width resulting from the finite size of the crystallites throughout this work. Since a is the length of the real space axis of the crystal, the extent of the crystal in this direction is $d = Na$. We thus obtain $d = \frac{2\pi}{\Gamma}$. The crystal size in the in-plane and out-of-plane directions are accordingly given by:

$$d_{\parallel} = \frac{2\pi}{\Gamma_{\parallel}} \tag{3.33}$$

$$d_{\perp} = \frac{2\pi}{\Gamma_{\perp}} \,, \tag{3.34}$$

where $\Gamma_{\parallel}$ and $\Gamma_{\perp}$ are the peak widths in the in-plane and out-of-plane directions, respectively. A detailed discussion of the above mentioned additional broadening mechanisms can be found in Section 3.6.4. For the case of Co deposition on Au(111) the obtained thin films were sufficiently flat to exhibit clearly visible subsidiary maxima as in Fig. 3.3. A detailed analysis of the shape of the Bragg peaks and the CTR including the modelling of a crystallite height distribution can be found in Section 5.6.3. For all other experiments shown in this work size distribution functions could not be obtained so that Γ was interpreted as an average peak width and likewise the resulting crystallite dimensions were interpreted as average values.

3.6.3 Amount of Material

The amount of material in a specific phase which exhibits an exact translational symmetry is proportional to the integrated intensity of the Bragg peaks. Therefore, the intensity of the peak can be used to monitor growth and dissolution. Furthermore, the intensity is also a measure of the amount of material that is converted to another phase during an electrochemical process like oxidation or reduction since the converted material loses the translational symmetry to the initial phase.

3.6.4 3D Peak Shape Analysis

A detailed analysis of the 3D peak shape and appropriate projections can provide further insight into the structure of the film. Fig. 3.4 shows three different views of the 3D reconstruction of a Bragg peak of Co_3O_4 deposited on Au(111). Fig. 3.4a shows a projection along the q_z axis (the surface normal direction). Now it becomes evident that q_x and q_y are not the best coordinates to capture the symmetry of the peak. More convenient is to consider the radial direction $q_{\parallel}$ which is the direction from the origin to the peak in the $q_x q_y$-plane. The second direction of interest is

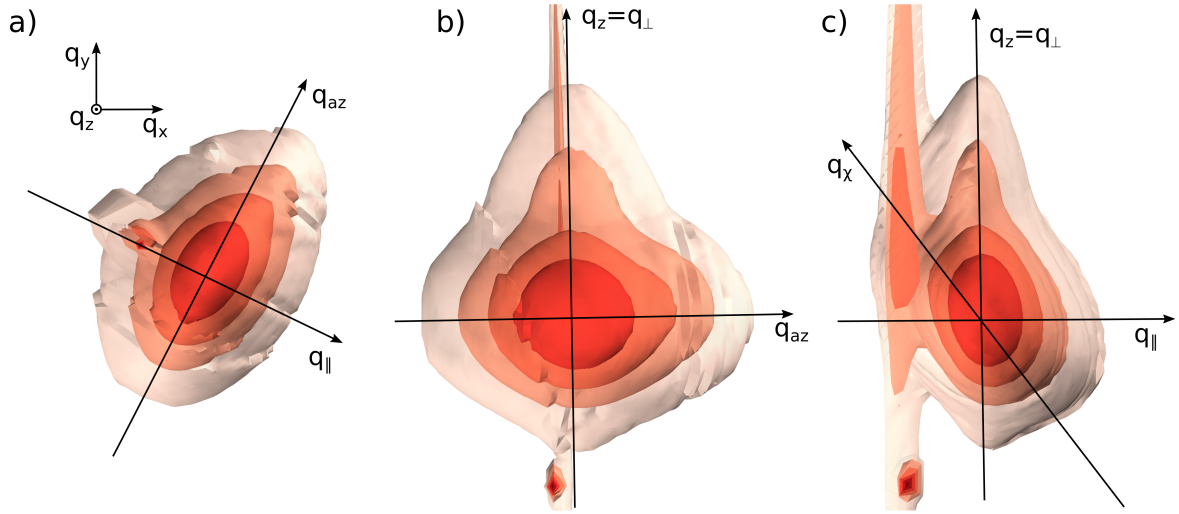

Fig. 3.4: Reconstruction of the 3D intensity distribution of a Co_3O_4 Bragg peak. The data was obtained from a series of 2D images recorded along the CTR. Shown are different projections of the peak: a) projection along q_z, b) projection along $q_{\parallel}$, c) projection along q_{az}. It can be seen that the peak is composed of two different contributions. Different broadening mechanisms leading to a broadening of the peak in different directions can be clearly identified.

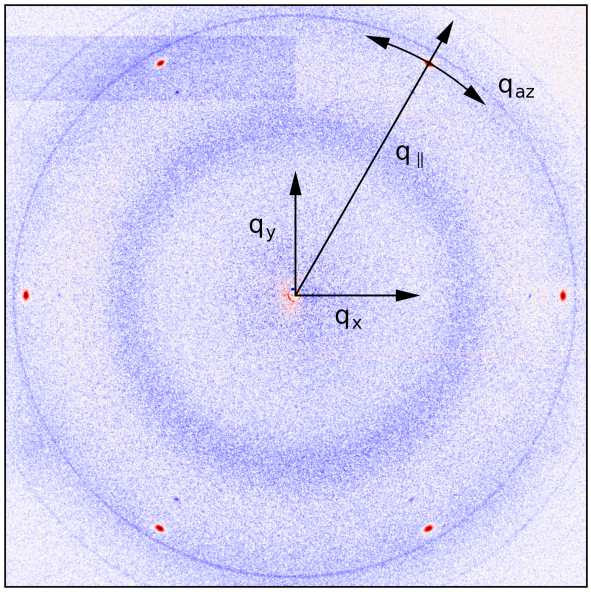

Fig. 3.5: TSD image of Co/Au/Si(111). Shown is the difference of images recorded before and after Co deposition. The red peaks in a hexagonal arrangement originate from Co. It can be seen that the peaks are broader along q_{az} than along $q_{\parallel}$.

the azimuthal direction q_{az}, which is perpendicular to $q_{\parallel}$ and lies in the same plane.

The peak is clearly broader in the azimuthal direction. This effect is commonly observed and can be easily understood by recalling that we probe a large ensemble of different crystallites. If the in-plane axes of the crystallites do not perfectly match the substrate, but have a distribution of mismatch, the peak will be broadened on a ring around the q_z-axis. This can be seen even better

in Fig. 3.5 which shows a transmission surface diffraction (TSD, see Chapter 8) difference image before and after Co deposition on Au/Si(111). Although this figure shows a different system the broadening mechanism is the same. In the TSD geometry the full in-plane structure is visible in one image and it can be clearly seen that the direction of the broadening of all peaks is along a ring around the origin. Therefore, if we are interested in the lateral extent of the crystallites, we have to consider the smallest peak width $\Gamma_{\parallel}$ which is along the direction of $q_{\parallel}$ and is independent of this broadening mechanism. Along q_{az} the peak is convoluted with the distribution function of the in-plane axes alignment. If we assume that the shape of the crystallites is isotropic, the width is a combination of $\Gamma_{\parallel}$ (the width due to the finite crystallite size) and Γ_{mis}, the width associated with the misalignment. With some simplifications we can isolate Γ_{mis}. If Γ_{mis} is small, the broadening which lies on an arc is approximately along a straight line perpendicular to $q_{\parallel}$. If we further assume that we can describe the peak by a convolution of two Gaussian functions, the resulting peak is another Gaussian with the width $\Gamma_{az} = \sqrt{\Gamma_{\parallel}^2 + \Gamma_{mis}^2}$ and we can extract Γ_{mis}. It is more instructive to calculate the angular width Γ_{θ} which is given by:

$$\Gamma_{\theta} = 2 \arctan\left(\frac{\sqrt{\Gamma_{az}^2 - \Gamma_{\parallel}^2}}{2q_{\parallel}}\right) , \tag{3.35}$$

since its value is independent of the in-plane position $q_{\parallel}$ at which it was measured.

A simple visual inspection of the peak in Fig. 3.4b reveals that it is composed of two contributions: an intense peak broadened in q_{az} and a less intense peak at larger q_z with a larger width along this direction but significantly less broad in q_{az}.

The view along the q_{az}-axis (Fig. 3.4c) shows that the more intense peak is broadened in the direction q_{χ}. A broadening of the peak in this direction occurs if the crystallites have a distribution of misalignment in the out-of-plane crystal axes (i.e. if they have a distribution of tilts). This leads to a broadening of the peak which lies on a spherical shell around the origin of reciprocal space. Consequently this broadening mechanism also effects the peak in the direction q_{az} and the expression in Eq. 3.35 would have to be modified accordingly. However, for all samples investigated this effect was either not present or small enough to be negligible.

Modelling all these effects is difficult, because an analytic description of the resulting peak shape could not be obtained. The reason for this is that the symmetry of the different broadening mechanisms is not easily described in a common coordinate system. While the broadening due to the finite size of the crystallites is best described in a Cartesian coordinate system, the broadening due to the misalignment of the axes is best described in spherical coordinates. Therefore, we usually analyzed 1D cuts through reciprocal space rather than the full 3D shape. To verify that this procedure yields reliable results, the 3D peak shown in Fig. 3.4 was fitted with the full model. This was achieved by binning the data into a spherical coordinate system and numerically calculating the model starting with a 3D Gaussian which was then convoluted with two Gaussian functions in the polar and azimuthal direction to model the two broadening mechanisms. The

results were in good agreement with those obtained by the 1D cuts. Since 1D cuts can be measured much faster and the data analysis is significantly easier this procedure was used primarily.

4 Experimental

This chapter focuses on the experimental details of the conventional reflection geometry which was primarily used in this work. Details of transmission surface diffraction are described in Section 8.1 and in[41].

4.1 Hanging Meniscus Cell

For the first part of the SXRD measurements in reflection geometry the hanging meniscus cell developed by Magnussen *et al.*[43] was employed. A schematical drawing of the cell can be seen in Fig. 4.1. The central part of the cell is a system of a PTFE tube inside a glass tube positioned $3-5\,\mathrm{mm}$ above a hat shaped sample. Between the sample surface and the glass rod a freestanding electrolyte meniscus makes contact between the working electrode, the counter electrode and the reference electrode. The size of the meniscus can be increased by pushing electrolyte into the cell through the inner tube, and decreased by withdrawing electrolyte through the outer tube. The flow of the electrolyte can be precisely controlled with a resolution of $4\,\mu\mathrm{L}$ using motorized syringes. A continuous exchange of electrolyte is also possible by simultaneously pushing electrolyte into the inlet and removing it at the same rate from the outlet. The liquid handling system will be described in more detail in the next section. A Ag/AgCl reference electrode is located at the top of the cell at the electrolyte inlet. In order to avoid contamination of the

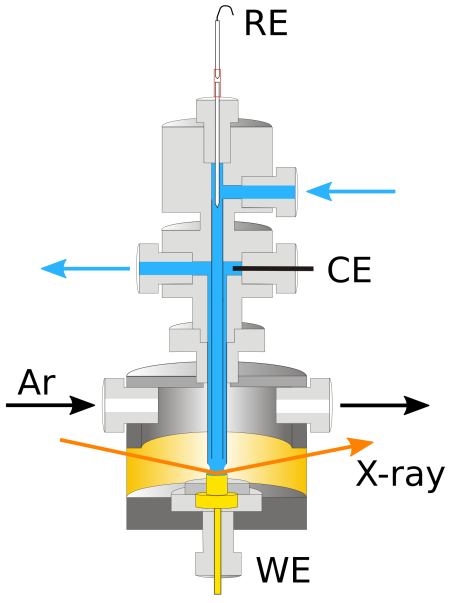

Fig. 4.1: Hanging meniscus cell used for the first part of the SXRD experiments in reflection geometry. The figure was adapted from Golks[42].

working electrode due to dissolution of the platinum counter electrode, the counter electrode is located at the electrolyte outlet. The sample is mounted on a PCTFE holder, which itself is mounted at the bottom of an aluminum chamber. The top part of the cell containing the two tubes described above is mounted at the top of the chamber and is made from PCTFE. Inside the aluminum chamber an argon atmosphere is maintained in order to prevent the contact of the meniscus with oxygen. The X-ray beam enters and leaves the chamber through a Kapton window.

The advantage of the hanging meniscus cell is that only the top surface of the working electrode is exposed to electrolyte permitting electrochemical measurements of surfaces with well defined orientation. Furthermore, the water volume is much larger than in thin film cells and since the meniscus is surrounded by argon, reactive processes can be investigated in an oxygen free environment. The disadvantage of the cell is its poor long-term stability. Since the reference electrode is located at the highest point in the cell small amounts of gas, which could enter during the exchange of electrolyte, can accumulate at the reference electrode. If the contact to the reference electrode is lost strong gas evolution due to the splitting of water in a water based electrolyte is a likely result. The reason for this is that the potentiostat will apply the maximum possible potential (either positive or negative) since its amplifier is driven into saturation without a proper feedback signal from the reference electrode. As a result the meniscus will collapse which terminates the experiment. Obviously the same applies for intentional gas evolution which makes the cell unsuitable for the investigation of water splitting. Furthermore, during long experiments, especially if a large amount of electrolyte was exchanged, a wetting of the sides of the electrode was observed which eventually results in the collapse of the meniscus.

4.2 Novel Electrochemical Cell for *Operando* SXRD

For the *operando* investigation of OER catalysts a new cell had to be designed which does not posses the stability issues of the hanging meniscus cell (Section 4.1) in order to perform measurements during strong gas evolution. Furthermore, during the experiments of Co electrodeposition (Chapter 5), we often noticed that we had to measure with an attenuated X-ray beam or had to perform certain steps completely without beam in order to avoid beam damage. For this reason, a complementary measurement technique had to be implemented into the new cell. A cell matching these specification as well as an improved electrolyte distribution system were developed within this work and are described in the following. Optical reflectivity was integrated into the cell with the help of our collaboration partner Fouad Maroun as a complementary measurement technique. Optical reflectivity does not influence the sample and can be used as a continuous monitor of the sample. Our cell is based on Carla *et al.*'s[44] improved version of a cell design by Foresti *et al*[45]. The advantages of our cell compared to these cells are listed at the end of this section.

The central part of the experimental setup is shown in color in Fig. 4.2. The electrochemical

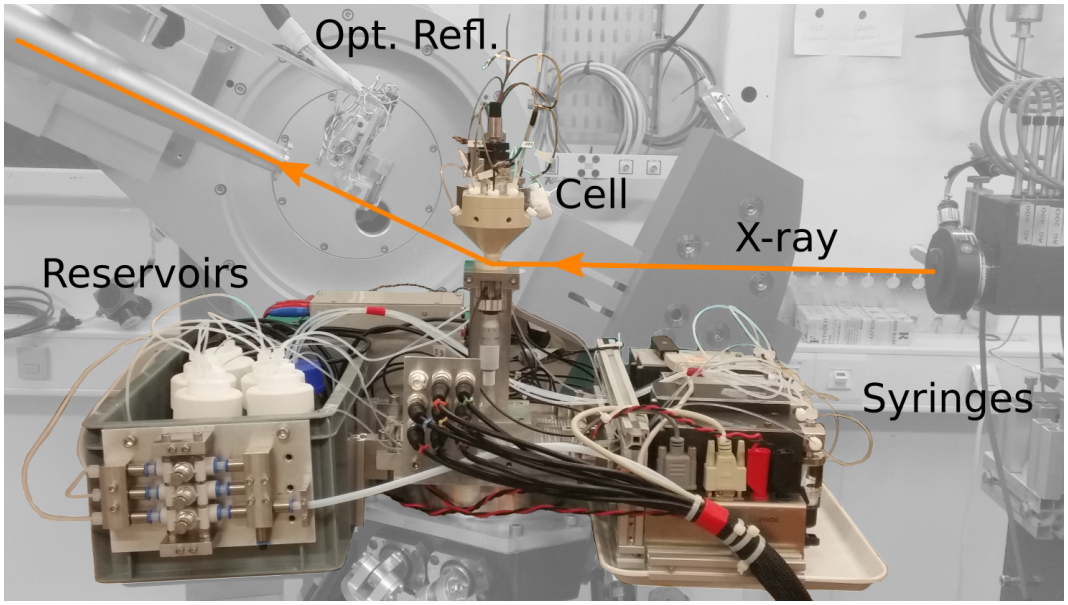

Fig. 4.2: Picture of the whole SXRD setup (color) mounted on the diffractometer at ID03 (gray). The cell (see Fig. 4.3) is located at the center of the setup. A box containing the reservoir and waste bottles is mounted on the left and a platform on which all syringes and valves are mounted is located on the right hand side. A box containing amplifiers and power supplies for the optical reflectivity setup can be seen at the back side. All cables and a tube for the Ar supply are routed from the diffractometer in a single cable sleeve. The path of the X-ray beam is indicated by an orange arrow.

cell (center), the electrolyte reservoirs (left), the distribution system for the electrolytes (right) and a box containing electronics for the optical reflectivity setup (left, back) are directly mounted on the diffractometer (gray scale). This has two main advantages, firstly the length of the flow-paths for the electrolytes is kept as short as possible and secondly, apart from one cable strand encapsulated in a single cable sleeve no other tubes or cables have to be run to the cell. This avoids that tubes or cables can be damaged by the diffractometer movement.

The potentiostat (Ivium, CompactStat) and an A/D-converter (National Instruments) as well as a PC are located inside the experimental hutch next to the diffractometer. The PC is used to control the A/D-converter, the potentiostat, a camera positioned inside the cell and the motorized syringes and valves (Hamilton) of the electrolyte distribution system. The A/D-converter records the signal of the optical reflectivity and the water level detector as well as the electrochemical current and potential. A separate A/D-converter belonging to the beamline records the same parameters (with the exception of the water level detector) to save these values along with the XRD data. This greatly eases data analysis and data synchronization. A remote desktop connection to the PC inside the experimental hutch is used to run the whole experiment from inside the control room.

Fig. 4.3b shows a schematical 3D view of the cell without the laser system. A cut through the cell reveals the concept of the cell design (Fig. 4.3a, Fig. 4.3c detail). The parts of the cell which

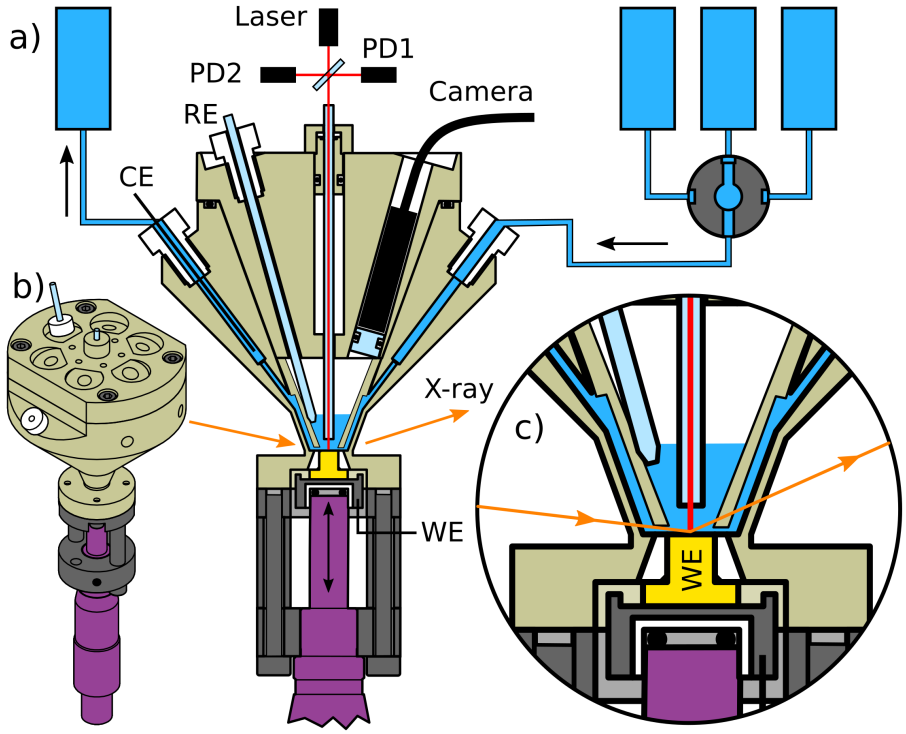

Fig. 4.3: Schematical drawings of the SXRD cell. A 3D view of the cell is shown in b). a) shows a cut through the center of the cell along with a simplified diagram of the electrolyte distribution system. The cell chamber is shown magnified in c). The cell consists of 5 PEEK parts (khaki): the main body which is permanently fixed to the diffractometer, a plug which seals the cell, a 1 mm thick funnel like inset to direct the water flow to the working electrode (WE) and a glass rod holder consisting of two parts. The WE is pressed into the main body by a micrometer screw (purple) and sealed with a PTFE seal (white). The electrolyte can be inserted by three independent syringes and removed by a single syringe through two outlets in the main body. The plug has 5 general purpose access ports to the cell with UNF $^1/_4{}''$ connectors and an inner diameter of 3 mm (port for reference electrode (RE) seen in cut). A camera is mounted in a sixth access port which is sealed by a glass window to monitor the electrolyte filling level and the formation of bubbles. On top of the cell a laser, a beam splitter and two photo diodes (PD1/2) are mounted which can be used to measure the optical reflectivity of the sample. Directly above the sample surface, the thickness of the main body is reduced to 1 mm to serve as a window for the X-ray beam.

are in contact with the electrolyte are made from PEEK (khaki). The main body (lowest PEEK part) has two conical openings along the central vertical axis: a small one at the bottom and a large one at the top. A hat shaped single crystal working electrode with an upper polished surface having a diameter of 4 mm (yellow) is used in this cell. On top of the working electrode a PTFE part in the shape of a truncated cone with a bore hole in the centre is attached to seal the working electrode to the lower conical opening of the main body. A micrometer screw (purple) presses the working electrode into the main body to make a tight connection. The advantage of this seal is that it seals the crystal directly below the polished surface, which minimizes the area of the crystal sides exposed to the electrolyte. Between the working electrode and the micrometer screw

a stainless steal part (grey) is used to contact the working electrode and a PTFE part (white) is used to insulate the working electrode from the micrometer screw. Between the insulator and the top of the micrometer screw an O-ring functions as a spring.

Electrolyte can be filled into the main body of the cell by a system of three syringes connected to a 3:1 valve and can be removed by a single syringe (see Fig. 4.3a). Between each of the three syringes and the 3:1 valve, an additional 3:1 valve is connected (not shown in figure) which connects the syringe with an electrolyte reservoir, a waste container or the 3:1 valve shown in the figure. A fritted glass tube can be used to purge the electrolyte reservoirs with gas. In most of the experiments argon was used to remove oxygen from the solution. In Fig. 4.3a the flow direction of the electrolyte is indicated by arrows. As in the case of the hanging meniscus cell, the platinum counter electrode is located in the electrolyte outlet to avoid contamination. The syringes can either be operated simultaneously to exchange electrolyte, or independently to adjust the water level in the cell. Due to geometrical constraints the electrolyte inlet and outlet in the main body are much higher than the surface of the working electrode. To guide the electrolyte flow along the surface, a funnel shaped inset with a thickness of 1 mm and two channels for electrolyte with a width of 4 mm and a thickness of 0.5 mm is placed inside the upper conical opening of the main body. On top of the funnel a plug is place to seal the cell from the top. The plug has 5 general purpose access ports to the cell with UNF $^1/_4{}''$ connectors and an inner diameter of 3 mm. These ports are usually used for a Ag/AgCl reference electrode (seen in the cut), an additional glassy carbon counter electrode, a Pt wire which serves as a water level detector and an inlet and an outlet for Ar. In a sixth port which is sealed by a glass window, a camera is mounted.

In the center of the plug a glass rod is located which serves as a beam guide for optical reflectivity measurements. Directly above the beam guide a beam splitter and a laser along with two photo diodes (PD1 and PD2) are mounted. PD2 is used as a monitor for the laser intensity, whereas PD1 measures the sample reflectivity. Optical reflectivity is extremely sensitive to small changes in the electronic configuration of the sample surface. Its penetration depth is comparable to that of the X-ray beam under grazing incidence and therefore probes the same part of the sample. Even changes in the sub-monolayer regime as in the case of chloride adsorption on Au(111) can be clearly seen. Furthermore, it was shown that the optical reflectivity decreases linearly with the film thickness during cobalt deposition[46] which makes it a good tool to monitor the growth process. It has to be stated that the optical reflectivity is only measured under normal incidence, i.e. at one angle. Modeling the optical reflectivity is therefore difficult. However, we mainly used the technique to make sure that the sample is stable. For example in the case of cobalt deposition, the electrolyte has to be exchanged after deposition and the stabilization potential has to be chosen in such a way that neither further uncontrolled deposition nor dissolution takes place before the exchange is finished and the film can be stabilized properly. With optical reflectivity we can make sure that the sample thickness is constant during this process with sub-monolayer precision.

In Fig. 4.3c the path of the X-ray is shown as an orange arrow. In the region above the sample surface the main body of the cell has a wall thickness of 1 mm and serves as a window for the X-ray beam. This is the reason for choosing PEEK as the cell material: contrary to PTFE and PCTFE, PEEK is very stable in the presence of intense X-ray radiation. For experiments under grazing incidence, the path of the beam through the electrolyte/PEEK is ≈ 7 mm/≈ 3 mm for $\gamma = 0°$ and ≈ 11 mm/≈ 6 mm for $\gamma = 45°$, where γ is the angle of the detector arm (see Fig. 4.4). At an X-ray energy of 22.5 keV, the resulting loss of intensity due to absorption is ≈ 40 % for $\gamma = 0°$ and ≈ 60 % for $\gamma = 45°$. In the calculations of the absorption, we have assumed that the electrolyte is water and the attenuation length of PEEK was approximated by that of water as well, which is a good approximation.

In comparison to the cell design by Foresti *et al.* mentioned above, our cell has the following advantages:

- Electrolyte flow is directed directly across the sample.
- The reference electrode is closer to the sample.
- The sample can be monitored by optical reflectivity.
- The sample can be monitored by a camera which is especially important to monitor the accumulation of gas bubbles.
- Only the top surface of the sample is exposed to electrolyte enabling electrochemistry of pure surface orientations.
- The electrolyte level in the cell can be adjusted and an argon atmosphere above the liquid can be used to reduce the oxygen content in the electrolyte.
- The cell can be emptied completely which is essential for multistage experiments which require the thorough removal of traces from the previous electrolyte.

4.3 Scattering Geometry

In the conventional reflection geometry the beam impinges the sample under an angle μ. For surface diffraction it is convenient to fix μ in order to keep the illuminated area of the sample constant. Since the penetration depth of the beam increases with μ it is favorable to keep the angle as small as possible to minimize scattering from the substrate. A small angle of μ however leads to a large beam footprint which can also reduce the signal if it becomes larger than the sample itself. Another complication of a small angle of incident is that the experiment becomes more prone to misalignment and drift of the beam. Apart from reflectivity measurements where μ has to be varied, an angle of $\mu = 0.34°$ was used throughout this work.

In reflection geometry a six-circle diffractometer was used. Four of the six circles (μ, θ, δ and γ) are shown in Fig. 4.4. The θ-circle rotates the sample around the surface normal direction

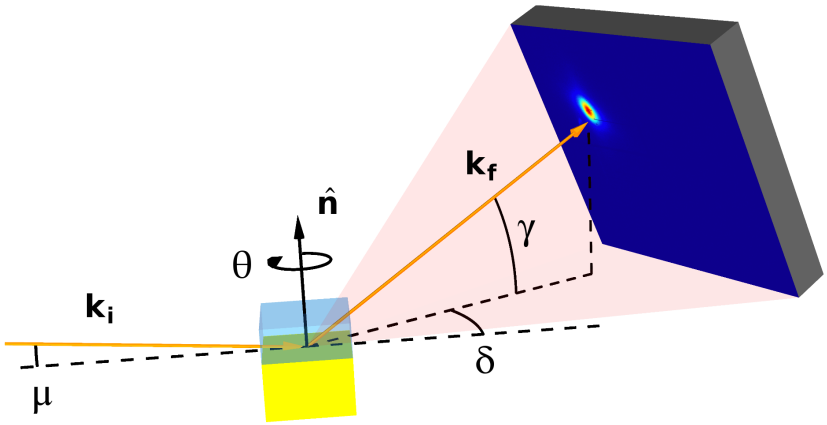

Fig. 4.4: Reflection geometry for SXRD. The beam is incident on the sample under an angle μ. The sample has three rotational degrees of freedom: θ, χ and ϕ. χ and ϕ are not shown since they only serve the purpose of aligning the surface normal parallel to the rotation axis of θ. The detector can be rotated on a spherical shell by the azimuthal angle δ and the polar angle γ.

$\hat{n}$. In order to align the sample in such a way that $\hat{n}$ is perpendicular to the rotation axis of θ, two further rotations χ and ϕ which have their rotation axes perpendicular and both in the horizontal plane are available. These rotations were only used for the aforementioned purpose and were fixed after alignment and are therefore not shown in Fig. 4.4. The detector has two degrees of freedom and can be moved on a spherical shell around the center of the sample. The azimuthal angle δ rotates the detector arm around the vertical axis and the γ-circle lifts the arm from the horizontal plane. After alignment of the diffractometer, all six rotation axes intersect in the pivot point. In order to move the center of the sample surface to this point a further translation stage which can move the sample in all directions is available. At ID03 at the ESRF where we performed these experiments the translation stage as well as the rotations χ and ϕ were provided by a single hexapod.

A MAXIPIX detector with 516×516 pixels and an active area of $28.4 \times 28.4\,\mathrm{mm}^2$ (pixel size $55 \times 55\,\mu\mathrm{m}^2$) was used. The distance between the sample and the detector was in the range of 600 to 1000 mm.

5 *In Situ* Surface X-ray Diffraction Study of Ultrathin Epitaxial Co Films on Au(111) in Alkaline Solution

This chapter is based on an article published in Electrochimica Acta[34].

Abstract

The oxidation behavior of ultrathin electrodeposited Co films on Au(111) in alkaline electrolyte was studied using *in situ* surface X-ray scattering techniques employing synchrotron radiation and complementary optical reflectivity and electrochemical measurements. The films are formed at pH 4 and consist of (001)-oriented hcp Co crystallites that are several nm high, a few ten nm in diameter, and remain largely unchanged after electrolyte exchange to pH 12 solution. In the pre-oxidation peak only minor changes were observed in the diffraction studies, excluding the formation of $Co(OH)_2$ layers. In the potential regime of Co hydroxide formation a rapid reduction of the amount of Co is observed, while the characteristic height of the islands decreases only slightly. On longer times scales, growth of 3D crystals of $Co(OH)_2$ occurs as well as irreversible Co dissolution into the electrolyte is found. On the basis of the structural observations oxidation of the Co film is proposed to proceed via fast formation of an ultrathin passivating layer, followed by nucleation and growth of 3D hydroxide crystals at the grain boundaries in the Co deposit.

5.1 Introduction

The oxidation of iron-group metals and their alloys has been intensely studied in the past decades, aiming at determining the origin of the very different passivating properties and corrosion behavior of those metals. More recently, iron-group oxides have received increasing interest as Pt-free catalysts for the hydrogen (HER) and oxygen (OER) evolution reaction in light-driven water splitting [47–51]. In particular, cobalt oxides are nowadays among the most promising

catalyst materials for oxygen evolution and have been extensively studied in the last years [20, 50, 52, 53]. In these applications typically Co oxide nanoparticles or nanostructured films are employed, which frequently are prepared by electrochemical methods [52, 54–56]. For further development of these materials deeper insight into their electrocatalytic reactivity as well as into suitable preparation procedures is highly desirable. This includes a more detailed characterization of the structure of these nanomaterials and of their interface to the electrolyte. The latter is also required for clarifying more complex, synergetic effects, such as the strong increase in the OER activity of Co oxide on Au surfaces as compared to the bare oxide [54].

For obtaining clear correlations between the structure and reactivity of these materials suitable model systems are necessary that are structurally better defined and thus accessible to modern characterization methods. Walton *et al.* very recently investigated the oxidation of Co oxide nano-islands on Au(111) surfaces under ultrahigh vacuum (UHV) conditions in detail by scanning tunneling microscopy (STM), X-ray photoelectron spectroscopy (XPS), and density functional theory (DFT) calculations [57]. These studies revealed facile insertion of oxygen underneath the Co layer at the edge of the nano-islands. For true understanding of the OER reaction similar studies in the native environment, i.e., in neutral or alkaline electrolyte, will be required, however. As a first step towards this objective we here present first in-depth studies of the structural changes in an electrodeposited epitaxial Co film on Au(111) upon electrochemical oxidation by *in situ* surface X-ray diffraction (SXRD) methods.

While there is an abundant literature about the electrochemical oxidation of cobalt, essentially in alkaline solutions [58–63], only a few structural studies by surface-sensitive techniques are available. First *in situ* STM studies of Co(001) electrodes in acidic solution were performed by Ando *et al.*, concentrating on anodic Co dissolution [64]. The initial stages of hydroxide formation and its reduction on Co(001) in 0.1 M NaOH were studied by Foelske *et al.* using *in situ* STM and *ex situ* XPS [65]. They reported the observation of a hexagonal surface lattice at the onset of oxidation, which was attributed to the formation of a (001)-oriented monolayer of β-$Co(OH)_2$. More recent electrochemical characterizations of the pre-oxidation stages coupled with DFT calculation are rather suggesting that the oxidation commences with the adsorption of a dense OH adlayer which also induces a surface restructuring [66].

In this work, we study the electrochemical oxidation of epitaxial Co films, formed by electrodeposition on Au(111) [21, 67]. The oxidation process is studied at various potentials by *in situ* SXRD and complementary electrochemical and optical reflectivity measurements. The structure of the oxide and its interface with Co are discussed and an oxide growth model is proposed. This approach presents several experimental advantages as compared to studies of single-crystals: Firstly, it allows direct preparation and conversion of the sample in the cell while it can be characterized by the employed *in situ* probes. This in particular avoids contact of the Co surface with the atmosphere. Secondly, the thin film geometry enables the quantitative determination of the amount of Co loss due to oxidation and dissolution. As we will show, the possibility to directly determine the structure and morphology of the Co in the film allows to

obtain detailed insights into the microscopic oxidation mechanism.

5.2 Experimental Methods

X-ray scattering experiments were performed at beam line ID03 at the ESRF. We used an X-ray energy of 22.5 keV at which the photon flux was 4×10^{11} counts/s. The beam was focused on the detector such that the beam size was $30 \times 250\,\mu\text{m}^2$ at the position of the sample. The detector was a MAXIPIX with 512×512 pixels and a pixel size of $55 \times 55\,\mu\text{m}^2$ located at a distance of 961 mm to the centre of rotation. The diffractometer was configured in a six circle geometry. For all measurements (apart from reflectivity) the incidence angle was fixed to 0.34°. At this angle, the beam footprint on the sample is $250\,\mu\text{m} \times 5\,\text{mm}$. For creation of reciprocal space maps from the 2D detector frames the BINocular software was employed [68]. For convenience, all positions in reciprocal space are given in coordinates (H, K, L) of the hexagonal reciprocal coordinate system of the Au(111) substrate with reciprocal lattice vectors

$$a^* = \frac{4\pi}{a_{nn}\sqrt{3}} = 2.51\,\text{Å}^{-1}\,, \tag{5.1a}$$

$$c^* = \frac{2\pi}{a_{nn}\sqrt{6}} = 0.89\,\text{Å}^{-1}\,, \tag{5.1b}$$

where $a_{nn} = 2.885$ is the nearest-neighbor separation of the Au surface atoms. A schematic of the hexagonal coordinate system is given in Fig. 5.1 together with positions of Bragg peaks from bulk fcc Au, hcp Co and hcp $Co(OH)_2$. Bragg reflections are indexed by conventional Miller indices.

For the X-ray experiments we used hat shaped Au(111) single crystals with an orientation uncertainty of $< 0.1°$. The wetted surface had a diameter of 4 mm and was polished to a roughness depth of $0.01\,\mu\text{m}$ (Mateck). Prior to the experiments the crystals were sputtered and annealed until a sharp LEED pattern was observed. Between different experiments the surface was electrochemically cleaned by 3 cycles of oxidation in 0.1 M $HClO_4$ via the application of 3 V between the crystal and a Pt wire and reduction in 0.1 M HCl to remove any remaining Co from the crystal. The crystal was then annealed in a butane flame for 5 min. Electrolyte solutions were prepared from $NaClO_4$ (Sigma, puriss.), HCl (Carlo Erba, for electronic use), $CoCl_2$ (Merck, pro analysis), NaOH (Sigma), and Milli-Q water.

The Au(111) crystal was mounted at open circuit potential (OCP) in our "hanging meniscus" transmission cell [43], which employs a Pt counter electrode and a Ag/AgCl (3 M KCl) reference electrode (all potentials in this work are referred to this electrode). The cell was initially filled with 0.1 M $NaClO_4$ + 1.3 mM HCl + 1 mM $CoCl_2$ with pH 4 and kept during sample alignment at a potential of $E = 0.4\,\text{V}$. Before and during the X-ray measurements the quality of the sample and

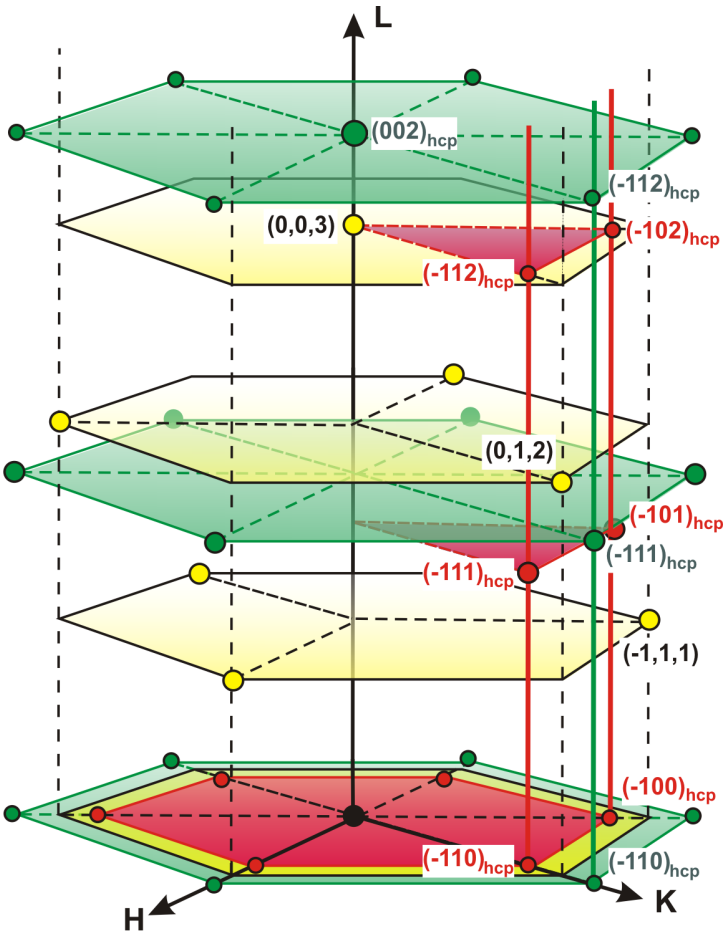

Fig. 5.1: Reciprocal space geometry of the experiments. The employed coordinates (H, K, L) are defined by the Bragg peaks of Au(111) substrate (yellow circles). Bragg peaks of the (001)-oriented hcp Co (green circles) and $Co(OH)_2$ (red circles) lattices are labeled by their conventional hcp Miller indices. The X-ray data were obtained by L-scans along the surface normal direction (red and green solid lines) and axial in-plane K-scans.

the electrochemistry was checked by cyclic voltammetry (CV). Exchange of the electrolytes after Co deposition to first 0.1 M $NaClO_4$ + 1.3 mM HCl and subsequently 0.1 M $NaClO_4$ + 0.01 M NaOH was performed using the remote-controlled fluid handling system of the instrumental setup, which allowed monitoring the X-ray intensity during the exchange. Typically, $\geq 8\,\mathrm{ml}$ were exchanged at 10 to $50\,\mu\mathrm{l s}^{-1}$, which ensured quantitative replacement of the electrolyte in the cell (cell volume $\sim 1\,\mathrm{ml}$), as also verified by measuring the pH in the cell outlet. The entire exchange procedure required a time period of $\geq 30\,\mathrm{min}$.

For the optical measurements, the Co films were deposited on a (111)-oriented Au buffer layer deposited on Si(111), following the procedures described in Ref. [66]. The sample was mounted in an electrochemical flow cell (cell volume $\sim 1\,\mathrm{ml}$, flow rate $\sim 1\,\mathrm{ml/min}$). The reflectivity was measured at normal incidence using a laser diode at 630 nm and a standard Si photodiode for the intensity measurements. The probed sample surface was $\sim 1\,\mathrm{mm}^2$ and the sample area exposed to the electrolyte was $0.5\,\mathrm{cm}^2$.

5.3 Results

5.3.1 Structure and Morphology of the Co Deposit

Cyclic voltammograms of Au(111) in 0.1 M $NaClO_4$ + 1.3 mM HCl + 1 mM $CoCl_2$ (pH 4) obtained in the "hanging meniscus" transmission cell (see supporting information, Fig. S1) are in good agreement to those in the literature [21, 67]. Thin Co films for the oxidation studies were deposited at a potential of -0.85 V for a time $t_{dep} = 10$ to 100 s. Deposition was stopped by stepping the potential to -0.65 V, where the film is stable against dissolution. The resulting film thickness for a given deposition time was obtained by subsequent anodic stripping and integrating the charge under the Co dissolution peak. A new layer with the desired thickness was then deposited and its structure investigated in detail (i) directly after deposition and (ii) prior to oxidation in pH 12 solution. For the latter the Co film was transferred into 0.1 M $NaClO_4$ + 0.01 M NaOH by a two-step procedure: First, an exchange to $CoCl_2$ free electrolyte of pH 3.5 at -0.65 V was performed to ensure a negligible concentration of Co^{2+} species. Then, this solution was exchanged by 0.1 M $NaClO_4$ + 0.01 M NaOH with the potential being kept at -1.05 V.

In accordance with previous *in situ* STM studies, *ex situ* AFM, *ex situ* magneto-optical measurements and *ex situ* XRD characterization [67, 69], electrodeposition results in a smooth (001)-oriented film of hcp Co. Fig. 5.2a presents a reciprocal space map of an as deposited Co layer (deposition time $t_{dep} = 100$ s). The primary diffraction maxima at $K = 1.137$ and $L = 0$, 1.75, and 3.5 can be identified with the Co(-110)$_{\text{hcp}}$, Co(-111)$_{\text{hcp}}$, and Co(-112)$_{\text{hcp}}$ Bragg peaks, respectively. Identical peaks are found after a 60° in-plane rotation of the sample, confirming that the majority of the film consists of epitaxial hcp Co with a (001) orientation which is aligned with the Au(111) substrate lattice within the surface plane. Specifically, a tilt or in-plane rotation of the Co lattice of the order of some degrees with respect to the substrate lattice, as found in other electrodeposited films with large lattice mismatch, was not observed [70]. From the positions of these peaks the vertical and in-plane Co hcp lattice constants c_{Co} and a_{Co} can be determined. The obtained values indicate a small tensile in-plane strain of $\varepsilon_{\parallel} = (a_{Co} - a_{Co,b})/a_{Co,b} = 1.4\,\%$ and a compensating compressive out-of-plane strain $\varepsilon_{\perp} = (c_{Co} - c_{Co,b})/c_{Co,b} = -0.5\,\%$ with respect to bulk Co (lattice parameters $a_{Co,b} = 2.507$ Å and $c_{Co,b} = 4.069$ Å). Similar strain values were obtained for other Co deposits. From the full width at half maximum (FWHM) Γ_L of the Co(-111)$_{\text{hcp}}$ Bragg peak along the L-direction the thickness of the epitaxial Co-layer $d_{Co} = (2\pi)/(\Gamma_L \cdot c^*)$, i.e., the characteristic size of the crystallites along the surface normal, was determined as $d_{Co} = 40$ Å. The precise meaning of this quantity will be discussed in more detail below.

The FWHM of the peaks in in-plane azimuthal scans is determined both by the in-plane crystallite size, which results in an intrinsic FWHM Γ_K, and the angular distribution of the in-plane orientation of the Co crystallites. A detailed analysis of the (H,K) maps around several hcp Co peaks gave an in-plane crystallite size $\xi_{\parallel} = (2\pi)/(\Gamma_K \cdot a^*)$ of 274 Å and a narrow in-plane

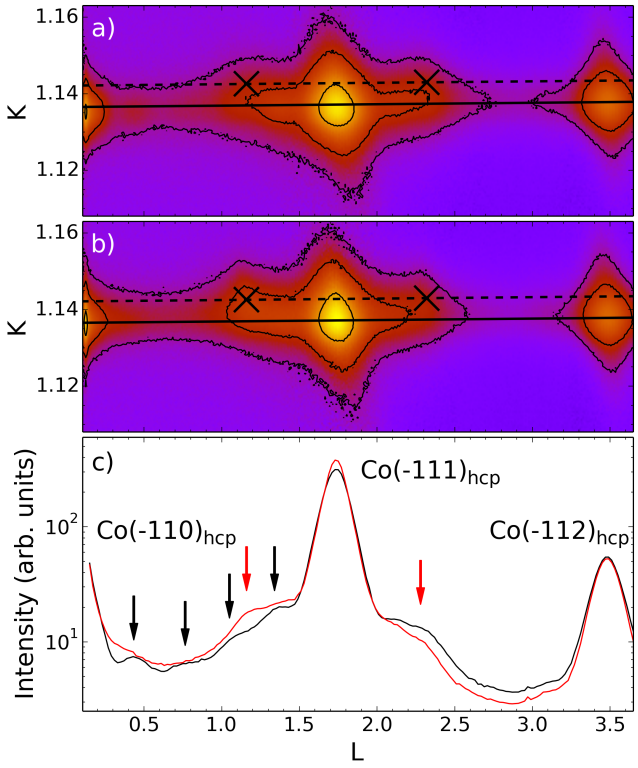

Fig. 5.2: (a,b) Reciprocal space maps (in logarithmic color scale) and (c) L-scans at $K = 1.137$ (marked by solid lines in (a,b)), obtained at -0.65 V 4 min after 100 s deposition of Co at -0.85 V in (a) acidic solution ($\approx$ 16 ML, black line in (c)) and (b) 40 min later at -1.05 V after transfer to alkaline solution ($\approx$ 18 ML, red line in (c)). The X-ray scattering data show the Co(-110)$_{hcp}$, Co(-111)$_{hcp}$, and Co(-112)$_{hcp}$ Bragg peaks, the Co(011)$_{fcc}$ and Co(012)$_{fcc}$ peaks of a minority phase (marked in (a,b) by crosses and broken line and in (c) by red arrows), and subsidiary maxima due to thickness oscillations (black arrows in (c)).

angular distribution around the K axis with a FWHM of $\Delta\theta = 0.6°$. Close inspection of the data reveals additional weaker features in the reciprocal space region between the Co Bragg peaks. In particular, along the L-scan through the Co Bragg reflections (Fig. 5.2c, black line) 4 subsidiary maxima (marked by black arrows) are visible between the Co(-110)$_{hcp}$ and Co(-111)$_{hcp}$ peak (similar maxima are also faintly recognizable between Co(-111)$_{hcp}$ and Co(-112)$_{hcp}$). The shape of the scan qualitatively resembles the N-slit interference function [39], indicating that the deposited Co film consists predominantly of a stack of $N = 6$ continuous unit cells, i.e., 6 hcp Co bilayers. The latter would correspond to a thickness of 24 Å, which is much smaller than the characteristic crystallite height d_{Co}, obtained from the FWHM of the Bragg peak. This discrepancy can be resolved by considering that the relative height of the subsidiary maxima as compared to the Bragg peaks is about one order of magnitude smaller than that expected for a perfect 6 bilayer thick film. We interpret the observed X-ray data as the result of a superposition of the X-ray intensity contributions of epitaxial Co crystallites, each of which consists of a defined number of bilayers $6 \leq N \leq N_{max}$.

A more detailed modeling of the L-scan intensity, which considers a Gaussian decay of

	$\varepsilon_{\parallel}$	$\xi_{\parallel}$	d_{Co}	$I/I_{pH12,ini}$	Co coverage
Co film (pH 4)	1.4%	274 Å	40 Å	88%	$\approx$ 16 ML
Co film (pH 12)	-	267 Å	47 Å	100%	$\approx$ 18 ML
2 $\times$ ox./red. cycles	1.3%	256 Å	46 Å	85%	$\approx$ 15 ML
Co ox. at $E = -0.7$ V	1.2%	227 Å	43 Å	54%	$\approx$ 10 ML
1.5 h at $E = -0.7$ V	0.9%	207 Å	46 Å	6%	$\approx$ 1 ML
ox. reduction	0.8%	123 Å	51 Å	13%	$\approx$ 2 ML

Table 5.1: Structural parameters of the hcp Co film at different stages of the oxidation experiment: In-plane strain $\varepsilon_{\parallel}$, in-plane crystallite size $\xi_{\parallel}$, characteristic size of the crystallites along the surface normal d_{Co}, integrated intensity of the Co(-111)$_{\text{hcp}}$ Bragg peak, normalized to its value immediately after transfer to alkaline solution (pH 12) and prior to oxidation $I/I_{pH12,ini}$, Co coverage (deposited amout of Co). The vertical strain $\varepsilon_{\perp} = -0.5\,\%$ has been found to be almost unchanged during the experiment.

the island height distribution function for $N > 6$ (see Suppl. Inf.), reveals that the amount of deposited Co corresponds in total to $\approx$ 16 full Co layers (in the following we define a Co coverage of 1 ML as one full Co layer). In this model the number of subsidiary maxima is dominated by the interference function of the uniform film. Scattering contributions of surface fraction covered by islands thicker than 6 bilayers are damping the oscillation amplitude due to the thickness distribution but contribute to the intensity and width of the Bragg peaks. In the following Co coverages of films directly after deposition were obtained by such modeling of the X-ray intensity distributions along L at the non-specular Co Bragg peak or from the oscillation period of the small angle specular reflectivity (see Fig. 5.4c). However, after oxidation steps subsidiary maxima usually vanish or are very weak. In this case changes of Co coverages were thus determined by respective changes of the integrated Co Bragg peak intensities (see Table 5.1). The height d_{Co} which is determined from the Bragg peak width is a characteristic value in between the Co coverage and the height of the highest islands in the distribution.

After transfer into pH 12 solution the film structure is essentially unaltered (see Fig. 5.2b) with no noticeable changes in the Bragg peak positions. Nevertheless, the electrolyte transfer leads to the modification of the Bragg peak intensities and shapes: First, the integrated intensity I of the Co(-111)$_{\text{hcp}}$ Bragg peak, calculated as $I = I_{max} \cdot \Gamma_L \cdot \Gamma_K^2$ (where I_{max} is the X-ray intensity at the peak position), increases by 14 % with respect to that of the initial deposit with a Co coverage of $\approx$ 16 ML. This leads to a Co coverage after electrolyte transfer of 18 ML. In parallel the vertical peak FWHM Γ_L decrease corresponds to a 17 % increase in d_{Co}. Furthermore, the subsidiary oscillations between the Bragg peaks almost completely disappear. All these observations indicate that additional Co electrodeposition and surface roughening could not be completely avoided during the transfer of the Co layer into the alkaline solution, which may partially be related to the rather long time (>30 min) required for the electrolyte exchange.

In both Fig. 5.2a and b we observe shoulders close to the Co(-111)$_{\text{hcp}}$ Bragg peak, which result

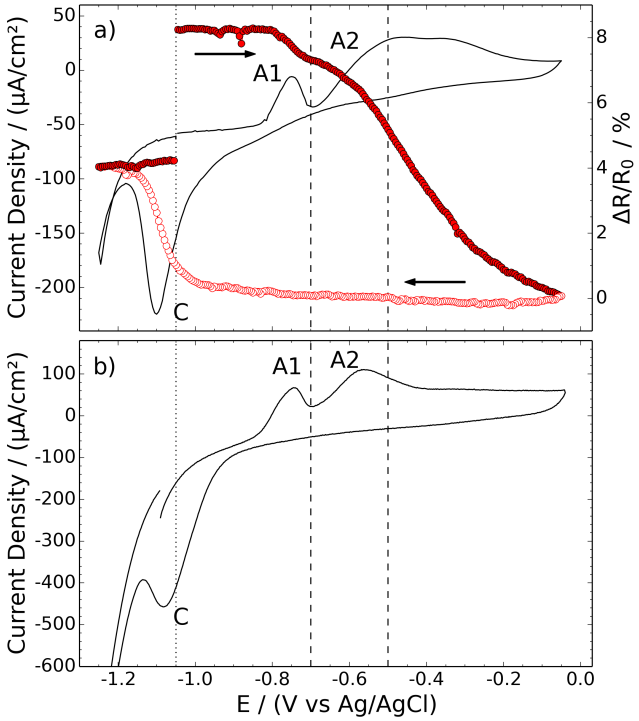

Fig. 5.3: Oxidation and reduction of a 4.1 ML Co film in 0.1 M $NaClO_4$ + 0.01 M NaOH (pH 12) solution. (a) Variation of the optical reflectivity $(R - R_0)/R_0$ (red line) with respect to that of bare Au/Si(111) (R_0) before Co deposition. The cyclic voltammogram (black line) is recorded in parallel in the *in situ* optical reflectivity cell ($dE/dt = 10\,\mathrm{mV/s}$). (b) Cyclic voltammogram in the *in situ* SXRD cell ($dE/dt = 20\,\mathrm{mV/s}$) of the 10 ML film after oxide reduction at -1.25 V. The vertical dashed lines indicate characteristic changes of the curves presented in Fig. 5.5.

from much weaker peaks at a slightly larger in-plane scattering vector $K = 1.142$ at $L = 1.2$ and 2.3 (marked by crosses in Fig. 5.2a, b and red arrows in Fig. 5.2c and become more prominent after electrolyte exchange. We assign these peaks to fcc $Co(011)_{fcc}$ and fcc $Co(012)_{fcc}$ Bragg reflections, respectively (here the Miller indices of the hexagonal coordinate system are used, see Fig. 5.1). The higher K values reveal that the fcc Co crystallites are less strained than the hcp Co ($\varepsilon_{||} = 0.8\,\%$). In all experiments the intensity of these peaks was more than an order of magnitude lower than that of the hcp Co peaks, indicating that at most a few percent of Co crystallized in the fcc structure. The influence of this minority phase will therefore be neglected in the subsequent discussion of the Co oxidation behavior.

5.3.2 Oxidation and Reduction of the Co Film

The oxidation in pH 12 solution of the deposited Co layers was characterized in detail. CVs of these deposits, obtained in the *in situ* optical reflectivity cell (Fig. 5.3a, black line) and in the *in situ* SXRD cell (Fig. 5.3b are in good agreement with previous data obtained on Co(001) single crystals [65]. They exhibit two anodic peaks (A1 and A2) in the positive going scan, corresponding to Co oxidation, and one cathodic reduction peak (C) in the reverse scan. At the

scan rate of 20 mV/s used in the subsequent *in situ* SXRD studies the anodic peaks are found at -0.76 (A1) and -0.56 V (A2), the cathodic peak C (dependent on the positive potential limit) in the range -1.1 to -0.93 V. In previous studies peak A1 was attributed to OH adsorption [66] and peak A2 to the formation of a thicker Co hydroxide layer [65]. Similar CVs were obtained for all epitaxial Co electrodeposits with a thickness larger than 4 atomic layers.

The Co oxidation is accompanied by a significant drop of the optical reflectivity (Fig. 5.3a, red line), where the optical reflectivity was acquired parallel to the CV. The reflectivity data is plotted as the relative reflectivity change, $\frac{\Delta R}{R_0} = \frac{R-R_0}{R_0}$, where R_0 is the optical reflectivity of Au/Si(111). This drop occurs in two stages, which are very well correlated with peaks A1 and A2. $\frac{\Delta R}{R_0}$ decreases from 8 % ($\frac{\Delta R}{R_0}$ of the Co film) to 0 % at -0.1 V. We attribute these potential-induced variations in reflectivity to changes in the thickness of the metallic Co film, caused by its oxidation. During the negative potential sweep, $\frac{\Delta R}{R_0}$ remains approximately constant until peak C is reached where it increases up to a value that is lower than the initial one. This indicates that the oxide reduction is only partially reversible, either due to formation of an irreversible oxide species or due to partial dissolution of the Co film. Taking into account that in the thin layer limit the relative reflectivity change with respect to that of the Au substrate is proportional to the thickness change of the film [71], the estimated amount of Co lost after one potential cycle is approximately 2 ML (see supporting information for more details on reflectivity modeling).

Structural changes in the Co film were first examined by monitoring the potential-dependent X-ray intensity of the Co(-111)$_{\mathrm{hcp}}$ Bragg reflection during oxidation/reduction cycles of a ≈ 10 ML thick Co film up to potentials just positive of peak A1. In this regime fully reversible changes in intensity were observed (Fig. 5.4a). In the positive scan a small intensity drop of about 3 % equivalent to a Co amount of 0.3 ML occurs at the potential of peak A1; in the negative potential scan the intensity is completely recovered in the regime of the reduction peak C. The same trend was observed in the optical reflectivity, as shown in Fig. 5.4b. The very small magnitude and the reversibility of the Co(-111)$_{\mathrm{hcp}}$ intensity changes rule out a process involving significant restructuring of the Co lattice, such as the conversion to Co hydroxide. The weak potential-dependence of the vertical FWHM Γ_L (≤ 1 % limited by the experimental noise) indicates corresponding very small changes in the characteristic height d_{Co} of the Co crystallites. In addition, X-ray reflectivity measurements (Fig. 5.4c) on a thinner Co film (≈ 5.4 ML) obtained negative ($E = -1.05$ V) of peak A1 and after a sweep through peak A1 and setting the potential to $E = -0.75$ V are virtually indistinguishable, indicating that the interface structure (averaged within the surface plane) is almost identical at the two potentials. A more detailed interpretation of these structural observations will be given in the discussion.

The oxidation/reduction processes in the potential regime of peak A2 have a much larger influence on the Co(-111)$_{\mathrm{hcp}}$ Bragg peak intensity and lead to irreversible modifications of the Co layer (Fig. 5.5a). In the positive sweep, the peak intensity decreases in the potential range of peak A2, whereas it remains quasi constant in the same range on the negative sweep. An analogue behavior is found for the change in the characteristic height d_{Co} of the Co crystallites,

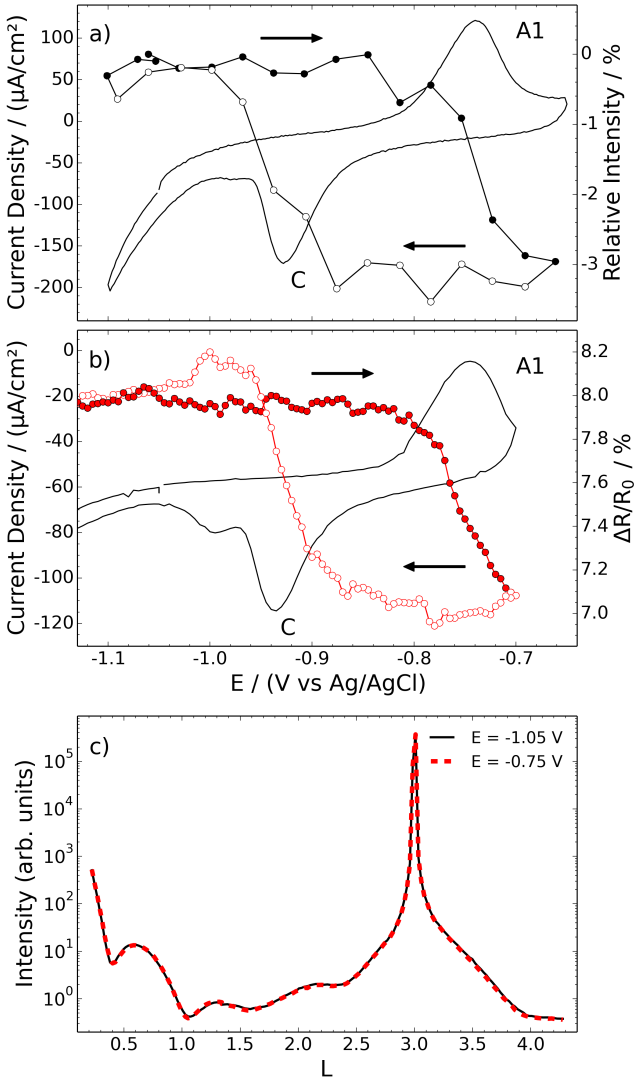

Fig. 5.4: OH adsorption/desorption process on the Co film in alkaline solution (pH 12). (a) Potential dependent integrated X-ray intensity of the Co(-111)$_{\mathrm{hcp}}$ Bragg peak of a ≈ 10 ML Co deposit (symbols connected with solid line) recorded at $dE/dt = 20\,\mathrm{mV/s}$ in parallel with the cyclic voltammogram (solid line). (b) Variation of the optical reflectivity $(R-R_0)/R_0$ (red symbols connected by lines) with respect to that of bare Au/Si(111) (R_0) before Co deposition. The 4.1 ML Co layer induces an increase of 8 % of $(R-R_0)/R_0$. The cyclic voltammogram at $dE/dt = 10\,\mathrm{mV/s}$ (black line) is recorded in parallel. (c) X-ray reflectivities of a Co film of 5.4 ML measured before OH adsorption at $E = -1.05\,\mathrm{V}$ (black solid line) and after a potential sweep to $-0.65\,\mathrm{V}$ and back to $E = -0.75\,\mathrm{V}$ (dashed red line).

obtained from the FWHM Γ_L of the Bragg peak, which likewise decreases in the oxidation regime (Fig. 5.5b). Both effects can be rationalized by the conversion of a fraction of the hcp Co film into a passivating Co oxide. On the negative sweep, no further Co oxidation occurs until peak C is reached where the Co peak intensity and the FWHM recover only partly. The shape of the Co intensity curve is very similar to that obtained by optical reflectivity (Fig. 5.3a).

The X-ray scattering data allows direct determination of the amount of Co involved in the

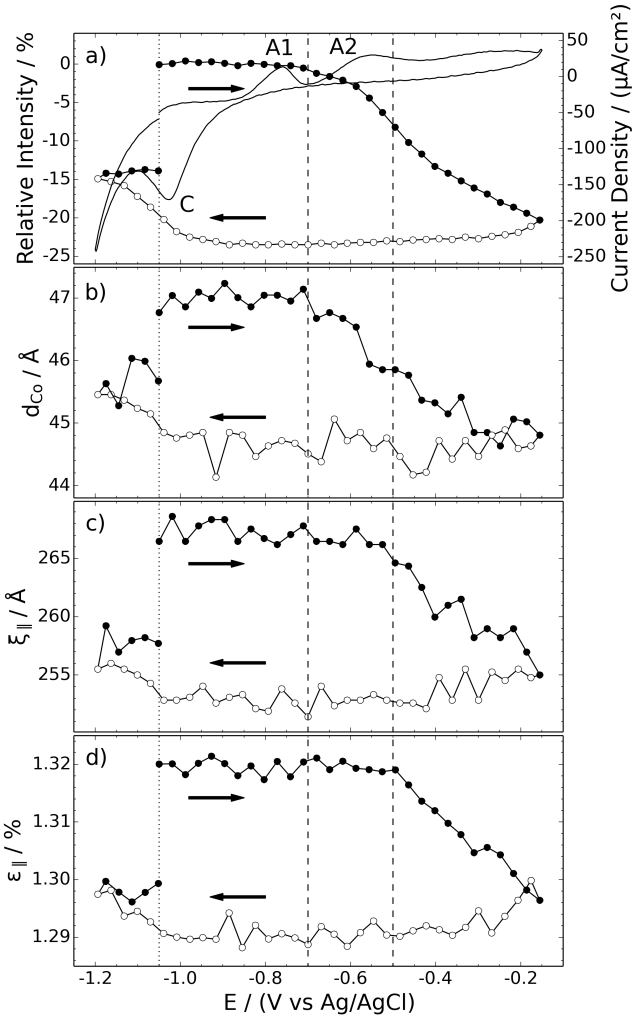

Fig. 5.5: Co hydroxide formation and reduction process of the 18 ML Co deposit in alkaline solution (pH 12). (a) Potential-dependent relative change of the integrated Bragg peak intensity, (b) characteristic height of the Co islands $d_{Co} = (2\pi)/(\Gamma_L \cdot c^*)$ resulting from the FWHM in L-direction Γ_L, (c) average in-plane size of the crystallites $\xi_{\|} = (2\pi)/(\Gamma_K \cdot a^*)$ as determined from the FWHM in the K-direction Γ_K, and (d) in-plane lattice strain $\varepsilon_{\|}$. The data were derived from measurements of the Co(-111)$_{\mathrm{hcp}}$ reflection of the deposit shown in Fig. 5.2b during a potential cycle at $dE/dt = 20\,\mathrm{mV/s}$ (experimental errors are comparable to the scatter in the data). Dashed lines indicate characteristic changes of the curves. In (a) the parallel recorded baseline-corrected voltammogram is included.

oxidation/reduction process, because the integrated Bragg peak intensity is approximately proportional to the number of atoms in the hcp Co lattice[1]. For the experiment shown in Fig. 5.5, which was obtained on the ≈ 18 ML thick Co film shown in Fig. 5.2b, 23 % of the Co film is oxidized on the positive sweep, which corresponds to a total loss of 4.1 ML. This is in good

[1]This assumption is strictly valid only for perfect crystallites. In the presence of defects diffuse scattering would occur and the Bragg peak intensity would be reduced. Since we do not observe significant diffuse scattering in our experiments, we ignore this effect. Furthermore, the crystallites should be homogenoeously strained due to their small size which would lead to low diffuse scattering.

agreement with the anodic charge of 2.55 mCcm^{-2} in the corresponding CV, which is equivalent to the oxidation of 4.3 ML of Co(0) into Co(II) (1 ML of Co(001) contains 1.85×10^{15} Co atoms/cm^2). In contrast, the characteristic height d_{Co} of the Co crystallites derived from the width Γ_L decreases by only ≈ 2 Å upon oxidation. Furthermore, also the characteristic lateral dimension $\xi_{\|}$ of the Co crystallites is shrinking during oxidation (Fig. 5.5c), as indicated by the increase in in-plane width Γ_K, and the small partial relaxation of the tensile in-plane strain is relaxing by $\Delta\varepsilon_{\|} = 0.03\,\%$. As will be shown in the discussion, these observations can only be rationalized if the oxidation is highly non-uniform. Interestingly, these changes of $\xi_{\|}$ and $\varepsilon_{\|}$ are delayed by $\approx +200$ mV with respect to the decrease in peak intensity and d_{Co} (indicated by dashed vertical lines in Fig. 5.5) and continue at potentials ≥ -0.35 V, where d_{Co} reaches its steady-state value. This indicates a second oxidation process, which occurs slower (based on the change in slope of the Bragg peak intensity above -0.35 V, see Fig. 5.5a) and progresses in lateral direction.

Upon reduction of the oxide layer approximately half of the intensity drop as well as of the drop in characteristic thickness d_{Co} recover instantly in the regime of peak C. During the rest of the scan and subsequently, at a fixed potential of -1.05 V, the intensity continues to increase over the following 20 min by a slower process. Nevertheless, the intensity does not completely recover, indicating an irreversible loss of Co in each oxidation/reduction cycle. The latter is illustrated in Fig. 5.6, where the Co Bragg peaks along the L and K directions are shown for the Co film described in Fig. 5.2 (for resulting values of structural parameters see Table 5.1). Obviously, the intensity of the Co(-111)$_{\mathrm{hcp}}$ and Co(-112)$_{\mathrm{hcp}}$ Bragg peaks after two oxidation/reduction cycles between -1.20 and -0.15 V (red lines) is lower than that obtained prior to oxidation (black and yellow lines). A more precise determination that employs the reciprocal space maps results in a reduction in integrated Bragg peak intensity of 15 % compared to the value obtained directly before the oxidation cycle (see Table 5.1). Furthermore, also the peak widths Γ_L and Γ_K are slightly larger after oxidation/reduction, indicating also a small decrease in the characteristic size of the Co crystallites. According to these results (i) the reduction of a significant fraction of the oxide occurs by a process with sluggish kinetics and (ii) small but noticeable Co losses via dissolution into the electrolyte occur during oxidation/reduction, even in cycles performed at conventional potential scan rates. The behavior described above is highly reproducible in successive potential cycles. Furthermore, very similar absolute changes were observed in experiments performed at similar potential scan rates on deposits of lower Co coverages. In particular, also in these measurements a Co loss due to oxidation of in total $\approx 3-5$ ML was found during the positive sweep to -0.2 V.

For more detailed studies of the structure and stability of the Co film in the oxidation regime, similar L- and K-scans were performed directly subsequent to the experiments in Fig. 5.5 by performing an additional potential cycle and stopping the negative going sweep at -0.70 V, i.e., a potential at the onset of oxidation (Fig. 5.6, green lines). These reveal a slow continuous decay of the Co film on a time scale of minutes, as evidenced by comparing the relative intensity changes

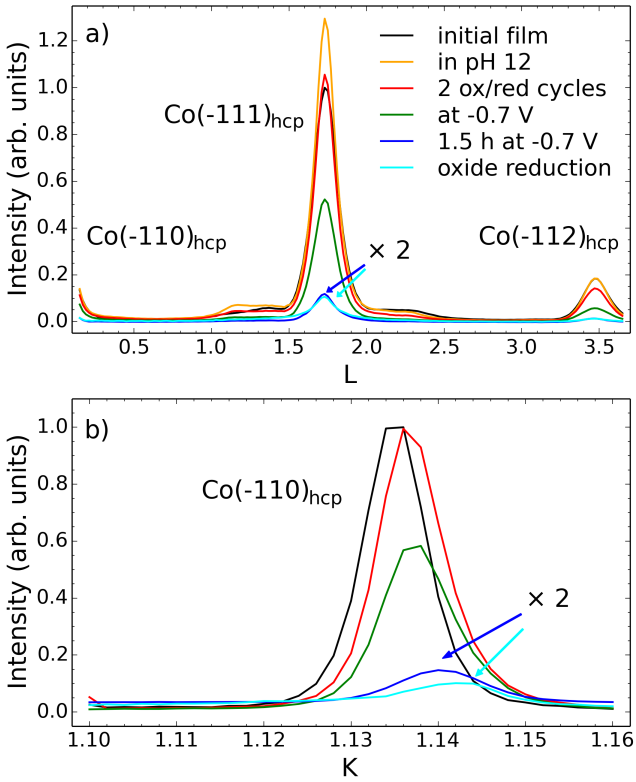

Fig. 5.6: Influence of oxidation and reduction on the Co Bragg peaks for the film shown in Fig. 5.2. (a) L-scans and (b) K-scans (obtained at $L = 0.15$) through the Co(-110)$_{hcp}$ peak, recorded for the initial Co film in acidic (≈ 16 ML, black line, $E = -1.05$ V) and alkaline (≈ 18 ML, yellow line, $E = -0.65$ V) solution, after two oxidation/reduction cycles between -1.20 and -0.15 V at 20 mV/s (red line, $E = -1.05$ V), after subsequent oxidation by a third cycle to -0.15 V (green line, $E = -0.70$ V), after further 1.5 h waiting at this potential (dark blue line, $E = -0.70$ V), and immediately after subsequent reduction of the oxide (light blue line, $E = -1.05$ V).

of the Co(-110)$_{hcp}$, Co(-111)$_{hcp}$, and Co(-112)$_{hcp}$ Bragg peaks, which were recorded 220, 440, and 640 s after the potential was stopped at -0.70 V and exhibit a continuous decrease to 65, 54, and 46 % of the original intensity, respectively. With time, the Co mass loss continues, leading to a reduction of the original peak intensity by 94 % after 1.5 h at $E = -0.70$ V (Fig. 5.6, dark blue lines). Very similar changes in Co coverage were observed in experiments at -0.4 V.

The Co mass loss is accompanied by a reduction of the Co hcp in-plane tensile strain $\varepsilon_{\parallel}$ from 1.3 % to 0.9 %, as indicated by the shift of the peaks in the K-scans (shown in Fig. 5.6b) towards larger values. However, the small vertical strain $\varepsilon_{\perp}$ of the Co film is less affected by oxidation. Surprisingly, the thickness d_{Co} of the hcp layer is increasing again slightly (by 7 %), suggesting that higher hcp Co islands are more stable than areas of lower thickness, consistent with a heterogeneous oxidation process.

Subsequent reduction of this sample by sweeping the potential to -1.2 V and bringing it back to -1.05 V results in a slightly lower, but broader Co(-111)$_{hcp}$ peak (Fig. 5.6, light blue lines).The integrated intensity recovers to 13 % of the original Co(-111)$_{hcp}$ peak intensity in

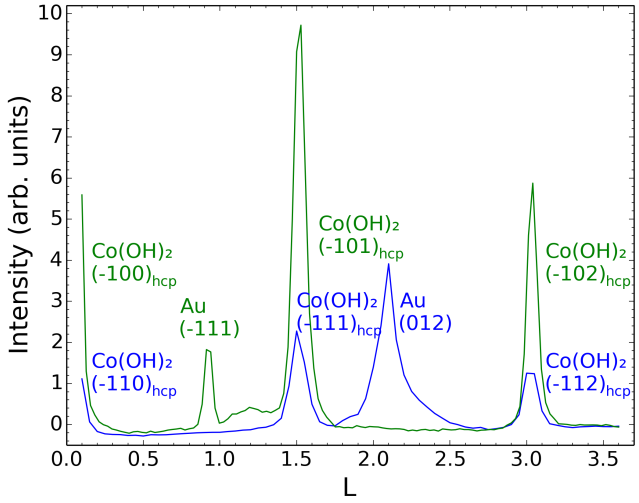

Fig. 5.7: Bragg peaks of the hydroxide layer at $E = -0.70\,\mathrm{V}$, recorded after the oxidation cycle (Fig. 5.6, green line) and keeping the potential at $-0.7\,\mathrm{V}$ for $\approx 1\,\mathrm{h}$. The L-scans were recorded at $K = 0.908$ (blue line) and after a 60° in-plane rotation of the sample (green line) and demonstrate the formation of a well-ordered epitaxial $Co(OH)_2$ hcp layer. The features labeled Au(-111) and Au(012) are tails of the Bragg peaks of the Au substrate.

alkaline solution and d_{Co} is further increased by 10 % (see Table 5.1). The absolute change in intensity upon reduction, equivalent to an increase of $1-2$ ML Co deposit, is comparable to that found in the potential cycle experiments, suggesting a similar oxide coverage. Therefore, the much lower peak intensity than that before oxidation has to be attributed to irreversible loss of Co via dissolution into the electrolyte.

In addition to these studies of the Co film also the structure of the Co oxide was investigated by *in situ* SXRD. Fig. 5.7 shows L-scans at $K = 0.908$ (blue line) and at 60° in-plane rotated reciprocal space positions (green line), which were recorded on the oxidized sample of the previously described experiment after keeping the potential for 55 min and 75 min at $-0.70\,\mathrm{V}$, respectively. They reveal Bragg peaks that can be clearly attributed to an epitaxial hcp $Co(OH)_2$ phase (additional peaks visible in Fig. 5.7 correspond to tails of neighboring Bragg peaks of the Au substrate, see also Fig. 5.1). The in-plane and out-of-plane lattice constants of the $Co(OH)_2$ structure are $a_{Co(OH)_2} = 3.18\,\text{Å}$ and $c_{Co(OH)_2} = 4.65\,\text{Å}$, which is in accordance with literature data on bulk $Co(OH)_2$ [72]. The $Co(OH)_2$ lattice is well (within $\leq 2°$) aligned with that of the hcp Co film, according to in-plane azimuthal scans (not shown).

The integrated intensity of the $Co(OH)_2(\text{-}111)_{\text{hcp}}$ peak is in the range of 0.5 % (55 min after oxidation) of that for the $Co(\text{-}111)_{\text{hcp}}$ peak of the film prior to oxidation. Even taking into account the (weak) influence of the OH groups on the structure factor and applying the appropriate correction factors for the different reciprocal space positions, the amount of $Co(OH)_2$ is two orders of magnitude lower than that of the initial Co film. This suggests that the observed $Co(OH)_2$ peaks correspond to islands with very low surface coverage. The thickness of the $Co(OH)_2$ islands was determined from the FWHM of the $Co(OH)_2(\text{-}111)_{\text{hcp}}$ peak in both L-scans

to $d_{ox} = 88\,\text{Å}$, which is twice the characteristic thickness value of hcp Co stacks $d_{Co} = 46\,\text{Å}$ before oxidation at $-0.7\,\text{V}$ (see Table 5.1). The in-plane crystallite size of these oxide islands is estimated from the FWHM of the $Co(OH)_2$(-111)$_{hcp}$ peak in K-scans to $\xi_{\parallel,ox} \approx 450\,\text{Å}$. The larger dimensions of these $Co(OH)_2$ crystals as compared to the values obtained for Co (Table 5.1) may be partly caused by the larger in-plane lattice spacing of the hydroxide.

The intensity of the $Co(OH)_2$ Bragg peaks continues to increase within the next 30 min to a constant (≈ 2 times higher) value. Nevertheless, the total intensity remains low, indicating that only a few percent of the initial Co film (i.e., < 1 ML Co) are converted into these 3D $Co(OH)_2$ islands. This is considerably less than the amount of Co, which is (reversibly) oxidized and reduced during a cycle (see Fig. 5.5a) and far below the Co loss found after 640 s at $-0.70\,\text{V}$ ($\approx 10\,\text{ML}$). Consequently, a large fraction of the Co hydroxide is either dissolved in the solution or is present in another form, for example an amorphous phase, or in another crystal orientation (e.g. as randomly oriented $Co(OH)_2$, which would result in weak powder rings). Direct evidence for such phases was not found in the SXRD experiments, however. Furthermore, we performed similar potential cycle experiments as in Fig. 5.5 at the position of the $Co(OH)_2$(-111)$_{hcp}$ Bragg peak. No formation of peaks indicative of a $Co(OH)_2$ phase was observed in these measurements, in agreement with the low intensity and slow growth rate found in the experiments at constant potential.

5.4 Discussion

The detailed *in situ* SXRD results on the structure of the Co and Co hydroxide film before, during, and after oxidation as well as after subsequent reduction allow to derive a detailed microscopic picture of these processes. We commence our discussion with the initial stage of Co oxidation (peak A1 in the CV) and then continue with the oxidation in peak A2.

It is clear from our study that the peak A1 is not associated with the formation of a $Co(OH)_2$ layer since we did not observe any significant decrease of the Co peak XRD intensity. This conclusion is in agreement with previous DFT calculations that either a chemisorbed (2×2)-OH adlayer or a (6×6)-CoOH layer (adlayer coverage of 0.69), in which the in-plane lattice constants of the topmost Co layer are expanded by a 20 % (with respect to the Co layer), is formed in this process [66]. This seems to be at variance with the conclusions of Ref. [65] where the authors assign the hexagonal surface structure observed by *in situ* STM on Co(001) single crystal in pH 12 solution at the positive end of peak A1 to $Co(OH)_2(001)_{hcp}$ [65]. This discrepancy may originate from the fact that the (6×6)-CoOH and the $Co(OH)_2$ layers have approximately the same in–plane lattice parameters. It may also come from different experimental conditions: the Co surface was observed by STM after 30 s at a potential at the positive end of peak A1, which is also the onset of peak A2 where the $Co(OH)_2$ forms.

The structure of the Co surface in peak A1 cannot be resolved completely unambiguously

on the basis of our measurements. On the one hand, the 3 % intensity decrease in the Co(-111)$_{hcp}$ peak intensity of the 10 ML Co deposit during the potential sweep (see Fig. 5.4a) may be interpreted as the formation of a (6×6)-CoOH layer. However, assuming that this decrease is solely caused by the conversion of hcp Co in the topmost atomic layer to a (6×6)-CoOH layer, the latter would cover only ≈ 40 % of the Co surface. Also the corresponding increase in the FWHM of the peak along the L-direction is much smaller than the expected change for the full conversion of the topmost Co atomic layer on the entire surface (≈ 5 %). Nevertheless, a partial (6×6)-CoOH covered surface during the sweep, e.g. due to a slow formation kinetics, may be possible. On the other hand, the fact that the reflectivity curves in Fig. 5.4c are quasi identical is speaking in favor of simple OH adsorption without surface restructuring. OH adsorption would provide an identical X-ray scattering contribution as interfacial water and thus would be almost undetectable. Within that hypothesis, it is however difficult to explain the above mentioned intensity drop in diffracted intensity because it is too large to be accounted by a surface relaxation. Simple vertical surface relaxations should not be able to account for these changes, but other explanations are possible, e.g., structural modifications at defect sites of the Co film (see below). More work is necessary to unambiguously determine the structure of the OH-adlayer in peak A1.

For the subsequent oxide formation in peak A2 we propose the mechanism described below (see Fig. 5.8). We will first discuss the oxide formation during a potential sweep and then the structural evolution on longer time scales at a fixed potential.

When the potential is scanned positively in the range of peak A2 (potential range between -0.7 and -0.54 V), the small reduction in Co coverage as well as in the characteristic height d_{Co} of the Co crystallites (Fig. 5.5a and b) indicates that an ultrathin passivating $Co(OH)_2$ layer forms homogeneously on the entire surface and that its thickness amounts to at most a few Å (Fig. 5.8b). Also the unchanged lateral dimension of the Co crystallites (Fig. 5.5c) supports such a surface oxidation process. Our conclusions are in agreement with the *in situ* STM observations [65], which show the formation of a (5×5) superstructure on the entire surface at the onset of peak A2 and suggest the presence of an epitaxial $Co(OH)_2(001)_{hcp}$ film on the Co surface. We did not succeed in the direct detection of such a layer by SXRD but this may be difficult, because its scattering would be weak and distributed over a wide L-range in reciprocal space, making it hard to separate it from the diffuse background by the electrolyte.

After this initial passivation, the Co oxidation proceeds via a second process, in which the characteristic height of the Co crystallites levels off whereas the lateral size decreases (Fig. 5.5b and c). This indicates that the hydroxide growth does not proceed by thickening of the initial passive layer, but by the local formation of 3D crystals and their subsequent lateral growth (Fig. 5.8c). Based on the decrease in Bragg peak intensity, which indicates already at -0.5 V a loss of ≈ 1.6 ML of Co during the potential sweep (Fig. 5.5a), this 3D oxidation process apparently commences in parallel to the formation of the passive surface oxide and continues until the onset of the negative sweep. Its growth kinetics is slower than that of the surface oxide, but likely increases towards more positive potentials. Interestingly, a rather well-defined amount

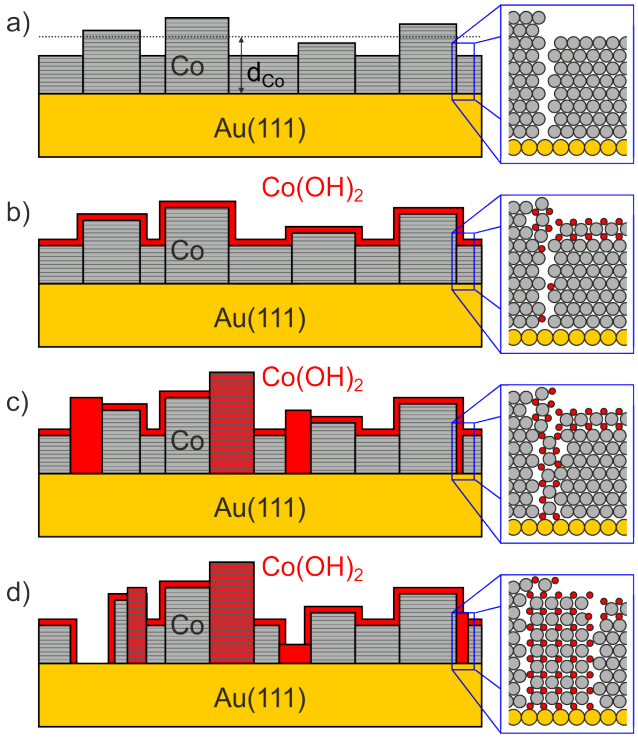

Fig. 5.8: Schematic model illustrating (a) the initial structure of the Co film, (b) the formation of an ultrathin $Co(OH)_2$ passivation layer directly at the onset of oxidation, (c) nucleation of thicker, epitaxial (hatched columns) and non-epitaxial hydroxide crystals at Co grain boundaries and (d) lateral growth of the hydroxide as well as chemical dissolution of hydroxyde on longer time scales.

of Co (≈ 4 ML for potentials sweeps at 20 mV/s to -0.2 V) is oxidized in this positive potential sweep.

During the negative potential sweep, no further change in the coverage of hcp Co is observed, which clearly indicates that the hydroxide layer formed in the first process is passivating and its dissolution rate is rather small. Hydroxide reduction in peak C is only partial, leading to an immediate recovery of ≈ 2 ML. However, on longer time scales further reduction is found, saturating at a Co coverage that is only a few percent lower than the original values. This supports low Co losses due to oxide dissolution during fast potential cycles. The height d_{Co} also increases during reduction and recovers its initial value after a few minutes at -1.05 V (not shown). These observations are consistent with a picture where the reduction of the surface hydroxide occurs rapidly, leading to Co crystallites of the initial thickness, whereas the 3D hydroxide is reduced more slowly.

After 55 minutes at fixed potential in the potential regime of oxidation $Co(OH)_2$ Bragg peaks are detected (Fig. 5.7). The hydroxide formation process under these conditions seems to proceed similar to the second process described above, i.e., by lateral 3D growth, since d_{Co} remains approximately constant even after oxidation of more than 90 % of the Co film. The surprisingly low intensity of the $Co(OH)_2$ peaks and the pronounced irreversible loss of Co

found after subsequent reduction indicate however substantial dissolution of Co hydroxide into the electrolyte. Using a simple planar diffusion model with a 0.5 mm diffusion layer thickness, a diffusion coefficient of $5 \times 10^{-6} \mathrm{cm}^2\mathrm{s}^{-1}$ and a Co hydroxide surface concentration of 5×10^{-7} M (saturation concentration in pH 12 [73]), we obtain a dissolution rate of 1.6 ML/min, equivalent to a Co dissolution rate of 1 ML/min. This is in reasonable agreement (considering the very simple planar diffusion model) with the experimental observations where we found 0.6 ML/min.

Finally, we consider in more detail the microscopic mechanism of the spatially inhomogeneous Co hydroxide formation occurring in the second stage of the oxidation process, which takes place during a potential sweep and at -0.7 V after a potential sweep. Most likely, this 3D hydroxide growth starts at structural defects, presumably at the grain boundaries between individual Co crystallites, which provide a high surface density of structural defects in the film (Fig. 5.8c). These grain boundaries are formed by coalescence of the individual Co islands of the film during its deposition, because the Co lattice is incommensurate to that of the Au substrate and the lattices of neighboring islands consequently may not match. They extend through the entire film, down to the Au substrate, and should provide an easy route of ingress for hydroxyl species into the Co film. This facilitates mass transport and thus nucleation and growth of thicker hydroxide crystals within the Co film. Because the structural defect at this location persists after hydroxide formation, facile vertical transport is sustained, enabling further lateral growth of the 3D hydroxide (Fig. 5.8d). A similar mechanism via penetration from the edges was recently suggested for oxidation of Co nanoislands on Au(111) under UHV conditions [57].

The proposed scenario allows to explain several other findings of the SXRD experiments. Since the conversion of hcp Co to hcp $Co(OH)_2$ leads to a 84 % expansion in volume, 3D growth of the hydroxide within the Co film is only possible, if a corresponding amount of Co is transported to the film surface. The latter will feed the vertical growth of the $Co(OH)_2$ crystallites outside of the Co film. Thus, this 84 % expansion is essentially in the vertical direction implying that the $Co(OH)_2$ crystallite height is that of the initial Co island times 1.84. In the case of the 18 ML film with $d_{Co} = 46$ Å, the obtained $Co(OH)_2$ height is 85 Å, very close to that observed. Also the reduction of tensile strain of the Co lattice indicates changes in the lateral structure. Furthermore, the proposed model could explain the discrepancy between the amount of Co consumption and (epitaxial) $Co(OH)_2$ formation. Specifically, the constrained geometry within the grain boundaries may inhibit formation of well-ordered $Co(OH)_2$ crystals. Because the lateral size of the Co crystallites is only a few ten nanometers, the grain boundary density is high, making nucleation and 3D growth at these defects an efficient mechanism for hydroxide formation. This is in accordance with our experiments that show that in the positive going potential sweep, i.e., within the first 20 s of the oxidation process > 20 % of the Co film is consumed. Subsequently, this rate slows down, which may be caused by the overgrowth of the grain boundaries at the Co film surface by hydroxide, which would inhibit the mass-transport processes involved in the oxidation process. Finally, on time scales of hours substantial irreversible Co loss occurs, most likely due to chemical dissolution of the hydroxide in the electrolyte.

5.5 Conclusion

In this study we employed *in situ* surface X-ray scattering to track the microscopic structural changes in electrodeposited epitaxial Co films on Au(111) electrodes during electrolyte exchange to alkaline solution, oxidation, and subsequent reduction. We show that these films have a (001)-orientation, thicknesses of a few nanometers, and 20 - 30 nm lateral grain size. The capability of parallel electrochemical and scattering measurements enabled us to unambiguously assign the characteristic features in the voltammograms to structural changes. Our results imply a stepwise oxidation mechanism, where the surface is first covered by a chemisorbed OH adlayer in peak A1 of the voltammogram. The $Co(OH)_2$ formation occurs in peak A2 and begins with a rapid growth of an ultrathin passive layer on the entire Co surface. Subsequent hydroxide growth occurs inhomogeneously on the surface via formation of 3D $Co(OH)_2$ crystallites. Our results are consistent with a $Co(OH)_2$ crystallite nucleation at the grain boundaries of the Co deposit, from where they slowly grow laterally. This mechanism outlines the important role played by the defect structure on Co oxidation. The *in situ* SXRD measurements in electrochemical environment presented here provide detailed structural insight of the oxidation mechanism of a well-defined nano-crystalline material. Similar studies may allow addressing structural changes of electroanalytical Co oxides under reaction conditions.

Acknowledgement

We gratefully acknowledge the European Synchrotron Radiation Facility for providing synchrotron radiation facilities and the ID03 beamline staff for technical support, especially F. Carlà. We further thank the Deutsche Forschungsgemeinschaft for financial support via MA 1618/13.

5.6 Supporting Information

5.6.1 Cyclovoltammogram of Au(111) in Co Containing Solution (pH 4)

After mounting the crystal in the "hanging meniscus" transmission cell, the quality of the preparation was determined in 0.1 M $NaClO_4$ + 1.3 mM HCl + 1 mM $CoCl_2$ (pH 4) by CVs in the double layer regime at $E = -0.2\,\mathrm{V} \rightarrow 0.8\,\mathrm{V}$. Fig. 5.9 shows a more extended CV in the range of $E = -1.0\,\mathrm{V} \rightarrow 0.4\,\mathrm{V}$ which was recorded to check the electrochemical deposition and dissolution signature as well. As described in previous literature [21, 67], the cathodic peak at $-0.8\,\mathrm{V}$ corresponds to deposition and the anodic peak at $-0.4\,\mathrm{V}$ to dissolution of Co. Thin Co film deposition was initiated by a potential step from 0.4 V to $-0.85\,\mathrm{V}$. The deposit was stabilized by stepping back to the stabilization potential of $-0.65\,\mathrm{V}$.

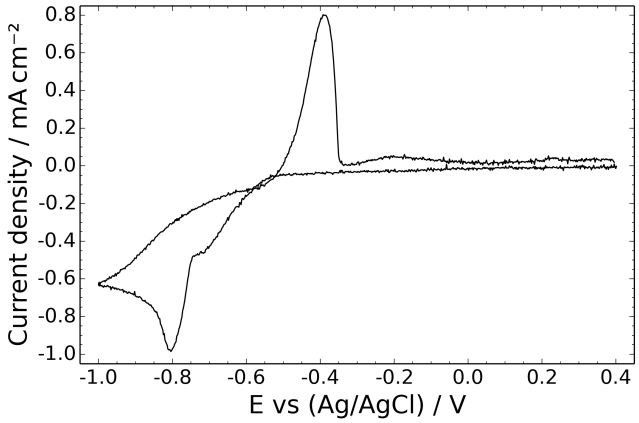

Fig. 5.9: Cyclic voltammogram of Au(111) in 0.1 M $NaClO_4$ + 1.3 mM HCl + 1 mM $CoCl_2$ (pH 4), showing the deposition and dissolution of a Co film ($dE/dt = 50$ mV/s).

5.6.2 Optical Reflectivity Modeling

The dependence of the relative reflectivity change ($\Delta R/R_0$) on the Co thickness has been calculated using standard matrix formalism yielding the reflectivity of a multilayer stack geometry. This formalism may be found in text books (for example [71]) and was implemented into a computer program which estimates the stack reflectivity as a function of the Co thickness. We considered roughness-free planar interfaces and used a Au thickness of 8 nm.
We used following complex refractive indices (at a wavelength of 630 nm):

$$n_{Electrolyte} = 1.33 \text{ (refractive index of water)}$$
$$n_{Co} = 2.22 + 4.2i$$
$$n_{Au} = 0.18 + 3i$$
$$n_{Si} = 3.88$$

These values have been found in Ref [74] for water and in Ref [75] for the others. The values of $\Delta R/R_0$ as a function of the Co thickness are shown in Fig. 5.10 where we can clearly observe that $\Delta R/R_0$ is linear with the Co thickness in a large range up to 25 ML of Co.

5.6.3 Determination of the Co Coverage of As-Deposited Films

In this section a simple approach to determine the Co coverage of as-deposited films (in pH 4) from the X-ray data is described. This semi-quantitative method models selected features along a single Co L-rod. In contrast, the ROD code [76] yields a detailed model of the crystalline structure of the film and the substrate, but requires extended sets of Au- and Co L-rods. However, the acquisition of extended data sets is greatly hampered by the restricted long time stability of ultrathin Co films in contact with the electrolyte. Moreover, a detailed analysis of the complete crystalline structure is out of the focus of this paper.

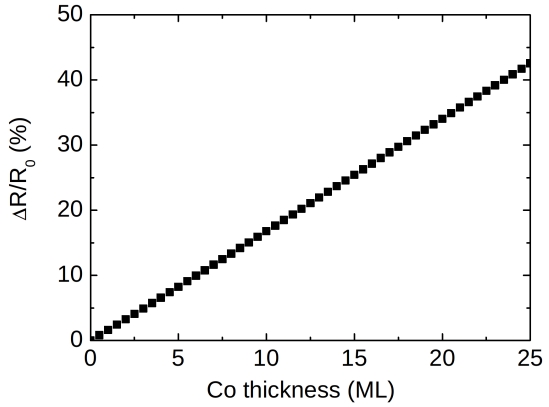

Fig. 5.10: The calculated $\Delta R/R_0$ (in %) for a four media stack, water/Co/Au(8 nm)/Si, as a function of the Co thickness in monolayers.

The Co film consists of an ensemble of Co crystallites of different heights (Fig. 5.11). Scattering amplitudes of different crystallites have no defined phase relationship, therefore for the calculation of the X-ray intensity along the hcp Co L-rod the superposition of the intensity contributions of the Co crystallites have to be considered. Within this simple model, surfaces of individual crystallites are assumed to be perfectly flat, i.e. atomic-scale surface roughness is neglected. Within the kinematical approximation the scattered intensity of a single crystallite with N hcp Co bilayers along a Co L-rod is represented by the N-slit interference function:

$$I_N(L) \propto \frac{\sin^2(NLc^*c_{Co}/2)}{\sin^2(Lc^*c_{Co}/2)} \tag{5.2}$$

with primary maxima at hcp Co Bragg peak positions and $N-2$ subsidiary maxima between neighboring primary maxima. Assuming a Gaussian decay of the (unnormalized) crystallite height distribution function

$$P(N) = \exp\left[\frac{-(N-N_{min})^2}{2\sigma^2}\right] \quad N_{min} \leq N \ , \tag{5.3}$$

the scattered intensity of the hcp Co layer consisting of N_{min} full Co bilayers, decorated with Co islands ($N_{min} \leq N$) is given by

$$I(L) \propto \sum_{N=N_{min}}^{\infty} P(N) I_N(L) \ . \tag{5.4}$$

The average thickness, i.e., the vertical position of the average Co surface with respect to the position of the Co/Au interface, is given by the center of the height distribution function $P(N)$

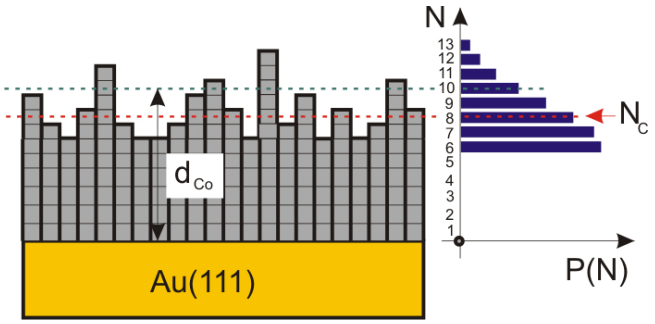

Fig. 5.11: Schematic representation of an as-deposited Co film (left), consisting of crystallites with heights $N \geq 6$, together with their height distribution function $P(N)$ (right). N_c denotes the center of $P(N)$ and the corresponding broken red line marks the position of the average surface position. The characteristic crystallite height d_{Co} is determined by the FWHM Γ_L of the Co(-111)$_{\text{hcp}}$ Bragg peak along the L-direction.

and thus the Co coverage (in ML) by

$$\theta_{Co} = 2 \cdot \frac{\sum_{N=N_{min}}^{\infty} NP(N)}{\sum_{N=N_{min}}^{\infty} P(N)} \text{ ML} . \tag{5.5}$$

"16 ML" Film

In order to determine the Co coverage θ_{Co} of the film shown in Fig. 5.2c (black curve), the decay σ of the height distribution function $P(N)$ has been varied until the primary peak FWHM Γ_L as well as the amplitude of the oscillations (subsidiary maxima) of simulation are in reasonable agreement.

Fig. 5.12 demonstrates that with increasing σ the amplitudes of subsidiary maxima as well as the FWHM Γ_L decrease. For $\sigma \approx 2.5 \pm 0.5$ the resulting FWHM Γ_L is within the errors identical to its measured value and the amplitudes of the subsidiary maxima are most similar to the measured ones. The resulting values for the Co coverage $\theta_{Co} \approx (16 \pm 1)$ ML and for the characteristic height of the Co crystallites $d_{Co} =$ are listed in Table 5.1.

"10 ML" Film

The Co coverage of the film shown in Fig. 5.4a ("10 ML") was determined as follows: The L-scan exhibits three subsidiary maxima (Fig. 5.13), thus the film consist predominantly of 5 full Co hcp bilayers with a thickness of 20 Å. Because the characteristic crystallite height d_{Co} determined by the FWHM Γ_L of the Co(-111)$_{\text{hcp}}$ has within the experimental errors the same value, the Co coverage for this film is $\theta_{Co} \approx (10 \pm 1)$ ML.

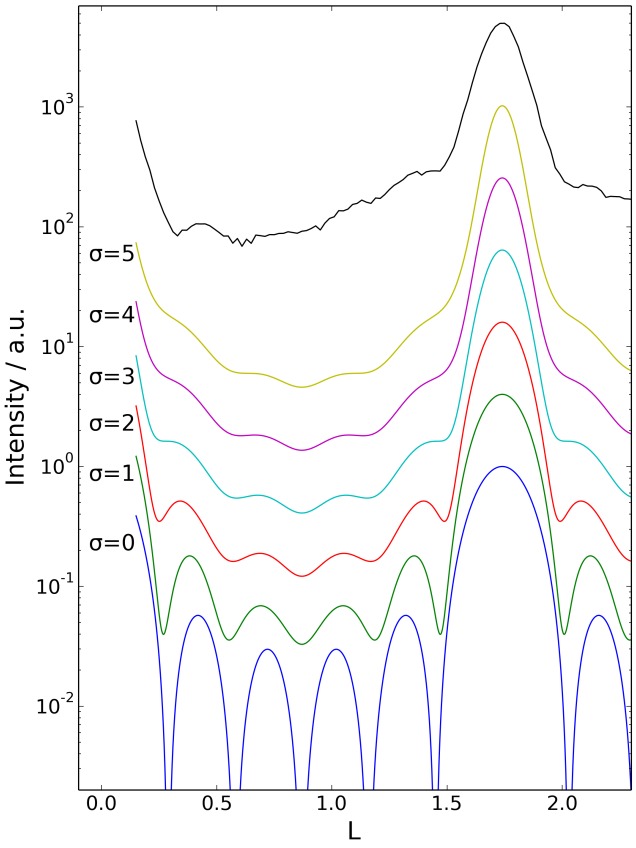

Fig. 5.12: L-Scan of the "16 ML" film at $K = 1.137$ in acidic solution (black line, pH 4, -0.65 V, see Fig. 5.2c) together with simulations for different values of σ which characterizes the Gaussian decay of the Co crystallite height distribution function $P(N)$.

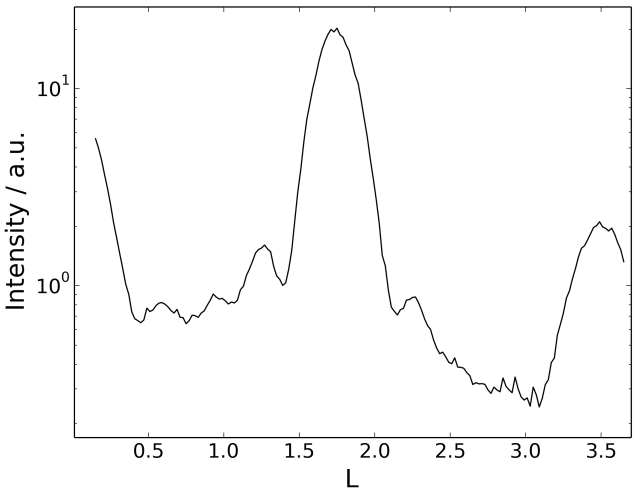

Fig. 5.13: L-Scan at $K = 1.137$ in acidic solution (pH 4, -0.65 V) of the "10 ML" film shown in Fig. 5.4a.

6 *Operando* Surface X-ray Diffraction Studies of Structurally Defined Co_3O_4 and CoOOH Thin Films During Oxygen Evolution

This chapter is based on an article published in ACS Catalysis[77].

Abstract

In the search for precious-metal-free electrode materials for electrochemical water splitting, transition-metal oxides have been receiving much recent interest as active and stable electrocatalysts for the anodic oxygen evolution reaction (OER). We present *operando* surface X-ray diffraction studies of two structurally well-defined epitaxial cobalt oxide thin films: Co_3O_4(111) and CoOOH(001) electrodeposited on Au(111). The potential-dependent structural changes during cyclic voltammograms were monitored with high time resolution up to OER current densities as high as 150 mA cm^{-2}. The CoOOH(001) film is found to be smooth and perfectly stable over a wide potential range. In the case of Co_3O_4(111), fast and fully reversible structural changes are observed. Specifically, the surface region of Co_3O_4(111) starts restructuring at potentials 300 mV negative of the onset of the OER, indicating that the process is related to the thermodynamically predicted Co_3O_4/CoOOH(001) transition rather than to the catalytic reaction. The formed skin layer is of defined thickness, which changes linearly with applied potential, and is the OER active phase. Surprisingly, the catalytic activity of the skin layer covered Co_3O_4 film and that of the smooth CoOOH(001) are almost identical, if the true microscopic surface area is taken into account. This indicates that the number of OER active sites on the two oxides is similar, despite the very different defect density, and is at variance with previous suggestions that di-μ-oxo bridged Co cations are exclusively responsible for the OER activity of Co oxides. For the smooth CoOOH(001), a turnover frequency of 4.2 s^{-1} per surface atom is determined

at an overpotential of 400 mV. Furthermore, our studies demonstrate that the pseudocapacitive charging current in the pre-OER potential range must be assigned to a bulk process that is accompanied by potential-dependent changes of the unit cell volume in the Co_3O_4 bulk.

6.1 Introduction

The need for environmental friendly and sustainable energy conversion, which allows scalable storage of wind and solar electricity into fuels, has triggered renewed interest into the electrochemical and photoelectrochemical splitting of water[78]. A key challenge in this field is the development of economically viable electrocatalyst materials for the oxygen evolution reaction (OER). Transition-metal oxides catalysts, in particular the different cobalt (hydr)oxide phases, have received large attention because they meet these requirements[52, 79, 80]. These materials are earth-abundant, easy to prepare, and present good catalytic properties and stability in alkaline and neutral electrolytes[79, 81–83]. Cobalt oxides may be prepared with an amorphous or a crystalline structure, using a variety of methods, including thermal salt decomposition[84], autoclave synthesis[85], photochemical reactions[86], sol–gel synthesis[87], Co electrodeposition and subsequent oxidation[55, 88, 89], and direct oxide electrodeposition[22, 79, 90].

For understanding and further developing Co oxide catalysts, it is necessary to clearly separate intrinsic structure–property relationships, which describe the dependence of the OER activity on the atomic-scale surface structure, from effects caused by the nano- and microscale material morphology. It was suggested that in comparing different catalysts, benchmarking protocols should be followed to determine at a defined overpotential the OER turnover frequency (TOF) – the average number of O_2 molecules formed per unit of time and per catalytic site[91, 92]. For this, the electrochemical surface area (ECSA) has to be measured, which is not trivial for these materials[81, 92]. As a further complication, often preconditioning of the catalyst is reported to be necessary for a stable OER current–potential characteristic. In general, an improved characteristic is obtained[93], which suggests a significant restructuring of the catalyst surface under reaction conditions. Such transformations were, for instance, evidenced in the case of nanocrystalline Co_3O_4, for which OER was reported to induce conversion of a nanometer thick surface region into another phase with a higher Co oxidation state and modified local arrangement[87, 93–95]. Ideally, the density and atomic configuration of the active sites should therefore be determined *operando* during oxygen evolution.

The mechanisms of the OER on cobalt oxides has been investigated in great detail[92, 96]. On the molecular scale, it is a complex four-step reaction which generally is proposed to start with bulk water nucleophilic attack, that is, the formation of an O−O bond after a water molecule has reacted with a terminal or bridging oxygen. This process implies a nominal increase of the oxidation state of surface atoms to $Co^{3+/4+}$. Indication for the latter was found by *operando* X-ray absorption spectroscopy (XAS)[55, 87, 93, 97, 98] and near-ambient-pressure X-ray

photoelectron spectroscopy (XPS)[95, 99]. The O_2 formation involves the participation of oxygen from the oxide lattice, as inferred from differential electrochemical mass spectroscopy (DEMS) measurements, conducted with samples prepared in $H_2{}^{18}O$ labeled water[100, 101] and with samples immersed in electrolytes prepared with labeled water[101]. Formation of superoxide/oxo intermediates at dicobalt sites, which were identified with step edge sites, was also observed by time-resolved IR spectroscopy[102, 103].

On the atomic scale, Dau *et al.*[104] concluded on the basis of X-ray absorption spectroscopy studies of electrodeposited amorphous Co oxide films (frequently referred to as CoCat) that the film consists of small clusters of Co-oxo cubanes, in which the oxygen atoms are coordinated to two neighboring Co ions (μ_2-O), and that this configuration corresponds to the catalytically active sites. This conclusion was supported by density functional theory (DFT) calculations, which predicted that CoOOH is the active phase during OER and discussed the stability of the surface orientation[20, 105]. Further support came from experiments with molecular Co compounds that are mimicking these sites[100, 106]. Because the amorphous CoCat films exhibit excellent OER catalytic activity[79, 107] it is now widely accepted that this motif is the most catalytically active sites on any cobalt oxide sample[92, 93, 100, 103, 108]. Nevertheless, direct evidence that the OER activity of μ_2-O is superior to other Co sites has not been reported so far.

A key problem in the unambiguous identification of the active sites is the complex (typically polycrystalline or amorphous) structure and morphology of the studied Co oxide samples. A number of studies have attempted to address this by employing catalyst materials with preferred surface orientations, such as shaped Co_3O_4 nanoparticles [88, 94, 109] and exfoliated CoOOH nanosheets[110, 111]. While these studies indicated an effect of the surface structure, measuring the ECSA remained a problem with these samples. For obtaining clear structure–reactivity correlations, structurally well-defined model OER catalysts are necessary. Such model catalysts may be single crystals or epitaxial layers of defined morphology, for which the atomic structure and density of surface sites can be precisely determined. While this is a well-established approach in heterogeneous catalysis and in electrocatalysis on metal electrode surfaces, OER studies with cobalt oxide model catalysts remain the exception. An exemplary study employing this strategy was recently published by Libuda and co-workers[112]. Here, ultrathin $Co_3O_4(111)$ epitaxial layer were grown by physical vapor deposition on Ir(001), characterized *ex situ* under ultrahigh vacuum (UHV) conditions, and transferred without exposure to air into an electrochemical cell for cyclic voltammetry (CV) and differential electrochemical mass spectroscopy studies.

In this work, we apply a similar approach, but we combine the use of epitaxial Co oxide films with an *operando* structural characterization of cobalt oxide model catalysts by surface X-ray diffraction (SXRD) during the electrochemical measurements. The Co oxide samples were prepared by electrodeposition of nanometer thick films on Au(111) single crystal electrodes, using a method adapted from that published by Switzer and co-workers[22, 88]. SXRD and complementary atomic force microscopy (AFM) measurements show that well-defined epitaxial $Co_3O_4(111)$ and CoOOH(001) oxide films are obtained. The *operando* SXRD studies reveal

remarkable differences in the potential-dependent surface structure of the two oxide surfaces, whereas their catalytic properties appear very similar. We discuss the implications of these results on the origin of the structural transformation of the near-surface layer of Co_3O_4 , the nature of the OER-active sites, and the pseudocapacitive charging/discharging of cobalt oxide in the pre-OER region.

6.2 Experimental Section

Thin films of cobalt oxides were electrodeposited on Au(111) substrates using a procedure adapted from that developed by Switzer and co-workers[22]. The method consists in electrooxidizing at 1 V_{RHE} at reflux temperature ($\sim$ 103 °C) a diluted oxygen-free solution of 1 mM $Co(NO_3)_2$ + 1.2 mM sodium tartrate (tart) in 2 or 5 M NaOH, prepared from high purity Co nitrate (Merck, $> 99.0\,\%$), Na tartrate (Sigma-Aldrich, ACS reagent $> 99.5\,\%$), NaOH (Merck, ACS reagent, Fe content $< 0.000\,05\,\%$), and Milli-Q water. A charge of 8 mC was passed to grow films with $15-25$ nm thickness. The substrate was a hat-shaped Au(111) single crystal (MaTeck) with an orientation uncertainty of $< 0.1°$. Prior to oxide film preparation, the Au crystals were immersed in a hot 1:2 mixture of 30 % H_2O_2 and 96 % H_2SO_4 (both Carlo Erba, RSE) for 1 min to remove any remaining oxide from previous experiments and then annealed in a butane flame for 5 min. After deposition, the samples were quickly removed from the reflux cell, rinsed with ultrapure water, dried with Ar, and inserted into the SXRD cell.

Operando SXRD studies were conducted at ESRF Beamline ID 03, at a photon energy of 22.5 keV with a flux of 4×10^{11} counts/s and a beam of 250 µm in width and 30 µm in height. Measurements were performed in six-circle geometry, using a fixed incident angle of 0.34° (see Fig. 6.7). The footprint of the beam on the sample was 250 µm × 5 mm. It is convenient in SXRD on (111) surfaces of fcc metal substrates[113] to employ a hexagonal reciprocal space geometry, where q_z is along the surface normal and q_x, q_y are oriented perpendicular to the main in-plane lattice directions (see Fig. 6.1c). Here, the reciprocal space positions (H, K, L) are given in units of the lattice vectors $a^* = \frac{4\pi}{\sqrt{3}a_{nn}} = 2.51\,\text{Å}^{-1}$ and $c^* = \frac{2\pi}{\sqrt{6}a_{nn}} = 0.89\,\text{Å}^{-1}$ with $a_{nn} = 2.885\,\text{Å}$ being the Au nearest neighbor spacing. However, the indices of the Bragg peaks of the studied Co_3O_4 and CoOOH films refers to the conventional simple cubic and hexagonal unit cells of these materials, respectively, to ease comparison with the literature.

During the measurements, the cylindrical sample was kept in a specifically designed electrochemical cell for SXRD studies, made from PEEK, and embedded in a Teflon seal. This way, only the polished Au(111) top part of the sample (geometric area 0.125 cm^2), on which the epitaxial film had been deposited, was exposed to the electrolyte. Potential control was established using a glassy carbon rod as counter electrode and a Ag/AgCl reference electrode. All potentials are referred to the reversible hydrogen electrode (RHE) to ease comparison with literature and are *iR* corrected. The electrolyte consists of 0.1 M NaOH, made from suprapure

NaOH (Aldrich) and Milli-Q water, and was continuously exchanged via computer controlled syringes at a rate of $5-20\,\mu L/s$ to avoid accumulation of species (radicals) generated by the X-ray beam as well as minimize O_2 bubble formation and transport limitations.

6.3 Results

6.3.1 Structure of As-Prepared Epitaxial Co Oxide Films

The SXRD studies show that structurally well-defined Co oxide films can be prepared by the employed electrodeposition procedure. Their structure is determined from the measured diffraction intensities in reciprocal space. Examples of such measurements, obtained on the as-prepared films in the SXRD cell under argon atmosphere, are shown for films deposited in 2 M (Fig. 6.1a) and 5 M (Fig. 6.1b) NaOH solution. Scans along the (0, 1, L) crystal truncation rods of the Au substrate reveal additional Bragg peaks, which can be assigned to crystalline (hydr)oxide phases (Fig. 6.1a,b), specifically Co_3O_4 and CoOOH. The first oxide is a spinel with a face centered cubic unit cell[114], the second has a hexagonal structure (called Heterogenite-3R[115] or β-CoOOH[20, 55, 80], JCPDS card 07-0169).

As illustrated by the schematic reciprocal space geometry in Fig. 6.1c , the peak positions along these and other (not shown) truncation rods coincide with those expected for a (111)-oriented Co_3O_4 film (red lines, Fig. 6.1a) and a (001)-oriented film of CoOOH (blue lines, Fig. 6.1b).

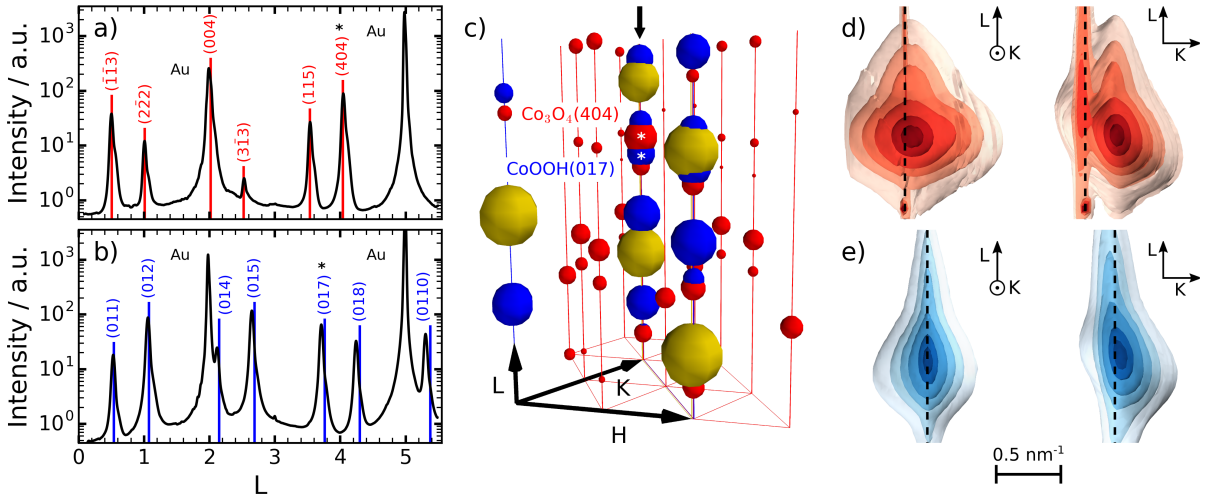

Fig. 6.1: Scans along the (0, 1, L) crystal truncation rods of oxide films electrodeposited in (a) 2 M and (b) 5 M NaOH, demonstrating the epitaxial growth of (a) pure Co_3O_4(111) and (b) pure CoOOH(001). The expected positions of the Bragg peaks for (unstrained) bulk Co_3O_4 and CoOOH are indicated by red and blue lines, respectively. (c) Corresponding schematic reciprocal space geometry, showing the Bragg peaks and crystal truncation rods of the Au(111) substrate (yellow), Co_3O_4(111) (red) and CoOOH(001) (blue). The axes H, K and L indicate the hexagonal unit cell of the Au(111) substrate. (d,e) Reciprocal space maps of (d) the Co_3O_4(404) and (e) the CoOOH(017) Bragg peaks (marked by * in a–c).

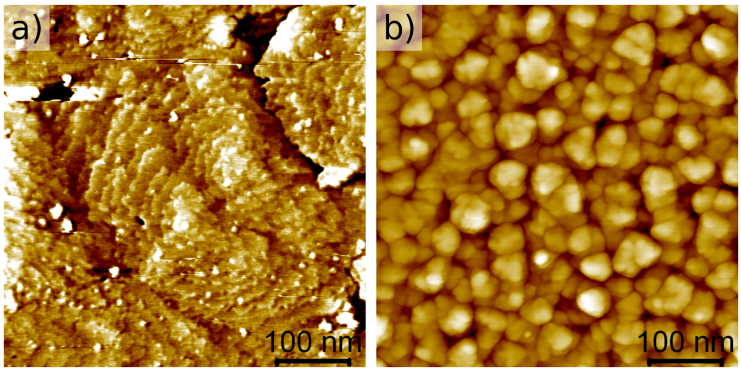

Fig. 6.2: AFM images (500 nm × 500 nm) of (a) CoOOH(001) and (b) Co_3O_4(111) layers electrodeposited on Au(111). Films are 18 and 20 nm thick, respectively, and were recorded after the *operando* SXRD studies on the samples shown in Fig. 6.1a,b.

The measured lattice parameters of the former agree well with the literature value (red lines in Fig. 6.1a), the CoOOH lattice is expanded by ≈ 1 %, adopting the Au substrate lattice spacing within the surface plane. Complementary in-plane characterizations confirm that the lattices of the deposits exhibit a 6-fold symmetry with respect to the surface normal, where the main in-plane directions (e.g., Co_3O_4[044] and CoOOH[100]) are aligned to the main in-plane axes of the Au surface (i.e., H or K). The in-plane angular spread of the crystallites is $\approx 1°$ for Co_3O_4 and below the detection limit for CoOOH. For the shown samples, no other Co oxide phases or orientations are found; that is, the deposits are pure phases and in excellent epitaxy with the Au(111) substrate. Proof of the latter is also that Bragg peaks, which are located along other CTRs (e.g., the Co_3O_4(333) or the Co_3O_4(422) peak), are not observed in the (0, 1, L) scans in Fig. 6.1a,b. Different samples of identical type exhibited very similar electrochemical and structural properties in the *operando* SXRD measurements, demonstrating that the observations are highly reproducible. In some preparations, mixed deposits of Co_3O_4(111) and CoOOH(001) were obtained, in which each of the two oxide phases exhibited its characteristic behavior, but these are not further discussed in the following. More details on the film preparation will be given in a future publication.

Additional detailed reciprocal space mapping of the Co oxide Bragg peaks, as illustrated for the cases of the Co_3O_4(404) and CoOOH(017) peaks (Fig. 6.1d,e), allows refinement of the film texture and morphology. This analysis indicates that both oxide films are composed of a thin flat film with thicker islands on top, suggesting a Stranski–Krastanov growth mode. The oxide grains exhibit a tilt distribution around the surface normal with a full width at half-maximum (fwhm) of $< 0.5°$ in both cases. For the discussed examples, the vertical/lateral coherence lengths of the oxide lattices ($d_\perp/d_\parallel$) derived from the Bragg peak shape analysis are 20 nm/31 nm for the Co_3O_4 and 18 nm/35 nm for the CoOOH film. We identify these coherence lengths with the out-of-plane and in-plane dimensions of the single crystalline grains of the oxide, respectively.

AFM studies of these samples, reveal clear differences in the surface morphology of the two

oxide phases (Fig. 6.2). The presented images were obtained after the *operando* SXRD studies presented in the following; however, very similar images were also obtained on analogously prepared as-deposited films. The CoOOH deposit (Fig. 6.2a) appears continuous and smooth (RMS ~ 2.4 nm). Close inspection reveals well-defined terraces, separated by 0.45 ± 0.05 nm high steps. The latter is consistent with the spacing of the O−Co−OH trilayers along the *c*-axis (0.438 nm), which is the main structural motive of this layered compound. The typical step separation is ≈ 10 nm, but the terraces can extend by more than 100 nm in the perpendicular direction, implying that they may consist of several crystal grains of identical height. This suggests that the film consists of tightly packed grains with narrow grain boundaries, in which the lattices of the neighboring grain nearly merge and mass transport of electrolyte species (e.g., OH ions and O_2) should be significantly impeded. In contrast, the Co_3O_4 deposit exhibits a clear granular morphology with clearly separated 3D islands (Fig. 6.2b). The surface of islands appears rough and no steps are discernible. The average distance between neighboring islands estimated from the AFM images is close to $d_{||}$, indicating that each 3D island consists of a single oxide grain.

From these detailed structural data, the true electrochemical surface area (ECSA) of the samples can be obtained, eliminating the need to refer to other electrochemical data such as the measured "double layer" current. Analysis of AFM images gives a roughness factor of 1.02 for CoOOH. Taking into account that the grain boundaries are apparently compact, the ECSA here must be close to the geometric surface area. For the Co_3O_4 film, the roughness determined from the AFM images is underestimated, because the tip finite size and the small island separation do not allow precise imaging of the grain boundaries. However, it may be estimated from the film morphology derived from SXRD and AFM, resulting in an ECSA that is ≈ 3 times larger than the geometric surface (Supporting Information, Section 6.7.5). This value depends only weakly on assumptions about the islands shape and coverage (less than 20 % within the spread of the experimental parameters). We consequently employ these ECSAs for the analysis of the electrochemical data.

6.3.2 *Operando* Studies of the Potential-Dependent Structure

Operando SXRD studies were conducted after injection of the 0.1 M NaOH electrolyte at a potential of 1.37 V, which is close to the measured open circuit potential. Similar characterization as in the argon atmosphere indicates that at this potential the oxide film structure remains unchanged. Subsequently, SXRD measurements during potential cycles in the range 0.77 to 1.57 V were performed, always using 1.37 V as rest potential. Two sweeps of potentials were recorded, of which only the second one is displayed for the sake of clarity, since the electrochemical current and structural data of both sweeps overlay very well.

As illustrated in Fig. 6.3 for the Co_3O_4 sample, potential-induced changes in the film structure result in modifications in the reciprocal space position and intensity distribution of the Bragg

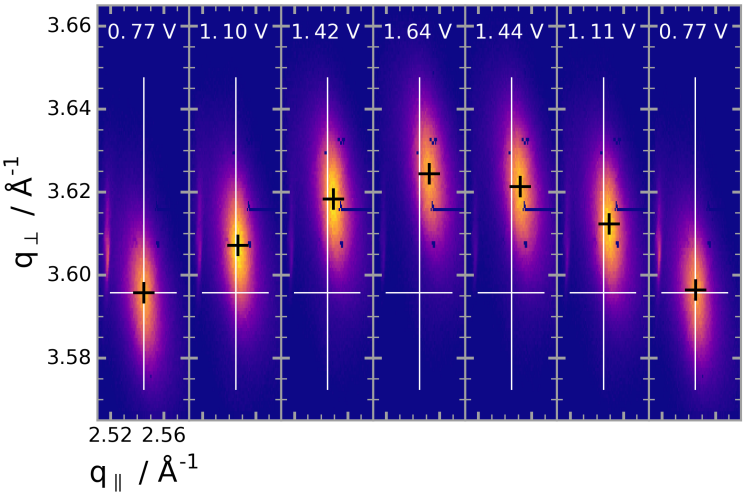

Fig. 6.3: X-ray detector images, illustrating the reversible potential-dependent structural changes of the Co_3O_4 deposit. The displayed images were selected from a continuous series, recorded at the (404) Bragg peak during a CV in 0.1 M NaOH at 10 mV/s. They are shown after conversion to in-plane ($q_{\parallel}$) and out-of-plane ($q_{\perp}$) positions in reciprocal space, with the small black crosses marking the current and the large white crosses the initial peak position. By quantitative fits of peak position and width in both directions, $\varepsilon_{\perp,\parallel}$ and $d_{\perp,\parallel}$ were determined.

peaks, which can be directly monitored with the 2D detector. For a quantitative determination of these changes, the peak in each detector frame was fitted in $q_{\parallel}$ and $q_{\perp}$ direction with pseudovoigt functions. The peak positions along $q_{\parallel}$ and $q_{\perp}$ directly yield the in-plane and out-of-plane strains $\varepsilon_{\parallel}$ and $\varepsilon_{\perp}$ in the oxide film, respectively; from the fwhm in these directions, the corresponding coherence lengths which are associated with the grain size $d_{\parallel}$ and $d_{\perp}$ are obtained. The Co_3O_4(404) and CoOOH(017) Bragg peaks were selected for these measurements, because they are intense and the out-of-plane structural modifications are best visible at high L-values. The high time resolution of this method (one detector image is recorded in 0.2 to 1 s), makes it possible to record these structural data during potential sweeps at rates of 10 to 50 mV/s with good potential resolution. This also allows measuring deep in the OER (up to 150 mA/cm^2) without accumulating too many O_2 bubbles at the surface.

The combined electrochemical and structural data for the two types of oxides, obtained simultaneously during a potential cycle at 10 mV/s, is shown in Fig. 6.4. The cyclic voltammogram (CV) of the Co_3O_4(111) layer (red line, Fig. 6.4a) exhibits two pairs of redox waves A1/C1 and A2/C2, superimposed on a large pseudocapacitive current. It reproduces all features of CVs obtained with Co_3O_4 samples of various crystallinity and prepared by different methods[35, 87, 112, 116], with the potentials of the redox waves approximately corresponding to the calculated equilibrium potentials for conversion of Co_3O_4 to CoOOH (A1/C1) and CoOOH to CoO_2 (A2/C2). In contrast, the CV of the CoOOH(001) film (blue line) appears almost featureless with one ill-defined oxidation/reduction wave discernible around 1.2 V/1.1 V. Table 6.1 gives the charge Q_0 measured in the pre-OER region (0.77 to 1.57 V) and the equivalent capacitance

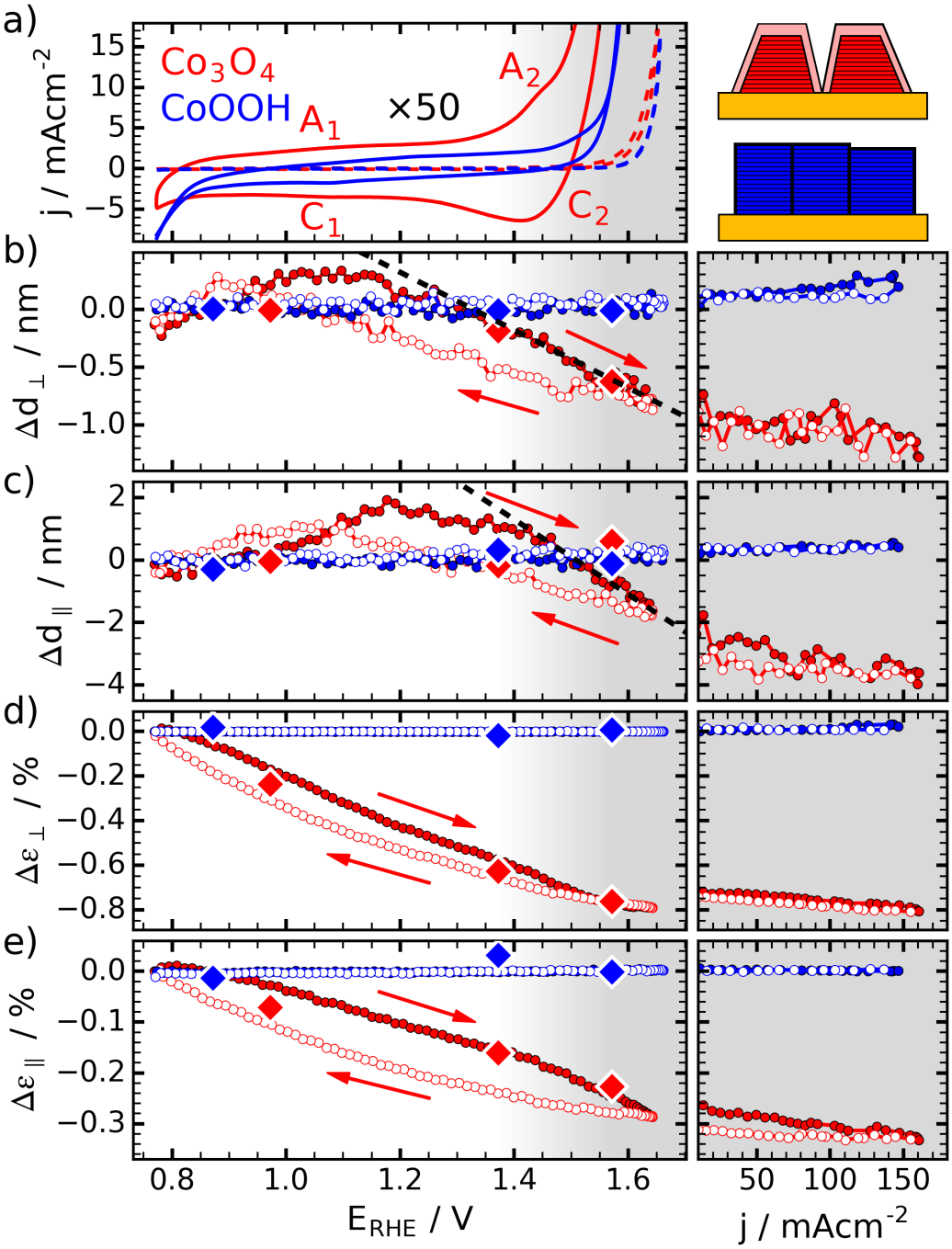

Fig. 6.4: (a) CV and (b–e) *operando* SXRD structural data for Co_3O_4/Au(111) (red) and CoOOH/Au(111) (blue), recorded simultaneously in 0.1 M NaOH at 10 mV/s. Presented are the potential-dependent changes in out-of-plane and in-plane (b,c) grain size $\Delta d_{\perp,\parallel}$ and (d,e) strain $\Delta\varepsilon_{\perp,\parallel}$ relative to the values at the lower potential limit. The right-hand panel in (b–e) show the variations of these structural parameters as a function of OER current, obtained in a similar experiment. In all panels, filled and open symbols refer to the positive and negative going potential sweep, respectively. In addition, results of the structure under steady-state conditions are included for comparison (diamonds) and a schematic illustration of the film morphologies is included (upper right corner). All current densities j are given with respect to the geometric surface area of the Au(111) single crystal.

	Q_0 (mC/cm^2)	C_{EL} (mF/cm^2)	b (mV/dec)	$j_{ECSA}(1.63\,\mathrm{V})$ (mA/cm^2)
Co_3O_4(111)	4.15	3.75	65	2.2
CoOOH(001)	1.4	1.2	52	3.9

Table 6.1: Electrochemical data for the two oxide films. Given are the charge Q_0 derived from CVs in the pre-OER region ($0.77-1.57\,\mathrm{V}$), the pseudocapacity C_{EL}, derived from the CV in the range $0.77-1.07\,\mathrm{V}$, the Tafel slope b of the OER, and the current density j with respect to the ECSA at an overpotential of 400 mV.

$C_KarstenTarhouniEL$ (determined in range 0.77 to 1.07 V). Note that Q_0 and C_{EL} are in the range of a few mC/cm^2 and mF/cm^2, respectively, in agreement with measurements on thin and compact cobalt oxide films[22, 95, 112].

In the *operando* SXRD studies, the structural changes in vertical and lateral grain size and strain during the CV were monitored. The results are displayed in Fig. 6.4b,c and Fig. 6.4d,e, respectively, taking the potential 0.77 V as reference state. These data evidence that the structure of the CoOOH layer (blue symbols) stays completely unaltered with $\Delta d_{\perp,\parallel} < 0.05\,\mathrm{nm}$ in the entire investigated potential range and strain changes $\Delta\varepsilon_{\perp,\parallel}$ remaining below the detection limit. In contrast, the Co_3O_4 layer (red symbols) exhibits a very different behavior, with pronounced changes during the potential cycle. $\Delta d_\perp$ and $\Delta d_\parallel$ pass through a shallow maximum at $\approx 1.15\,\mathrm{V}$ before decreasing up to the onset of OER by 1 and 4 nm, respectively (Fig. 6.4b,c). The decreases in vertical grain size indicate that an ≈ 1 nm thick layer at the surface of the Co_3O_4 grains is converted into another phase, in good agreement with the results by Bergmann *et al.*[87]. The larger decrease in lateral size $\Delta d_\parallel$ indicates the formation of a slightly thicker layer (≈ 2 nm) along the sides of the grains. Scanning the potential back to 0.77 V restores $\Delta d_{\perp,\parallel} = 0$; that is, completely reverts the skin layer back to epitaxial crystalline Co_3O_4 without any loss of material. Forward and reverse potential scan exhibit some hysteresis, with the maximum grain size in the latter being slightly lower and shifted negatively. In parallel, one observes reversible changes of both $\Delta\varepsilon_\perp$ and $\Delta\varepsilon_\parallel$ (Fig. 6.4d,e) during the cycle. Both decrease toward positive potentials, indicating a volume change of the unit cell by ca. $-1.2\,\%$ between 0.77 and 1.6 V. The change is anisotropic ($\Delta\varepsilon_\perp > \Delta\varepsilon_\parallel$) which is not too surprising, since the oxide islands are in strong epitaxy with the substrate and therefore laterally clamped to its surface lattice. As $\Delta d_{\perp,\parallel}$, also $\Delta\varepsilon_{\perp,\parallel}$ exhibit small hysteresis between positive and negative going scans.

The differences between the CoOOH and the Co_3O_4 samples also are visible in simultaneous optical reflectivity measurements (Fig. 6.14), where the former exhibits only small changes ($\approx 2\,\%$), whereas the latter decreases by 17 % over the same potential range, which is much larger than expected for a mere surface change. In agreement with previous reports[98], these reflectance changes are proportional to the pseudocapacitive charge accumulated during the potential scan (Fig. 6.15).

In complementary measurements on this as well as other Co oxide deposits, all these structural

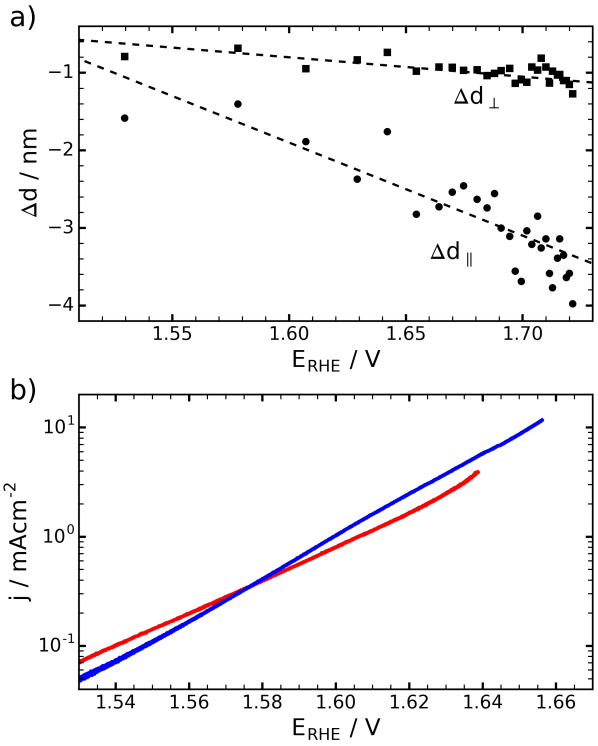

Fig. 6.5: (a) Potential-dependent changes of the out-of-plane and in-plane grain size $\Delta d_{\perp,\parallel}$ of Co_3O_4/Au(111) in the OER regime. (b) *iR*-corrected Tafel plots of CoOOH(001) (blue) and Co_3O_4(111) (red) films, recorded on the structurally characterized samples in the SXRD cell. The current density is given with respect to ECSA, accounting for the roughness factor ~ 1 and ~ 3, respectively, for CoOOH(001) and Co_3O_4(111) layers.

modifications were reproducibly measured with the same amplitude upon successive potential sweeps, even at higher sweep rates (see Fig. 6.10). Potential step experiments further show that these modifications are fast and completed within several seconds. In addition to these potentiodynamic studies, we also measured at selected potentials the steady-state structure by recording full L-rods, of the type presented in Fig. 6.1a,b. The resulting structural data (indicated by diamonds in Fig. 6.4b–e) agree well with those of the potentiodynamic curves. All these results demonstrate clearly that the structural changes observed for the Co_3O_4 film are a genuine potential effect (i.e., largely reflect the equilibrium structure that is characteristic for the given potential).

Extending the potential to more positive values, deep in the OER range (up to a current density of 150 mA/cm^2, see right side panels in Fig. 6.4b–e), does not lead to noticeable structural changes in the case of CoOOH(001), indicating that this surface is extremely stable even at large current densities of oxygen evolution. For Co_3O_4, we find a further slight decrease in $\Delta d_{\perp,\parallel}$ and $\Delta\varepsilon_{\perp,\parallel}$ with increasing OER current density. The structural parameters are very similar in the positive and the negative potential sweep, suggesting that the presence of the evolved O_2 has little influence on the oxide film structure. Plotting the thickness of the forming skin layer versus the *iR*-corrected voltage, reveals that the skin continues to increase approximately linearly with

potential and with a similar rate $\partial d_{\perp}/\partial E \approx 2.5\,\mathrm{nm/V}$ in OER (Fig. 6.5a) and in the pre-OER region above 1.4 V (Fig. 6.4b, dashed line). In the in-plane direction $\partial d_{\parallel}/\partial E \approx 12\,\mathrm{nm/V}$ in the OER as well as in the pre-OER regime ($\geq 1.4\,\mathrm{V}$), which corresponds to an increase by $\approx 6\,\mathrm{nm/V}$ of the skin layer on the sides of the grains and thus is in agreement with the 2-fold larger thickness of this side wall skin layer found at 1.63 V. Also the strain variations take place in the entire potential range, including the OER regime.

The corresponding *iR*-corrected OER Tafel plots, measured in the *operando* cell in parallel to the SXRD studies and normalized to the ECSA obtained from the structural data, are shown in Fig. 6.5b. They exhibit well-defined Tafel slopes b (given in Table 6.1), indicating no major transport limitations, as expected due to the high OH^- concentration at pH 13. Obviously, both materials have rather similar current densities at moderate overpotentials, if the microscopic surface area is taken into account. Above $\approx 1\,\mathrm{mA\,cm^{-2}}$, the current density of CoOOH(001) becomes higher than that of the $Co_3O_4(111)$ film, reflecting its smaller Tafel slope. A more detailed analysis of the catalytic properties, focusing on the turnover frequency, is provided in Table 6.2 of the discussion, Section 6.4.3.

For both types of deposits, irreversible structural and morphological changes are only observed, if the cathodic potential limit becomes sufficiently negative, albeit with clear differences between the two materials. For $Co_3O_4(111)$ the grains start to significantly shrink at potentials $< 0.8\,\mathrm{V}$ (see Fig. 6.11), whereas for CoOOH(001) such changes only occur below 0.4 V, indicating a wider stability range of the latter film. We interpret these changes as being due to the electrochemical reduction of Co_3O_4 and CoOOH into $Co(OH)_2$[35, 112]. Upon scanning the potential back to positive values, the formed $Co(OH)_2$ is not fully converted back into the epitaxial $Co_3O_4(111)$ and CoOOH(001) films, respectively, resulting into an apparent loss of material. As this work focuses on the structure and properties near the OER regime, this point is not discussed in more detail here.

6.4 Discussion

Our studies rely on the preparation of pure phase epitaxial $Co_3O_4(111)$ and CoOOH(001) thin epitaxial layers on Au(111). While the electrodeposition of epitaxial $Co_3O_4(111)$ was already demonstrated in ref[22], obtaining a well-defined epitaxial CoOOH layer is new.

Before starting the discussion, it is briefly recalled that, according to thermodynamics, the potential regions, where the different cobalt oxides are stable, are defined by redox reactions (6.1–6.3)[35, 117]:

$$3\,Co(OH)_2 + 2\,OH^- \leftrightarrow Co_3O_4 + 4\,H_2O + 2\,e^- \qquad (0.81\,V_{RHE}) \qquad (6.1)$$

$$Co_3O_4 + OH^- + H_2O \leftrightarrow 3\,CoOOH + e^- \qquad (1.22\,V_{RHE}) \qquad (6.2)$$

$$CoOOH + OH^- \leftrightarrow CoO_2 + H_2O + e^- \qquad (1.56\,V_{RHE}) \qquad (6.3)$$

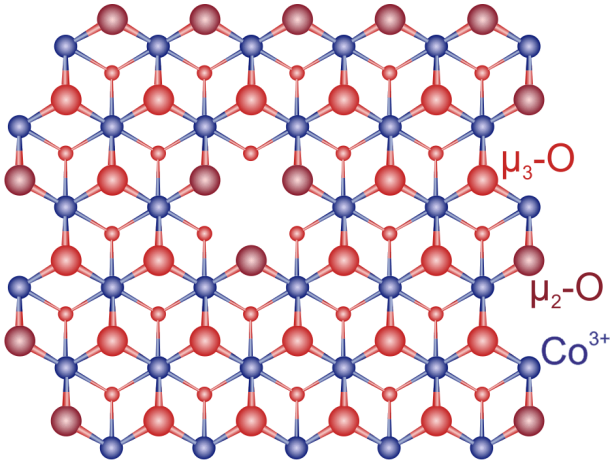

Fig. 6.6: Atomic model (top view) of the topmost plane of the CoOOH(001) surface. Oxygen atoms are red and cobalt blue. O atoms on the ideal surface are 3-fold coordinated (μ_3-O sites), whereas at steps and next to Co vacancies, μ_2-O sites (dark red) are found.

The discussion below is organized in different sections dealing with the stability of the CoOOH(001) layer, the restructuring of the $Co_3O_4(111)$ spinel oxide near surface region, and the catalytic properties of both layers. The last section discusses the pseudo capacitive current in pre-OER region.

6.4.1 Origin of the CoOOH(001) Layer Stability

In view of Eqs.(6.1–6.3), the wide stability range of the CoOOH(001) layer is remarkable. The CoOOH film does not exhibit structural changes down to 0.4 V (see Fig. 6.11) and is perfectly stable in the OER region. Negative of 0.4 V, the CoOOH layer is converted most probably into $Co(OH)_2$ without previous formation of the Co_3O_4 phase in an intermediate potential range. These results are in qualitative agreement with more recent thermodynamic considerations, but even here the $Co(OH)_2$/CoOOH transition was found at more positive potentials (≤ 1.0 V vs RHE)[105]. Consequently, we assign the wide stability range of the CoOOH(001) film to its smooth surface, which is composed of close-packed (001)-terminated terraces. The electrochemical reduction into $Co(OH)_2$ or Co_3O_4 requires nucleation of these phases, which is expected to start at steps and point defects in the (001)-planes (see Fig. 6.6). That this process is kinetically hindered is in accordance with the relatively small fraction of Co step edge atoms (≈ 3 %), estimated from the terrace width, and suggests that also the surface density of point defects is low.

In the OER range, the structural changes, characterized by $\Delta d_{\perp,\parallel}$ and $\Delta\varepsilon_{\perp,\parallel}$, are also totally absent, indicating that the CoOOH lattice remains unchanged in this range and the natural (001) cleavage plane is thus stable and is the active phase present during OER. In particular, formation of bulk crystalline CoO_2 can be excluded. Concretely, no CoO_2 formation was found in the detailed structure determination at a constant potential (Fig. 6.4, diamonds) of 1.57 V, that is,

just above the potential where CoO_2 formation should become thermodynamically favorable, even though the potential was kept at this potential for 40 min. Furthermore, even short-term potential excursions to ≈ 200 mV higher potentials, where the driving force for CoO_2 formation should be much higher, did not result in any structural changes. According to DFT calculations, the CoOOH(001) surface termination gradually changes from OH to O in this potential regime, reaching a fully O-terminated surface at 1.5 V vs RHE[105]. Similar changes in the surface protonation state of the CoOOH grains may also occur in the grain boundaries, since these defects should allow some proton diffusion, even if the grains are tightly packed. SXRD measurements are not sensitive to such changes in the state of the surface oxygen species, because of the very small scattering cross section of hydrogen.

6.4.2 Potential-Dependent Restructuring of Co_3O_4 Film Surface: Formation of the Skin Layer

The Co_3O_4(111) film is stable in a much more restricted potential range than the smooth CoOOH(001) layer. At potentials more negative than 0.8 V (Fig. 6.11), transformation into the more thermodynamically stable phase $Co(OH)_2$ commences, and above this potential, small reversible structural changes take place at the surface and also in the bulk. In this section, we specifically focus on surface modifications in the potential range $0.77 - 1.7$ V (i.e., the variations of $\Delta d_{\perp,\parallel}$). The volume modifications ($\Delta\varepsilon_{\perp,\parallel}$) will be discussed in the final section of this paper.

The good agreement between the values of $d_{\perp,\parallel}$ and the dimension of the 3D islands imaged by AFM indicates that the latter consist of single grains and are directly probed by the *operando* SXRD measurements. The small changes in $\Delta d_{\perp,\parallel}$ between 0.77 and 1.0 V can be assigned to a gradual onset of the $Co(OH)_2/Co_3O_4$ transition in the first atomic planes. Between 1.2 and 1.67 V, the changes in $\Delta d_{\perp,\parallel}$ indicate the fully reversible formation of a ≈ 1 nm thick skin layer on the top and side walls of the Co_3O_4(111) grains.

This observation is in excellent agreement with the previous results by Bergmann *et al.* for polycrystalline Co_3O_4[87]. However, the time and potential resolved data obtained in our study provide important additional insights into the formation mechanism and nature of this skin layer.

Our first main observation is that the skin layer emerges ≈ 300 mV negative of the onset of OER and thus is not directly related to the catalytic reaction as previously assumed. In these earlier studies, identification of the skin layer with an amorphous or highly defective $CoO_x(OH)_y$ phase was proposed on the basis of X-ray spectroscopy and photoemission data[87, 94, 95]. Furthermore, the skin layer was only observed at one potential (1.62 V) in the OER regime and thus thought to be caused by this reaction. The results presented here indicate that this near surface restructuring rather reflects the thermodynamics of the Co_3O_4/CoOOH phase transition, because its formation starts at a potential close to the equilibrium potential of reaction 6.2. In explaining this structural transition, we have to consider that it is not only fast but also fully reversible, which excludes simple kinetic effects, such as slow skin layer growth. We have also to

take into account that the skin layer is not accompanied by cobalt dissolution into the electrolyte, as evidenced by the absence of any irreversible loss of Co_3O_4 for potentials ≥ 1 V. This is seen in the *operando* studies during CVs (as, for example, in Fig. 6.4) as well as in auxiliary experiments where the sample was found to be completely stable for many hours at 1.4 V (i.e., a potential in the range of the skin layer).

In an atomistic picture, the formation of a skin layer in pre-OER region plausibly relies on displacements of the Co^{2+} cations from tetrahedral to octahedral symmetry because the Co oxidation state increases from Co^{2+}/Co^{3+} to Co^{3+} for potentials above 1.2 V. This restructuring requires significant transport of oxygen and Co ions through the oxide lattice. However, because the skin layer is only of nm-thickness, this transport still can be rapid, which explains why the skin layer forms rapidly and is reversibly converted back into epitaxial Co_3O_4 upon reverting the potential to more negative values. In the OER region, the cobalt redox state increases further from Co^{3+} to Co^{3+}/Co^{4+}[87, 94, 95] but this does not imply further modification of the Co local O-coordination shell, explaining why the skin thickness is only weakly affected by the catalytic reaction. It is noted in this context that even in our epitaxial systems the skin layer does not form on a perfectly smooth $Co_3O_4(111)$ surface, but on nanoscale 3D islands that expose other facets to the electrolyte (most probably $Co_3O_4(100)$)[118, 119]. This might facilitate the layer formation, for example, by providing channels for cation (vacancy) migration within the oxygen framework. Indeed, the ≈ 4 times larger potential-dependence in the in-plane as compared to the out-of-plane direction may be rationalized by more facile ion migration parallel to the (111)-planes (see below).

Our second main observation regarding the skin layer is that its thickness is a linear function of applied potential. Namely, it gradually increases with identical slopes $\partial d_{\perp,\parallel}/\partial E$ in the pre-OER and in the OER range, confirming that the oxygen evolution reaction does not substantially affect the skin layer growth. In other words, the thickness is determined by applied electrode potential alone. The linear change of the skin layer thickness with potential strongly resembles the behavior of passive films and implies the presence of a constant electric field within the skin layer, which is independent of the potential. Thus, also for the oxide system studied here, models developed for describing passive film formation on iron group metals may be applicable, in particular since for those passive films often a duplex structure was reported, consisting of two stacked layers of different oxide phases[29, 61]. These models should be well suited to describe skin layer formation on oxides, as found in the Co_3O_4 system, since they likewise describe the formation of a kinetically limited surface layer, consisting of cation species in a higher oxidation state and (additional) oxygen anions, due to a thermodynamic driving force. Whether this is an oxide layer on a metal or a (hydr)oxide layer on an oxide substrate should *per se* not matter fundamentally. Unfortunately, many models of passive film growth yield a linear variation of the layer thickness, for example, the high field model, the point defect model, and variations of those (see refs[120, 121] and references therein). Unambiguous identification of the skin layer formation mechanism thus will require much more detailed data, for example, on its dependence

on pH and the growth kinetics, that will allow to distinguish between the different scenarios.

6.4.3 Catalytic Properties and Structure of Active Sites

On the basis of the structural results, we will now discuss the catalytic properties of our epitaxial samples. The *b*-value of Co_3O_4(111) and CoOOH(001) films given in Table 6.1 are in good agreement with that reported by Switzer and co-workers for µm thick electrodeposited epitaxial Co_3O_4 layers[22] and exfoliated CoOOH nanosheets[110, 111]. Table 6.2 gives the turnover frequency of our samples and the overpotential that is necessary to flow a current density of $10\,mA\,cm^{-2}$. The latter parameter compares very well with literature, even for the smooth CoOOH(001) films, if one accounts for the true microscopic surface area. The reported TOF is defined here as the number of O_2 molecules generated per second and per surface site. As surface site, we consider any Co−O surface bond. Details for the calculation of the TOF are given in the Supporting Information (Section 6.7.5). For CoOOH(001) layers, we find a TOF of $\approx 4.2\,s^{-1}$, which is in between that of thick CoOOH(001) oriented films of known ECSA[89] and that of exfoliated CoOOH nanosheets[110, 111]. We consider these examples because the surface structure of these samples is *a priori* the closest to that of our sample. In the case of the Co_3O_4(111) layer, it is not possible to calculate a TOF with the above definition, since the real density of sites in the 3D skin layer is unknown. Assuming conservatively only sites on the surface are active, we estimate a TOF $\approx 3.2\,s^{-1}$, as explained in Section 6.7.5, for the purpose of comparison with CoOOH and literature. We have to bear in mind that this value of $\approx 3.2\,s^{-1}$ only represents the order of magnitude of the TOF. It is yet much larger than most of those reported in the literature for Co_3O_4 and CoCat (see Table 6.2) and compares well with only a few references. This point will be addressed in more detail later on.

At this stage, our main finding is that a smooth epitaxial CoOOH(001) layer with a well-defined structure is nearly as good a catalyst as a Co_3O_4(111) layer or any Co_3O_4 catalyst of the literature, if one accounts for the true microscopic surface area. This is in contrast with general assumptions in the literature and not easy to reconcile with the current conceptions on the nature of the OER-active site on Co oxide catalysts. Moreover, reaching these catalytic performances does not require "pre-conditioning" of the CoOOH film, because it is structurally stable. This last point appears again to be in contrast with the general behavior reported in the literature (see, for instance, refs[93, 110]) and reinforces the interest of studying well-defined epitaxial films.

It was proposed in previous studies of amorphous CoCat catalyst films[104] that the OER active sites are di-µ-oxo-bridged (μ_2−O) ion clusters, in which Co atoms are in a near-octahedral coordination by 6 oxygen ligands with a Co−Co distance of 2.81 Å and oxygen atoms bound to two Co atoms only, a configuration which is similar to that in Co-oxo cubanes[123]. On the (001) plane of CoOOH, only μ_3−O/OH sites exist, where the oxygen is 3-fold coordinated to Co^{3+}, and μ_2−O configurations only exist at steps of CoOOH(100) surface or near Co^{3+} surface vacancies (Fig. 6.6). According to our structural data, the coverage of μ_2−O/OH sites on our

oxide	structure/morphology	TOF(s^{-1}) ($\eta = 0.4\,V$)	η(V) ($j = 10\,mA/cm^2$)	ref
CoOOH(001)	epitaxial (001)	4.2	0.42	this work
	oriented (001)	0.4[a)]	0.43	[89]
	exfoliated nanosheets	15[b)]	0.3	[111]
	exfoliated nanosheets	0.023[b)]	0.39	[110]
Co_3O_4(111)	epitaxial (111)/Au	3.2	0.42	this work
	epitaxial (111)/Au	0.4[a)]	0.43	[89]
poly-Co_3O_4	nanocystalline	1.36×10^{-3}[c)]	0.44	[87]
	nanocystalline/Au (80 ML)	5×10^{-2}[c)]	na	[54]
	nanocystalline/Au (0.4 ML)	1.5[c)]	na	[54]
CoCat	amorphous	8×10^{-4}[b)]	na	[122]

a) Estimated using ECSA derived from capacitance measurements in acetonitrile.
b) Estimated assuming all Co centres within the material are active.
c) Estimated using ECSA derived from capacitance measurements in aqueous alkaline electrolyte.

Table 6.2: Estimated TOF for $\eta = 0.4\,V$ and overpotential η for a current density of $j = 10\,mA/cm^2$ with respect to the ECSA. TOF values reported in the literature are given for comparison.

CoOOH is only a few percent. Assuming that the latter are the predominant active sites of the OER, the reaction would occur at a small fraction of the surface sites only, and the true TOF would be of the order of $100\,s^{-1}$.

In the case of the Co_3O_4(111) film, we have seen previously that a skin layer is covering the islands (see scheme in Fig. 6.4, top right corner) before the OER, which is only marginally thickening further in OER. This skin layer is probably a highly defective, 3D reaction zone for the OER, in analogy with the behavior of CoCat[107]. It should therefore be more active than a smooth CoOOH(001) film since defects are thought to improve the catalytic activity[124]. In previous studies, it was concluded on the basis of XAS measurements that the skin layer consists of a $CoO_x(OH)_y$ phase with an increased amount of octahedrally coordinated di−μ−O/OH-bridged $Co^{3+/4+}$ ions and these sites were considered as indispensable for the OER activity of Co_3O_4[87]. The very similar activity of Co_3O_4 and CoOOH in our study is therefore difficult to rationalize in this scenario and can only be explained in two different ways: Either, the number of μ_2−O/OH sites in the skin layer is only a few percent of the ECSA, which seems unlikely because a strong local structural disorder is expected within the skin, or the high catalytic activity of the CoOOH(001) surface is not caused by μ_2−O/OH sites alone and other sites of this surface, specifically μ_3−O/OH sites, significantly contribute to the OER. The latter seems not unlikely, taking into account that in μ_2−O/OH and μ_3−O/OH sites the Co−O bond length and the spacing of the oxygen atom to neighboring O is very similar. At least in terms of the local geometry, the OER reaction mechanisms proposed in previous studies[87, 102] therefore should be possible for both sites.

6.4.4 Pseudo Capacitive Charge in Pre-OER Region

We now discuss the electrochemical charge Q_0 measured in the pre-OER region (Table 6.1). As explained in Section 6.7.6, for CoOOH(001) the charge $Q_0 \approx 1.4\,\mathrm{mC\,cm^{-2}}$ may be attributed simply to adsorption/desorption on the oxide surface, specifically protonation/deprotonation of the outermost oxygen atoms on the top surface plane and within the grain boundaries. According to a previous DFT study, the deprotonation of the CoOOH(001) surface indeed extends over a wide potential regime, with the stability ranges of the fully H-terminated and the fully O-terminated surface at ≤ 0.3 V and ≥ 1.5 V vs RHE, respectively[105]. We note, as an additional proof that the changes in the optical reflectivity of this sample are consistent with a surface effect (Supporting Information, Section 6.7.7, Fig. 6.14). A pure surface charging is further in agreement with the absence of structural modifications in the pre-OER region.

In the case of Co_3O_4, the charge $Q_0 \approx 4.15\,\mathrm{mC/cm^2}$ for the sample in Fig. 6.4 corresponds to a charge $q_0 = 0.86\,e_0$ per formula unit of oxide within the deposited film (see Supporting Information, Section 6.7.6) which reduces to $q_0 = 0.58\,e_0$ after subtraction of the charge necessary to form the 1 nm thick skin. A logical conclusion is that the pseudocapacitive charge transfer involves the bulk of the Co_3O_4 epitaxial film. This is also supported by the optical reflectivity measurements, which mirror the corresponding charge transfer (see Section 6.7.7, Fig. 6.15a) and is in accordance with previous observations for CoCat[98]. The changes in the bulk charge state are probably linked to the reversible changes in unit cell volume, which occur in the same potential region. This is also in agreement with XAS results that likewise found a decrease in bond distances upon oxidation of Co^{2+} to Co^{3+}[87]. Furthermore, these fast and reversible bulk structural changes explain the excellent performances and cyclability of Co_3O_4 in supercapacitor applications[125].

A pending question is the identification of the charges associated with the substantial pseudocapacitive charge/discharge in Co_3O_4. The discussion must also take into account the rate of this process, which is fast for a bulk phenomenon (≤ 1 s for anodic charging). If this process would be related to a bulk Co redox reaction, the predominant fraction of the Co^{2+} ions in the 20 nm thick Co_3O_4 film would have to be converted into Co^{3+}. This seems very unlikely, given that the spinel lattice is largely maintained and that the mean oxidation state of the material remains close to that of the spinel phase. In previous studies, intercalation of solution species, such as cations or hydroxyls, was proposed to explain the large pseudocapacitive current[89, 126], which is sustained by the fact that no such bulk charging is observed in organic electrolyte, such as acetonitrile (interfacial capacitance is of the order of a few $10\,\mu\mathrm{F/cm^2}$ in this solvent)[22, 89]. More work is necessary to check this hypothesis and identify the nature of the bulk charge transfer.

An important practical consequence of these findings is that, contrary to general practice in electrocatalytic studies of Co oxide materials, the current in the pre-OER range cannot be easily employed to estimate the electrochemical surface area or redox-active surface sites. Concretely,

dividing the pseudocapacitance of the oxide by a standard double layer capacitance of 60 μF/cm^2, as usually done in literature[81, 88], leads to an erroneous electrochemical surface area (ECSA) that is several order of magnitude larger than derived from independent structural characterization. This has already been noted in previous studies[22, 101, 127] where the ECSA was estimated by other methods (e.g., impedance measurements in an organic solvent), but has been largely ignored in the community. Our results for structurally well-characterized samples reinforce the need for independent ECSA determination as good practice in electrocatalytic studies of Co oxides.

6.5 Conclusions

In summary, we studied the OER on Co oxides by combining structurally well-defined model catalysts – thin epitaxial Co_3O_4(111) and CoOOH(001) films – and advanced *operando* X-ray surface diffraction techniques. This approach enables direct correlation of the potential-dependent microscopic surface structure and the electrochemical current, which are measured simultaneously. It specifically allows independent determination of the electrochemical surface area and thus straightforward comparison of the catalytic activity.

According to our results, Co_3O_4(111) and CoOOH(001) behave quite differently from a structural viewpoint, whereas their catalytic performances appear very similar, suggesting that the two materials have a similar surface density of OER active sites. The surface structure of CoOOH(001) is very stable, even at high OER current densities. It is primarily terminated by oxygen atoms that are 3-fold Co-coordinated (μ_3-O) and only exhibits a small number of the di-μ-oxo bridged Co sites (μ_2-O) at surface defects (steps and terrace cation vacancies), that are typically associated with the good OER activity of cobalt oxides.

On Co_3O_4(111), the OER occurs on a skin layer, whose formation is highly reversible, fast, and commences in the pre-OER range, near the CoOOH/Co_3O_4 equilibrium potential, indicating that it is not induced by the catalytic reaction, but reflects the oxide electrochemistry. The skin layer thickness is increasing almost linearly with potential, even in the OER regime. We suggest that this behavior may be explained by models derived for passive film formation. Following the current assumption in the literature that the skin layer corresponds to a defective 3D reaction zone with a high number of μ_2-O sites, the very similar catalytic properties of Co_3O_4 and CoOOH(001) suggests that the μ_3-O sites may also contribute to the OER on the latter surface.

In addition, we find over a wide potential range reversible changes of the bulk lattice constant (i.e., a change in the density of the Co_3O_4 film), which may be attributed to the reversible creation/annihilation of a high density of volume stoichiometric defects. Together with the charge caused by skin layer formation/removal, these seem to be associated with the large pseudocapacitive current of this material in the pre-OER range, a phenomenon that also explains why this oxide is a good material for supercapacitor applications.

6.6 Acknowledgements

We gratefully acknowledge financial support by the Agence Nationale de la Recherche (ANR) and the Deutsche Forschungsgemeinschaft (DFG) via project EC-MEC (ANR-15-CE30-0024-01 and MA1618/20) and thank the ESRF / ID03 beamline staff, in particular Francesco Carla, for technical support.

6.7 Supporting Information

6.7.1 Experimental Details

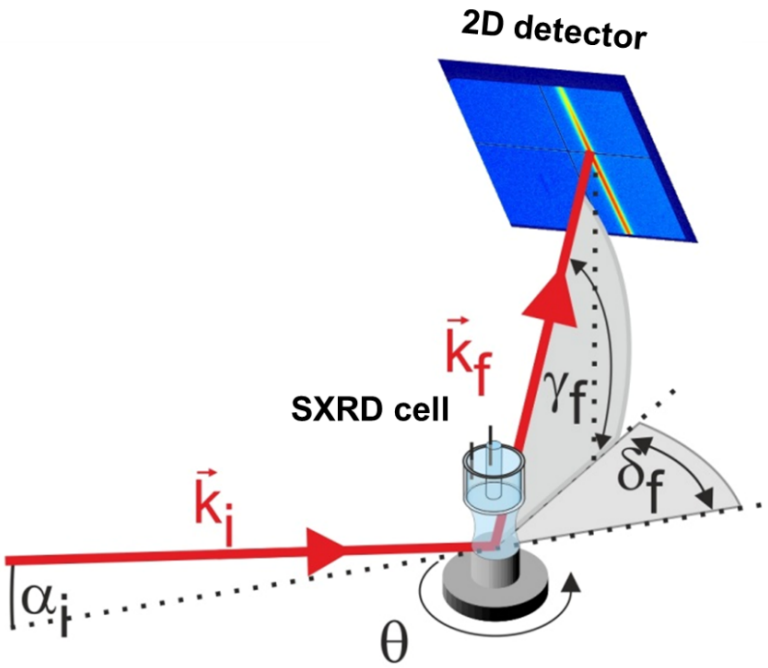

Fig. 6.7: Schematics of the scattering geometry of the *operando* SXRD measurements.

6.7.2 Principle of Structural Analysis from *Operando* SXRD Measurements

The potential dependence of the Co oxide structure during cyclic voltammograms was determined by continuously measuring 2D X-ray detector frames at a Bragg peak position (see Fig. 6.3) in intervals of 1 s. Because the detector images the diffracted intensity on the Ewald sphere, which crosses the investigated peaks at a steep angle (see reciprocal space geometry, shown in Fig. 6.8), the x and y axes of the frames approximately correspond to the intensity distribution in the (K,L) plane. From each frame, peak profiles along the out-of-plane and in-plane direction were taken

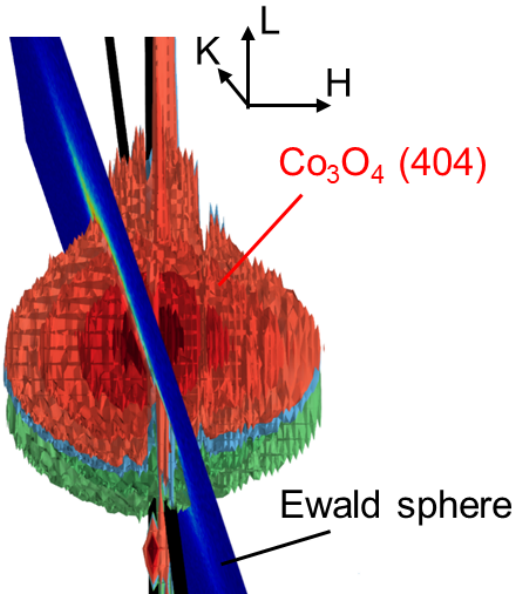

Fig. 6.8: Reciprocal space geometry of the *operando* SXRD measurements, illustrated for the case of the Co_3O_4(404) peak. Shown is the Co_3O_4(404) peak at 0.97 (green), 1.37 (light blue), and 1.57 V (red). The surface of the Ewald sphere is shown in dark blue.

and fitted by pseudo-voigt functions (Fig. 6.9). The peak positions $q_{\perp,\parallel}$ and full width at half maximum ($\mathrm{fwhm}_{\perp,\parallel}$) values, obtained from these fits, were used to calculate the film strain $\varepsilon_{\perp,\parallel} = \frac{q_{\perp,\parallel,nom}}{q_{\perp,\parallel}} - 1$, where $q_{\perp,\parallel,nom}$ are the peak positions that correspond to the literature values of the lattice parameters, and the coherence length $d_{\perp,\parallel} = 2\pi/\mathrm{fwhm}_{\perp,\parallel}$, which is associated with the grain size. Since detector and sample are fixed during these measurements, the resolution of this method allows detection of relative strain changes down to $\approx 10^{-4}$ and changes in grain size down to ≈ 0.1 nm. In complementary SXRD measurements, full reciprocal space maps of the Bragg peaks of the type shown in Fig. 6.1d,e were recorded at selected potentials and quantitatively analyzed (Table 6.3 and 6.4). These result in similar strain and grain size changes, which provides further support for the validity of our method.

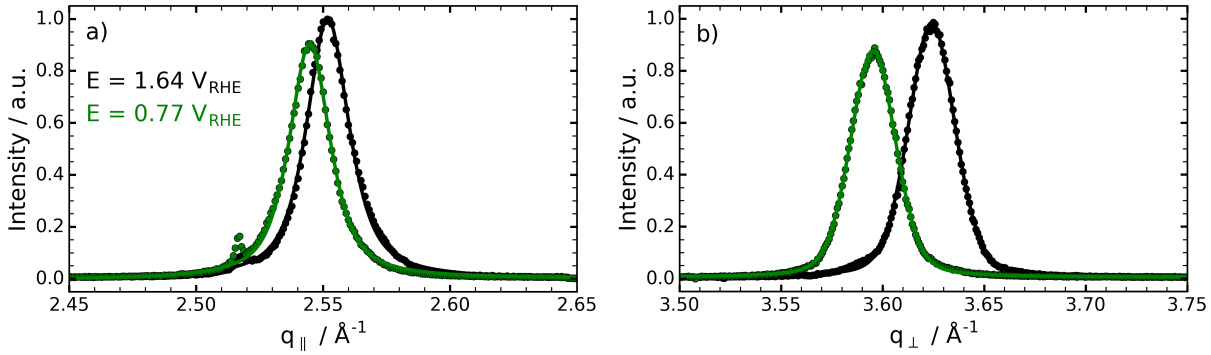

Fig. 6.9: Examples of measured cross sections (circles) and fits (solid lines) of the Co_3O_4(404) peak along the (a) in-plane and (b) out-of-plane direction, obtained from detector frames at 0.77 and 1.65 V with 1 s counting time.

6.7.3 Additional SXRD Data

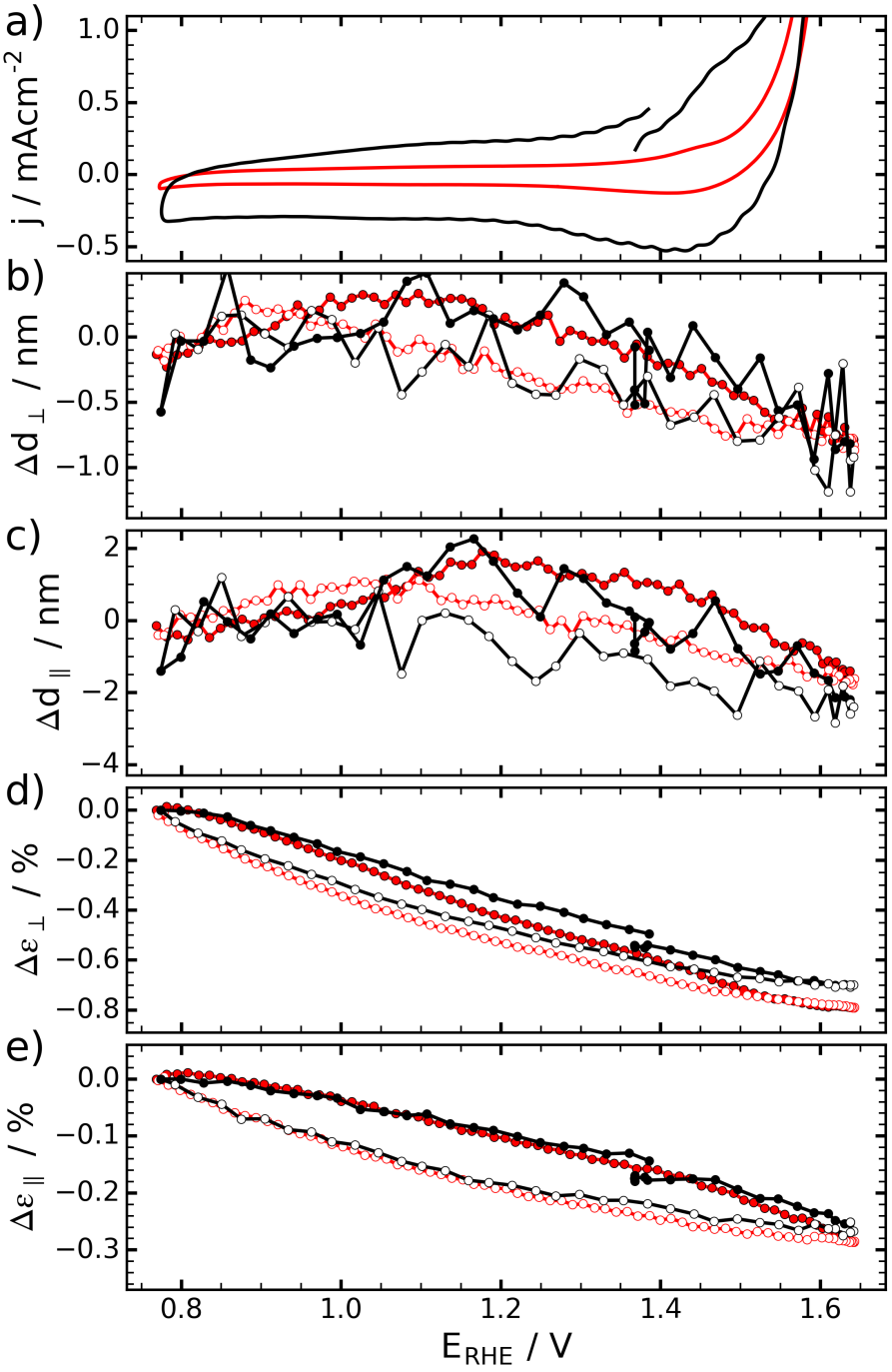

Fig. 6.10: Comparison of the *operando* SXRD data for the Co_3O_4(111) film in 0.1 M NaOH obtained in potential cycles with sweep rates of 10 mV/s (red) and 50 mV/s (black). The similar behavior of strain and grain size indicates a fast kinetics of the structural changes.

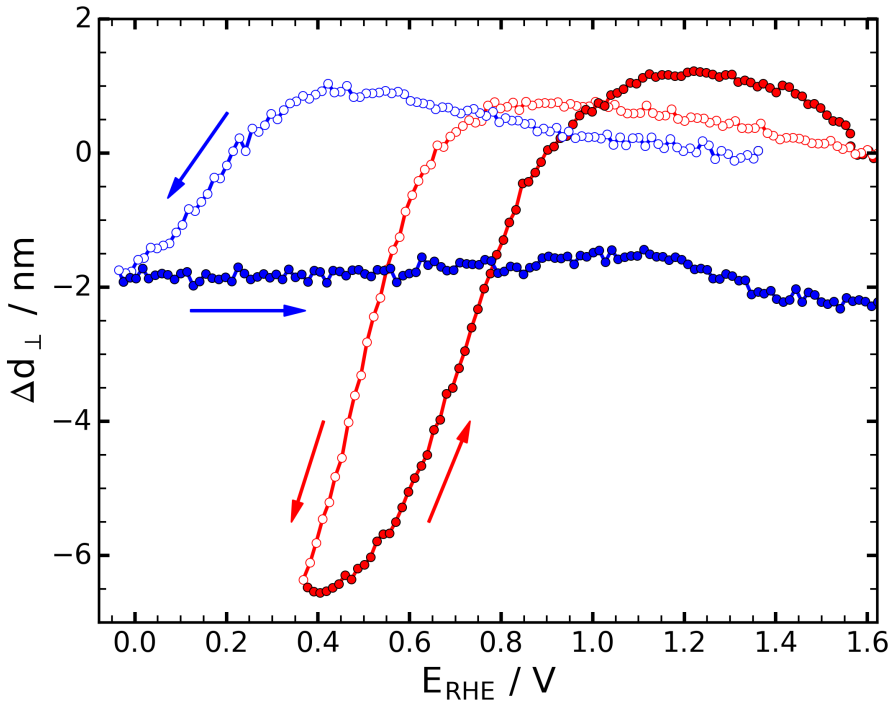

Fig. 6.11: Change in vertical grain size $\Delta d_\perp$ of CoOOH(001) (blue) and Co_3O_4(111) (red) films during a potential sweep in 0.1 M NaOH (sweep rate 10 mV/s), showing an irreversible decrease in film thickness due to conversion to $Co(OH)_2$. The potential sweeps were performed at the end of long SXRD experiments (25 h in the case of CoOOH), where the samples had undergone numerous potential cycles and been kept for longer times at potentials < 0.6 V. This lead to some degradation of the samples, which probably accounts for the slight increase in the $\Delta d_\perp$ of CoOOH in the negative potential sweep between 1.4 and 0.4 V, which never was observed on freshly prepared samples kept at potential ≥ 0.77 V.

	Argon	0.97 V	1.37 V	1.57 V
$\varepsilon_{\perp}/\%$	-0.068	0.393	0.003	-0.134
$\varepsilon_{\parallel}/\%$	-0.161	-0.124	-0.213	-0.304
$\mathrm{fwhm}_{\perp}/\mathrm{nm}^{-1}$	0.311	0.310	0.312	0.319
$\mathrm{fwhm}_{\parallel}/\mathrm{nm}^{-1}$	0.222	0.212	0.212	0.208
$d_{\perp}/\mathrm{nm}$	20.226	20.290	20.115	19.676
$d_{\parallel}/\mathrm{nm}$	28.456	29.957	29.809	30.592

Table 6.3: Structural data for the Co_3O_4(111) film shown in Fig. 6.4 (diamonds), obtained from full reciprocal space maps of the Bragg peaks of the as prepared film installed in the SXRD cell filled with argon (1st column) and after immersion in electrolyte (last 3 columns) at selected potentials under stationary conditions. The data represent the average of the fit results for the $(2\bar{2}2)$, (115), and (404) peak. Shown are the out-of-plane and in-plane values of film strain $\varepsilon_{\perp,\parallel}$ (relative to literature lattice parameters), full width at half maximum $\mathrm{fwhm}_{\perp,\parallel}$, and grain size $d_{\perp,\parallel}$.

	Argon	0.87 V	1.37 V	1.57 V
$\varepsilon_{\perp}/\%$	1.197	1.418	1.381	1.406
$\varepsilon_{\parallel}/\%$	0.751	0.760	0.805	0.772
$\mathrm{fwhm}_{\perp}/\mathrm{nm}^{-1}$	0.350	0.355	0.355	0.356
$\mathrm{fwhm}_{\parallel}/\mathrm{nm}^{-1}$	0.179	0.183	0.180	0.183
$d_{\perp}/\mathrm{nm}$	17.976	17.703	17.688	17.688
$d_{\parallel}/\mathrm{nm}$	35.276	34.304	34.924	34.480

Table 6.4: Structural data for the CoOOH(001) film shown in Fig. 6.4 (diamonds), obtained from full reciprocal space maps of the Bragg peaks of the as prepared film installed in the SXRD cell filled with argon (1st column) and after immersion in electrolyte (last 3 columns) at selected potentials under stationary conditions. The data represent the average of the fit results for the (012), (015), and (017) peak. Shown are the out-of-plane and in-plane values of film strain $\varepsilon_{\perp,\parallel}$ (relative to literature lattice parameters), full width at half maximum $\mathrm{fwhm}_{\perp,\parallel}$, and grain size $d_{\perp,\parallel}$.

6.7.4 Structure of the Studied Co Oxides

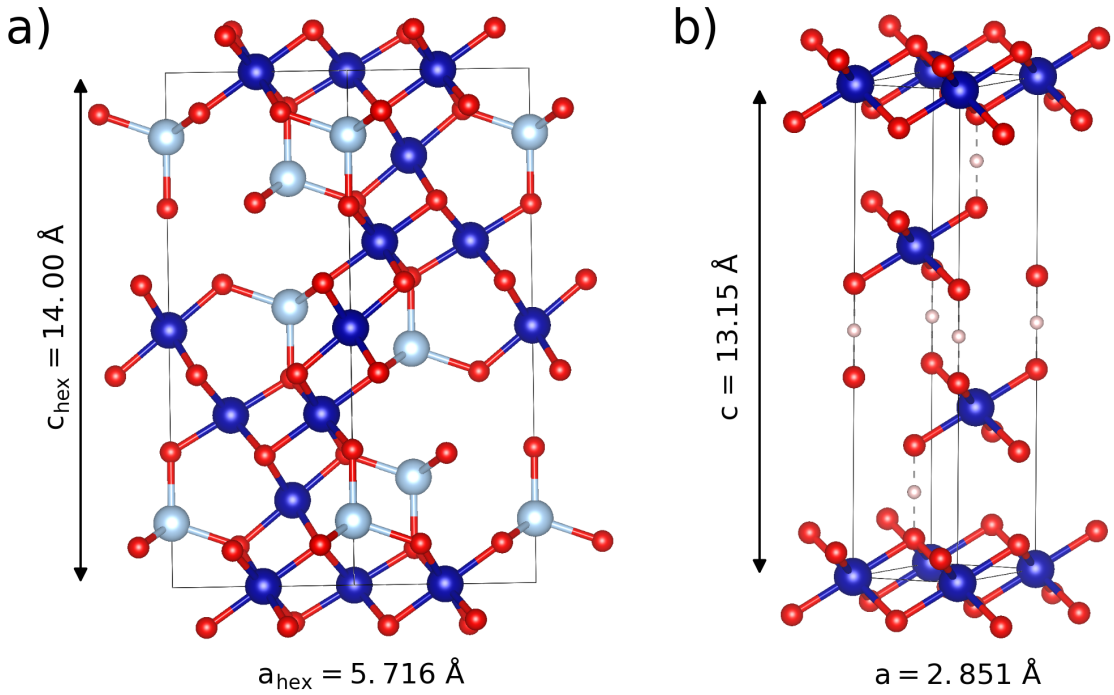

Fig. 6.12: Unit cell geometry (side view) of (a) the spinel Co_3O_4 (space group $Fd\bar{3}m$) and (b) the layered CoOOH compound (space group $R\bar{3}m$), containing (a) 8 Co_3O_4 and (b) 3 CoOOH formula units in the unit cell, respectively. The vertical axes correspond to the surface normal directions. Co^{2+} and Co^{3+} cations are displayed in light blue and dark blue, respectively, oxygen atoms in red, and the hydrogen atoms in CoOOH in white. The atomic positions in Co_3O_4 and CoOOH were taken from the crystallography open database[128] the crystallographic data in Ref.[114] (Co_3O_4) and Ref.[115] (CoOOH).

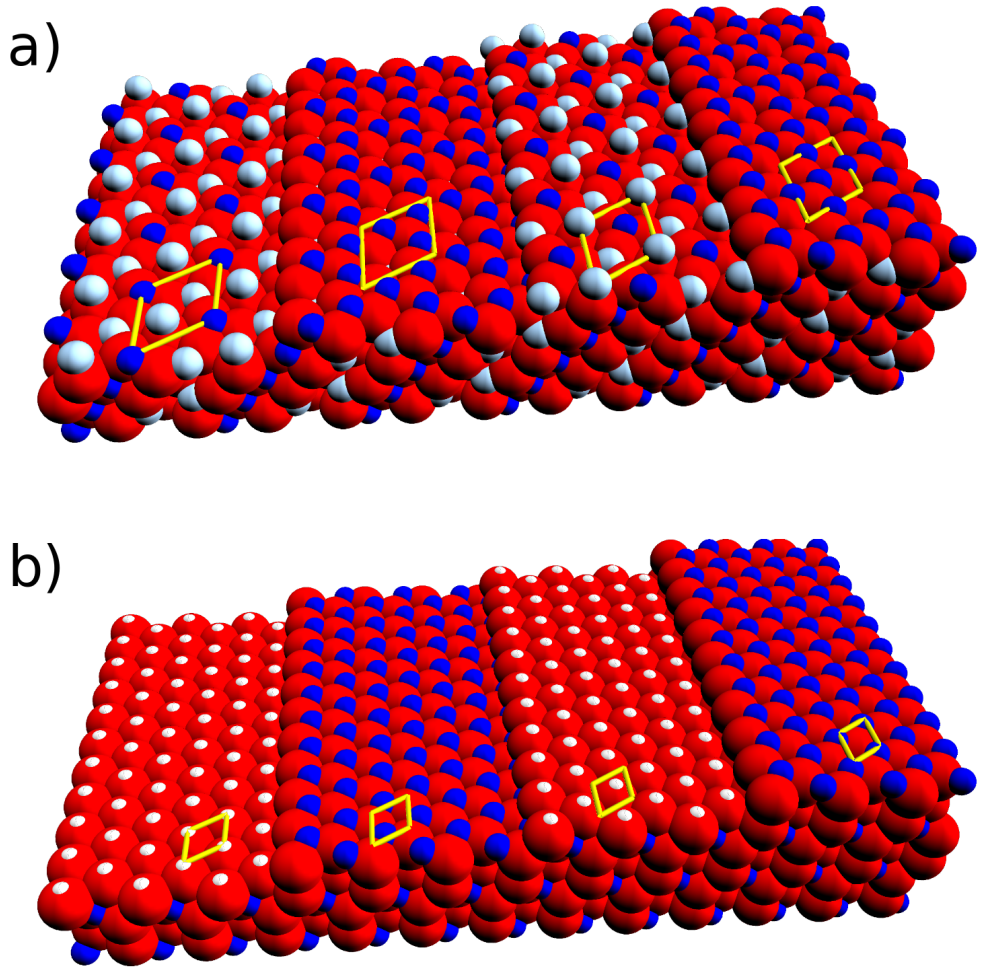

Fig. 6.13: Schematic illustration of the atomic arrangement in the hexagonally ordered planes of (a) $Co_3O_4(111)$ and (b) CoOOH(001). Co^{2+} and Co^{3+} cations are displayed in light blue and dark blue, respectively, oxygen atoms in red, and the hydrogen atoms in CoOOH in white. For the surfaces of these oxides in the electrochemical environment, the topmost plane most likely is terminated by oxygen or hydroxyls groups.

6.7.5 Estimate of ECSA and TOF

The CoOOH(001) layer is smooth and its ECSA is close to unity as derived from AFM observations. The Co_3O_4(111) sample is clearly composed of disconnected 3D islands. Its ECSA may be estimated by assuming the grains are columnar with a circular section and cover 0.85 of the geometric area. Using the grain dimension (see Table 6.3) gives a roughness factor of 3.2. A very similar value is obtained for an ellipsoid island shape. We conservatively use the value of 3 in the manuscript.

The TOF is defined here as the number of O_2 molecules generated per second and per surface site. As site, we consider any (O-terminated) Co surface atom. The density of sites on the CoOOH(001) surface is $N = 1.42 \times 10^{15}$ Co sites/cm^2 (the hex surface unit cell has an in-plane lattice spacing of 2.851 Å and contains one Co site). The total number of sites is N $\times$ ECSA, with ECSA ~ 1.02 in our case.

Since the OER is a four electron reaction with 100 % efficiency, the TOF for a given current density j (relative to ECSA) equals j/zeN with $z = 4$ the valence of the reaction and $e = 1.6 \times 10^{-19}$ C. For an overpotential of 0.4 V, i.e., a potential of 1.63 V, the current density is $j = 3.9$ mA/cm^2 on CoOOH(001), which corresponds to a TOF of ≈ 4.2 molecules of O_2 per second and per surface site.

In the case of Co_3O_4(111), the active surface is the ≈ 1 nm thick skin layer, for which the density of sites is unknown. For the purpose of comparison of the two materials, we tentatively calculate the TOF by assuming that the number of OER-active Co atoms is equal to that of a defect free (111) surface of Co_3O_4. This will roughly give the right order of magnitude. With this approximation, $N = 1.06 \times 10^{15}$ Co sites/cm^2 on the (111) plane and $j \approx 2.2$ mA/cm^2 for the ECSA normalized current density. Therefore, a TOF of $\approx 3.2\,s^{-1}$ is estimated for this material.

6.7.6 Estimate of the Pseudo-Capacitive Charge Stored in Pre-OER Region

For Co_3O_4, the charge Q_0 in the pre-OER regime (0.77 to 1.57 V) is much too large to be consistent with double layer charging or adsorption/desorption at the oxide surface. In this case it is interesting to convert $Q_0 = 4.15\,\mathrm{mCcm^{-2}}$ (relative to the geometric electrode surface area) into a charge transfer per formula unit of the Co oxide. From the lattice parameters, which give a bulk density of the Co_3O_4 units of $8/(8.0837\,\text{Å})^3 = 1.51 \times 10^{22}\,\mathrm{cm^{-3}}$, and the film thickness of 20 nm we calculate 3.0×10^{16} Co_3O_4 units/cm^2 in the Co_3O_4(111) film under study. Therefore, the charge Q_0 corresponds to $0.86\,e_0$ per Co_3O_4 formula unit of the film. Part of this charge transfer corresponds to the formation of the skin layer around the grains. This layer reaches a thickness of ≈ 1 nm in the out-of-plane and ≈ 2 nm in the in-plane direction, corresponding to ≈ 28 % of the grain volume. Assuming that the material in this skin layer is converted from Co_3O_4 to CoOOH would thus account for $0.28\,e_0$ per formula unit. At potentials in the OER range, further conversion of the Co^{3+} to Co^{4+} is expected on the basis of spectroscopic studies, but this is only expected near the upper end of the potential region used for the charge integration (above the Co^{3+}/Co^{4+} redox potential of 1.39 V)[93]. It therefore should not lead to significant contribution to Q_0. This leaves a residual charge of $\approx 0.58\,e_0$ per Co_3O_4 formula unit, which needs to be accounted for by additional processes, involving the oxide bulk, which is fitting very well with the large amplitude of reflectivity changes (see Section 6.7.7). Moreover, we performed a similar analysis of CVs, obtained on structurally defined epitaxial Co_3O_4 films[22, 95, 112] and obtained a similar charge transfer.

In the case of CoOOH(001) film the surface looks continuous since the grains are tightly packed with no visible grain boundary in AFM images. Moreover, a surface phenomenon in this case appears more likely since the amplitude of reflectivity changes is much smaller (see Section 6.7.7). Assuming the charge Q_0 originates from the protonation/deprotonation of the oxygen groups on the surface of the CoOOH film accounts for a charge of $0.23\,\mathrm{mCcm^{-2}}$ (the surface density of oxygen groups is $1.42 \times 10^{15}\,\mathrm{cm^{-2}}$ for an ideal CoOOH(001) surface). This is significantly smaller than the charge $Q_0 = 1.4\,\mathrm{mCcm^{-2}}$ measured for the 18 nm thick film. Because of the absence of structural changes in the SXRD data, we tentatively assign the residual charge to (de)protonation of the grain boundaries. From the grain dimensions obtained via SXRD (Table 6.4), the surface ratio of inner grain boundaries to the top of the grains would be $4d_\perp/d_\parallel = 2.66$ for perfectly straight and atomically smooth grain boundaries. The surface density of oxygen groups in the grains can be approximated by that of the CoOOH(100) surface ($1.60 \times 10^{15}\,\mathrm{cm^{-2}}$), resulting in a charge contribution of $0.68\,\mathrm{mCcm^{-2}}$. The experimentally observed charge could then be accounted for by a roughness factor of 1.7 of the inner grain boundary surface, which seems realistic.

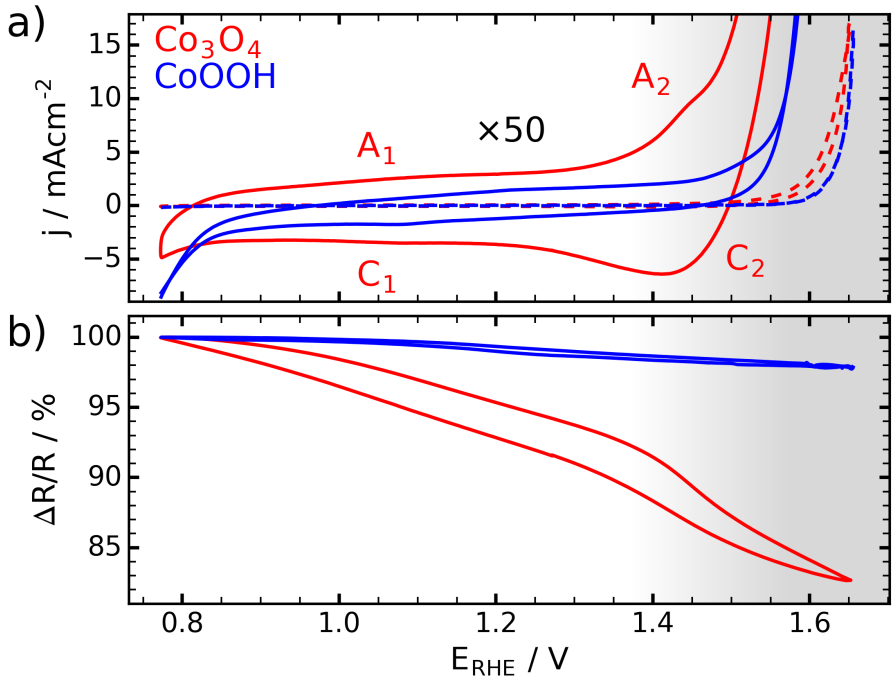

Fig. 6.14: Top panel: CVs presented in Fig. 6.4; Bottom panel: Relative changes of the optical reflectivity of the Co_3O_4(111) and CoOOH(001) samples, obtained in parallel to the operando SXRD data shown in Fig. 6.4.

6.7.7 Optical Reflectivity

The top panel of Fig. 6.14 shows the CVs of Co_3O_4(111) (red) and CoOOH(001) (blue) presented in Fig. 6.4. The bottom displays the corresponding relative changes of the optical reflectivity R of the sample, measured parallel to the SXRD and electrochemical data in the SXRD cell. It was reproducibly found that the change $\Delta R/R$ over the potential range 0.77 to 1.57 V is $\approx 15\,\%$ for the Co_3O_4 film and only $\approx 2\,\%$ for CoOOH. Assuming that these changes are linked to changes in the samples charge state, it makes sense to compare the changes in R with the electrochemical current density. Fig. 6.15 therefore shows the derivative dR/dV of these data (red curves) together with the CV in the double layer range (black curves) for both oxide phases. A similar analysis was proposed by Dau and co-worker[98], though in a different geometry.

In the case of Co_3O_4 (Fig. 6.14, red curve, bottom), the reflectivity variations $\Delta R/R$ are too large to be assigned to surface modifications of the oxide film bulk. Moreover, dR/dV (see Fig. 6.15a) perfectly overlaps with the current density at potentials more negative than the maximum of peak A2, which clearly indicates that dR/dV can be considered as a quantity directly proportional to the electrochemical current due to pseudo-capacitive charge transfer, while OER has no impact. The potential dependence of dR/dV also demonstrates that peaks A2 and C2, which are hidden by the OER current, largely extend into the OER range. This is consistent with the observation that during a potential sweep, the entire film undergoes strain variations and not only the surface layer. Consequently, the pseudo-capacitive electrochemical

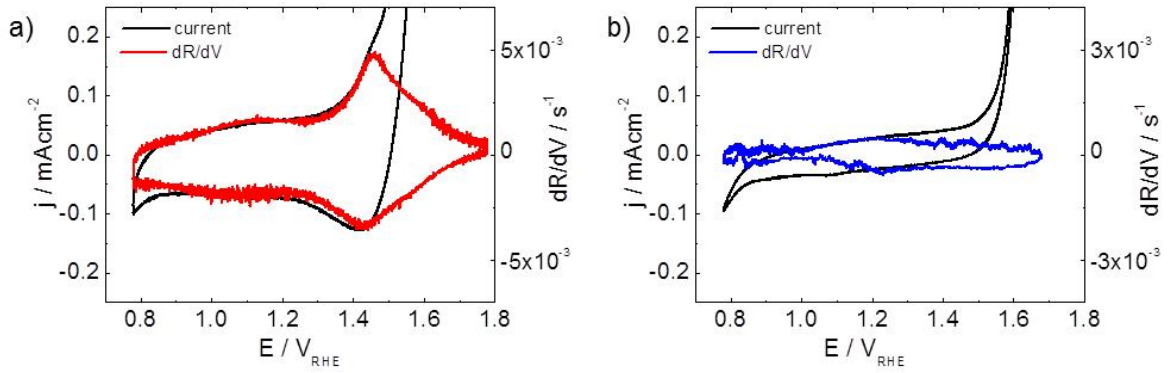

Fig. 6.15: CVs (black lines) and reflectivity changes dR/dV (red/blue lines) of the Co_3O_4(111) (left) and CoOOH(001) (right) samples in 0.1 M NaOH (sweep rate = 10 mV/s).

current is due to volume processes and not, as usually considered, to double layer charging and adsorption/desorption at the surface.

In the case of CoOOH (Fig. 6.14, blue curve, bottom), the amplitude of reflectivity variations is small and within a range, which is typical for modification of the surface termination, e.g., via adsorption. For example, comparable changes were found for electrochemical OH adsorption on metallic cobalt[34]. Also the overlap between the pseudo-capacitive current and dR/dV is less good (see Fig. 6.15b). These observations support the results of the electrochemical analysis, that indicate the absence of charge transfer to the bulk of the CoOOH.

7 Potential Dependence of the Structure and Magnetism of Electrodeposited Pd/Co/Au(111) Layers

This chapter is based on an article published in the Journal of Electroanalytical Chemistry[129].

Abstract

In this work we investigate the magnetic properties and structure of ultrathin Pd/Co/Au(111) stacks prepared by sequential electrodeposition. A combination of *in situ* real-time magneto optical Kerr effect (MOKE), *in situ* surface X-ray diffraction (SXRD), and complementary *in situ* scanning tunneling microscopy, electrochemical studies, and optical reflectivity measurements is employed to characterize the formation of the Pd/Co deposit and its potential-dependent structure. For the preparation of the Pd/Co film a specific procedure is used that prevents Co dissolution. The SXRD results reveal a 2D growth of a (111)-oriented Pd layer, which is in epitaxy with the underlying Co(001)/Au(111). A potential dependent study demonstrates that the Co magnetic properties are reversibly modified upon hydrogen absorption in and release out of the Pd capping film, respectively. Analysis of the SXRD data indicates a Pd lattice expansion upon H-absorption, which is strongly inhibited within the surface plane due to clamping by the substrate. The transmission of hydrogen-induced strain to the Co layer is measured and the resulting impact on the magnetic properties is estimated and discussed.

7.1 Introduction

The growth of epitaxial magnetic ultrathin 2D films which magnetization is perpendicular to the film surface has attracted wide attention during the past few decades because these are involved in spintronic and data storage devices [130, 131]. In 2D films, a sufficiently large positive value of the magnetization anisotropy energy (MAE) is necessary to keep the film magnetization

normal to the sample surface [132]. Experimentally, MAE value (K_{MAE}) is positive for films of a few atomic layers in thickness [133–135]. It depends on different film properties in addition to other parameters, such as the materials at the film interfaces and the presence of strain in the film.

It has been demonstrated that electrodeposition is a reliable technique to grow 2D epitaxial metal films on single crystal electrodes [136]. The epitaxial electrochemical growth of ferromagnetic films of Co [21, 67, 137], Ni [21, 138] and Fe/Au(111) [139], Co on Pt(111) [140], as well as Fe and Co on Cu(001) [141] has been investigated by *in situ* scanning tunneling microscopy (STM) and/or *in situ* surface X-ray diffraction (SXRD). Magnetic characterizations of such films capped by a noble metal demonstrated that electrodeposited ferromagnetic ultrathin layers exhibit magnetic properties very similar to those measured with the same systems grown by physical deposition methods (molecular beam epitaxy, sputtering) [67, 142]. The influence of small molecule adsorption has also received strong attention, because it also influences the magnetic properties as in the case of CO adsorption on Co/Pd(111) in ultrahigh vacuum (UHV) [143] or on Co/Au(111) at the electrochemical interface [144]. In the latter case, it has been demonstrated that the changes in the magnetic properties upon CO adsorption are not due to structural changes of the Co films [137]. In contrast, H-adsorption/desorption causes a reversible modification of the magnetic properties of a Ni/Cu layer that is strongly coupled with reversible structural changes [12], illustrating how strain modifies the magnetic properties of ultrathin films [134]. In line with the latter behavior, previous reports on Co/Pd bilayers showed that gas phase hydrogenation of Pd capped Co layers leads to reversible change of the Co magnetic properties [11–13]. This system was used to develop spintronic based H_2 sensors [145]. However, the origin of the modification of the Co magnetic properties in these bilayers upon H loading is still unresolved.

Transposed to the electrochemical interface, the Pd/Co system appears particularly attractive, because electrochemical hydrogenation of Pd is fast and reversible at room temperature. In addition, this would enable voltage control of the magnetic properties, which is presently an important topic in magnetism (see for instance Refs. [146, 147]). It is well-known that hydrogen may be reversibly inserted into or released from Pd electrodes [148–150] and Pd thin films [151–153]. In early stages, the insertion of hydrogen into bulk Pd leads to the formation of the α-phase; upon further H-absorption a transition to the H-rich β-phase occurs, for which the H:Pd ratio saturates at approximately 0.6 [154]. The lattice constant of the β-phase is expanded by 3.5 % with respect to Pd. The solubility of hydrogen in Pd thin films was investigated using electrochemical charge measurements [151–153], electrochemical quartz crystal microbalance [155], impedance spectroscopy [156], *in situ* surface X-ray diffraction [152, 157], and *in situ* stress measurements [158]. All these studies indicate a reduced solubility of H, when the Pd layer becomes thinner than a critical thickness. In the case of Pd layer on Au(111), the critical thickness is ca. 12 ML [151]. A more extended literature survey on this subject is given in Ref. [159].

In relation with the work on sputtered Co/Pd bilayers and the influence of H insertion in Pd on the Co magnetic properties [11–13], the question arises as to whether also in electrochemical environment H absorption can be utilized for driving changes in the MAE of Pd/Co bilayers and whether this phenomenon is induced by elastic strains or other effects. To this end, we present an electrochemical procedure for preparing epitaxial Pd/Co/Au(111) stacks by sequential electrodeposition and investigate *in situ* the potential dependence of the MAE and the strain in these deposits. The MAE is characterized by *in situ* real time magneto optical Kerr effect (MOKE) measurements [160] and the deposit structure and strain by *in operando* surface X-ray diffraction (SXRD). The large MAE changes observed upon hydrogen absorption and release cycles are discussed in light of the structural data.

7.2 Experimental

7.2.1 Sample Characterization

All X-ray scattering experiments were carried out at beam line ID03 at the ESRF, employing an X-ray energy of 22.5 keV with a flux of 1×10^{12} counts/s. A 2D MAXIPIX detector with 512×512 pixels and a pixel size of $55 \times 55\,\mu m^2$ was used. The data was recorded during two separate experiments with slightly different configurations. The sample detector distance was 914 (662) mm and the beam size at the sample was 240 (215) $\times$ 30 μm^2 in the two experiments we refer to as "A" and "B", respectively. A six circle geometry with a fixed angle of incidence of 0.34° was used, corresponding to a beam footprint on the sample of 240 (215) µm $\times$ 5 mm. For convenience the hexagonal coordinate system (H, K, L) of the Au(111) single crystal substrate is used for all positions in reciprocal space. The reciprocal lattice constants are $a^* = 2.51\,\text{Å}^{-1}$ and $c^* = 0.89\,\text{Å}^{-1}$. The Co and Pd Bragg reflections are indexed by the conventional Miller indices and refer to the conventional crystal structures of these materials (i.e., hcp and fcc, respectively). Fig. 7.1 shows a schematic of the coordinate system along with the Bragg peaks and crystal truncation rods of Au(111), Co(001), Pd (111) and $PdH_{0.6}$(111). *In operando* measurements were carried out at the Pd(011) and Co(011) Bragg peaks, which are labeled "1" and "2" in Fig. 7.1b.

In SXRD experiments "A" we used the "hanging meniscus" transmission cell, employed extensively in past experiments [34]. For experiment "B", a new electrochemical cell was designed, which allows faster electrolyte exchange and parallel optical reflectivity measurements (at 630 nm) to control deposit stability. In this second cell the electrolyte is confined in a vessel made of PEEK, with a wall thickness of $1.5 - 2$ mm in the region where the X-ray beam enters and leaves the cell. In both flow cells a Pt counter electrode, placed in the output circuit to avoid possible Pt contamination, and a Ag/AgCl reference electrode were used. Electrolyte exchange was handled by a remote controlled system of 3 inlet syringes, containing the three electrolytes (Co electrolyte, Pd electrolyte and supporting electrolyte), and an outlet syringe which allowed a

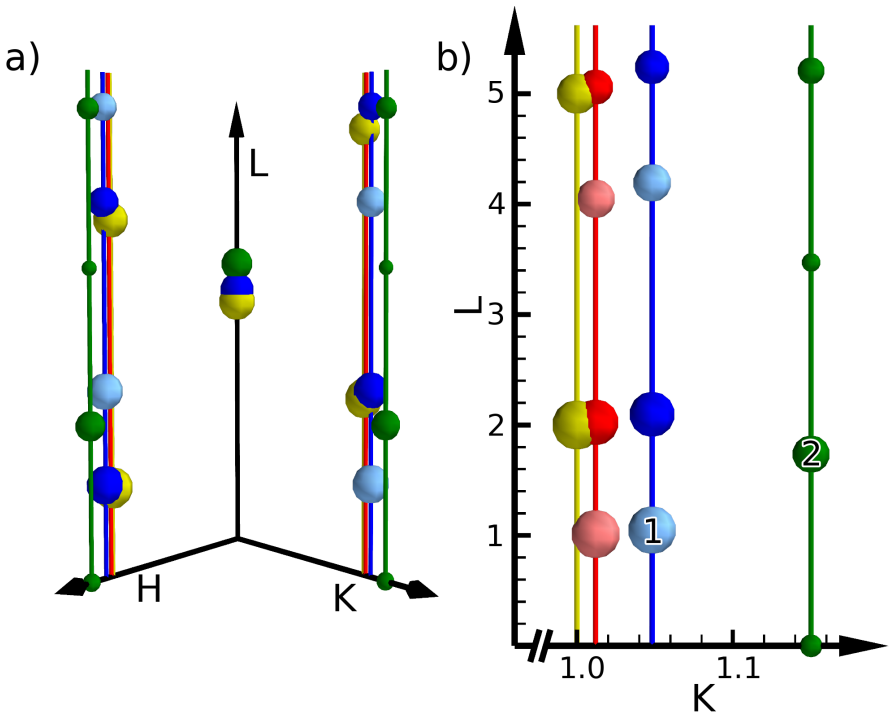

Fig. 7.1: (a) Reciprocal space geometry of Pd/Co/Au(111). The coordinate system (H, K, L) is defined by the Au(111) substrate (yellow). Bragg peaks of (001)-oriented hcp Co (green), of two fcc Pd(111) phases (blue, light blue), rotated against each other by an angle of 60°, and of $PdH_{0.6}$ (red) are shown. The vertical lines indicate the positions of the corresponding crystal truncation rods. b) Magnification of the relevant regime along the K-axis. In the *in operando* measurements the Bragg peaks marked with "1" and "2" were investigated, which are the Pd(011) and Co(011) peak, respectively.

fast and efficient exchange.

The magnetic properties of the samples were studied using a custom *in situ* magneto optical Kerr effect (MOKE) setup, which is equipped with a three-electrode electrochemical flow cell (Kel-F), connected to a potentiostat. We used a Mercury sulfate electrode (MSE) as reference of potential and a Pt wire as counter electrode placed in the output circuit of the cell. However, all potentials will be given with respect to the Ag/AgCl reference electrode. The whole setup and principle of the MOKE measurements are described in details in Ref. [160]. We briefly remind here that the MOKE signal is proportional to the projection of the sample magnetization $\boldsymbol{M}$ on the sample surface normal. The setup sensitivity is $0.1 - 0.2$ ML of cobalt.

For *in situ* electrochemical STM observations a home-built scanning tunneling microscope was used [161]. Tungsten tips were prepared by electrochemical etching in 2 M NaOH and coated with Apiezon wax. The counter electrode was a Pt wire (0.5 mm diameter, 10 mm length). The tip potential during STM imaging of the Co films was typically -0.55 V. STM images (512×512 pixels, 3 min per image) were recorded in constant current mode with a tunneling current of $0.5 - 5$ nA. Images are presented as top views after plane fit correction using SPIP

software (Image Metrology).

For *in situ* surface X-ray diffraction (SXRD) and *in situ* STM characterizations, we used top hat-shaped Au(111) single crystals (Mateck) [34], with a surface exposed to solution oriented to better than 0.1° (diameter of 4 mm, area 12.5 mm^2). Prior to all experiments, the Au(111) single crystals were cleaned by 5 cycles of electrochemical oxidation in 1 M $HClO_4$ *via* the application of 3 V between the crystal and a Pt wire and subsequent reduction in 1 M HCl to remove any Co and Pd from the crystal. The working electrode for MOKE experiments was an ultra-flat 14 nm-thick Au(111) layer electrodeposited on Si(111) [162, 163].

7.2.2 Sample Preparation

The Pd/Co/Au(111) stacks were grown by sequential electrodeposition in potentiostatic mode. Cobalt was deposited on Au(111) substrates from 0.1 M $NaClO_4$ + 1.3 mM HCl + 1 mM $CoCl_2$ solution (pH $\sim$ 4). Two types of epitaxial Co/Au(111) layers were prepared. The first consists of flat 2D Co films grown at -0.9 V where 2D epitaxial growth occurs [21, 34, 67, 137]. The second type of Co layer is deposited using double step potential deposition: During the 1st step a sub-surface coverage of 2D bilayers islands is formed by applying for 1 s a potential of -0.9 V. Based on past measurements [164], we estimate that ~ 20 % of the surface is covered by Co islands after this step. In the 2nd step, the potential is set to -0.78 V to promote Co island growth along the surface normal [165]. This second type of Co film is therefore expected to consist of 3D flat top Co islands, covering partially the Au surface. We will designate in the following the two types of samples by 2D and 3D Co layers. The desired Co average thickness was adjusted by stripping experiments, where the Co thickness was determined from the anodic charge of the Co dissolution peak (see Refs. [21, 34, 67, 137]). To stabilize the final Co deposit used for the subsequent experiments, a potential of -0.71 V was applied and the cobalt solution subsequently exchanged by the supporting electrolyte (0.1 M $NaClO_4$ + 1.3 mM HCl, pH $\sim$ 4).

To deposit the Pd capping layer the electrolyte was exchanged by 0.1 M $NaClO_4$ + 1.3 mM HCl + 0.1 mM K_2PdCl_4 (pH $\sim$ 4), keeping the same potential of -0.71 V. Therefore, Pd deposition commences only when the Pd solution reaches the cell, which results in some small uncertainties (50 s) regarding the actual deposition times ($>$ 600 s, see below). In fact the Pd deposition cannot be monitored using the electrochemical current because the HER current is rather large at this potential. Pd was deposited in a 1st step for a nominal time of 600 s at a potential of -0.71 V, where Co is electrochemically stable. This leads to formation of an initial Pd cover layer that inhibits Co dissolution. Subsequently, the potential was swept at 10 mV/s to -0.4 V and maintained at this value for a nominal time of 600 s (2nd step), leading to further Pd growth. Pd deposition was stopped by changing the potential back to -0.71 V and exchanging the Pd solution with the supporting electrolyte. In some experiments the 2nd step was repeated to vary the Pd thickness.

7.3 Results

7.3.1 Electrochemical and Magnetic Properties

Fig. 7.2 shows the potential dependence of the electrochemical current (top panel), the relative optical reflectivity ($\Delta R/R$, middle panel), and the magnetic properties (bottom panel) for a Pd/Co/Au(111) sample in contact with the supporting electrolyte. The sample was a 4 ML-thick 2D Co layer on Au(111) layer with a Pd capping layer. The black plots correspond to a Pd layer deposited in two steps, as described in Section 7.2. The red plots correspond to the same sample onto which the 2nd Pd deposition step was applied one more time after the optical and magnetic characterizations. This necessitated appropriate solution exchanges.

The cyclic voltammograms (CVs) in Fig. 7.2a resemble those found in past reports for Pd(111) surfaces [151], although the peaks associated with H desorption are not visible due to large anodic currents associated with the oxidation of atomic H which was absorbed into the Pd layer and the oxidation of molecular H_2 which was formed during the potential sweep in HER

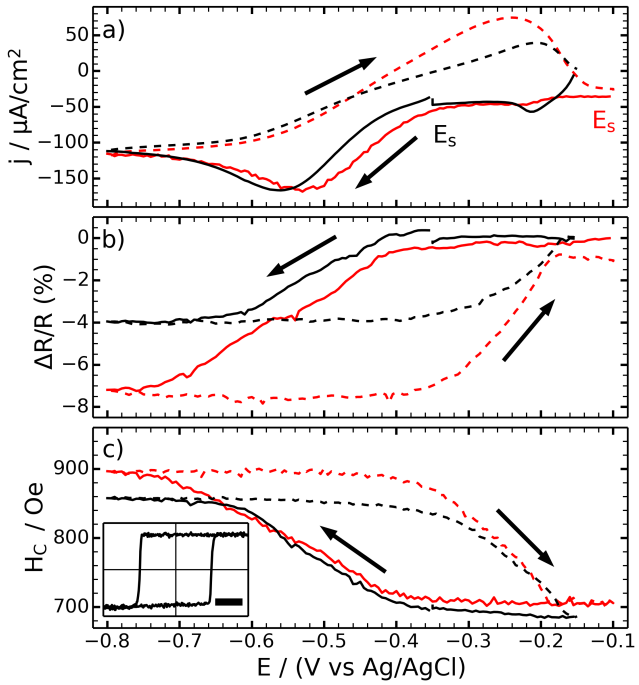

Fig. 7.2: (a) Cyclic voltammograms (10 mV/s) in supporting electrolyte of two Pd/Co/Au(111) samples, consisting of the same 4.3 ML thick 2D Co layer and subsequently covered with a two-step Pd deposits (black line) and then with an additional Pd layer (red line) (see text for details). (b) Potential dependence of the corresponding relative changes in optical reflectivity $\Delta R/R$. (c) Corresponding variations of the coercive field H_C. Inset: typical magnetization curve $M(H)$, showing that the sample is perpendicularly magnetized. The scale bar corresponds to 500 Oe. E_S in (a) marks the starting potential of the sweep towards more negative potentials. Arrows indicate the sweeping direction. Solid (dashed) lines refer to negative (positive) going sweep of potential (10 mV/s).

region. The anodic peak at $-0.25\,\mathrm{V}$ (charge Q_A) is associated with H_2 oxidation and the release of H absorbed into the Pd layer. Q_A clearly increases with Pd thickness. The relative optical reflectivity changes $\Delta R/R$ (middle panel) decreases from $\sim -0.4\,\mathrm{V}$ on the negative sweep and reach a saturation value. On the positive going sweep, $\Delta R/R$ remains equal to this saturation value up to $\sim -0.4\,\mathrm{V}$ where it starts increasing and reaches its original value. The variations of $\Delta R/R$ are well correlated with the onset of HER and the anodic peak at $-0.25\,\mathrm{V}$. It is reversible and is consistent with a self-limiting process. It can be attributed to H insertion into the Pd layer during the HER and release from Pd during H_2 oxidation. The drop of $\Delta R/R$ upon H insertion is in fact consistent with previous reports where it has been shown that the reflectivity drop is due to changes of the refractive index of Pd upon H insertion. The larger $\Delta R/R$ changes of the 2nd sample (red curve) as compared with the 1st sample (black curve) are consistent with the thicker Pd layer of this sample (Pd deposition step 2 was repeated twice). These changes are concomitant with the increase of the electrochemical charge Q_A, which is partly due to the oxidation of absorbed H (an increase of Q_A with increasing Pd thickness is commonly observed, *e.g.* [149, 150]).

The magnetization curve (magnetization as a function of the applied magnetic field) of the sample is shown in the inset of Fig. 7.2c. It has a square shape indicating that the magnetization in the absence of an external magnetic field is oriented perpendicular to the sample surface. The hysteresis between the sweeps up and down of the magnetic field may be characterized by the coercive field $H_C \sim 600\,\mathrm{Oe}$ (the value of the magnetic field when the magnetization changes sign). The magnetization curves of the two samples remain square in the potential region $-0.8\,\mathrm{V} < U < -0.1\,\mathrm{V}$, and the only observed variations are those of the coercive field H_C (Fig. 7.2c). H_C increases in the negative going sweep starting at $-0.4\,\mathrm{V}$, and decreases back during the positive sweep to reach its initial value in the potential range -0.4 to $-0.15\,\mathrm{V}$. The potential dependence of H_C is almost identical to that of $\Delta R/R$ clearly demonstrating that these modifications of the Co magnetic properties are due to H insertion in and release from the Pd capping layer. The effect depends only slightly on the Pd thickness. To elucidate the origin of this effect, *in situ* structural studies were performed, which are presented in the next section.

7.3.2 *In Situ* STM

Fig. 7.3 shows an *in situ* STM image ($42\,\mathrm{nm} \times 39\,\mathrm{nm}$) of a Au(111) electrode surface, partly covered by a Co bilayer deposited at $-0.9\,\mathrm{V}$ (surface coverage about 0.5), onto which a submonolayer of Pd was subsequently deposited at $-0.71\,\mathrm{V}$ using a protocol that was used in Ref. [166] for sequential deposition of different metals on Ni submonolayers. The Co islands were grown in 2 s at $-0.9\,\mathrm{V}$ from the nominal 1 mM $CoSO_4$ solution in supporting electrolyte of pH ~ 3.5 and stabilized at $-0.71\,\mathrm{V}$. The submonolayer of Pd was deposited at $-0.71\,\mathrm{V}$ in 300 s from a $10\,\mu\mathrm{M}$ $PdCl_4$ solution in supporting electrolyte of pH ~ 3.5. To avoid alloy deposition, the $CoSO_4$ electrolyte was first exchanged with the supporting electrolyte of pH

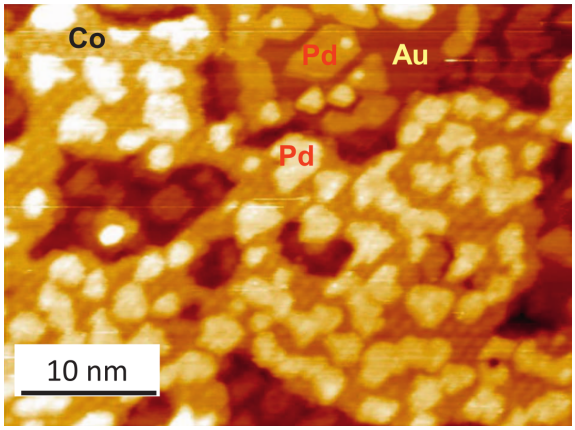

Fig. 7.3: *In situ* STM image (42 nm × 39 nm) of a Au(111) surface covered partly by a Co bilayer and then by a submonolayer of Pd. See text for details about sequential deposition procedure. All Co islands are bilayer (2 atomic planes) and all Pd islands are monatomic.

~ 3.5 and the latter was then exchanged with the diluted $PdCl_4$ electrolyte. The height of the Co islands (0.34 nm) corresponds to 2 atomic planes and they exhibit a moiré pattern in Pd-free areas that is characteristic for a Co(001) deposit [164]. Under these deposition conditions, Pd grows on top of the Co layer as well as on the bare Au surface and all deposited Pd islands are monatomic, providing clear evidence that Pd grows in a 2D mode on Co and on Au(111). The height of Pd islands is 0.17 nm with respect to the Au surface because atomic H is adsorbed at this potential [167]. The STM image shows that Pd nucleation on Co is homogeneous and involves the formation of a high density of nm sized monatomic islands ($\sim 10^{13}$ islands cm^{-2}).

7.3.3 *In Situ* Surface X-ray Diffraction

Characteristic results on the Co structure at different stages of the preparation of the stack are shown in Fig. 7.4. For this 2D sample, the initial Co thickness was 5.4 ML (determined from the electrochemical dissolution charge). Directly after Co deposition (green symbols), the Bragg peaks at L = 1.73 and K = 1.134 (Fig. 7.4a, b) are consistent with a hcp Co(001) structure, which is in epitaxy with the Au(111) lattice and aligned parallel to the latter [137]. The Bragg peak FWHM (0.39 $Å^{-1}$) in the L-scan corresponds to a thickness of 7.9 ML, while the oscillations between peaks are consistent with a thickness of 6 ML. This difference is attributed to the formation of a few thicker Co crystallites [34]. These data confirm that the layer is smooth on the atomic scale. After the first Pd capping step, the above scans (black symbols in Fig. 7.4a and b) do not change appreciably, except for a ~ 13 % (respectively 21 %) loss of the integrated peak intensities for the K scan (respectively the L scan) and an increase of ~ 2.5 % of the FWHM in K- and a decrease of ~ 2.2 % in L-direction, respectively. A further loss of cobalt of ~ 11 % (respectively ~ 8 %) for the K scan (respectively the L scan) is observed after the second Pd deposition step (red symbols). The Co peak FWHM remains unchanged during this second Pd deposition step. The reduction of the Co peak intensity most likely stems from a partial Co

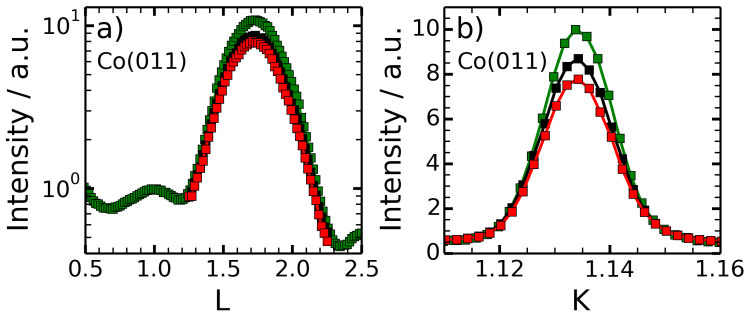

Fig. 7.4: Scans at the Co(011) peak along the L- (a) and K-direction (b) of a 5.4 ML Co 2D-layer at different stages of the sample preparation. The green symbols correspond to as deposited layer. The other scans were recorded after deposition of Pd at −0.71 V for 600 s (black) and further deposition of Pd at −0.41 V for 600 s (red). Partial Co dissolution is observed (see text).

dissolution during the Pd growth. However, since the peak positions remain quasi unchanged (no measurable change in the K-scan and a peak position shift by −0.4 % only in L-scan), we may assess that the structure and morphology of the Co layer remaining after Pd deposition is essentially unaltered.

Structural results on the Pd capping layer are displayed in Fig. 7.5. Fig. 7.5a shows a series of scans along the L-direction at H = 0 and K in the range $1.02 - 1.03$, which is close to the position of the first-order CTR of Pd(111). In addition to the sharp Au(012) and Au(015) Bragg peaks at L = 2 and 5 and the sharp peak at L = 3.9, which is also produced by scattering from the Au substrate, broad peaks at L = 1, 2, 4, and 5 are present (indicated by blue lines in Fig. 7.5a, some appearing as shoulders of the stronger Au peaks), which can be assigned to Pd. In L-scans measured at a 60° equivalent position (data not shown) the same Pd peaks are observed with quasi identical intensities to that in Fig. 7.5a. According to these data, we may conclude that (i) the deposit grows as an epitaxial fcc film with a (111) surface orientation and (ii) Pd grows with equal probability in two orientations, rotated with respect to each other by 180° around the surface normal (corresponding to an inversion of the stacking sequence). The latter accounts for the four Pd peaks along each CTR instead of the two expected for an fcc structure (see Fig. 7.1a) and for symmetry reasons may be expected for the growth of a layer crystal with threefold symmetry (fcc Pd(111)) on a hexagonal substrate (hcp Co(001)). Other explanations such as stacking faults within the Pd film have a very low probability [168] and can be excluded.

The effect of Pd thickness on the L scan may be seen in Fig. 7.5a: the purple curve corresponds to 300 s at −0.71 V, the black and grey curves to 600 s at −0.71 V and the red curve to 600 s at −0.71 V followed by another 600 s at −0.41 V. The black and red curves correspond to the same sample with increasing amounts of Pd, whereas the other curves originate from different preparations. The perfect overlap between the black and grey curves, demonstrates the high reproducibility of the Pd deposition procedure. The Pd(011) peak integrated intensity (Fig. 7.5c black symbols) and the Pd thickness (Fig. 7.5c red symbols) determined from the Pd(011) peak FWHM along the L direction (*via* $2\pi/\text{FWHM}\ c^*$), exhibit a roughly linear increase as a function

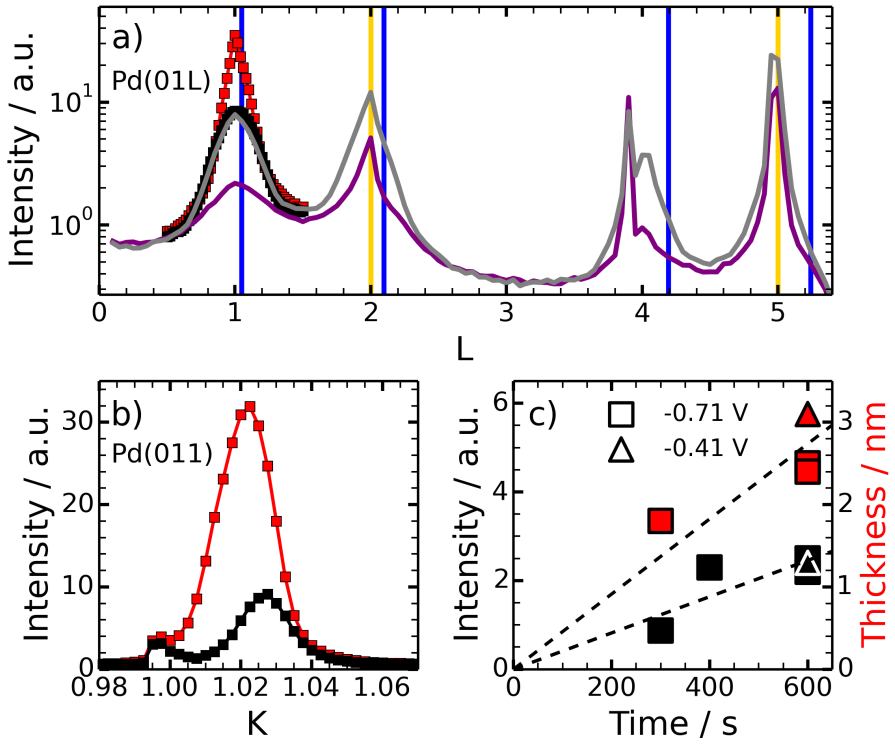

Fig. 7.5: Pd deposition on top of the 5.4 ML 2D-Co/Au(111) of Fig. 7.4. (a) Scans along the L-direction at the Pd(011) peak after 600 s of Pd deposition at −0.71 V (black) and further 600 s of deposition at −0.41 V (red). The purple and grey curves show more extended scans for other films deposits at −0.71 V with a deposition time of 300 s and 600 s, respectively. The overlap of the grey and black curves demonstrates the good reproducibility of the deposition procedure. Yellow and blue vertical lines indicate the theoretical positions of the Au and Pd Bragg peaks, respectively. (b) Scans across the Pd(011) peak along the K direction, corresponding to the deposits depicted with the same symbols in the scans in (a). (c) Integrated Pd(011) peak intensity (black) and film thickness obtained from the peaks FWHM (red) for Pd films deposited on flat Co films. Pd deposition at −0.71 V (square) and −0.41 V (triangle) shows very similar behavior.

of deposition time at both deposition potentials (−0.71 V and −0.41 V). This result suggests that the Pd deposition is independent of the potential in this potential range and probably limited by mass transport. In the scans along the K direction (Fig. 7.5b), the peak is located at K = 1.027 after the 1st Pd deposition step during 600 s at −0.71 V (black symbols). It shifts to K = 1.021 after the 2nd Pd deposition step during 600 s at −0.41 V (red symbols). In both cases, the Pd lattice parameter is expanded with respect to its bulk value (expected K value 1.048). This expansion may be due to the presence of H in the Pd layer. The lattice expansion increases with increasing Pd thickness, suggesting that the thicker the Pd layer, the larger is the amount of H it can absorb. This is consistent with previous reports [151]. Scans at the Pd peak as a function of the sample rotation angle around the normal to the surface (not shown) yield peaks separated by 60°, one of them centered on the K axis. This indicates that the Pd lattice is aligned with the Co(001)/Au (111) lattice. From the peak FWHM of 1.3° we obtain the rotational disorder of the Pd film. It is partly due to the rotational disorder of Co/Au(111) (FWHM = 0.6°) [34].

Fig. 7.6 shows the influence of H-insertion/release on the Pd and Co lattice structure. Here, the prepared Pd(3 nm)/Co(4.9 ML)/Au(111) stack was first polarized above -0.2 V to release all absorbed H from the deposit. Then, the Pd(011) peak was monitored with the 2D detector, while the potential was swept into the H absorption regime. Fig. 7.6a presents the X-ray intensity distributions around the peak as a function of K and L at selected potentials. A clear shift in the peak position (marked by red crosses) in K- and L-direction can be seen, which corresponds to a change in the Pd in-plane strain and out-of-plane strain. Specifically, the peak starts by moving to lower L values and then moves to smaller K-values while its L position continues decreasing. These observations indicate an in plane and out-of-plane lattice expansion upon H-insertion. For a more detailed analysis of this behavior, peak profiles along the K-direction were obtained by integrating the intensity along the L-direction (Fig. 7.6b). These profile show that first, the diffracted intensity at the initial peak position decreases and then, a subsequent rise of the intensity at lower K-values is observed. We assign this behavior to the formation of a Pd hydride phase, which at intermediate potentials coexists with the original (H-free) Pd lattice. However, the final value K = 1.038 is substantially larger than that expected for pure $PdH_{0.6}$ (K = 1.012), suggesting a substantial clamping of the lattice expansion by the underlying substrate. On the other hand, the expansion along the surface-normal direction is close to that expected for a transition to $PdH_{0.6}$. For the same sample, also the in-plane profiles of the Co(011) peak were obtained at potentials corresponding to the H-loaded (red) and H-free (blue) case (Fig. 7.6c), allowing direct comparison with the Pd data. A small peak shift along K in the same direction as for the Pd peak is observed (see difference between scans, black line).

The full potential-dependence of the structural changes of the sample studied in Fig. 7.6 are illustrated in Fig. 7.7. In the sample CV (5 mV/s) (Fig. 7.7a) hydrogen adsorption and desorption around -0.15 V is observed, in addition to HER and H oxidation peaks. The potential dependence of in-plane strains was determined from the Pd(011) diffraction peak position in the 2D images of the X-ray detector. We also measured the FWHM of this peak as a function of potential. These parameters were determined by quantitative fits with a 2D Gaussian function. This method allowed determination of changes in the in-plane strain $\Delta\varepsilon_{\parallel}$ with an accuracy of 1×10^{-4}. Fig. 7.7b shows the corresponding potential-dependent strain changes, obtained from the Pd(011) and Co(011) Bragg peak shifts. Here, we define the in-plane strain as $\varepsilon_{\parallel} = (a - a_b)/a_b$ and the strain in surface-normal direction $\varepsilon_{\perp} = (c - c_b)/c_b$, where a and c are the lattice constants and a_b and c_b are the bulk values of the respective layer. It can be seen that the Pd strain variations $\Delta\varepsilon_{\mathrm{Pd},\parallel}$ (red symbols with solid line) and $\Delta\varepsilon_{\mathrm{Pd},\perp}$ (red symbols with dashed line) show a very similar behavior, albeit with ten times smaller changes in $\Delta\varepsilon_{\mathrm{Pd},\parallel}$ as compared to $\Delta\varepsilon_{\mathrm{Pd},\perp}$. The strain increases during H-insertion into Pd and saturates below -0.6 V, meaning that H-loading is completed. The change in strain is reversible and shows a small hysteresis, in accordance with the hysteresis in the electrochemical data. Interestingly, the changes in $\varepsilon_{\mathrm{Pd},\perp}$ seem to precede those in $\varepsilon_{\mathrm{Pd},\parallel}$. The in-plane strain changes in the Co lattice $\Delta\varepsilon_{\mathrm{Co},\parallel}$ (black symbols with solid line) are even one order of magnitude smaller than $\Delta\varepsilon_{\mathrm{Pd},\parallel}$ (total change $\Delta\varepsilon_{\mathrm{Co},\parallel} = 0.04\,\%$), but

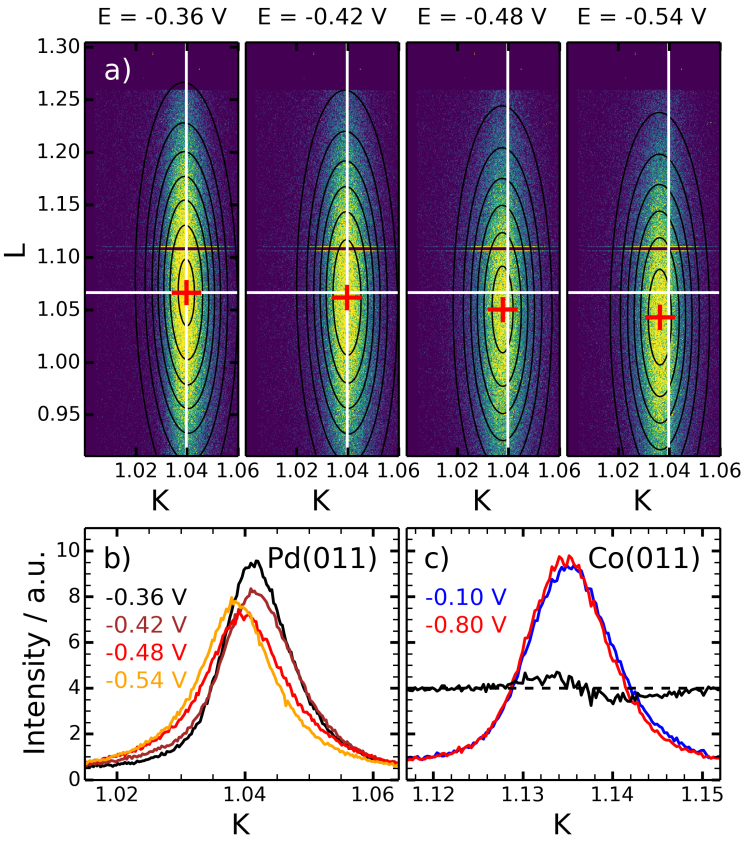

Fig. 7.6: Influence of H-insertion for a Pd(3 nm)/Co(4.9 ML)/Au(111) sample (2D Co layer). (a) Intensity distribution in the K-L plane, obtained from detector images of the Pd(011) peak. The images were recorded at different potentials and show a peak shift during H-loading, as visible by comparing the peak center obtained from a 2D Gaussian fit (marked by red crosses) with the initial peak position (marked by white lines). Contour lines of the fitted Gaussian profile are shown in black. (b) Peak profiles along the K-direction of the Pd peaks shown in (a). (c) In-plane Co(011) peak profiles after H-absorption (red) and H-release (blue) at potentials obtained analog to the Pd data shown in (a) and (b). The black line is the difference between the blue and red curve (zero position indicated by dashed line). A small peak shift in the same direction as for the Pd peak is observed, indicating a coupling of the in-plane strain in Co and Pd lattice.

are clearly correlated with the changes in Pd strain $\Delta\varepsilon_{\mathrm{Pd},\parallel}$. Thus, they can be unambiguously assigned to the effect of strain-coupling to the Pd lattice. Fig. 7.7c shows the in-plane FWHM of the Pd(011) and Co(011) Bragg peaks $\Gamma_{\mathrm{Pd},\parallel}$ and $\Gamma_{\mathrm{Co},\parallel}$, which also both exhibit highly reversible potential changes. $\Gamma_{\mathrm{Pd},\parallel}$ increases when Pd is H-loaded and passes through a maximum around the onset of the HER. $\Gamma_{\mathrm{Co},\parallel}$ decreases slightly and saturates in the HER region.

Similar experiments were performed by applying potential steps. In Fig. 7.8a we show the change in Co(011) in-plane strain $\Delta\varepsilon_{\mathrm{Co},\parallel}$ during potential steps between -0.7 V (red symbols) and -0.1 V (blue symbols) for three different Pd-covered samples: 4.9 ML-thick 2D (left), 4.5 ML-thick 3D Co films (center), and the same 4.5 ML Co deposit after further roughening by intentional partial Co dissolution (right). The two latter were studied in cell "B", which allowed to measure in parallel to the SXRD data the changes in optical reflectivity $\Delta R/R$

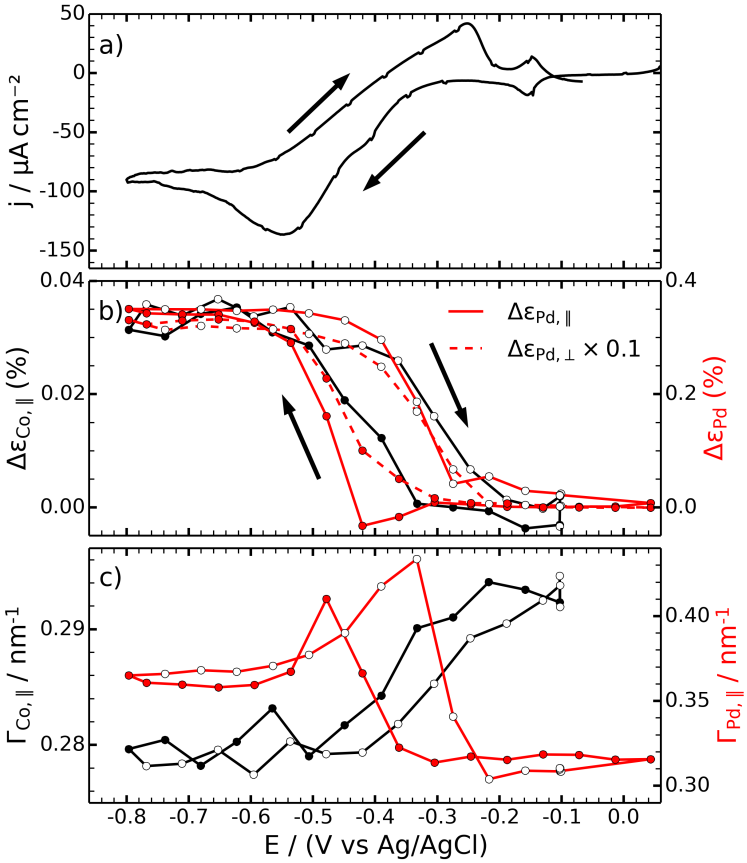

Fig. 7.7: *In situ* SXRD at the Co(011) and Pd(011) Bragg peaks for the sample of Fig. 7.6 during CVs with sweep rates of 5 mV/s. (a) CV, obtained during measurements of the Pd(011) peak. (b) Change in in-plane strain $\Delta\varepsilon_{\parallel}$ (solid) of Co(011) (black line) and Pd(011) (red, solid line) and change in out-of-plane strain $\Delta\varepsilon_{\perp}$ of Pd(011) (red, dashed line) during the CV. (c) Corresponding variations of the FWHM $\Gamma_{\parallel}$ of Co(011) and Pd(011). The data shows that H-absorption impacts the Co and Pd microstructure and that the effect is reversible. In (b) and (c) filled and open circles are used for the cathodic and anodic sweep, respectively.

(yellow line). $\Delta\varepsilon_{\mathrm{Co},\parallel}$ reproducibly follows the potential steps. In addition, there is a perfect correspondence between the change in Co in-plane strain and the $\Delta R/R$ increase, which again supports that the structural changes are correlated with H-insertion. The strain change in the 3D layer $\Delta\varepsilon_{\mathrm{Co},\parallel} = 0.07\,\%$ is almost twice as large as that of the 2D layer. At the same time, the change in Pd in-plane strain $\Delta\varepsilon_{\mathrm{Pd},\parallel}$ increases (see vertical bars in inset). In addition, with increasing Co roughness the change in Co in-plane strain $\Delta\varepsilon_{\mathrm{Co},\parallel}$ increases and $\Delta R/R$ increase in almost the same proportions.

In Fig. 7.8b-c, we focus on a single potential pulse to characterize the transition time at H-insertion and at H-release. To easily compare the different strain changes plots have been normalized to $\Delta\varepsilon = -1\,\%$ by dividing the different strain changes by the factors given in the figure caption (we have seen above that the amplitudes of the different strains are quite different, see Fig. 7.7). These plots correspond to 3D Co layer presented in Fig. 7.8a right panel. Upon H-insertion (Fig. 7.8b), we observe that all strain changes in Pd and Co are perfectly concerted

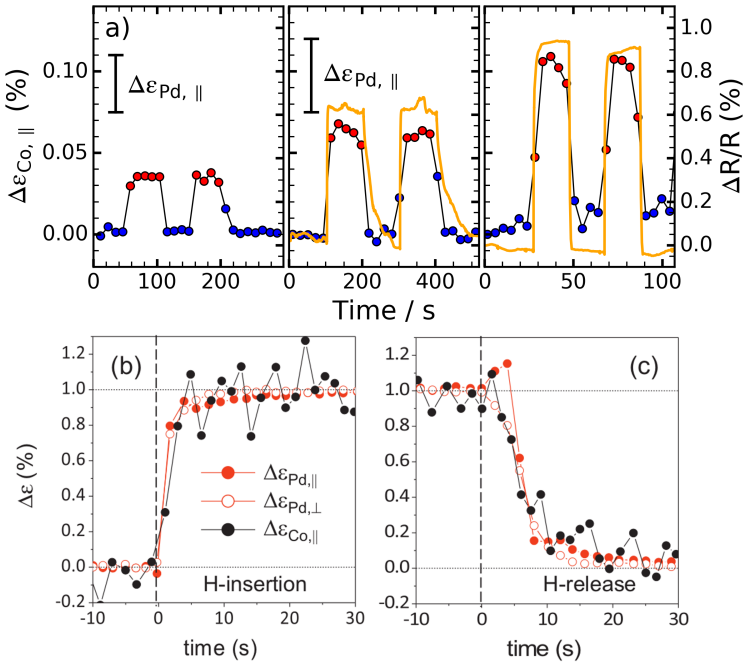

Fig. 7.8: (a) *In situ* SXRD studies of the Co(011) peak during potential steps between -0.7 V (red) and -0.1 V (blue) for three different samples (all covered with 6 nm of Pd): 4.9 ML 2D (left), 4.5 ML 3D Co films (middle), and same 4.5 ML film after roughening (right). Note that increasing the Co roughness induces larger Co in-plane strain $\Delta\varepsilon_{Co,\parallel}$. At the same time the change in Pd in-plane strain $\Delta\varepsilon_{Pd,\parallel}$ increases (see vertical bars). The optical reflectivity $\Delta R/R$ (yellow line) was measured in the SXRD cell "B" for the 4.5 ML Co films. (b-c) Normalized strain changes upon application of a single potential pulse between -0.1 V and -0.7 V (b) and between -0.7 V and -0.1 V (c). The ascending or descending step of potential is applied at $t = 0$. Strain changes $\Delta\varepsilon$ have been normalized to 1 % for the sake of comparison. Normalization factors are 0.07 ($\Delta\varepsilon_{Co,\parallel}$), 0.41 ($\Delta\varepsilon_{Pd,\parallel}$) and 5.4 ($\Delta\varepsilon_{Pd,\perp}$). Note that the changes $\Delta\varepsilon$ are faster upon H-insertion than upon H-release. See text for more explanations.

and are completed within < 2 s. The picture is somewhat different upon H-release (Fig. 7.8c): $\Delta\varepsilon_{Pd,\perp}$ and $\Delta\varepsilon_{Co,\parallel}$ decrease straight away and in a concerted manner but with a much longer characteristic time of *ca.* 10 s. Moreover, $\Delta\varepsilon_{Pd,\parallel}$ changes are delayed with respect to the application of the potential step. The latter behavior was systematically observed upon all anodic potential steps and we may note it is symmetrical to that observed upon slow H-insertion into Pd (in Fig. 7.7b, changes in $\varepsilon_{Pd,\parallel}$ are delayed with respect to those in $\varepsilon_{Pd,\perp}$).

7.4 Discussion

7.4.1 Pd/Co/Au(111) Morphology and Structure

Our *in situ* SXRD data indicate that the electrodeposited Pd capping layer has an fcc structure and is in epitaxy with the Co(001) film on the Au(111) substrate. Specifically, the main directions of all three lattices are well aligned with each other. The presence of two in–plane orientations

in the Pd layer rotated by 60° around the surface normal, can be rationalized considering that the hcp lattice of the underlying Co layer has a six-fold symmetry. The approximately linear increase of Pd thickness with deposition time (Fig. 7.5c) suggests that Pd deposition is limited by mass transport. This may be expected, because the deposition potentials are ~ 1 V more negative than the calculated Nernst potential of $PdCl_4^{2-}$/Pd. The slope of the plot thickness *vs.* time gives a Pd growth rate of ~ 0.025 ML/s. This yields a diffusion layer thickness of 240 µm (assuming a $PdCl_4^{2-}$ diffusion coefficient of 1.4×10^{-5} cm^2/s), which is consistent with the exchange rate of the electrolyte during Pd deposition, employed in the *in situ* SXRD studies. Interestingly, the Pd deposition rate is the same within ($U = -0.71$ V) and outside ($U = -0.4$ V) the HER region. This behavior differs from the case of Pt, for which self-terminated growth is observed in the HER region [169]. A 2D layer morphology may be inferred from STM observations (Fig. 7.3) and also from the fact that, according to SXRD measurements, even a 3 nm Pd film effectively protects the Co layer, leading to partial dissolution through pinholes when the potential is shifted positively to -0.41 V (Fig. 7.4).

7.4.2 Pd Microstructure Upon H-Absorption/Release

Our data evidence that $\varepsilon_{Pd,\parallel}$ is much smaller than the 3.5 % expected for the β-phase and also a strongly anisotropic distortion of the Pd lattice upon H-insertion, which is about 10 times larger in the vertical direction than within the surface plane (Fig. 7.7). At saturation a sub β-phase PdH_x with $x < 0.6$ with an uniaxially distorted fcc lattice is therefore formed. Such a lattice distortion, also observed upon gas phase hydrogenation of sputtered Pd thin films [170], can be explained by strong clamping of the Pd film to the underlying Co(001) surface. The latter strongly restricts the lattice in plane expansion, whereas in the vertical direction the film can expand freely. Our structural characterizations provide therefore an explanation to past reports indicating that the β-phase is not reached upon electrochemical H-insertion into Pd layers thinner than a critical thickness (see literature survey in Introduction). The above uniaxial lattice distortion provides also an explanation to the small compressive stress measured *in situ* (-2 GPa while -9.6 GPa would be expected) [159]. A reduced H-solubility was also reported in *in situ* SXRD studies of $4-16$ ML (0.8 to 3.2 nm) thick Pd/Pt(111) films [157] and in studies of Pd gas phase hydrogenation [170].

The characteristic time constant to saturate a 6 nm-thick Pd film with atomic hydrogen is about $1-2$ s (Fig. 7.8b). It is a bit surprising that it is very close to values found in Ref. [159] for Pd/Au(111) layer in contact with a solution of pH = 1. Theoretically, forming a PdH_x phase, requires the insertion of 4×10^{-8} mol of atomic H per cm^2 for a 6 nm Pd layer and for $x \sim 0.6$ (β-phase). Even though the β-phase is not formed, the above mentioned amount of atomic H requires the reduction of $> 4 \times 10^{-8}$ mol of protons per cm^2 because the electrochemical yield of H-insertion process is below unity (H-insertion is only a side process of HER). The time τ to pass a charge > 4 mC/cm^2 that is necessary to saturate the Pd capping layer may be

estimated using the Cottrell equation $i = \mathrm{nF}C_\mathrm{H}\sqrt{D_\mathrm{H}/(\pi t)}$ where $D_\mathrm{H} \sim 10^{-4}\,\mathrm{cm}^2/\mathrm{s}$ is the proton diffusion coefficient [16] and C_H is the proton concentration ($1.2 \times 10^{-6}\,\mathrm{cm}^{-3}$ in our conditions). Other symbols have their usual significance. Numerically $\tau > 10\,\mathrm{s}$. Therefore mass transport is too slow to explain that H-insertion is completed within $1-2\,\mathrm{s}$. One possibility is that water molecules are dissociating sufficiently quickly at the Pd surface to replenish the adsorbed H monolayer and thereby supply necessary atomic H for bulk insertion. H-UPD takes place and palladium hydrogenation is in fact possible in alkaline solutions [171, 172]. Regarding H-release, application of a potential step (Fig. 7.8c) leads to a longer characteristic time (10 s) than upon H-insertion ($1-2\,\mathrm{s}$). This difference, also observed by others [159], may be attributed to a positive shift of the Nernst potential E_H of the electrochemical hydrogen oxidation reaction $\mathrm{H} \rightarrow \mathrm{H}^+ + \mathrm{e}$, due to the accumulation of protons close to the electrode surface. A positive shift of E_H slows down the electrochemical oxidation of protons.

The limiting mechanism of H-insertion and release is thought to be the phase transition $\alpha \leftrightarrow \beta$ phase [156], and this could account for the structural inhomogeneity discussed below. Our data indeed evidence that the rate of H-insertion and release has an impact on the PdH layer structure. Sweeping slowly the potential to insert hydrogen leads to a delay of $\Delta\varepsilon_{\mathrm{Pd},\parallel}$ with respect to $\Delta\varepsilon_{\mathrm{Pd},\perp}$ in initial stages (Fig. 7.7b). The corresponding local maxima of $\Gamma_{\mathrm{Pd},\parallel}$ (Fig. 7.7c), which may be explained with the existence of two contributions to the Pd peak with very close K positions, is suggesting that the Pd layer is composed of regions with different H-contents at these stages of hydrogenation. At saturation ($U < -0.6\,\mathrm{V}$) the PdH_x layer becomes however homogenous and its structure is rather ordered because $\Gamma_{\mathrm{Pd},\parallel}$ saturates to a lower value. By analogy, the delay between $\Delta\varepsilon_{\mathrm{Pd},\perp}$ and $\Delta\varepsilon_{\mathrm{Pd},\parallel}$ observed in Fig. 7.8c suggests local variations of "x" in the PdH_x phase upon fast H-release. We infer that locally different H-oxidation reaction rates are promoted by spatial variations of E_H in relation to fast accumulation of a large amount of protons close to the electrode surface. H-release by sweeping the potential avoids proton accumulation at the electrode surface and corresponding changes of $\Delta\varepsilon_{\mathrm{Pd},\parallel}$ and $\Delta\varepsilon_{\mathrm{Pd},\perp}$ are well-concerted (Fig. 7.7b). The maximum of $\Gamma_{\mathrm{Pd},\parallel}$ (Fig. 7.7c) suggests however again spatial structural inhomogeneity in latter stages of release.

7.4.3 Transmission of Elastic Strain Between Pd and Co

There is a clear coupling between the in plane strain changes in Pd and in Co (Figs. 7.7-7.8). The strain changes in Pd and Co are concerted upon fast H-insertion (Fig. 7.8b) or slow H-release (Fig. 7.7b). However, as a consequence of the above mentioned anisotropic expansion (in vertical direction) of the Pd lattice, the lateral Co strains variations $\Delta\varepsilon_{\mathrm{Co},\parallel}$ remain very small ($\Delta\varepsilon_{\mathrm{Co},\parallel}$ is 10 times smaller than $\Delta\varepsilon_{\mathrm{Pd},\parallel}$). The strain change is significantly improved within the 3D Co layers, with a progressive increase of $\Delta\varepsilon_{\mathrm{Co},\parallel}$ as one roughens the Co layer (see Fig. 7.8). This is possibly because clamping of the Pd layer is reduced on 3D Co islands, which allows larger lattice expansion as evidenced by the increase of $\Delta\varepsilon_{\mathrm{Pd},\parallel}$ (see vertical bars in inset of Fig. 7.8).

The ratio of $\frac{\Delta\varepsilon_{Co,\parallel}}{\Delta\varepsilon_{Pd,\parallel}}$ is however nearly unchanged, meaning the strain coupling is independent of the cobalt layer morphology.

Looking at the Co Bragg peak FWHM ($\Gamma_{Co,\parallel}$) upon H insertion (Fig. 7.7c) is also instructive. The reversible $\sim 5\,\%$ decrease may plausibly be explained by the difference between the Co Bragg peaks (black line in Fig. 7.6c). A careful examination of Fig. 7.6c shows in fact that upon H insertion in Pd, the Co peak shift is not uniform: the diffracted intensity increases at low K values whereas the contribution at high K values decreases. This suggests that the regions of the Co layer that are less strained (large K values) are affected in the opposite way with respect to region of larger strains (low K values) by the H induced lattice expansion. Therefore a reduction of the strain dispersion occurs upon expanding the Co layer and this may explain the decrease of $\Gamma_{Co,\parallel}$ upon H insertion into Pd. The lateral distribution of strains with the Co layer may come from growth but may be also induced by structural inhomogeneity of the PdH_x film (see discussion in Section 7.4.2).

7.4.4 Voltage Dependence of Magnetic Properties

The data in Fig. 7.2 demonstrate that H_C increases upon H-incorporation into the Pd layer, a behavior that is consistent with past results obtained for sputter-deposited Pd/Co/Pd samples [11, 12]. Let us estimate the changes of the K_{MAE} , originating from the strain in the Co layer (ΔK_{ME}) [134].

$$\Delta K_{ME} = (B_1 + 2B_3)\,\Delta\varepsilon_{Co,\parallel} + B_2\,\Delta\varepsilon_{Co,\perp} \tag{7.1}$$

where the B_i are cobalt magneto-elastic coefficients $B_1 = -0.8\times10^8\,\mathrm{erg/cm^3}$, $B_2 = -2.9\times10^8$ erg/cm^3 and $B_3 = 2.8\times10^8\,\mathrm{erg/cm^3}$ [173]. For the sake of simplicity, we consider that the Co layer is 2D and that the strain in the Co layer is uniform. To estimate ΔK_{ME} we can use the measured strains variations $\Delta\varepsilon_{Co,\parallel} = +0.04\,\%$ (Figs. 7.7 and 7.8a). $\Delta\varepsilon_{Co,\perp}$ could not be accurately determined from the X-ray 2D detector images because the Co diffracted signal yields a broad contribution along L. $\Delta\varepsilon_{Co,\perp}$ may be estimated assuming that (i) the strain coupling between Pd and Co normal to the surface is negligible, and (ii) in an elastic deformation, $\Delta\varepsilon_{Co,\parallel}$ and $\Delta\varepsilon_{Co,\perp}$ are related by the elastic constants c_{13} and c_{33}: $\Delta\varepsilon_{Co,\perp} = -2\left(\frac{c_{13}}{c_{33}}\right)\Delta\varepsilon_{Co,\parallel}$[174]. For hcp Co, $c_{13} = 1.0\times10^{11}\,\mathrm{Pa}$ and $c_{33} = 3.6\times10^{11}\,\mathrm{Pa}$ [175], yielding $\Delta\varepsilon_{Co,\perp} = -0.55\Delta\varepsilon_{Co,\parallel}$. Consequently, we can write $\Delta K_{ME} = 6.4\times10^8\,\Delta\varepsilon_{Co,\parallel} = 2.5\times10^5\,\mathrm{erg/cm^3}$. The value of K_{MAE} of the Co layer may be estimated from Co bulk values and from tabulated interface anisotropy energies [67, 144]. We obtain $K_{MAE} = 5.7\times10^6\,\mathrm{erg/cm^3}$ for a Co thickness of 0.8 nm (4 ML). Consequently, ΔK_{ME} represents about 4.3 % of the estimated total K_{MAE}. From Fig. 7.2c, we obtain relative variations of $\Delta H_C/H_C$ of 26 %. Even though H_C is not directly related to K_{MAE}, its relative variations is a reasonable approximation of the relative changes of $\Delta K_{MAE}/K_{MAE}$ *i.e.*, in this case of the order of 26 %. Consequently, the strain in the Co layer induced by H insertion in the Pd capping layer can account only partly for the modification of K_{MAE}. Another possible

origin of the K_{MAE} change may be the modification of the Co/Pd interface upon H insertion.

7.5 Conclusions

In this work, we have demonstrated that the magnetic properties of the Pd/Co/Au(111) system may be reversibly controlled *via* the applied potential by promoting H-insertion into or release from the Pd capping layer. This might be useful in applications such as magneto-optical sensors. From a structural viewpoint, the Pd and Co lattices are in epitaxy and aligned with respect to each other and with respect to the Au(111) substrate. Different Co morphologies could be deposited and capped with a rather uniform (although not perfectly pinhole-free) Pd layer. The electrochemical insertion of H into the Pd lattice leads to a lattice expansion, which is significantly quenched within the surface plane. In spite of clear coupling of in-plane strains in Co and Pd, the amount of in-plane strain transmitted to the cobalt layer appears too small to account for the enhanced magnetic anisotropy energy upon insertion of atomic hydrogen into the Pd layer. A modification of interface magnetic energy K_S at the Co/Pd boundary must be inferred.

Acknowledgments

This work was partially financed by projects EC + MEC and ELECSPIN (contracts ANR-15-CE30-0024-01 and ANR-16-CE24-0018-04). We thank also the Deutsche Forschungsgemeinschaft for financial support *via* Ma1618/2020. We gratefully acknowledge the European Synchrotron Radiation Facility for providing synchrotron radiation facilities and the ID03 beamline staff, in particular Francesco Carla, for efficient technical support.

8 Transmission Surface Diffraction for *Operando* Studies of Heterogeneous Interfaces

This chapter is based on an article published in the Journal of Physical Chemistry Letters[176].

Abstract

Processes at material interfaces to liquids or to high-pressure gases often involve structural changes that are heterogeneous on the micrometer scale. We present a novel *in situ* X-ray scattering technique that uses high-energy photons and a transmission geometry for atomic-scale studies under these conditions. Transmission surface diffraction gives access to a large fraction of reciprocal space in a single acquisition, allowing direct imaging of the in-plane atomic arrangement at the interface. Experiments with focused X-ray beams enable mapping of these structural properties with micrometer spatial resolution. The potential of this new technique is illustrated by *in situ* studies of electrochemical surface phase transitions and deposition processes.

Understanding atomic-scale processes at condensed matter interfaces is a subject of great interest in material science. Examples include areas of major technological importance, such as electrochemical energy storage and conversion, heterogeneous catalysis, corrosion, lithographic etching, and deposition of thin films and nanostructures, as well as natural processes in geo- and bioscience, e.g., reactions at mineral surfaces and biomineralization. In all these cases a solid material interacts with a liquid or gaseous environment, often leading to complex structural changes at the surface. Those can be studied only by experimental methods that can determine the atomic-scale interface structure *in situ* under ambient conditions. In contrast to studies in an ultrahigh vacuum (UHV) environment where numerous surface science techniques are available, only a few surface-sensitive *in situ* methods exist, most notably high-resolution scanning probe microscopy[177, 178], environmental electron microscopy [179, 180], and synchrotron-based X-ray spectroscopic and scattering techniques [39, 181–192].

In particular, surface X-ray diffraction (SXRD) can provide unsurpassed *in situ* data on the full atomic surface structure of crystalline samples with down to picometer precision [43, 184, 185, 193–200]. Here, an incident X-ray beam, which conventionally impinges under grazing incidence angles on the surface, is scattered by the atomic lattice of the solid (Fig. 8.1A). Because of the broken symmetry at the interface, streaks along the surface normal direction emerge between the Bragg reflections in reciprocal space. The intensity distributions along these crystal truncation rods (CTRs) as well as of corresponding rods caused by two-dimensional (2D) interface structures contain detailed information on the positions of the surface atoms. This allows the determination of the structure of surface reconstructions, layers of adsorbates, or thin films at the interface. Because hard X-rays can deeply penetrate into matter, these methods are easily applicable to interfaces between condensed phases such as liquids and solid materials. Although the intensities of CTRs and 2D adlayer rods are weak (typically 10^{-7} of the substrate Bragg peak intensities), they can be easily measured at synchrotron sources, even with millisecond time resolution[200]. However, in grazing incidence diffraction methods the beam is typically spread out over millimeters of the sample surface along the incident direction. Thus, large single-crystal samples of high surface quality are required and studies of heterogeneous materials are not possible. Furthermore, for a full structure determination at conventional photon energies ($10-20\,\mathrm{keV}$), these measurements typically require time-consuming scans of the sample orientation and detector position.

The latter problem has been overcome with the availability of surface scattering instruments that employ high-brilliance X-ray beams of high photon energy ($40-150\,\mathrm{keV}$) and large 2D detectors [201, 202]. The 2D detector allows the simultaneous collection of the scattering of the sample into a large solid angle. This allows direct imaging of the intensity distribution in reciprocal space on a part of the Ewald sphere. The latter is defined by the locations of the wave vectors $\mathbf{k_f}$ of all scattered beams for a given incident beam direction (defined by a wave vector $\mathbf{k_i}$). At high photon energies the curvature of the Ewald sphere is low and the scattering is located in the near-forward direction. Consequently, the slice through reciprocal space imaged by the

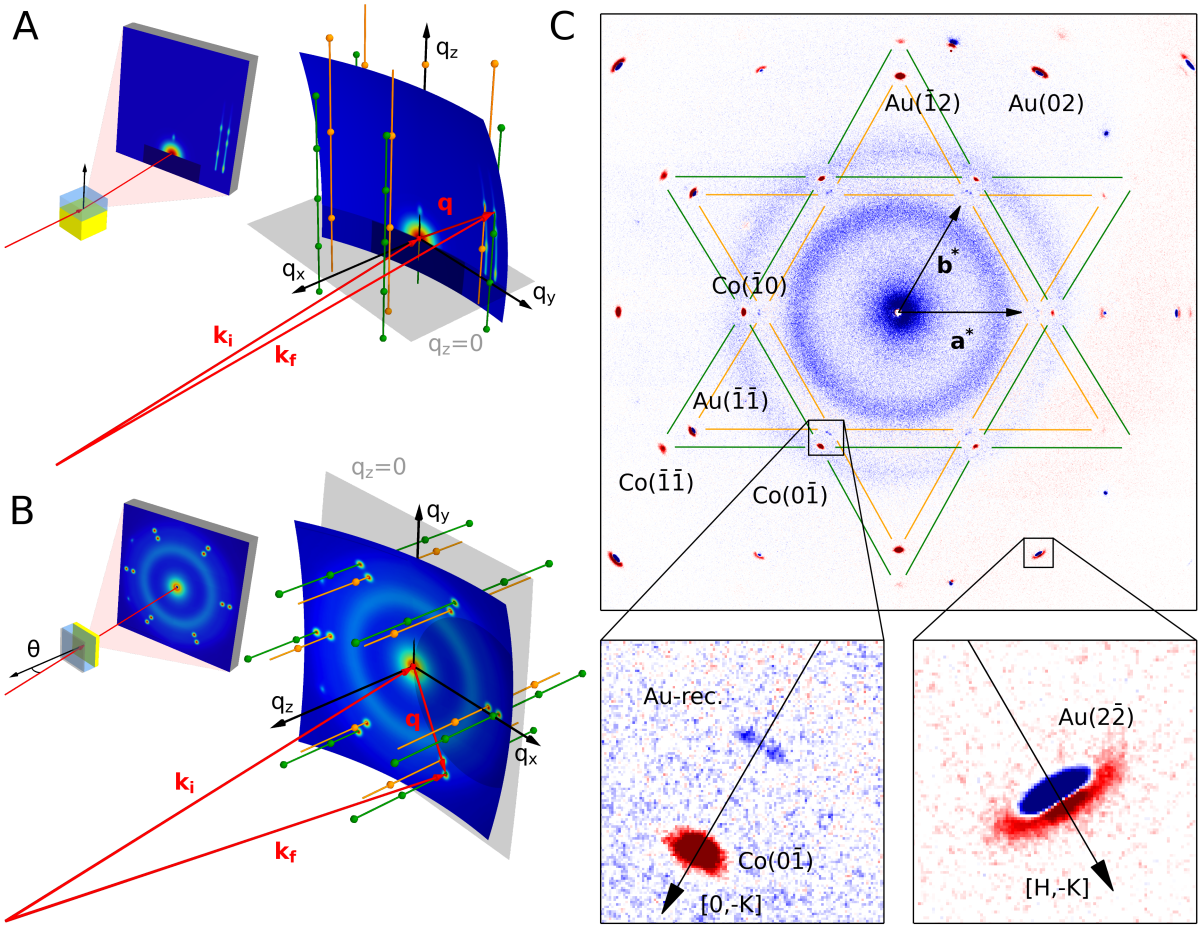

Fig. 8.1: Surface structure determination by TSD. Schematic scattering geometry in real and reciprocal space of (A) grazing incidence surface diffraction and (B) transmission surface diffraction, where the incident beam passes through the sample and adjacent liquid. X-ray diffraction peaks are located at the intersections of the CTRs and adlayer rods with the Ewald sphere. (C) *In situ* TSD of an epitaxial Au(111) thin-film electrode on Si(111) in 0.1 M $NaClO_4$ + 1.3 mM HCl + 1 mM $CoCl_2$, recorded at 40 keV and a tilt angle $\theta = 4.1°$ between surface normal and direct beam. Shown is the intensity difference between detector images of the bare Au substrate at $-0.2\,V_{Ag/AgCl}$ and after electrochemical deposition of a 20 ML thick epitaxial Co(001) film at $-1.05\,V_{Ag/AgCl}$. Sixteen Au CTRs and 12 Co CTRs are visible, with blue colors indicating a decrease and red an increase in intensity after deposition.

detector is nearly planar and a wide range of reciprocal space can be recorded simultaneously. As recently demonstrated in studies of CO oxidation on palladium in the gas phase [202], SXRD at high energies (HESXRD) allows rapid acquisition of the surface structural data and is thus well-suited to *operando* studies under reaction conditions. In that study, the conventional grazing incidence geometry was employed (Fig. 8.1A). This optimizes the scattered intensity from the surface but requires very precise sample alignment at such high photon energies and is highly sensitive to small changes in the beam position on the sample (e.g., due to thermal expansion).

Here we suggest an alternative geometry which we term *in situ* transmission surface diffraction (TSD) in which the incident beam is oriented at or near the surface normal and passes through

the solid sample (Fig. 8.1B). In contrast to grazing incidence scattering methods, the probed surface area is in this case of the size of the beam diameter, which can be focused to micro- or even nanometer dimensions at modern synchrotron sources. This enables studies of the atomic scale interface properties on these length scales. In TSD the Ewald sphere is almost parallel to the interface in the region defined by the detector. This results in sharp X-ray diffraction peaks at intersections with CTRs or 2D adlayer rods, which allows the direct visualization of the symmetry of the in-plane surface lattice. In this respect, the obtained images are similar to those obtained from conventional Bragg peaks (i.e., the bulk crystal structure) in traditional Laue diffraction. Through the recording of images at different tilt angles of the sample relative to the incident beam, or at different photon energies, TSD can access different out-of-plane positions along a diffraction rod, which in principle allows determination of the full in-plane atomic arrangement at the interface. A similar approach was employed by Takahashi and co-workers, who studied the surfaces of micrometer thin Si samples under UHV conditions in transmission geometry using conventional X-ray photon energies[203, 204]. TSD is particularly well-suited for *operando* studies of interface reactions, because it allows direct monitoring of phase formation and of surface phase transitions (e.g., due to adsorption or deposition processes) without lengthy searches in reciprocal space. This is especially valuable if the in-plane surface structure is unknown, in particular in the case of incommensurate phases. In contrast to SXRD at grazing incidence angles, the transmission geometry makes sample alignment fast and easy and drastically reduces any influence of small changes in the beam position on the sample.

To demonstrate the power of *in situ* TSD, we performed studies of electrochemical processes on Au(111) electrodes in aqueous electrolytes. We start by discussing studies with an unfocused X-ray beam to show the general feasibility of such measurements. In Fig. 8.1C an experiment on Co electrodeposition is presented as a first example, illustrating that TSD provides a direct image of the full in-plane structure in reciprocal space. Displayed is the difference in the X-ray intensity measured before and after electrodeposition of an ultrathin Co film. This difference imaging mode not only largely removes static background (e.g., from thermal diffuse scattering of the solid and bulk liquid scattering) but also allows the immediate identification of structural changes due to interface processes, which is intuitive and useful for *operando* studies. In the present case, Co deposition results in the emergence of a hexagonal diffraction pattern, reflecting the formation of an epitaxial (001)-oriented hexagonal close-packed Co film[21, 137]. The same detector images yield simultaneously the CTRs of the thin epitaxial Au film that is used as substrate. They clearly reveal a small outward shift of these CTR peaks, indicating a deposition-induced epitaxial strain of 5×10^{-4}. Furthermore, Co deposition leads to the disappearance of the characteristic twin peaks near the position of the (01) Au CTRs, which can be unambiguously assigned to the Au $(22 \times \sqrt{3})$ surface reconstruction. This provides clear evidence that structural changes of monolayer phases can be accessed; in this case, the deposition induced restructuring of the Au surface layer. As shown by these results, TSD can provide *in situ* data on the atomic-scale interface structure and captures the full in-plane geometry within a single detector image. Thus,

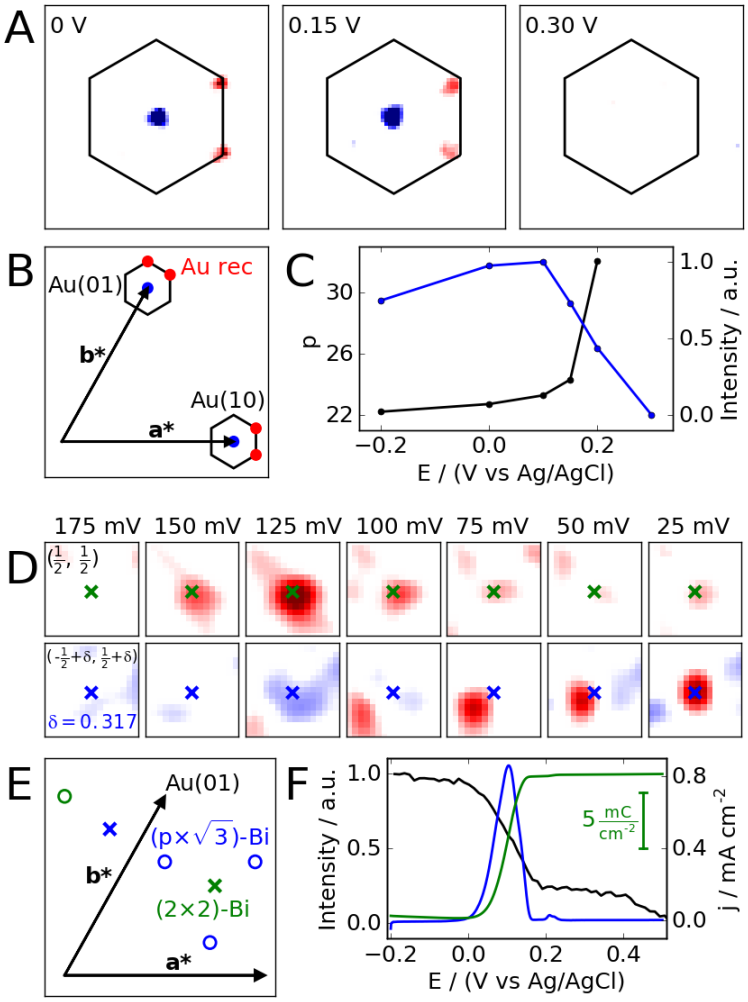

Fig. 8.2: Measurements of surface phase transitions, adsorption, and dissolution processes on Au(111) single-crystal electrodes by *in situ* TSD. (A) TSD difference images (relative to reference image obtained at 0.70 V) in 0.1 M $NaClO_4$ + 0.13 mM HCl of the reciprocal space area near the first-order Au CTR (see scheme in panel B), showing the satellite peaks of the $(p \times \sqrt{3})$ Au surface reconstruction at potentials ≤ 0.20 V. (C) Unit cell length p (black line) and peak intensity of the Au reconstruction (blue line) as a function of potential. (D) TSD measurements (reference image obtained at 0.25 V) and (E) schematic in-plane scattering geometry of the underpotential deposition of a Bi monolayer on Au(111) in 0.1 M $HClO_4$ + 1 mM Bi^{3+}. With decreasing potential, first the peak of the (2×2) Bi adlayer (green symbols) is observed, followed by a transition to the $(p \times \sqrt{3})$ structure (blue symbols), in which the Bi layer is continuously compressed (indicated by the change in peak position). (F) Electrochemical dissolution of a ≈ 30 ML thick Bi film on Au(111) during a positive-going potential sweep at 5 mV/s. The intensity decay of the Bi(110) Bragg peak (black) occurs in parallel to the charge transfer (green) seen in the simultaneously measured current density (blue).

structural changes in different surface phases can be directly correlated. Acquiring a comparable data set by conventional grazing incidence surface diffraction would require sequential radial and azimuthal scans through all relevant peaks and correspondingly longer recording times.

Further proof-of-principle experiments on the potential-dependent changes of the Au surface

reconstruction and other well-known electrochemical surface phase transitions and adsorption phenomena are presented in Fig. 8.2. These demonstrate that TSD is a versatile technique, capable of monitoring structural modifications in single atomic layers with high sensitivity and in different systems. In Fig. 8.2A, difference images of the reciprocal space region near the first-order Au CTR are displayed (recorded in Co-free solution) which clearly show the presence of the characteristic satellite peaks of the Au(111) surface reconstruction at potentials ≤ 0.20 V. In agreement with previous *in situ* SXRD studies[194], the reconstruction peak intensity decays and the unit cell length p increases (indicated by a shift of the peaks toward the Au CTR) near the potential of the phase transition to the unreconstructed surface (Fig. 8.2C). Above 0.20 V the peaks disappear completely and the intensity of the first-order Au CTRs increases (manifesting in a corresponding increase in intensity in the difference image), while subsequent reversal of the potential to negative values restores the diffraction pattern of the reconstructed surface. In similar TSD experiments the structural phase behavior of an adsorbed Bi monolayer formed by underpotential deposition was investigated (Fig. 8.2D,E). With decreasing potential, first a commensurate (2×2) and then a uniaxially incommensurate $(p \times \sqrt{3})$ structure with potential-dependent spacing p were observed, in full agreement with previous results[205]. Furthermore, studies of the electrochemical dissolution of a bulk Bi deposit during a potential scan in the positive direction are shown as an example of a true time-resolved *operando* measurements during an interface reaction (Fig. 8.2F). Here, the decay in Bi peak intensity can be clearly correlated with the parallel electrochemical charge transfer. In this experiment the time resolution was restricted to 1 s, but faster measurements will be easily possible with future instrumental improvements. All measurements shown in Fig. 8.2 were performed on 400 µm thick Au(111) single crystals, which attenuate a 70 keV X-ray beam by about 1 order of magnitude. Taking into account that Au is one of the most strongly absorbing materials, similar TSD studies should be possible for a wide range of different samples, which proves the broad applicability of this technique.

The central advantage of TSD as compared to grazing incidence SXRD, its greatly increased resolution in real space, is demonstrated in Fig. 8.3. Here, TSD with a microfocused X-ray beam was employed for *in situ* mapping of the local structural properties of a Co electrodeposit on an ultrathin epitaxial Au(111) film on Si(111) (Fig. 8.3). In these surface microdiffraction experiments, the atomic-scale structural data come from the diffraction pattern, whereas the beam size defines the area over which these (average) data are obtained. In the experiment in Fig. 8.3, the surface normal of the sample was tilted by 4.1° relative to the incident beam. This allows simultaneous measurements of symmetrically equivalent CTRs at different surface-normal scattering vectors L, providing insight into the deposit's out-of-plane structure (see below). Because all structural data at a specific location are obtained from the same detector frame, they can be unambiguously correlated.

Real space maps of the peak intensity at the Co(100) Bragg peak position [measured at $L = 0$, i.e., at the Co($\bar{1}$0) CTR] reveal that the film thickness strongly varies on the micrometer scale.

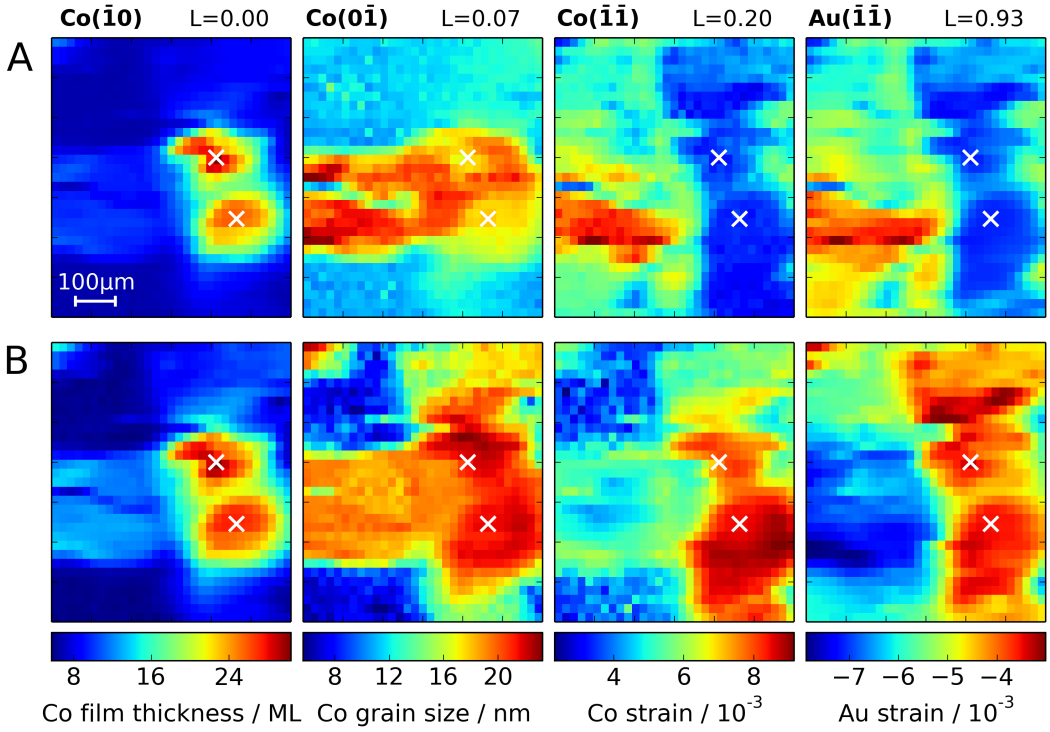

Fig. 8.3: TSD surface microdiffraction studies of Co films on Au(111) in 0.1 M $NaClO_4$ + 1.3 mM HCl, demonstrating mapping of the local structural properties. Local *in situ* real space maps ($600 \times 700\,\mu m^2$) of the surface properties of a Co film electrodeposited on an 8 nm thick epitaxial Au(111) film on Si and measured in Co-free solution at $-1.05\,V_{Ag/AgCl}$ ($10 \times 20\,\mu m^2$ beam, 40 keV, $\theta = 4.1°$). (A) Normalized intensities of selected Co and Au CTRs. (B) Extracted local thickness, in-plane grain size, and strain of the Co deposit as well as strain in the Au thin-film substrate. The data were obtained from a quantitative analysis of the peak intensities, widths, and positions in all of the 961 TSD detector images used for generating the maps.

Specifically, it is significantly increased in two areas (marked by crosses) near the right-hand side of the imaged surface. Maps at higher L values [Co($0\bar{1}$) and Co($\bar{1}\bar{1}$) CTRs] show similar spatial variations, but with a different intensity distribution: the locally enhanced scattering intensity in the marked locations is reduced while at other positions the intensity is increased at higher L values. These changes reflect a spatial dependence of the scattered intensity along L. They originate from the local variations of the Co thickness, which lead to corresponding variations in the Bragg peak width along the surface normal direction. Indeed, this inversion in the intensity maps can be reproduced within a simple model (see the Supporting Information). The obtained local variations in Co film thickness are well-correlated with those in the average Co grain size and strain, obtained from the radial peak width and position, respectively (Fig. 8.3B). According to these results thicker deposits consist of (laterally) larger grains and exhibit extended in-plane lattice distances. The intensity maps of the Au CTRs qualitatively resemble those obtained at related Co CTR positions (compare Co($\bar{1}\bar{1}$) and Au($\bar{1}\bar{1}$) intensities in Fig. 8.3A). Consequently, the substantial variations in the deposition behavior most probably originate from heterogeneities of the Au(111) thin-film substrate that also manifest in the maps of the

Au in-plane strain (Fig. 8.3B, right). Correlation of the Co(100) film thickness with the strain distributions indicates that deposition is preferred in areas where the Co and Au strain, i.e., in-plane lattice spacing, is particularly large. This local growth enhancement may be explained by an increased Co nucleation probability in these areas[206]. As shown by these measurements, microdiffraction in the TSD mode allows simultaneous microscale mapping of multiple structural interface properties of heterogeneous materials, enabling their direct correlation. Maps obtained at symmetrically equivalent reciprocal space positions are almost indistinguishable (see the Supporting Information), verifying that the method is reproducible and robust.

These experiments prove TSD to be a powerful tool for *in situ* and *operando* structural studies of interfaces on the atomic scale. It is an intuitive and robust method that provides full in-plane information. In comparison to surface diffraction under grazing incidence angles, TSD is experimentally less demanding in terms of sample alignment and beam stability, making it accessible also for research groups with limited experience in synchrotron scattering techniques. TSD can be easily combined with a sample cell geometry that provides well-controlled hydrodynamics and thus well-defined rates of the interface reactions, e.g., thin-layer flow cells or microfluidic cells. This will be a huge benefit for *operando* studies of interface kinetics. TSD studies should be possible on a wide range of materials, including air- and moisture-sensitive materials. Particularly suitable samples may be 2D or layered materials, e.g., oxides for energy storage and conversion.

The central advantage of TSD is its suitability for micro- and, with future improvements, even nanodiffraction studies of interface properties. Nanofocusing (to $1 \times 0.3\,\mu m^2$) is currently set up at ID31. It will result in a decrease in X-ray intensity by approximately 1 order of magnitude of the beam, which will already allow measurements at fixed local spots and the recording of small maps. With the upcoming diffraction-limited synchrotron sources, which will provide small, low-divergent sources and orders of magnitude higher brilliance, it should be possible to record extended maps as in Fig. 8.3 within less than 1 h. This is a particularly attractive feature, not only for electrochemical systems, but also for other solid-liquid and solid-gas interfaces. In the future TSD measurements may be employed for studies of heterogeneous interfaces and of materials that exhibit high-quality surfaces only over (sub-) micrometer length scales. This is relevant for a wide range of real-world interface systems, for example, lithographic processes or interface processes at natural materials, and thus opens up many applications of this new technique. A particularly interesting application may be investigations of systems exhibiting strong local variations in interface reactivity, e.g., spatiotemporal dynamic behavior[207]. In addition, studies that employ local excitations, such as ultrafast scattering experiments of interface processes induced by laser pulses, will benefit from the small probed surface area. For static heterogeneous samples, full structural information (i.e., acquisition of complete CTRs) may be obtained in tomographic measurements, where TSD images are recorded at different sample tilt angles. In the long-term, even a TSD-based imaging technique (similar to low-energy electron microscopy) or a combination with coherent diffraction techniques seem feasible. Ongoing developments

toward even brighter sources of hard X-rays will greatly assist this development.

Acknowledgements

The authors gratefully acknowledge financial support by the Deutsche Forschungsgemeinschaft via MA1618/13-5 and MA1618/20-1 and thank the ID31 staff for technical support.

8.1 Supporting Information

8.1.1 Materials and Methods

The X-ray surface diffraction studies were performed at the high photon energy beamline ID31 of the ESRF, devoted to buried interfaces studies. The X-ray beam from an undulator source was monochromatized by a multilayer monochromator and focused by a set of X-ray lenses. Photon energies of 40 to 70 keV were employed. The irradiated area on the sample was $0.5\,\mathrm{mm} \times 0.5\,\mathrm{mm}$ for a parallel and $10\,\mu\mathrm{m} \times 20\,\mu\mathrm{m}$ for a focused beam, respectively. TSD images were recorded with a large-area Perkin-Elmer 2D detector, placed at a distance of 0.745 m behind the sample, or with a Pilatus 3 X CdTe detector placed at 1.25 m distance.

The cell (Fig. 8.4) was made of PCTFE. The sample and a 0.15 mm thick microscope cover glass served as windows for the incoming and outgoing X-ray beam and were sealed with FFPM O-rings. In the TSD experiments, the X-ray beam passed through the solid sample, 4 mm of electrolyte solution, and the glass window of the electrochemical cell. The cell can be mounted either with the sample or with the glas window towards the incident beam, i.e., with the beam either entering or leaving the cell through the sample. Both orientations were employed in the measurements with similar results. The cell was connected to a liquid handling system for remote-controlled electrolyte exchange, consisting of syringe pumps and motor-driven valves. A Ag/AgCl (3M KCl) reference electrode was connected to the electrolyte inlet via a salt bridge. A Pt wire counter electrode was placed in the electrolyte outlet. Potentials were controlled by a potentiostat (CompactStat, Ivium).

The Au thin film sample consisted of a $11\,\mathrm{mm} \times 11\,\mathrm{mm} \times 0.5\,\mathrm{mm}$ Si(111) wafer with an 8 nm thick epitaxial Au(111) film, electrochemically deposited according to the procedure described in Ref. [162]. These films are aligned with the Si substrate and exhibit large atomically flat terraces. Prior to the experiments, the samples were cleaned by placing them in cold peroxymonosulfuric acid (95 % H_2SO_4 and 30 % H_2O_2 with a ratio of 2:1) for 1 min. The Au(111) single crystal was purchased from Surface Preparation Laboratory (SPL), had a diameter and thickness of 10 and 2 mm, respectively, was oriented better than 0.1°, and polished down to 0.03 µm roughness. In the center of the sample a 4 mm diameter bore hole was machined from the back side, leaving only a 400 µm Au membrane, through which the beam passed in the TSD measurements. The

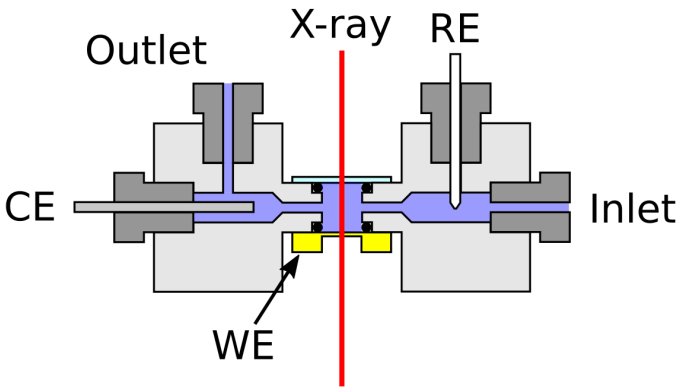

Fig. 8.4: Geometry of the TSD sample cell.

single crystal sample was first sputtered and annealed in a vacuum system and then prepared prior to each experiment by 30 min annealing in an induction oven at light orange glow.

Base solution for the studies was 0.1 M $NaClO_4$ + 1.3 mM HCl, prepared from high-purity $NaClO_4$ (Sigma, puriss.), HCl (Carlo Erba, for electronic use), and Milli-Q water. The Co films were deposited from 0.1 M $NaClO_4$ + 1.3 mM HCl containing 1 mM $CoCl_2$ (Merck, pro analysis). After Co deposition, the electrolyte was replaced within 1 min with Co-free base solution to stabilize the deposit. Bi deposition was performed in 0.1 M $HClO_4$ + 1 mM Bi_2O_3.

8.1.2 Scattering Geometry and TSD Measurements

The tilt angles θ and φ of the surface normal to the incident beam were varied by the sample stage of the ID31 diffractometer; an additional rotation stage directly underneath the sample cell

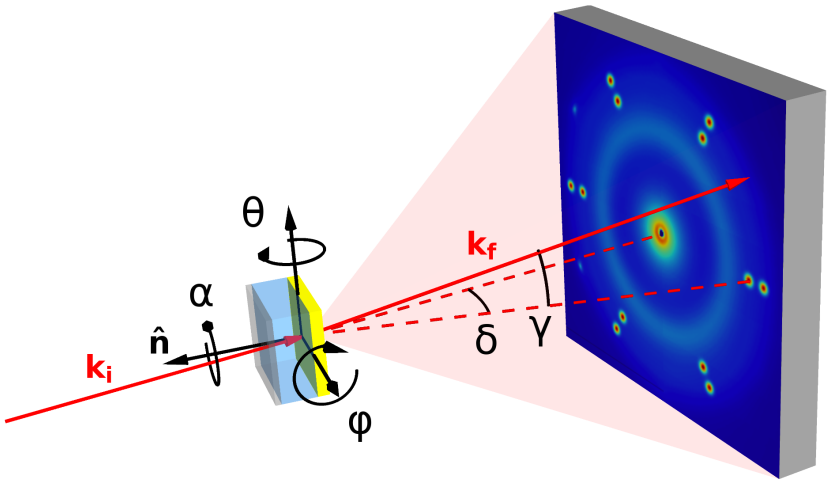

Fig. 8.5: Schematic illustration of the coordinate system employed in the TSD measurements. The diffractometer rotation angles (θ, φ, α) define the sample orientation with respect to the incident beam. The surface normal vector $\hat{\boldsymbol{n}}$ is antiparallel to the incident beam when $\theta = \varphi = 0$. γ and δ define the direction of the scattered beam.

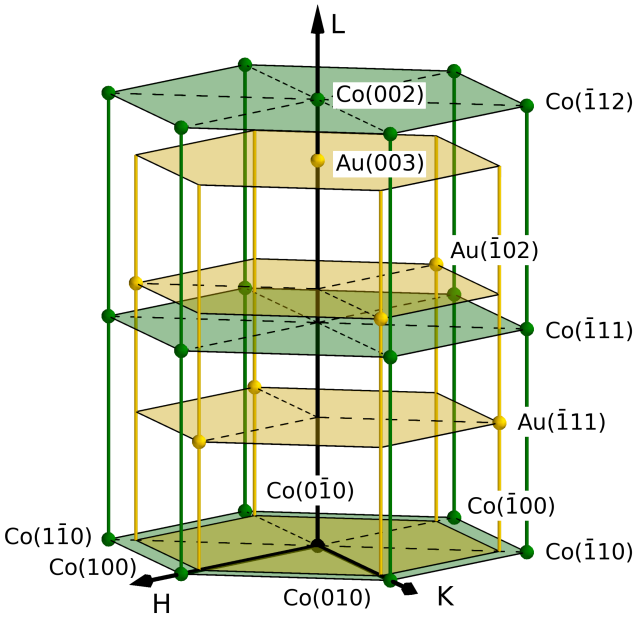

Fig. 8.6: Reciprocal space geometry showing the CTRs and Bragg reflections of the Au(111) substrate and of the epitaxial hcp Co film.

allowed rotation by an angle α around the surface normal direction (see Fig. 8.5). Each pixel on the 2D detector corresponds to an orientation of the scattered beam described by two angles δ and γ, which are the angles between $\mathbf{k_f}$ and the incident beam direction in the vertical and the horizontal plane, respectively.

For indexing the gold Bragg reflections and CTRs, the hexagonal reciprocal coordinate system of the Au(111) substrate [194] with reciprocal lattice vectors

$$|\boldsymbol{a}^*| = |\boldsymbol{b}^*| = 4\pi/\sqrt{3}\,a_{\mathrm{NN}}$$
$$|\boldsymbol{c}^*| = 2\pi/\sqrt{6}\,a_{\mathrm{NN}}$$

was used, where $\boldsymbol{a}^*$ and $\boldsymbol{b}^*$ are in the surface plane, $\boldsymbol{c}^*$ is along the surface normal direction, and $a_{\mathrm{NN}} = 4.08/\sqrt{2}\,\text{Å}$ is the spacing between neighboring Au atoms. For cobalt, the conventional hcp reciprocal lattice with

$$|\boldsymbol{a}^*| = |\boldsymbol{b}^*| = 4\pi/\sqrt{3}\,a_{\mathrm{Co}}$$
$$|\boldsymbol{c}^*| = 2\pi/c_{\mathrm{Co}}$$

and the Co lattice parameters $a_{\mathrm{Co}} = 2.51\,\text{Å}$ and $c_{\mathrm{Co}} = 4.07\,\text{Å}$ was employed. These reciprocal lattice vectors define the units of the coordinates (H, K, L) used for denoting the Au and Co peaks, respectively. For both lattices, H and K refer to the in-plane and L refers to the out-of-plane direction. A schematic illustration of the hexagonal coordinate system with positions of the Bragg peaks from bulk fcc Au and hcp Co is given in Fig. 8.6.

During sample alignment the sample rotation angle α was adjusted in such a way that the a^*_{Au} axis was oriented precisely along the horizontal direction. Then the sample was rotated around the horizontal axis in order to set the tilt angle φ in such a way that the beam impinged at normal incident onto the sample. By rotating the sample around the vertical axis, the zero position of the θ angle was determined. Because the TSD geometry was not yet implemented in the SPEC program used for controlling the diffractometer at the time of the experiment, a separate software package had been developed that allows simulation of the TSD images. This software was used for guiding the sample adjustment and fast identification of the observed peaks. Since this software did not replace a full orientation matrix of the diffractometer geometry, only θ was changed during the experiments after the alignment was finished.

8.1.3 TSD Microdiffraction Measurements

The maps were created by moving the sample with respect to the beam in a grid-like fashion and recording a TSD image at each point on the grid. A focused beam (10 µm × 20 µm beam, 40 keV, $\theta = 4.1°$) was used to sample an area of 600 µm × 700 µm by taking 31 × 31 images with an integration time of 3 seconds. In order to fit the peaks, automated fitting routines were used since fitting more than 10 peaks on 961 images individually would have been too time

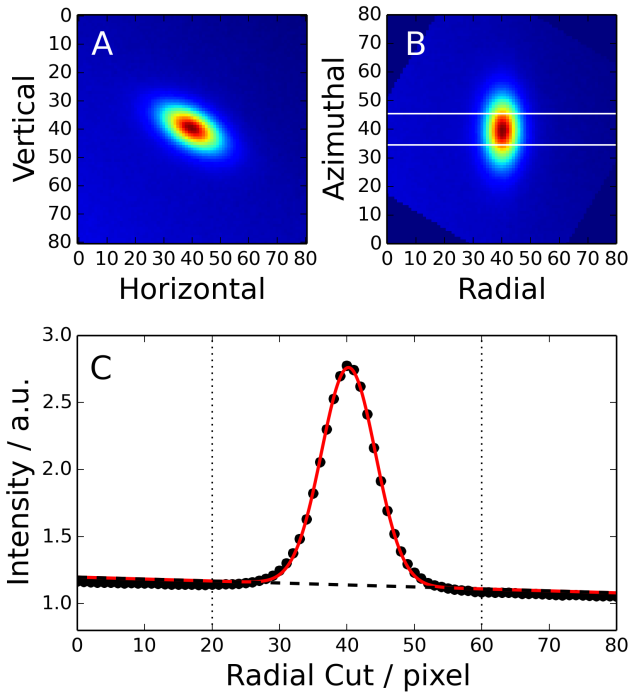

Fig. 8.7: Example of automated peak fitting (Au(02) CTR). (A) A square cutout of the detector image centered on the peak is taken and rotated so that the radial direction is collinear with the horizontal image axis (B). A radial cut (C) is obtained by integrating the image along the azimuthal direction in the region marked by white lines in B. The latter is fitted with a Gaussian profile and a linear background in the region marked by dotted lines.

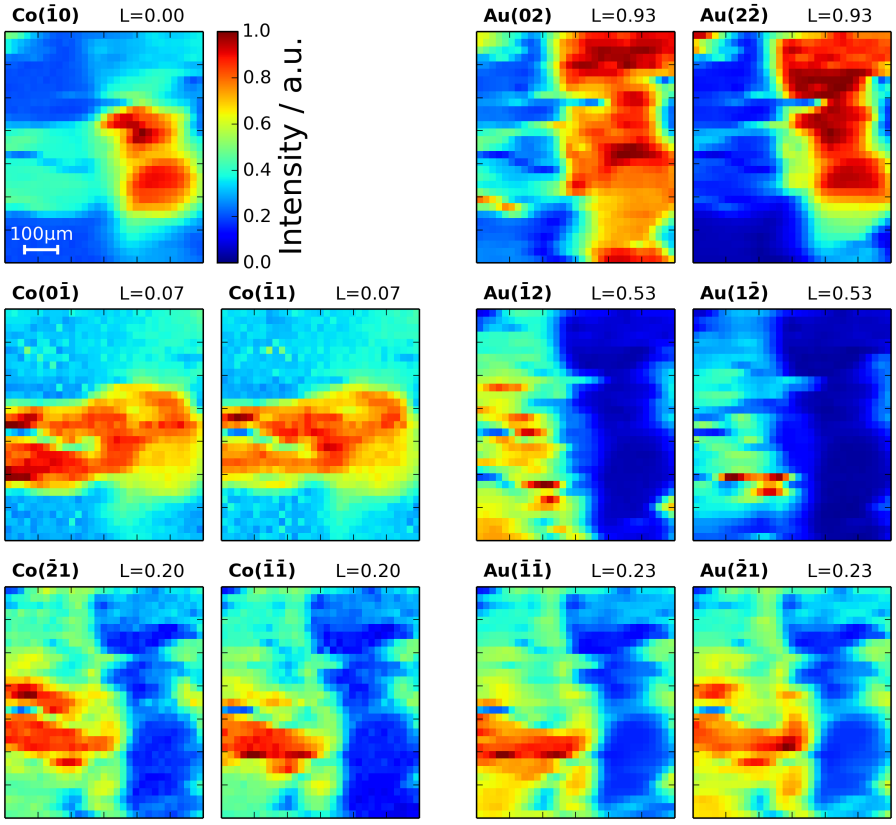

Fig. 8.8: Real space maps obtained by TSD microdiffraction, showing the integrated intensities of 5 Co peaks and 6 Au CTRs. Maps of symmetrically equivalent peaks (Co($0\bar{1}$) and Co($\bar{1}1$), Co($\bar{2}1$) and Co($\bar{1}\bar{1}$), Au(02) and Au($2\bar{2}$), Au($\bar{1}2$) and Au($1\bar{2}$), Au($\bar{1}\bar{1}$) and Au($\bar{2}1$), respectively) exhibit very similar intensity distributions. The intensity values were normalized and plotted using the same color map ranging from 0 to 1 for all maps.

consuming. Both, the Au peaks of the thin film sample and the Co peaks are broadened in the azimuthal direction due to the in-plane angular distribution and finite size of the crystallites. The peak width in radial direction is only affected by the crystal size distribution and was used for determining the average in-plane size of the crystallites. In order to simplify and speed up the fitting, first the TSD image was reduced to a square cutout centered on the peak (Fig. 8.7A). The cutout was then rotated so that the radial direction was collinear with the horizontal axis of the image (Fig. 8.7B). The intensities of the resulting image were integrated in vertical direction over an 11 pixels wide strip centered on the peak (indicated by white lines in Fig. 8.7B), resulting in a one-dimensional radial cut (Fig. 8.7C). The peak and background in this cut were then fitted with a Gaussian profile and a linear background. A similar cut was taken for the azimuthal direction and fitted as well. The fit quality was checked by plotting maps of χ^2 and by more detailed inspections of the fit quality at selected pixels.

In the intensity maps (Fig. 8.3A and Fig. 8.8), the height of the Gaussian profiles is plotted. The intensity was normalized to the highest intensity of each individual map. In Fig. 8.8, 2 pairs of symmetrically equivalent Co peaks (Co($0\bar{1}$) and Co($\bar{1}1$), Co($\bar{2}1$) and Co($\bar{1}\bar{1}$)) and 3 pairs

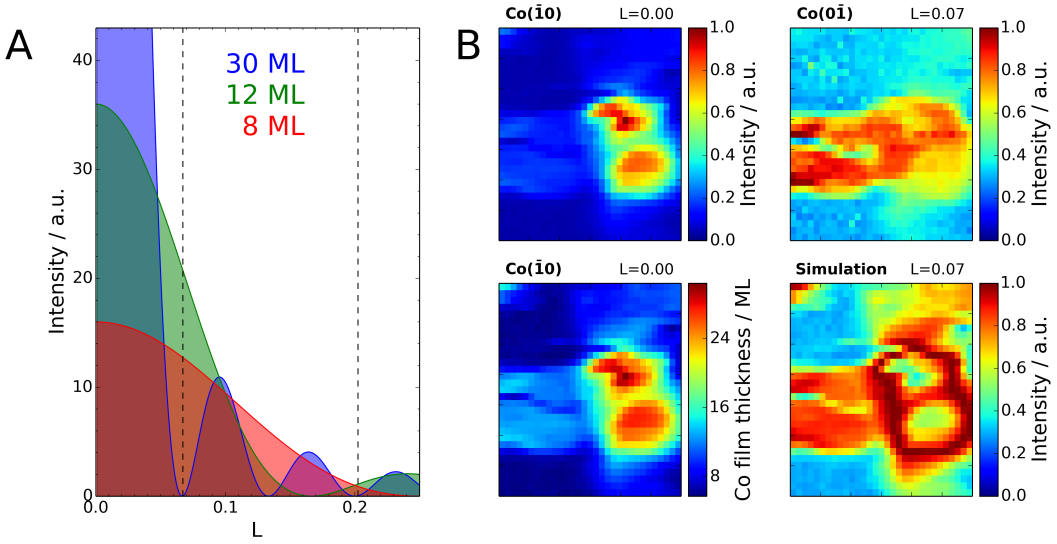

Fig. 8.9: (A) L dependence of the intensity along the Co CTRs for different Co film thickness, calculated using the N-slit scattering function. (B) Measured intensity of the Co CTRs at $L = 0$ and $L = 0.07$ (top panel), Co film thickness calculated from the intensity at $L = 0$ (bottom, left), and simulated intensity map at $L = 0.07$, obtained from the local Co thickness assuming a Gaussian intensity profile of the Co peak along L (bottom, right).

of symmetrically equivalent Au peaks (Au(02) and Au(2$\bar{2}$), Au($\bar{1}$2) and Au(1$\bar{2}$), Au($\bar{1}\bar{1}$) and Au($\bar{2}$1)) are shown. Maps created from different but symmetrically equivalent peaks exhibit very similar intensity distributions. Even some small structural details of only a few pixels in size are reproduced, providing confidence in the reliability of this method. Maps obtained at different positions along L show very different intensity distributions. Nevertheless, the characteristic structural features of the sample can clearly be identified in all of the maps.

The large differences in the intensity distributions of the Co peaks, obtained at different L values, can be understood within a simple model that takes the finite thickness of the Co film into account. Here we describe the intensity distribution along L by the N-slit scattering function (see Fig. 8.9A). Directly on the Bragg peak, the intensity $I \propto N^2$, where N is the number of Co bilayers. At higher values of L, the intensity is not proportional to the film thickness, but exhibits a complex dependence on N, determined by the N-slit function. Specifically, thicker films (i.e., larger N values) will result in a steeper decay in the wings of the Bragg peaks. This analysis is complicated by the given height distribution of the Co thin film. Even in the microdiffraction mode still approximately 10^6 Co crystallites are illuminated at each pixel position. Thus the measured intensity originates from the incoherent superposition of X-rays scattered from crystallites with an unknown distribution of heights. This effect will effectively wash out the subsidiary maxima and makes the analysis of data far away from the Bragg peaks unreliable in the absence of measurements at a larger number of L values. However, near the Bragg peak the effect of the finite crystal height can be approximated by assuming a Gaussian intensity profile $I(L) \propto N^2 \exp(-L^2/2\sigma_L^2)$ with a width given by $\sigma_L = 1/(2\sqrt{2\ln 2}N)$. This is

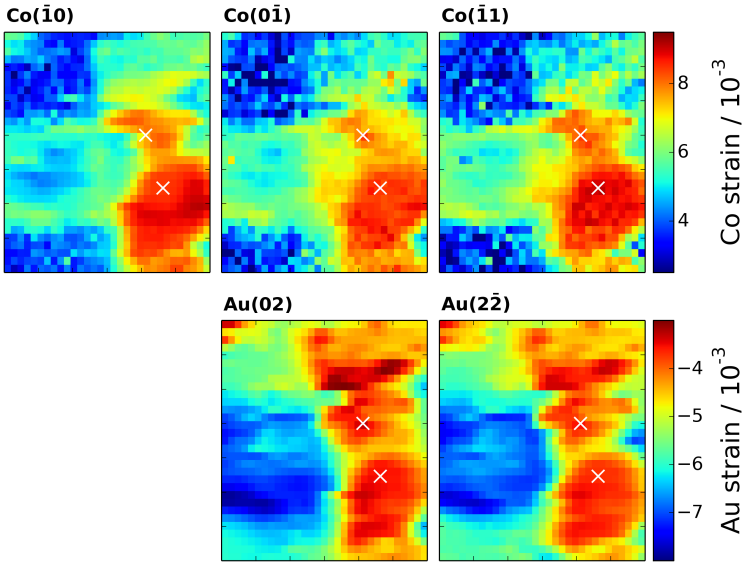

Fig. 8.10: Real space maps obtained by TSD microdiffraction, showing the Co and Au strain obtained from different peaks. The strain obtained from the symmetrically equivalent peaks is identical.

illustrated in Fig. 8.9B, where this procedure was used to calculate the intensity at $L = 0.07$ (i.e., at the $(\bar{1}0)$ CTR). Here, N was determined by taking the root of the Co(100) peak intensity measured at $L = 0$ (i.e., at the $(0\bar{1})$ CTR). The good qualitative agreement between the measured and simulated images provides strong support for our hypothesis that the differences in the intensity distributions originate from the variations in Co film thickness.

The Co grain size $\xi_{\|}$ (Fig. 8.3B) was determined by the FWHM (in units of Å^{-1}) of the Co$(\bar{1}0)$ peak in radial direction with $\xi_{\|} = \frac{2\pi}{FWHM}$. Here, the width has to be measured directly at the Bragg peak, because the peak broadens at higher values of L due to the miscut of the sample. The strain maps (Fig. 8.3B) were calculated from the radial positions of the Co and Au peaks via:

$$\varepsilon_{\|} = \frac{a - a_{bulk}}{a_{bulk}} = \frac{\frac{4\pi}{\sqrt{3}a^*} - a_{bulk}}{a_{bulk}},$$

where a^* is equal to the in-plane position $q_{\|}$ of the Co$(\bar{1}00)$ peak or half of the in-plane position of the Au(020) peak, respectively. The determination of $q_{\|}$ requires the knowledge of the exact origin in reciprocal space, i.e., the position where $q_{\|} = 0$ (the position where the direct beam hits the detector). Furthermore, misalignment in both α or θ shifts the peaks with respect to the zero position and therefore has to be compensated for. In the case of the Co strain, the zero position was determined from the positions of the symmetrically equivalent Co$(\bar{1}00)$, Co$(\bar{1}10)$, and Co$(0\bar{1}0)$ peaks. The Au strain obtained from the Au(020) peak position was determined in a similar way. Here, the Au(020) and the Au$(2\bar{2}0)$ peaks were used to determine the zero position and to compensate for misalignment. Fig. 8.10 shows the strain maps obtained from the 3 Co and 2 Au peaks mentioned above. The maps obtained from symmetrically equivalent peaks show an identical strain distribution for both Co and Au.

8.1.4 *In Situ* TSD Studies of Au(111) Surface Reconstruction and Bi UPD

The potential-dependent surface reconstruction of Au(111) electrodes is a well-known model system that has been extensively studied by X-ray surface scattering under grazing incidence angles [113, 194] and thus is highly suitable to demonstrate the true surface sensitivity of TSD. This surface reconstruction is characterized by a $(p \times \sqrt{3})$ unit cell with $p \approx 22$ for a well-ordered reconstructed surface. The corresponding in-plane superstructure in reciprocal space is a hexagon of satellite peaks around the Au CTRs, of which typically only the two outer ones are clearly visible (Fig. 8.2A,B). In electrochemical environment this structure is stable negative of a critical potential to an unreconstructed (1×1) surface. Near the phase transition the onset of the lifting of the reconstruction leads to a gradual increase of the unit cell length p, manifesting in a reduced distance to the Au CTR.

TSD studies of the Au(111) reconstruction were performed on Au single crystals in 0.1 M $NaClO_4$ + 0.13 mM HCl with a parallel beam of cross-section 0.5 mm × 0.5 mm and with a photon energy of 70 keV. First, a reference image with a counting time of 300 s was taken at $E = 0.70$ V, where the Au surface is unreconstructed. TSD images were then recorded for $E = -0.20$ V and 0 V with a counting time of 300 s, and for $E = 0.10$ V, 0.15 V, 0.20 V and 0.30 V with a counting time of 100 s. The reference image was subtracted from each of these images, resulting in a series of background-subtracted difference images which were used for further analysis. This procedure helps significantly in improving the signal-to-noise ratio, because the intensity of the Au reconstruction peaks is only 10 % of the random intensity variations caused by the imperfect linearity of the detector pixels. A similar data analysis as described in section 3 was employed. For each potential, the six first-order Au CTRs were identified on the respective image, and cutouts centered on them were taken. Each of these cutouts was then rotated so that the (H,K) vector of the respective CTR was parallel to the horizontal image axis. The average of these six cutouts therefore combines information obtained from two symmetrically equivalent triples of Au CTRs. For the images shown in Fig. 8.2A, Gaussian blurring with a sigma of 1×1 pixels was applied to improve visibility of the peaks.

For determining the stripe separation p and intensity of the $(p \times \sqrt{3})$ reconstruction shown in Fig. 8.2C, the intensity along a line from the Au CTR to the reconstruction peak was averaged over all 12 symmetrically equivalent reconstruction peaks in the image (6 first-order Au CTRs with 2 visible reconstruction peaks each). The average reconstruction peak intensity and the average stripe separation $= \frac{\sqrt{3}}{2\delta}$, where δ is the distance between the CTR and the reconstruction peak, were then plotted as a function of potential.

Employing this methodology, also studies of Bi underpotential deposition (UPD) were performed in 0.1 M $HClO_4$ + 1 mM Bi^{3+} on the same sample. In these experiments the potential was changed stepwise in negative direction, starting at 0.5 V. Within this process a sequence of ordered Bi monolayer phases is found [205]. With decreasing potential, first adlayer rods at $(\frac{1}{2}H\ \frac{1}{2}K)$ are observed, indicating a (2×2) superstructure. Then, at more negative potentials, a

phase transition to the uniaxially-incommensurate ($p \times \sqrt{3}$) Bi adlayer structure occurs, with lowest-order in-plane peaks at $(-\frac{1}{2}+\delta, \frac{1}{2}+\delta)$ and $(2\delta, 2\delta)$. The parameter $\delta = \frac{1}{2}p$ depends on potential, with $\delta = 0.317$ close to the onset of Bi bulk deposition. All these Bi adlayer peaks are observed at corresponding potentials in the TSD data, as visualized for the peaks at 2 selected reciprocal space positions in Fig. 8.2D. At potentials negative of the Nernst potential Bragg peaks of a Bi bulk deposit are found, which can be assigned to Bi(110) reflections (using the rhombohedral Bi unit cell) that are located in the surface plane. This is in agreement with the epitaxial arrangement reported in previous ex-situ XRD studies [208]. In the experiment in Fig. 8.2F such a Bi bulk deposit was stabilized at ≈ 30 ML thickness by exchange with Bi-free base solution. Subsequently, the film was electrochemically dissolved by sweeping the potential at 5 mV/s from -0.20 to 0.50 V. Because the Bi bulk reflections are strong compared to the scattering from the UPD monolayer, peak intensities where determined directly from (background-corrected) detector images without subtraction of a reference image.

9 Conclusions

In this work thin epitaxial films of electrodeposited metals and metal oxides were investigated by *in situ* and *operando* SXRD. The combination of electrochemical studies with advanced SXRD techniques and optical reflectivity enabled an unambiguous correlation of the electrochemical processes with structural modifications of the reactive interfaces. While SXRD is commonly employed for the investigation of well-defined interfaces like those found on single crystals, we focused on the interfaces of thin films deposited on single crystal substrates. Although being less well-defined, these films more closely resemble surfaces of technological relevance. Due to their rougher and more heterogeneous nature, the modelling of the crystal truncation rods is often not possible, which complicates the structural characterization. In the presented studies we explored how a detailed analysis of the thin film Bragg peaks can be applied to determine the film structure, regardless. Besides the crystalline structure, which is readily determined from the position of the Bragg peaks, their widths and shape also contain information about the crystallite dimensions and the morphology of the film. Complementing the detailed structural analysis, we developed a strategy to obtain structural data from a single detector frame, by making use of the full 2D image. With this method, even small changes in the crystallite size and the strain of a known phase can be monitored with a time resolution of 1 s.

For the investigation of complex electrochemical interfaces, we developed an advanced electrochemical SXRD cell which possesses a high stability enabling operation for tens of hours. With this cell, *operando* measurements, even under the extreme conditions of large current densities and massive gas evolution during water splitting, were shown to be feasible. The cell permits fast and efficient exchange of electrolytes which greatly simplifies complicated electrochemical experiments, such as multi-stage deposition.

The main focus of the investigations presented in this work was placed on Co oxides as promising candidates for the precious-metal-free catalysis of the OER. In the process of determining a suitable preparation method of thin epitaxial oxide films, the anodic oxidation of Co was studied. Co was electrodeposited on Au(111) electrodes resulting in epitaxial films with a (001) orientation, a thickness of a few nanometer and a lateral size of $20-30\,\mathrm{nm}$. The subsequent anodic oxidation commences with the adsorption of OH. At higher potential $Co(OH)_2$ formation begins with the rapid formation of an ultra thin passive layer on the entire Co surface. Subsequently, $Co(OH)_2$ grows inhomogeneously on the surface forming 3D crystallites. The anodic oxidation of Co to higher oxidation states, which are present during OER, did not result in films which we could detect by SXRD. The formed oxide films are very thin and the large lattice mismatch of Co and its oxides likely prevents the formation of well ordered epitaxial films which complicated their detection by X-ray diffraction.

Therefore, thin epitaxial films of Co_3O_4 and CoOOH were directly electrodeposited on

Au(111) for the investigations during OER. The films were deposited in a reflux cell, where a concentration of 2 M and 5 M NaOH in the solution resulted in Co_3O_4 and CoOOH phases, respectively. After transfer to the novel *operando* SXRD cell, the film structures were investigated as a function of potential deep into the OER regime (up to 150 mA cm^{-2}). The morphology of the films is quite different. CoOOH forms a continuous flat layer with tight grain boundaries and a roughness factor of 1.02. Co_3O_4 exhibits a granular structure with detached islands with a rough surface and a roughness factor of ≈ 3. The structure of CoOOH remains stable even at high OER current densities. Co_3O_4 on the other hand forms a skin layer of ≈ 1 nm. The formation of this skin layer is fast, highly reversible and commences 300 mV negative of the onset of OER. It is therefore rather related to the thermodynamically predicted oxidation to CoOOH than to the OER. The thickness of the film increases linearly with the applied potential, similar to the passive film formation on metals. Additionally, a reversible change in the bulk lattice constants, which could be associated with the reversible creation and annihilation of a high density of volume stoichiometric defects, was observed over a large potential range. Further work is required for the confirmation of this hypothesis and the determination of the defects source and nature. Even though the structural behaviour of the two films is completely different, their catalytic activity is similar. This suggests that the surface density of OER active sites is comparable. This observation disagrees with previous assumptions that di-μ-oxo bridged Co cations are solely responsible for the OER activity of Co oxides.

Beyond its application in catalysis, Co also possesses interesting magnetic properties. Therefore, magnetic Pd/Co/Au(111) stacks were investigated in electrochemical environment. *In situ* MOKE measurements by our collaborators showed a reversible modification of the Co magnetic properties upon the electrochemical hydrogen absorption in and release out of the Pd capping layer. An *in situ* structural characterization using SXRD was employed to identify the origin of the observed changes. Thin films of Co(001)/Au(111) were deposited by the same procedure used for the oxidation experiments to grow flat films, and a slightly modified procedure to grow rougher films. Subsequently, Pd deposition resulted in a thin epitaxial capping layer with (111) orientation. The lattice expansion of Pd upon H-insertion/removal could be clearly identified, showing changes in the lattice parameters in the out-of-plane direction which were about ten times larger than in the in-plane direction. This was explained by clamping to the underlying Co substrate which is in agreement with the observation that the magnitude of the changes were larger for rougher films. The lattice expansion/contraction of Pd induced a small change in the Co in-plane strain which was about ten times smaller than the change in the Pd in-plane strain. Despite the clear coupling of the strain, the magnitude appeared to be too small to account for the full changes observed in the magnetic anisotropy.

Furthermore, transmission surface diffraction (TSD), a novel high-energy SXRD technique, was developed. TSD uses a transmission geometry rather than a reflection geometry which is commonly employed for surface scattering. Several advantages arising from this geometry were demonstrated. Since the beam penetrates the sample, a large 2D detector can be placed behind

the sample which captures a significant fraction of the in-plane structure in a single acquisition. This simplifies the detection of crystal truncation rods from unknown structures, for example surface reconstructions. Multiple structures can be monitored simultaneously since CTRs of the whole sample are present in the same frame. The interpretation of the detector images is straight forward, since symmetries can be easily identified. In this respect, TSD is reminiscent of LEED. Due to the normal (or near normal) incidence of the X-ray beam, the beam footprint is comparable to the cross section of the beam. Therefore, spatially resolved measurements are possible, which enables the creation of real-space maps of the structural properties like strain and film thickness. Further work is required to make this new technique more user friendly. Although the sample alignment for TSD is easy, the implementation of an orientation matrix would significantly facilitate the navigation in reciprocal space. A further improvement would be the realization of an automated absorber positioning system, which would greatly speed up measurements in which the sample has to be tilted, for example the recording of CTRs.

Our studies show that the structural characterization under operation conditions is essential for interfaces at which reactive processes occur. We demonstrated that advanced *in situ* and *operando* SXRD methods are well suited for the investigation of such systems. SXRD offers high precision and an excellent time resolution in the order of seconds. The combination of our novel electrochemical cell with advanced Bragg peak analysis is a powerful tool which enables measurements under extreme conditions such as large current densities and massive gas evolution. The methods developed in this work can be applied to a variety of reactive interfaces to determination the correlation between reactive processes and the structure of the interfaces at which they occur. Especially research in the fields of catalysis, batteries and supercapacitors, where the interfaces are often complex and devices are operated in experimentally demanding conditions, can greatly benefit from these structural characterization methods.

Bibliography

[1] J. A. Turner. Sustainable Hydrogen Production. *Science* **305** (2004), 972.

[2] P. J. Hall and E. J. Bain. Energy-storage technologies and electricity generation. *Energy Policy* **36** (2008), 4352.

[3] P. Denholm, E. Ela, B. Kirby, M. Milligan, P. Denholm, E. Ela, B. Kirby, and M. Milligan. The Role of Energy Storage with Renewable Electricity Generation. *NREL Technical Report* (2010).

[4] G. W. Crabtree, M. S. Dresselhaus, and M. V. Buchanan. The Hydrogen Economy. *Physics Today* (2004), 39.

[5] J. Ohi. Hydrogen energy cycle: An overview. *Journal of Materials Research* **20** (2005), 3180.

[6] H. Dau, C. Limberg, T. Reier, M. Risch, and S. Roggan. The Mechanism of Water Oxidation: From Electrolysis via Homogeneous to Biological Catalysis. *ChemCatChem* **2** (2010), 724.

[7] I. Katsounaros, S. Cherevko, A. R. Zeradjanin, and K. J. J. Mayrhofer. Oxygen Electrochemistry as a Cornerstone for Sustainable Energy Conversion. *Angewandte Chemie International Edition* **53** (2014), 102.

[8] R. Frydendal, E. A. Paoli, B. P. Knudsen, B. Wickman, P. Malacrida, I. E. L. Stephens, and I. Chorkendorff. Benchmarking the Stability of Oxygen Evolution Reaction Catalysts: The Importance of Monitoring Mass Losses. *ChemElectroChem* **1** (2014), 2075.

[9] E. Fabbri, A. Habereder, K. Waltar, R. Kötz, and T. Schmidt. Developments and perspectives of oxide-based catalysts for the oxygen evolution reaction. *Catalysis Science & Technology* **4** (2014), 3800.

[10] R. L. Doyle and M. E. G. Lyons. The Oxygen Evolution Reaction: Mechanistic Concepts and Catalyst Design. *Photoelectrochemical Solar Fuel Production: From Basic Principles to Advanced Devices*. Ed. by S. Giménez and J. Bisquert. Cham: Springer International Publishing, 2016, 41.

[11] S. Okamoto, O. Kitakami, and Y. Shimada. Enhancement of magnetic anisotropy of hydrogenated Pd/Co/Pd trilayers. *Journal of Magnetism and Magnetic Materials* **239** (2002), 313.

[12] W. C. Lin, C. J. Tsai, B. Y. Wang, C. H. Kao, and W. F. Pong. Hydrogenation induced reversible modulation of perpendicular magnetic coercivity in Pd/Co/Pd films. *Applied Physics Letters* **102** (2013), 252404.

[13] K. Munbodh, F. A. Perez, and D. Lederman. Changes in magnetic properties of Co/Pd multilayers induced by hydrogen absorption. *Journal of Applied Physics* **111** (2012), 123919.

[14] J. O. Bockris and A. K. N. Reddy. *Modern Electrochemistry Volume 2*. New York: Plenum Press, 1970.

[15] W. Schmickler and E. Santos. *Interfacial Electrochemistry*. Second Edition. Berlin: Springer-Verlag, 2010.

[16] A. J. Bard and L. R. Faulkner. *ELECTROCHEMICAL METHODS Fundamentals and Applications*. Second Edition. New York: John Wiley & Sons, Inc., 2001.

[17] C. H. Haman, A. Hamnett, and W. Vielstich. *Electrochemistry*. Weinheim: Wiley-VCH Verlag GmbH & Co. KGaA, 2007.

[18] R. Guidelli, R. G. Compton, J. M. Feliu, E. Gileadi, J. Lipkowski, W. Schmickler, and S. Trasatti. Defining the transfer coefficient in electrochemistry: An assessment (IUPAC Technical Report). *Pure and Applied Chemistry* **86** (2014), 245.

[19] J. Chivot, L. Mendoza, C. Mansour, T. Pauporté, and M. Cassir. New insight in the behaviour of Co-H_2O system at 25-150 °C, based on revised Pourbaix diagrams. *Corrosion Science* **50** (2008), 62.

[20] M. Bajdich, M. García-Mota, A. Vojvodic, J. K. Nørskov, and A. T. Bell. Theoretical Investigation of the Activity of Cobalt Oxides for the Electrochemical Oxidation of Water. *Journal of the American Chemical Society* **135** (2013), 13521.

[21] P. Allongue, L. Cagnon, C. Gomes, A. Gündel, and V. Costa. Electrodeposition of Co and Ni/Au(111) ultrathin layers. Part I: nucleation and growth mechanisms from in situ STM. *Surface Science* **557** (2004), 41.

[22] J. A. Koza, Z. He, A. S. Miller, and J. A. Switzer. Electrodeposition of crystalline Co_3O_4 - A catalyst for the oxygen evolution reaction. *Chemistry of Materials* **24** (2012), 3567.

[23] D. D. Macdonald. On the Existence of Our Metals-Based Civilization. *Journal of The Electrochemical Society* **153** (2006), B213.

[24] A. Güntherschulze and H. Betz. Neue Untersuchungen über die elektrolytische Ventilwirkung. I. Die Oxydschicht des Tantals. *Zeitschrift für Physik* **68** (1931), 145.

[25] E. Verwey. Electrolytic conduction of a solid insulator at high fields. *Physica* **2** (1935), 1059.

[26] N. Cabrera and N. F. Mott. Theory of the oxidation of metals. *Reports on Progress in Physics* **12** (1949), 163.

[27] F. P. Fehlner and N. F. Mott. Low-Temperature Oxidation. *Oxidation of Metals* **2** (1970), 59.

[28] N. Sato and M. Cohen. The Kinetics of Anodic Oxidation of Iron in Neutral Solution: I. Steady Growth Region. *Journal of The Electrochemical Society* **111** (1964), 512.

[29] K. J. Vetter. General kinetics of passive layers on metals. *Electrochimica Acta* **16** (1971), 1923.

[30] K. J. Vetter and F. Gorn. Kinetics of layer formation and corrosion processes of passive iron in acid solutions. *Electrochimica Acta* **18** (1973), 321.

[31] R. Kirchheim. Growth kinetics of passive films. *Electrochimica Acta* **32** (1987), 1619.

[32] H. J. Engell. Stability and Breakdown Phenomena of Passivating Films. *Electrochimica Acta* **22** (1977), 987.

[33] D. Macdonald. The Point Defect Model for the Passive State. *Journal of The Electrochemical Society* **139** (1992), 3434.

[34] F. Reikowski, F. Maroun, N. Di, P. Allongue, J. Stettner, and O. M. Magnussen. In situ surface X-ray diffraction study of ultrathin epitaxial Co films on Au(111) in alkaline solution. *Electrochimica Acta* **197** (2016), 273.

[35] W. K. Behl and J. E. Toni. Anodic oxidation of cobalt in potassium hydroxide electrolytes. *Journal of Electroanalytical Chemistry and Interfacial Electrochemistry* **31** (1971), 63.

[36] T. R. Jayaraman, V. K. Venkatesan, and H. V. K. Udupa. Cyclic Voltammetric Studies of Electroless Cobalt in NaOH. *Electrochimica Acta* **20** (1975), 209.

[37] B. Warren. *X-ray diffraction*. New York: Dover Publications, Inc., 1990.

[38] J. Als-Nielsen and D. McMorrow. *Elements of Modern X-ray Physics*. Second Edition. John Wiley & Sons, Ltd, 2011.

[39] I. K. Robinson and D. J. Tweet. Surface X-ray diffraction. *Reports on Progress in Physics* **55** (1992), 599.

[40] D. Waasmaier and A. Kirfel. New analytical scatteringfactor functions for free atoms and ions. *Acta Crystallographica Section A* **51** (1995), 416.

[41] T. Wiegmann. Charakterisierung dünner Au(111)-Schichten auf H-Si(111) mittels Röntgenstreuung in Transmissionsgeometrie. MA thesis. Christian-Albrechts-Universität, 2015.

[42] F. Golks. In situ Surface X-Ray Diffraction Studies of the Copper-Electrolyte Interface: Atomic Structure and Homoepitaxial Growth. PhD thesis. Christian-Albrechts-Universität, 2011.

[43] A. H. Ayyad, J. Stettner, and O. M. Magnussen. Electrocompression of the Au(111) Surface Layer during Au Electrodeposition. *Physical Review Letters* **94** (2005), 066106.

[44] F. Carla, O. Balmes, J. Drnec, and R. Felici. Electrochemical flow cell setup for in-situ Surface X-ray Diffraction. *221st ECS Meeting, The Electrochemical Society* (2012).

[45] M. L. Foresti, A. Pozzi, M. Innocenti, G. Pezzatini, F. Loglio, E. Salvietti, A. Giusti, F. D'Anca, R. Felici, and F. Borgatti. In situ X-ray analysis under controlled potential conditions: An innovative setup and its application to the investigation of ultrathin films electrodeposited on Ag(111). *Electrochimica Acta* **51** (2006), 5532.

[46] W. Schwarzacher, J. Gray, and X. D. Zhu. Oblique Incidence Reflectivity Difference as an In Situ Probe of Co Electrodeposition on Polycrystalline Au. *Electrochemical and Solid-State Letters* **6** (2003), 73.

[47] S. Royer and D. Duprez. Catalytic Oxidation of Carbon Monoxide over Transition Metal Oxides. *ChemCatChem* **3** (2011), 24.

[48] R. Subbaraman, D. Tripkovic, K.-C. Chang, D. Strmcnik, A. P. Paulikas, P. Hirunsit, M. Chan, J. Greeley, V. Stamenkovic, and N. M. Markovic. Trends in activity for the water electrolyser reactions on 3d M(Ni,Co,Fe,Mn) hydr(oxy)oxide catalysts. *Nature Materials* **11** (2012), 550.

[49] A. Singh and L. Spiccia. Water oxidation catalysts based on abundant 1st row transition metals. *Coordination Chemistry Reviews* **257** (2013), 2607.

[50] R. Frydendal, M. Busch, N. B. Halck, E. a. Paoli, P. Krtil, I. Chorkendorff, and J. Rossmeisl. Enhancing Activity for the Oxygen Evolution Reaction: The Beneficial Interaction of Gold with Manganese and Cobalt Oxides. *ChemCatChem* **7** (2015), 149.

[51] J. W. Schultze and A. W. Hassel. Passivity of Metals, Alloys and Semiconductors. *Encyclopedia of Electrochemistry, Volume 4, Corrosion and Oxide Films*. Ed. by A. J. Bard, M. Stratmann, and G. S. Frankel. Weinheim: Willey-VCH, 2003, 188.

[52] X. Deng and H. Tüysüz. Cobalt-Oxide-Based Materials as Water Oxidation Catalyst: Recent Progress and Challenges. *ACS Catalysis* **4** (2014), 3701.

[53] L. Liao, Q. Zhang, Z. Su, Z. Zhao, Y. Wang, Y. Li, X. Lu, D. Wei, G. Feng, Q. Yu, X. Cai, J. Zhao, Z. Ren, H. Fang, F. Robles-Hernandez, S. Baldelli, and J. Bao. Efficient solar water-splitting using a nanocrystalline CoO photocatalyst. *Nature Nanotechnology* **9** (2013), 69.

[54] B. S. Yeo and A. T. Bell. Enhanced Activity of Gold-Supported Cobalt Oxide for the Electrochemical Evolution of Oxygen. *Journal of the American Chemical Society* **133** (2011), 5587.

[55] D. Friebel, M. Bajdich, B. S. Yeo, M. W. Louie, D. J. Miller, H. Sanchez Casalongue, F. Mbuga, T.-C. Weng, D. Nordlund, D. Sokaras, R. Alonso-Mori, A. T. Bell, and A. Nilsson. On the chemical state of Co oxide electrocatalysts during alkaline water splitting. *Physical Chemistry Chemical Physics* **15** (2013), 17460.

[56] M. Grdeń and J. Jagiełło. Oxidation of electrodeposited cobalt electrodes in an alkaline electrolyte. *Journal of Solid State Electrochemistry* **17** (2012), 145.

[57] A. S. Walton, J. Fester, M. Bajdich, M. A. Arman, J. Osiecki, J. Knudsen, A. Vojvodic, and J. V. Lauritsen. Interface Controlled Oxidation States in Layered Cobalt Oxide Nanoislands on Gold. *ACS Nano* **9** (2015), 2445.

[58] R. D. Cowling and A. C. Riddiford. The Anodic Behaviour of Cobalt in Alkaline Solutions. *Electrochimica Acta* **14** (1969), 981.

[59] H. Meier, J. Vilche, and A. Arvía. The electrochemical behaviour of cobalt in alkaline solutions part II. The potentiodynamic response of $Co(OH)_2$ electrodes. *Journal of Electroanalytical Chemistry and Interfacial Electrochemistry* **138** (1982), 367.

[60] I. Novoselsky and N. Menglisheva. Investigation of kinetics of initial stages of cobalt electrode passivation by voltamperometric method. Experiment and theory of consecutive surface electro-chemical reaction complicated by chemical steps of dissolution intermediates. *Electrochimica Acta* **29** (1984), 21.

[61] W. A. Badawy, F. M. Al-Kharafi, and J. R. Al-Ajmi. Electrochemical behaviour of cobalt in aqueous solutions of different pH. *Journal of Applied Electrochemistry* **30** (2000), 693.

[62] K. M. Ismail and W. A. Badawy. Electrochemical and XPS investigations of cobalt in KOH solutions. *Journal of Applied Electrochemistry* **30** (2000), 1303.

[63] I. Epelboin, C. Gabrielli, and P. Morel. Etude de la passivation du cobalt en milieu sulfurique. *Electrochimica Acta* **18** (1973), 509.

[64] S. Ando, T. Suzuki, and K. Itaya. In situ electrochemical scanning tunneling microscopy of Co(0001) single crystal electrodes in acidic solution. *Journal of Electroanalytical Chemistry* **431** (1997), 277.

[65] A. Foelske, J. Kunze, and H.-H. Strehblow. Initial stages of hydroxide formation and its reduction on Co(0001) studied by in situ STM and XPS in 0.1 M NaOH. *Surface Science* **554** (2004), 10.

[66] N. Di, J. Kubal, Z. Zeng, J. Greeley, F. Maroun, and P. Allongue. Influence of controlled surface oxidation on the magnetic anisotropy of Co ultrathin films. *Applied Physics Letters* **106** (2015), 122405.

[67] L. Cagnon, T. Devolder, R. Cortes, A. Morrone, J. Schmidt, C. Chappert, and P. Allongue. Enhanced interface perpendicular magnetic anisotropy in electrodeposited Co/Au(111) layers. *Physical Review B* **63** (2001), 104419.

[68] S. Roobol, W. Onderwaater, J. Drnec, R. Felici, and J. Frenken. BINoculars: data reduction and analysis software for two-dimensional detectors in surface X-ray diffraction. *Journal of Applied Crystallography* **48** (2015), 1324.

[69] P. Prod'homme, F. Maroun, R. Cortès, P. Allongue, J. Hamrle, J. Ferré, J.-P. Jamet, and N. Vernier. Preparation, characterization and magneto-optical investigations of electrodeposited Co/Au films. *Journal of Magnetism and Magnetic Materials* **315** (2007), 26.

[70] Y. Gründer, F. U. Renner, T. L. Lee, D. L. Dheeraj, B. O. Fimland, and J. Zegenhagen. The electrodeposition of copper onto UHV-prepared GaAs(001) surfaces. *Surface Science* **603** (2009), L105.

[71] M. Born and E. Wolf. *Principles Of Optics*. London: Pergamon Press, 1970.

[72] W. Feitknecht and W. Lotmar. Über Mischfällungen von Nickel-Zink- und Kobalt-Zink-Hydroxyd (4. Mitteilung über topochemische Reaktionen kompakt-disperser Stoffe). *Helvetica Chimica Acta* **18** (1935), 1369.

[73] K. Gayer and A. Garrett. The solubility of cobalt hydroxide, $Co(OH)_2$, in solutions of hydrochloric acid and sodium hydroxide at 25°. *Journal of the American Chemical Society* **72** (1950), 8.

[74] G. M. Hale and M. R. Querry. Optical Constants of Water in the 200-nm to 200-microm Wavelength Region. *Applied Optics* **12** (1973), 555.

[75] E. D. Palik. *Handbook of Optical Constants of Solids*. London: Academic Press, 1985.

[76] E. Vlieg. ROD: A program for surface X-ray crystallography. *Journal of Applied Crystallography* **33** (2000), 401.

[77] F. Reikowski, F. Maroun, I. Pacheco, T. Wiegmann, P. Allongue, J. Stettner, and O. M. Magnussen. Operando Surface X-ray Diffraction Studies of Structurally Defined Co_3O_4 and CoOOH Thin Films during Oxygen Evolution. *ACS Catalysis* **9** (2019), 3811.

[78] N. S. Lewis and D. G. Nocera. Powering the planet: Chemical challenges in solar energy utilization. *Proceedings of the National Academy of Sciences* **103** (2006), 15729.

[79] M. W. Kanan and D. G. Nocera. In Situ Formation of an Oxygen-Evolving Catalyst in Neutral Water Containing Phosphate and Co^{2+}. *Science* **321** (2008), 1072.

[80] N.-T. Suen, S.-F. Hung, Q. Quan, N. Zhang, Y.-J. Xu, and H. M. Chen. Electrocatalysis for the oxygen evolution reaction: recent development and future perspectives. *Chemical Society Reviews* **46** (2017), 337.

[81] C. C. L. McCrory, S. Jung, I. M. Ferrer, S. M. Chatman, J. C. Peters, and T. F. Jaramillo. Benchmarking Hydrogen Evolving Reaction and Oxygen Evolving Reaction Electrocatalysts for Solar Water Splitting Devices. *Journal of the American Chemical Society* **137** (2015), 4347.

[82] M. S. Burke, S. Zou, L. J. Enman, J. E. Kellon, C. A. Gabor, E. Pledger, and S. W. Boettcher. Revised Oxygen Evolution Reaction Activity Trends for First-Row Transition-Metal (Oxy)hydroxides in Alkaline Media. *The Journal of Physical Chemistry Letters* **6** (2015), 3737.

[83] R. L. Doyle, I. J. Godwin, M. P. Brandon, and M. E. G. Lyons. Redox and electrochemical water splitting catalytic properties of hydrated metal oxide modified electrodes. *Physical Chemistry Chemical Physics* **15** (2013), 13737.

[84] C. Pirovano and S. Trasatti. The point of zero charge of Co_3O_4: Effect of the preparation procedure. *Journal of Electroanalytical Chemistry and Interfacial Electrochemistry* **180** (1984), 171.

[85] Y. Dong, K. He, L. Yin, and A. Zhang. A facile route to controlled synthesis of Co_3O_4 nanoparticles and their environmental catalytic properties. *Nanotechnology* **18** (2007), 435602.

[86] S. R. Alvarado, Y. Guo, T. P. A. Ruberu, A. Bakac, and J. Vela. Photochemical versus Thermal Synthesis of Cobalt Oxyhydroxide Nanocrystals. *The Journal of Physical Chemistry C* **116** (2012), 10382.

[87] A. Bergmann, E. Martinez-Moreno, D. Teschner, P. Chernev, M. Gliech, J. F. de Araújo, T. Reier, H. Dau, and P. Strasser. Reversible amorphization and the catalytically active state of crystalline Co_3O_4 during oxygen evolution. *Nature Communications* **6** (2015), 8625.

[88] A. J. Esswein, M. J. McMurdo, P. N. Ross, A. T. Bell, and T. D. Tilley. Size-Dependent Activity of Co_3O_4 Nanoparticle Anodes for Alkaline Water Electrolysis. *The Journal of Physical Chemistry C* **113** (2009), 15068.

[89] C. M. Hull, J. A. Koza, and J. A. Switzer. Electrodeposition of epitaxial $Co(OH)_2$ on gold and conversion to epitaxial CoOOH and Co_3O_4. *Journal of Materials Research* **31** (2016), 3324.

[90] Y. Surendranath, M. Dinca, and D. G. Nocera. Electrolyte-Dependent Electrosynthesis and Activity of Cobalt-Based Water Oxidation Catalysts. *Journal of the American Chemical Society* **131** (2009), 2615.

[91] M. B. Stevens, L. J. Enman, A. S. Batchellor, M. R. Cosby, A. E. Vise, C. D. M. Trang, and S. W. Boettcher. Measurement Techniques for the Study of Thin Film Heterogeneous Water Oxidation Electrocatalysts. *Chemistry of Materials* **29** (2017), 120.

[92] F. Song, L. Bai, A. Moysiadou, S. Lee, C. Hu, L. Liardet, and X. Hu. Transition metal oxides as electrocatalysts for the oxygen evolution reaction in alkaline solutions: An application-inspired renaissance. *Journal of the American Chemical Society* **140** (2018), 7748.

[93] A. Bergmann, T. E. Jones, E. Martinez Moreno, D. Teschner, P. Chernev, M. Gliech, T. Reier, H. Dau, and P. Strasser. Unified structural motifs of the catalytically active state of Co(oxyhydr)oxides during the electrochemical oxygen evolution reaction. *Nature Catalysis* **1** (2018), 711.

[94] C. W. Tung, Y. Y. Hsu, Y. P. Shen, Y. Zheng, T. S. Chan, H. S. Sheu, Y. C. Cheng, and H. M. Chen. Reversible adapting layer produces robust single-crystal electrocatalyst for oxygen evolution. *Nature Communications* **6** (2015), 8106.

[95] M. Favaro, J. Yang, S. Nappini, E. Magnano, F. M. Toma, E. J. Crumlin, J. Yano, and I. D. Sharp. Understanding the Oxygen Evolution Reaction Mechanism on CoO_x using Operando Ambient-Pressure X-ray Photoelectron Spectroscopy. *Journal of the American Chemical Society* **139** (2017), 8960.

[96] L. Giordano, B. Han, M. Risch, W. T. Hong, R. R. Rao, K. A. Stoerzinger, and Y. Shao-horn. pH dependence of OER activity of oxides : Current and future perspectives. *Catalysis Today* **262** (2016), 2.

[97] C. H. M. van Oversteeg, H. Q. Doan, F. M. F. de Groot, and T. Cuk. In situ X-ray absorption spectroscopy of transition metal based water oxidation catalysts. *Chemical Society Reviews* **46** (2017), 102.

[98] M. Risch, F. Ringleb, M. Kohlhoff, P. Bogdanoff, P. Chernev, I. Zaharieva, and H. Dau. Water oxidation by amorphous cobalt-based oxides: in situ tracking of redox transitions and mode of catalysis. *Energy and Environmental Science* **8** (2015), 661.

[99] J. Yang, J. K. Cooper, F. M. Toma, K. A. Walczak, M. Favaro, J. W. Beeman, L. H. Hess, C. Wang, C. Zhu, S. Gul, J. Yano, C. Kisielowski, A. Schwartzberg, and I. D. Sharp. A multifunctional biphasic water splitting catalyst tailored for integration with high-performance semiconductor photoanodes. *Nature Materials* **16** (2017), 335.

[100] A. M. Ullman, C. N. Brodsky, N. Li, S. L. Zheng, and D. G. Nocera. Probing Edge Site Reactivity of Oxidic Cobalt Water Oxidation Catalysts. *Journal of the American Chemical Society* **138** (2016), 4229.

[101] H. M. A. Amin and H. Baltruschat. How many surface atoms in Co_3O_4 take part in oxygen evolution? Isotope labeling together with differential electrochemical mass spectrometry. *Physical Chemistry Chemical Physics* **19** (2017), 25527.

[102] M. Zhang, M. De Respinis, and H. Frei. Time-resolved observations of water oxidation intermediates on a cobalt oxide nanoparticle catalyst. *Nature Chemistry* **6** (2014), 362.

[103] M. Zhang and H. Frei. Water Oxidation Mechanisms of Metal Oxide Catalysts by Vibrational Spectroscopy of Transient Intermediates. *Annual Review of Physical Chemistry* **68** (2017), 209.

[104] M. Risch, V. Khare, I. Zaharieva, L. Gerencser, P. Chernev, and H. Dau. Cobalt - Oxo Core of a Water-Oxidizing Catalyst Film. *Journal of the American Chemical Society* **131** (2009), 6936.

[105] J. Chen and A. Selloni. First Principles Study of Cobalt (Hydr)oxides under Electrochemical Conditions. *The Journal of Physical Chemistry C* **117** (2013), 20002.

[106] C. P. Plaisance and R. A. Van Santen. Structure Sensitivity of the Oxygen Evolution Reaction Catalyzed by Cobalt(II,III) Oxide. *Journal of the American Chemical Society* **137** (2015), 14660.

[107] K. Klingan, F. Ringleb, I. Zaharieva, J. Heidkamp, P. Chernev, D. Gonzalez-Flores, M. Risch, A. Fischer, and H. Dau. Water Oxidation by Amorphous Cobalt-Based Oxides: Volume Activity and Proton Transfer to Electrolyte Bases. *ChemSusChem* **7** (2014), 1301.

[108] M. Zhang and H. Frei. Towards a Molecular Level Understanding of the Multi-Electron Catalysis of Water Oxidation on Metal Oxide Surfaces. *Catalysis Letters* **145** (2015), 420.

[109] J. Xiao, Q. Kuang, S. Yang, F. Xiao, S. Wang, and L. Guo. Surface Structure Dependent Electrocatalytic Activity of Co_3O_4 Anchored on Graphene Sheets toward Oxygen Reduction Reaction. *Scientific Reports* **3** (2013), 2300.

[110] F. Song and X. Hu. Exfoliation of layered double hydroxides for enhanced oxygen evolution catalysis. *Nature Communications* **5** (2014), 4477.

[111] J. Huang, J. Chen, T. Yao, J. He, S. Jiang, Z. Sun, Q. Liu, W. Cheng, F. Hu, Y. Jiang, Z. Pan, and S. Wei. CoOOH Nanosheets with High Mass Activity for Water Oxidation. *Angewandte Chemie International Edition* **54** (2015), 8722.

[112] F. Faisal, M. Bertram, C. Stumm, S. Cherevko, S. Geiger, O. Kasian, Y. Lykhach, O. Lytken, K. J. Mayrhofer, O. Brummel, and J. Libuda. Atomically Defined Co_3O_4(111) Thin Films Prepared in Ultrahigh Vacuum: Stability under Electrochemical Conditions. *The Journal of Physical Chemistry C* **122** (2018), 7236.

[113] J. Wang, B. M. Ocko, A. J. Davenport, and H. S. Isaacs. In situ x-ray-diffraction and -reflectivity studies of the Au(111)/electrolyte interface: Reconstruction and anion adsorption. *Physical Review B* **46** (1992), 10321.

[114] X. Liu and C. T. Prewitt. High-Temperature X-ray Diffraction Study of Co_3O_4: Transition from Normal to Disordered Spinel. *Physics and Chemistry of Minerals* **17** (1990), 168.

[115] R. G. Delaplane, J. A. Ibers, J. R. Ferraro, and J. J. Rush. Diffraction and spectroscopic studies of the cobaltic acid system $HCoO_2$-$DCoO_2$. *The Journal of Chemical Physics* **50** (1969), 1920.

[116] S. Trasatti and O. A. Petrii. Real Surface Area Measurements in Electrochemistry. *Journal of Electroanalytical Chemistry* **327** (1992), 353.

[117] T. Binninger, R. Mohamed, K. Waltar, E. Fabbri, P. Levecque, R. Kötz, and T. J. Schmidt. Thermodynamic explanation of the universal correlation between oxygen evolution activity and corrosion of oxide catalysts. *Scientific Reports* **5** (2015), 12167.

[118] M. García-Mota, M. Bajdich, V. Viswanathan, A. Vojvodic, A. T. Bell, and J. K. Nørskov. Importance of Correlation in Determining Electrocatalytic Oxygen Evolution Activity on Cobalt Oxides. *The Journal of Physical Chemistry C* **116** (2012), 21077.

[119] F. Zasada, J. Grybos, W. Piskorz, and Z. Sojka. Cobalt Spinel (111) Facets of Various Stoichiometry - DFT+U and Ab Initio Thermodynamic Investigations. *The Journal of Physical Chemistry C* **122** (2018), 2866.

[120] D. D. Macdonald. The history of the Point Defect Model for the passive state: A brief review of film growth aspects. *Electrochimica Acta* **56** (2011), 1761.

[121] A. Veluchamy, D. Sherwood, B. Emmanuel, and I. S. Cole. Critical review on the passive film formation and breakdown on iron electrode and the models for the mechanisms underlying passivity. *Journal of Electroanalytical Chemistry* **785** (2017), 196.

[122] Y. Surendranath, M. W. Kanan, and D. G. Nocera. Mechanistic Studies of the Oxygen Evolution Reaction by a Cobalt-Phosphate Catalyst at Neutral pH. *Journal of the American Chemical Society* **132** (2010), 16501.

[123] T. Ama, M. Rashid, T. Yonemura, H. Kawaguchi, and T. Yasui. Cobalt(III) complexes containing incomplete Co_3O_4 or complete Co_4O_4 cubane core. *Coordination Chemistry Reviews* **198** (2000), 101.

[124] R. Zhang, Y.-C. Zhang, L. Pan, G.-Q. Shen, N. Mahmood, Y.-H. Ma, Y. Shi, W. Jia, L. Wang, X. Zhang, W. Xu, and J.-J. Zou. Engineering Cobalt Defects in Cobalt Oxide for Highly Efficient Electrocatalytic Oxygen Evolution. *ACS Catalysis* **8** (2018), 3803.

[125] T. Deng, W. Zhang, O. Arcelus, J.-G. Kim, J. Carrasco, S. J. Yoo, W. Zheng, J. Wang, H. Tian, H. Zhang, X. Cui, and T. Rojo. Atomic-level energy storage mechanism of cobalt hydroxide electrode for pseudocapacitors. *Nature Communications* **8** (2017), 15194.

[126] R. Boggio, A. Carugati, and S. Trasatti. Electrochemical surface properties of Co_3O_4 electrodes. *Journal of Applied Electrochemistry* **17** (1987), 828.

[127] Y. C. Liu, J. A. Koza, and J. A. Switzer. Conversion of electrodeposited $Co(OH)_2$ to CoOOH and Co_3O_4, and comparison of their catalytic activity for the oxygen evolution reaction. *Electrochimica Acta* **140** (2014), 359.

[128] S. Grazulis, D. Chateigner, R. T. Downs, A. F. T. Yokochi, M. Quiro, L. Lutterotti, E. Manakova, J. Butkus, P. Moeck, and A. Le Bail. Crystallography Open Database – an open-access collection of crystal structures cif applications. *Journal of Applied Crystallography* **42** (2009), 726.

[129] F. Maroun, F. Reikowski, N. Di, T. Wiegmann, J. Stettner, O. M. Magnussen, and P. Allongue. Potential dependence of the structure and magnetism of electrodeposited Pd/Co/Au(111) layers. *Journal of Electroanalytical Chemistry* **819** (2018), 322.

[130] P. Grünberg. Layered magnetic structures: History, highlights, applications. *Physics Today* **54** (2001), 31.

[131] C. Chappert, A. Fert, and F. N. Van Dau. The emergence of spin electronics in data storage. *Nature Materials* **6** (2007), 813.

[132] U. Gradmann and J. Müller. Flat Ferromagnetic, Epitaxial 48Ni/52Fe(111) Films of few Atomic Layers. *Physica Status Solidi B* **27** (1968), 313.

[133] M. T. Johnson, P. J. H. Blomen, F. J. A. den Broeder, and J. J. de Vries. Magnetic anisotropy in metallic multilayers. *Reports on Progress in Physics* **59** (1996), 1409.

[134] D. Sander, A. Enders, and J. Kirschner. Stress and magnetic properties of surfaces and ultrathin films. *Journal of Magnetism and Magnetic Materials* **200** (1999), 439.

[135] C. A. F. Vaz, J. A. C. Bland, and G. Lauhoff. Magnetism in ultrathin film structures. *Reports on Progress in Physics* **71** (2008), 056501.

[136] P. Allongue and F. Maroun. Metal electrodeposition on single crystal metal surfaces mechanisms, structure and applications. *Current Opinion in Solid State and Materials Science* **10** (2006), 173.

[137] C. A. Lucas, F. Maroun, N. Sisson, P. Thompson, Y. Gründer, R. Cortès, and P. Allongue. Film and Interface Atomic Structures of Electrodeposited Co/Au(111) Layers: An in Situ X-ray Scattering Study as a Function of the Surface Chemistry and the Electrochemical Potential. *The Journal of Physical Chemistry C* **120** (2016), 3360.

[138] F. A. Möller, J. Kintrup, A. Lachenwitzer, O. M. Magnussen, and R. J. Behm. In situ STM study of the electrodeposition and anodic dissolution of ultrathin epitaxial Ni films on Au(111). *Physical Review B* **56** (1997), 12506.

[139] H. F. Jurca, A. Damian, C. Gougaud, D. Thiaudière, R. Cortès, F. Maroun, and P. Allongue. Epitaxial Electrodeposition of Fe on Au(111): Structure, Nucleation, and Growth Mechanisms. *The Journal of Physical Chemistry C* **120** (2016), 16080.

[140] Y. Kuo, P. Yen, W. Chen, S. Chen, and S. Yau. In situ scanning tunneling microscopy study of cobalt thin film electrodeposited on Pt(111) electrode. *Electrochimica Acta* **112** (2013), 831.

[141] W. Schindler, O. Schneider, and J. Kirschner. Electrodeposition of ultrathin magnetic films of Fe and Co. *Journal of Applied Physics* **81** (1997), 3915.

[142] J. Bubendorff, E. Beaurepaire, C. Mény, P. Panissod, and J. Bucher. Perpendicular magnetization in ultrathin electrodeposited cobalt films. *Physical Review B* **56** (1997), R7120.

[143] T. Yokoyama, K. Amemiya, Y. Yonamoto, D. Matsumura, and T. Ohta. Anisotropic magnetization of CO adsorbed on ferromagnetic metal thin films studied by X-ray magnetic circular dichroism. *Journal of Electron Spectroscopy and Related Phenomena* **119** (2001), 207.

[144] N. Tournerie, A. P. Engelhardt, F. Maroun, and P. Allongue. Influence of the surface chemistry on the electric-field control of the magnetization of ultrathin films. *Physical Review B* **86** (2012), 104434.

[145] C. S. Chang, M. Kostylev, and E. Ivanov. Metallic spintronic thin film as a hydrogen sensor. *Applied Physics Letters* **102** (2013), 142405.

[146] F. Matsukura, Y. Tokura, and H. Ohno. Control of magnetism by electric fields. *Nature Nanotechnology* **10** (2015), 209.

[147] B. Dieny and M. Chshiev. Perpendicular magnetic anisotropy at transition metal/oxide interfaces and applications. *Reviews of Modern Physics* **89** (2017), 025008.

[148] M. W. Breiter. Dissolution and adsorption of hydrogen at smooth Pd wires at potentials of the alpha phase in sulfuric acid solution. *Journal of Electroanalytical Chemistry and Interfacial Electrochemistry* **81** (1977), 275.

[149] C. Gabrielli, P. P. Grand, A. Lasia, and H. Perrot. Investigation of Hydrogen Adsorption and Absorption in Palladium Thin Films II. Cyclic Voltammetry. *Journal of The Electrochemical Society* **151** (2004), A1937.

[150] H. Duncan and A. Lasia. Mechanism of hydrogen adsorption/absorption at thin Pd layers on Au(111). *Electrochimica Acta* **52** (2007), 6195.

[151] M. Baldauf and D. M. Kolb. A hydrogen adsorption and absorption study with ultrathin Pd overlayers on Au(111) and Au(100). *Electrochimica Acta* **38** (1993), 2145.

[152] C. Lebouin, Y. S. Olivier, E. Sibert, P. Millet, M. Maret, and R. Faure. Electrochemically elaborated palladium nanofilms on Pt(111): Characterization and hydrogen insertion study. *Journal of Electroanalytical Chemistry* **626** (2009), 59.

[153] L. B. Sheridan, Y. G. Kim, B. R. Perdue, K. Jagannathan, J. L. Stickney, and D. B. Robinson. Hydrogen adsorption, absorption, and desorption at palladium nanofilms formed on Au(111) by electrochemical atomic layer deposition (E-ALD): Studies using voltammetry and in situ scanning tunneling microscopy. *The Journal of Physical Chemistry C* **117** (2013), 15728.

[154] A. J. Maeland and T. R. P. Gibb. X-RAY DIFFRACTION OBSERVATIONS OF THE Pd-H_2 SYSTEM THROUGH THE CRITICAL REGION. *The Journal of Physical Chemistry* **65** (1961), 1270.

[155] C. Gabrielli, P. P. Grand, A. Lasia, and H. Perrot. Study of the hydrogen/palladium system by fast quartz microbalance techniques. *Electrochimica Acta* **47** (2002), 2199.

[156] C. Gabrielli, P. P. Grand, A. Lasia, and H. Perrot. Investigation of Hydrogen Adsorption and Absorption in Palladium Thin Films III. Impedance Spectroscopy. *Journal of The Electrochemical Society* **151** (2004), A1943.

[157] Y. Soldo-Olivier, E. Sibert, B. Previdello, M. C. Lafouresse, F. Maillard, and M. De Santis. H electro-insertion into Pd/Pt(111) nanofilms: An original method for isotherm measurement coupled to in situ surface X-ray diffraction structural study. *Electrochimica Acta* **112** (2013), 905.

[158] G. R. Stafford and U. Bertocci. In Situ Stress and Nanogravimetric Measurements During Underpotential Deposition of Pd on (111)-Textured Au. *The Journal of Physical Chemistry C* **113** (2009), 261.

[159] G. R. Stafford and U. Bertocci. In Situ Stress and Nanogravimetric Measurements During Hydrogen Adsorption/Absorption on Pd Overlayers Deposited onto (111)-Textured Au. *The Journal of Physical Chemistry C* **113** (2009), 13249.

[160] N. Tournerie, A. Engelhardt, F. Maroun, and P. Allongue. Probing the electrochemical interface with in situ magnetic characterizations: A case study of Co/Au(111) layers. *Surface Science* **631** (2015), 88.

[161] P. Allongue, H. Brune, and H. Gerischer. In situ STM observations of the etching of n-Si(111) in NaOH solutions. *Surface Science* **275** (1992), 414.

[162] P. Prod'homme, F. Maroun, R. Cortès, and P. Allongue. Electrochemical growth of ultraflat Au(111) epitaxial buffer layers on H–Si(111). *Applied Physics Letters* **93** (2008), 171901.

[163] P. Prodhomme, S. Warren, R. Cortès, H. F. Jurca, F. Maroun, and P. Allongue. Epitaxial growth of gold on H-Si(111): the determining role of hydrogen evolution. *ChemPhysChem* **11** (2010), 2992.

[164] N. Di, A. Damian, F. Maroun, and P. Allongue. Influence of Potential on the Electrodeposition of Co on Au(111) by In Situ STM and Reflectivity Measurements. *Journal of The Electrochemical Society* **163** (2016), D3062.

[165] A. Damian, F. Maroun, and P. Allongue. Selective growth and dissolution of Ni on a PdAu bimetallic surface by in situ STM: Determining the relative adsorbate-substrate interaction energy. *Physical Review Letters* **102** (2009), 196101.

[166] F. Lecadre, F. Maroun, and P. Allongue. Electrodeposition of Ag, Pd and Au on Ni monolayer islands on (1 × 1)-Au(111) by in-situ scanning tunneling microscopy. *Electrochimica Acta* **197** (2016), 241.

[167] A. Damian. PhD thesis. Ecole Polytechnique, 2009.

[168] M. Takahasi, K. Tamura, J. Mizuki, T. Kondo, and K. Uosaki. Orientation dependence of Pd growth on Au electrode surfaces. *Journal of Physics: Condensed Matter* **22** (2010), 474002.

[169] Y. Liu, D. Gokcen, U. Bertocci, and T. P. Moffat. Self-terminating growth of platinum films by electrochemical deposition. *Science* **338** (2012), 1327.

[170] A. E. Munter and B. J. Heuser. Deuterium phase behavior in thin-film Pd. *Physical Review B* **58** (1998), 678.

[171] M. H. Martin and A. Lasia. Study of the hydrogen absorption in Pd in alkaline solution. *Electrochimica Acta* **53** (2008), 6317.

[172] J. W. Shin, U. Bertocci, and G. R. Stafford. In Situ Stress Measurement During Hydrogen Sorption on Ultrathin (111)-Textured Pd Films in Alkaline Electrolyte. *Journal of The Electrochemical Society* **158** (2011), F127.

[173] R. Vollmer, T. Gutjahr-Löser, J. Kirschner, S. van Dijken, and B. Poelsema. Spin-reorientation transition in Ni films on Cu(001): The influence of H_2 adsorption. *Physical Review B* **60** (1999), 6277.

[174] M. Sakamaki, T. Konishi, T. Fujikawa, A. Persson, C. Andersson, O. Karis, D. Arvanitis, H. Rossner, and E. Holub-Krappe. Correlation of magnetism and structure for ultra thin Au/Co/Au films: Evidence for magnetoelastic effects. *Journal of Physics: Conference Series* **190** (2009), 012113.

[175] D. Sander. The correlation between mechanical stress and magnetic anisotropy in ultrathin films. *Reports on Progress in Physics* **62** (1999), 809.

[176] F. Reikowski, T. Wiegmann, J. Stettner, J. Drnec, V. Honkimäki, F. Maroun, P. Allongue, and O. M. Magnussen. Transmission Surface Diffraction for Operando Studies of Heterogeneous Interfaces. *The Journal of Physical Chemistry Letters* **8** (2017), 1067.

[177] A. A. Gewirth and B. K. Niece. Electrochemical Applications of in Situ Scanning Probe Microscopy. *Chemical Reviews* **97** (1997), 1129.

[178] K. Itaya. In situ scanning tunneling microscopy in electrolyte solutions. *Progress in Surface Science* **58** (1998), 121.

[179] M. J. Williamson, R. M. Tromp, P. M. Vereecken, R. Hull, and F. M. Ross. Dynamic microscopy of nanoscale cluster growth at the solid-liquid interface. *Nature Materials* **2** (2003), 532.

[180] H. Zheng, Y. S. Meng, and Y. Zhu. Frontiers of in situ electron microscopy. *MRS Bulletin* **40** (2015), 12.

[181] H. D. Abruna. *Electrochemical Interfaces. Modern Techniques for in-situ Interface Characterization*. VCH: New York, 1991.

[182] A. A. Gewirth and H. Siegenthaler. *Nanoscale probes of the solid/liquid interface*. Kluwer Academic Publishers, 1995.

[183] M. F. Toney and J. McBreen. In Situ Synchrotron X-Ray Techniques for Determining Atomic Structures at Electode/Electrolyte Interfaces. *Electrochemical Society Interface* **2** (1993), 22.

[184] E. Vlieg. X-Ray Diffraction from Surfaces and Interfaces. *Surface and Interface Science, Vol. 1*. Ed. by K. Wandelt. New York: Wiley-VCH, 2014.

[185] D. D. Fong, C. A. Lucas, M.-I. Richard, and M. F. Toney. X-Ray Probes for In Situ Studies of Interfaces. *MRS Bulletin* **35** (2010), 504.

[186] K. L. Mulfort, A. Mukherjee, O. Kokhan, P. Du, and D. M. Tiede. Structure-function analyses of solar fuels catalysts using in situ X-ray scattering. *Chemical Society Reviews* **42** (2013), 2215.

[187] A. Ulvestad, A. Singer, J. N. Clark, H. M. Cho, J. W. Kim, R. Harder, J. Maser, Y. S. Meng, and O. G. Shpyrko. Topological defect dynamics in operando battery nanoparticles. *Science* **348** (2015), 1344.

[188] A. M. Beale, S. D. M. Jacques, and B. M. Weckhuysen. Chemical imaging of catalytic solids with synchrotron radiation. *Chemical Society Reviews* **39** (2010), 4656.

[189] M. A. Bañares. Operando Spectroscopy: the Knowledge Bridge to Assessing Structure–Performance Relationships in Catalyst Nanoparticles. *Advanced Materials* **23** (2011), 5293.

[190] A. I. Frenkel, J. A. Rodriguez, and J. G. Chen. Synchrotron Techniques for In Situ Catalytic Studies: Capabilities, Challenges, and Opportunities. *ACS Catalysis* **2** (2012), 2269.

[191] U. Jung, A. Elsen, Y. Li, J. G. Smith, M. W. Small, E. A. Stach, A. I. Frenkel, and R. G. Nuzzo. Comparative in Operando Studies in Heterogeneous Catalysis: Atomic and Electronic Structural Features in the Hydrogenation of Ethylene over Supported Pd and Pt Catalysts. *ACS Catalysis* **5** (2015), 1539.

[192] F. Tao and P. A. Crozier. Atomic-Scale Observations of Catalyst Structures under Reaction Conditions and during Catalysis. *Chemical Reviews* **116** (2016), 3487.

[193] M. G. Samant, M. F. Toney, G. L. Borges, L. Blum, and O. R. Melroy. Grazing incidence x-ray diffraction of lead monolayers at a silver (111) and gold (111) electrode/electrolyte interface. *The Journal of Physical Chemistry* **92** (1988), 220.

[194] J. I. A. Wang, A. J. Davenport, H. S. Isaacs, and B. M. Ocko. Surface Charge-Induced Ordering of the Au(111) Surface. *Science* **255** (1992), 1416.

[195] I. M. Tidswell, N. M. Markovic, and P. N. Ross. Potential dependent surface relaxation of the Pt(001)/electrolyte interface. *Physical Review Letters* **71** (1993), 1601.

[196] C. A. Lucas, N. M. Markovic, and P. N. Ross. Surface Structure and Relaxation at the Pt(110)/Electrolyte Interface. *Physical Review Letters* **77** (1996), 4922.

[197] M. F. Toney, A. J. Davenport, L. J. Oblonsky, M. P. Ryan, and C. M. Vitus. Atomic Structure of the Passive Oxide Film Formed on Iron. *Physical Review Letters* **79** (1997), 4282.

[198] S. A. de Vries, P. Goedtkindt, S. L. Bennett, W. J. Huisman, M. J. Zwanenburg, D.-M. Smilgies, J. J. De Yoreo, W. J. P. van Enckevort, P. Bennema, and E. Vlieg. Surface Atomic Structure of KDP Crystals in Aqueous Solution: An Explanation of the Growth Shape. *Physical Review Letters* **80** (1998), 2229.

[199] H. Reichert, O. Klein, H. Dosch, M. Denk, V. Honkimäki, T. Lippmann, and G. Reiter. Observation of five-fold local symmetry in liquid lead. *Nature* **408** (2000), 839.

[200] F. Golks, K. Krug, Y. Gründer, J. Zegenhagen, J. Stettner, and O. M. Magnussen. High-speed in situ surface X-ray diffraction studies of the electrochemical dissolution of Au(001). *Journal of the American Chemical Society* **133** (2011), 3772.

[201] H. Reichert, V. Honkimäki, A. Snigirev, S. Engemann, and H. Dosch. A new X-ray transmission-reflection scheme for the study of deeply buried interfaces using high-energy microbeams. *Physica B: Condensed Matter* **336** (2003), 46.

[202] J. Gustafson, M. Shipilin, C. Zhang, A. Stierle, U. Hejral, U. Ruett, O. Gutowski, P.-A. Carlsson, M. Skoglundh, and E. Lundgren. High-Energy Surface X-ray Diffraction for Fast Surface Structure Determination. *Science* **343** (2014), 758.

[203] T. Takahashi, S. Nakatani, N. Okamoto, T. Ishikawa, and S. Kikuta. A study of the Si(111)$\sqrt{3} \times \sqrt{3}$-Ag surface by transmission X-ray diffraction and X-ray diffraction topography. *Surface Science* **242** (1991), 54.

[204] H. Tajiri, O. Sakata, and T. Takahashi. Surface X-ray diffraction in transmission geometry. *Applied Surface Science* **234** (2004), 403.

[205] C. Chen, K. D. Kepler, A. A. Gewirth, B. M. Ocko, and J. Wang. Electrodeposited Bismuth Monolayers on Au(111) Electrodes: Comparison of Surface X-Ray Scattering, Scanning Tunneling Microscopy, and Atomic Force Microscopy Lattice Structures. *The Journal of Physical Chemistry* **97** (1993), 7290.

[206] H. Brune and K. Kern. Chapter 5 Heteroepitaxial metal growth: the effects of strain. *Growth and Properties of Ultrathin Epitaxial Layers*. Ed. by D. A. King and D. P. Woodruff. Vol. 8. The Chemical Physics of Solid Surfaces. Amsterdam: Elsevier Science B.V., 1999.

[207] K. Krischer, N. Mazouz, and P. Grauel. Fronts, Waves, and Stationary Patterns in Electrochemical Systems. *Angewandte Chemie International Edition* **40** (2001), 850.

[208] C. A. Jeffrey, S. H. Zheng, E. Bohannan, D. A. Harrington, and S. Morin. X-ray characterization of as-deposited, epitaxial films of Bi(012) on Au(111). *Surface Science* **600** (2006), 95.

List of Acronyms

AFM Atomic Force Microscopy

CE Counter Electrode

CTR Crystal Truncation Rod

CV Cyclic Voltammetry

DEMS Differential Electrochemical Mass Spectroscopy

DFT Density Functional Theory

ECSA Electrochemical Surface Area

ESRF European Synchrotron Radiation Facility

FFPM Perfluoroelastomer

FWHM Full Width at Half Maximum

HER Hydrogen Evolution Reaction

HESXRD High Energy Surface X-ray Diffraction

ID Insertion Device

JCPDS Joint Committee on Powder Diffraction Standards

LEED Low-Energy Electron Diffraction

ML Monolayer

MOKE Magneto-Optical Kerr Effect

MSE Mercury Sulfate Electrode

OCP Open Circuit Potential

OER Oxygen Evolution Reaction

PCTFE Polychlorotrifluoroethylene

PDM Point Defect Model

PEEK Polyether Ether Ketone

PTFE Polytetrafluoroethylene

RDS Rate Determining Step

RE Reference Electrode

RHE Reversible Hydrogen Electrode

RMS Root Mean Square

SHE Standard Hydrogen Electrode

STM Scanning Tunneling Microscopy

SXRD Surface X-ray Diffraction

TOF Turnover Frequency

TSD Transmission Surface Diffraction

UHV Ultrahigh Vacuum

UPD Underpotential Deposition

WE Working Electrode

XAS X-ray Absorption Spectroscopy

XPS X-ray Photoelectron Spectroscopy

XRD X-ray Diffraction

Scientific Contributions

Publications

- ***Operando* Surface X-ray Diffraction Studies of Structurally Defined Co_3O_4 and CoOOH Thin Films During Oxygen Evolution**
  F. Reikowski, F. Maroun, I. Pacheco, T. Wiegmann, P. Allongue, J. Stettner, O. M. Magnussen
  ACS Catalysis **9** (2019), 3811-3821

- **Potential Dependence of the Structure and Magnetism of Electrodeposited Pd/Co/Au(111) Layers**
  F. Maroun, F. Reikowski, N. Di, T. Wiegmann, J. Stettner, O. M. Magnussen, P. Allongue
  Journal of Electroanalytical Chemistry **819** (2018), 322-330

- **Transmission Surface Diffraction**
  F. Reikowski, T. Wiegmann, J. Stettner, J. Drnec, V. Honkimäki, F. Maroun, P. Allongue, O. M. Magnussen
  ESRF Highlights 2017 (2018), 134-135

- **Transmission Surface Diffraction for *Operando* Studies of Heterogeneous Interfaces**
  F. Reikowski, T. Wiegmann, J. Stettner, J. Drnec, V. Honkimäki, F. Maroun, P. Allongue, O. M. Magnussen
  The Journal of Physical Chemistry Letters **8** (2017), 1067-1071

- ***In Situ* Surface X-ray Diffraction Study of Ultrathin Epitaxial Co Films on Au(111) in Alkaline Solution**
  F. Reikowski, F. Maroun, N. Di, P. Allongue, M. Ruge, J. Stettner, O. M. Magnussen
  Electrochimica Acta **197** (2016), 273-281

- **Initial Stages of Pt(111) Electrooxidation: Dynamic and Structural Studies by Surface X-ray Diffraction**
  J. Drnec, M. Ruge, F. Reikowski, B. Rahn, F. Carlà, R. Felici, J. Stettner, O. M. Magnussen, D. A. Harrington
  Electrochimica Acta **224** (2017), 220-227

- **Structural Reorganization of Pt(111) Electrodes by Electrochemical Oxidation and Reduction**
  M. Ruge, J. Drnec, B. Rahn, F. Reikowski, D. A. Harrington, F. Carlà, R. Felici, J. Stettner, O. M. Magnussen
  Journal of the American Chemical Society **139** (2017), 4532-4539

- **Electrochemical Oxidation of Smooth and Nanoscale Rough Pt(111): An *In Situ* Surface X-ray Scattering Study**
  M. Ruge, J. Drnec, B. Rahn, F. Reikowski, D. A. Harrington, F. Carlà, R. Felici, J. Stettner, O. M. Magnussen
  Journal of The Electrochemical Society **164** (2017), H608-H614

- **Pt Oxide and Oxygen Reduction at Pt(111) Studied by Surface X-ray Diffraction**
  J. Drnec, M. Ruge, F. Reikowski, B. Rahn, F. Carlà, R. Felici, J. Stettner, O. M. Magnussen, D. A. Harrington
  Electrochemistry Communications **84** (2017), 50-52

Oral Presentations

- ***In Situ* Surface X-ray Scattering Studies of Co/Au(111) Electrochemical Deposition and Oxidation**
  F. Reikowski, M. Ruge, N. Di , F. Carlà, F. Maroun, P. Allongue, J. Stettner, O. M. Magnussen
  Electrochem 2015
  Durham, September 2015

Poster Presentations

- ***Operando* Surface X-ray Diffraction Studies of Electrodeposited Co Oxide Thin Films During Oxygen Evolution**
  F. Reikowski, F. Maroun, T. Wiegmann, P. Allongue, J. Stettner, O. M. Magnussen
  DIPC School: PhotoElectroCatalysis at the Atomic Scale
  San Sebastián, June 2017

- **Transmission Surface Diffraction for *Operando* Studies of Heterogeneous Interfaces**
  F. Reikowski, T. Wiegmann, J. Stettner, J. Drnec, V. Honkimäki, F. Maroun, O. M. Magnussen
  Faraday Discussion - Single Entity Electrochemistry
  York, August 2016

- ***In Situ* Surface X-ray Scattering Studies of Pt(111) Electrochemical Oxidation**
  F. Reikowski, M. Ruge, B. Rahn, F. Carlà, J. Drnec, J. Stettner, D. A. Harrington, R. Felici, and O. M. Magnussen
  583. WE-Heraeus-Seminar
  Bad Honnef, January 2015

Awards

- **Royal Society of Chemistry Poster Prize**
  Faraday Discussion - Single Entity Electrochemistry
  York, August 2016

Acknowledgments

During the past years, I received great support from various people of different institutions who have considerably contributed to this work in one or the other way.

At first, I would like to express my sincere gratitude to my supervisor Prof. Dr. Olaf M. Magnussen for giving me the opportunity to work on this exciting project. His guidance and continuous support, combined with his extensive knowledge, were invaluable. What I appreciated in particular, was his ability and willingness to answer questions in a concise and comprehensible way at any time.

Likewise, I thank my second supervisor Dr. Jochim Stettner for his dedicated support, his insightful comments and for answering all my questions regarding the mysteries of reciprocal space.

I am very grateful for the exceptionally fruitful collaboration with Prof. Dr. Fouad Maroun and Prof. Dr. Philippe Allongue from the École Polytechnique in Palaiseau. In particular, I thank Fouad for building the optical reflectivity setup and for his help with the initial test of the cell. I had a great time during my two very exciting and instructive stays in Palaiseau and the productive and enjoyable shifts at the ESRF will be a long-lasting memory. Thanks for your warm hospitality and all your commitment.

In addition, I thank the numerous people involved in the experiments at the ESRF for the great teamwork. You always made the work enjoyable, even during beam dumps at 3 am. I particularly thank Dr. Jakub Drnec and Dr. Francesco Carla for a great collaboration and their tireless support at the beamlines ID03 and ID31, even at the craziest hours.

Many thanks go to Dr. Martin Ruge for introducing me to electrochemistry and surface X-ray diffraction. Beyond that, I owe him my excellent skills in cleaning glassware.

I sincerely thank all my fellow colleagues for stimulating discussions, and for all the fun we have had in the last four and a half years. I am particularly grateful to my office mates Dr. Sonja Lemke, Dr. Martin Ruge, Nicolai Krekiehn, Talina Rusch and Reihaneh Amirbeigiarab for a mostly peaceful coexistence, a great team spirit and the friendly atmosphere in the office. It was a pleasure to work with you.

Many thanks go to the administrative university staff, in particular to Monika Seeger and Claudia Läufer. Thank you for your precious support in administration and organization and for successfully preventing chaos. Beyond that, I like to thank Arnd Seeger and Karsten Tarhouni for technical support and the IEAP Workshop for building the custom equipment, in particular the electrochemical cell.

Finally, I thank my family and friends who provided moral and emotional support and helped me in every possible way.

Sworn Declaration

I hereby declare that – apart from the guidance of my supervisors Prof. Dr. O. M. Magnussen and Dr. J. Stettner – the content and design of this thesis is my own work. No other sources than those stated have been used. This work or parts of it have not been submitted as part of a doctoral examination procedure to another examining body. The thesis was prepared adhering to the Rules of Good Scientific Practice of the German Research Foundation. None of my academic degrees have ever been withdrawn. Part of this work is already published, my own contributions to these publications are summarized below.

Electrochimica Acta 197 (2016), 273-281, Chapter 5 Contributions to the preparation of the experiment. Participation in the experiments. Execution of the data analysis. Creation of the figures except Fig. 5.1, Fig. 5.8 and Fig. 5.11. Contributions to the writing of the manuscript.

ACS Catalysis 9 (2019), 3811-3821, Chapter 6 Preparation of the experiments (except the synthesis of the samples), including the development and construction of a novel electrochemical cell. Substantial contributions to the execution of experiments. Data analysis. Creation of the figures except Fig. 6.2, Fig. 6.6, Fig. 6.7 and Fig. 6.15. Substantial contributions to the writing of the manuscript. Substantial contributions to the interpretation of the results.

The Journal of Electroanalytical Chemistry 819 (2018), 322-330, Chapter 7 Preparation of the experiments (except the synthesis of the samples). Substantial contributions to the execution of experiments. Data analysis of the X-ray scattering experiments. Creation of the figures except Fig. 7.3 and Fig. 7.8 b,c. Substantial contributions to the writing of the manuscript. Substantial contributions to the interpretation of the results.

The Journal of Physical Chemistry Letters 8 (2017), 1067-1071, Chapter 8 Preparation of the experiments (except the synthesis of the samples). Substantial contributions to the execution of experiments. Data analysis. Creation of the figures except Fig. 8.2. Substantial contributions to the writing of the manuscript. Substantial contributions to the interpretation of the results.

Kiel, _____ _____

Finn Reikowski